Technische Universität München
TUM School of Natural Sciences

# Entanglement distribution with continuous and discrete variable systems

Joan Agustí Bruzón

Vollständiger Abdruck der von der TUM School of Natural Sciences der Technischen Universität München zur Erlangung des akademischen Grades eines

**Doktors der Naturwissenschaften (Dr. rer. nat.)**

genehmigten Dissertation.

Vorsitz: Prof. Dr. Eva Weig

Prüfer der Dissertation:

1. Prof. Dr. Peter Rabl
2. Hon-Prof. Ignacio Cirac, Ph.D.

Die Dissertation wurde am ______________ bei der Technischen Universität München eingereicht und durch die TUM School of Natural Sciences am ______________ angenommen.

# Abstract

The distribution of remote entanglement within small- and large-scale quantum networks is becoming a fundamental task as quantum computing and quantum communication mature into more advanced fields. Once entanglement has been remotely prepared and distributed, each node in the quantum network can generate, process, and store quantum information locally. However, due to the intrinsic decoherence of qubits over time, the protocols must operate faster than the system's decoherence rate. Therefore, identifying efficient entanglement distribution strategies that are fast, parallelizable, and require minimal external control is a crucial open challenge for the scalability of quantum technologies.

This thesis investigates autonomous entanglement distribution protocols between two and multiple physically separated qubits. The general idea behind these protocols is to use a nondegenerate parametric amplifier to generate Gaussian-entangled pairs of photons. By driving the qubits with the output of the parametric amplifier, the photons' correlations are mapped onto the qubits, generating a stationary entangled state. This work presents an in-depth theoretical analysis of such quantum networks, performing both analytical and numerical calculations, and investigates how much entanglement can be extracted in a realistic system. We also study the protocol's robustness by considering the most relevant experimental imperfections and provide concrete predictions for upcoming experimental realizations of our protocol with superconducting circuits. We then consider a larger network with an increasing number of qubits located along two separate waveguides. We demonstrate how to generate programmable entangled states by adjusting each qubit's detuning. With this approach, we can not only generate multiple bipartite entangled states on demand but also distribute genuine multipartite entangled states across the entire network. We provide a detailed estimate of the number of qubit pairs that can be achieved, assuming state-of-the-art experimental parameters. Finally, based on our analysis of finite-bandwidth effects in the photon source, we identify a completely novel mechanism for generating remote entanglement, which relies solely on a thermal photon source. This is particularly surprising since, for two qubits driven by a Markovian thermal source, remote qubit entanglement is generally not possible. However, we observe that as the bandwidth of the thermal source is reduced, the qubits gradually become more entangled. This protocol demonstrates how non-Markovian effects of otherwise highly incoherent photons can be exploited. As a potential application, we show that this mechanism can be used to generate highly entangled states in superconducting or phononic quantum networks by driving them with room-temperature thermal noise.

The protocols presented in this thesis provide an intriguing new approach for distributing large amounts of entanglement in a robust manner and with limited classical control.

The theoretical insights gained regarding their scalability and performance under realistic conditions serve as a guideline for initial experiments in this direction and highlight their significant potential for realizing large-scale quantum networks in the future.

# Kurzzusammenfassung

Die Verteilung von Verschränkung in kleinen und großen Quanten-Netzwerken wird zu einer zentralen Aufgabe für die Skalierung von Quantencomputing- und Quantenkommunikationanwendungen. Sobald Verschränkung erzeugt und verteilt wurde, kann jeder Knoten im Quantennetzwerk quantenmechanische Informationen lokal weiterverarbeiten und speichern. Aufgrund der intrinsischen Dekohärenz von Qubits im Laufe der Zeit müssen die Protokolle jedoch schneller sein als die Dekohärenzrate des Systems. Daher ist die Identifizierung effizienter Verschränkungsverteilungsstrategien, die schnell, parallelisierbar und mit minimaler externer Kontrolle umsetzbar sind, eine zentrale offene Herausforderung für die Skalierbarkeit quantentechnologischer Systeme.

Diese Dissertation untersucht autonome Protokolle zur Verteilung von Verschränkung zwischen zwei und mehreren physikalisch getrennten Qubits. Die Grundidee dieser Protokolle besteht darin, einen parametrischen Verstärker zu nutzen, um gaußsche verschränkte Photonenzustände zu erzeugen. Durch das Treiben der Qubits mit dem Ausgangssignal des parametrischen Verstärkers werden die Korrelationen der Photonen auf die Qubits übertragen, wodurch ein stationärer verschränkter Zustand entsteht. Diese Arbeit präsentiert eine detaillierte theoretische Analyse solcher Quantennetzwerke, führt sowohl analytische als auch numerische Berechnungen durch und untersucht, wie viel Verschränkung in einem realistischen System auf diese Weise generiert werden kann. Zudem wird die Robustheit des Protokolls unter Berücksichtigung der relevantesten experimentellen Unvollkommenheiten untersucht, und es werden konkrete Vorhersagen für zukünftige experimentelle Realisierungen unseres Protokolls mit supraleitenden Schaltkreisen gemacht. Anschließend betrachten wir ein größeres Netzwerk mit einer wachsenden Anzahl von Qubits, die entlang zweier getrennter Wellenleiter angeordnet sind. Wir zeigen, wie sich programmierbare verschränkte Zustände erzeugen lassen, indem die Detuning jedes Qubits angepasst wird. Mit diesem Ansatz können nicht nur mehrere bipartite verschränkte Zustände nach Bedarf generiert, sondern auch echte multipartite verschränkte Zustände über das gesamte Netzwerk verteilt werden. Wir geben eine detaillierte Schätzung der Anzahl der erreichbaren Qubit-Paare unter der Annahme realistischer experimenteller Parameter. Schließlich identifizieren wir, basierend auf unserer Analyse der Endlich-Bandbreiten-Effekte in der Photonenquelle, einen völlig neuartigen Mechanismus zur Erzeugung von Fernverschränkung, der ausschließlich auf einer thermischen Photonenquelle beruht. Dies ist besonders überraschend, da für zwei Qubits, die von einer Markovschen thermischen Quelle angetrieben werden, eine Fernverschränkung in der Regel nicht möglich ist. Wir beobachten jedoch, dass die Qubits mit abnehmender Bandbreite der thermischen Quelle zunehmend verschränkt werden. Dieses Protokoll demonstriert, wie nicht-Markovsche Effekte von ansonsten stark

inkohärenten Photonen genutzt werden können. Als mögliche Anwendung zeigen wir, dass dieser Mechanismus dazu verwendet werden kann, hochverschränkte Zustände in supraleitenden oder phononischen Quantennetzwerken zu erzeugen, indem diese mit thermischem Rauschen bei Raumtemperatur angetrieben werden.

Die in dieser Dissertation vorgestellten Protokolle bieten einen vielversprechenden neuen Ansatz zur robusten Verteilung großer Mengen an Verschränkung mit begrenzter klassischer Kontrolle. Die gewonnenen theoretischen Erkenntnisse über ihre Skalierbarkeit und Leistungsfähigkeit unter realistischen Bedingungen dienen als Leitfaden für erste Experimente in diesem Bereich und unterstreichen ihr enormes Potenzial für die Realisierung großflächiger Quantennetzwerke in der Zukunft.

# Contents

# List of Figures

# Chapter 1

# Introduction

The year 2025 has been declared the *International Year of Quantum Science and Technology* [1], marking a century since the establishment of the foundational principles of quantum mechanics. This milestone recognizes the first quantum revolution initiated by Werner Heisenberg [2], who introduced a novel framework to describe the behaviour of microscopic systems. The 20th century also witnessed the second quantum revolution, marking the transition from a theoretical understanding of quantum mechanics to a stage where quantum principles are applied to develop practical quantum technologies [3–7]. Today, quantum mechanics is the foundation for various fields, including quantum information and computation [8–17], quantum communication [18–25] and cryptography [26–28], quantum sensors and metrology [29–31], among others. Among these technologies, quantum computation has seen remarkable progress thanks to technological advances [32–39]. However, as quantum computing systems with an increasing number of coherently integrated components scale up, it is becoming evident that they will rely on quantum networks that distribute entanglement among many physically separated quantum processors [5, 40–48].

The availability of many highly entangled qubit pairs, shared among different nodes, is thus a universal and, in practice, one of the most essential resources for quantum network applications. Once established, entanglement can be locally purified [49–54] and used for quantum teleportation and remote gate operation protocols that then require classical communication only [14, 18].

The primary challenges in realizing a large-scale quantum network lie in transmitting quantum states over long distances, preserving quantum coherence, and scalability of the network infrastructure. It is then envisioned that, in future quantum devices, entanglement must be generated and interchanged among thousands of qubits within a limited coherence time. Given this challenge, there is a strong motivation to go beyond a serial application of existing protocols and search for more efficient quantum communication strategies that are fast, parallelizable, and, ideally, require minimal classical control. Existing protocols for distributing remote entanglement in realistic systems are primarily based on one of the following two strategies [42, 46]:

The first strategy relies on the excitation of a qubit and the entanglement generated between the qubit and the emitted photon [55–59]. Then, when two photons emitted from different qubits interfere on a balanced beamsplitter, the detection of the output modes of the beamsplitter heralds the creation of an entangled state between the physically separated qubits [55, 60–72]. The first successful demonstration of this protocol was achieved with two ensembles of atoms [73, 74], surprisingly as they constitute macroscopic objects. This approach has the advantage of requiring very little local control and is intrinsically robust with respect to photon losses. It is, however, only probabilistic and for many implementations [62, 66–68], the scalability of this approach is limited by the low probability of detecting a photon, which also decreases exponentially with the number of qubit pairs that must be entangled simultaneously in this way [46].

The second strategy, which does not rely on the probabilistic nature of heralding, is to generate a pair of entangled qubits locally and then transfer one of the states to the distant node, for example, through a controlled emission and reabsorption of optical or microwave photons [41, 75–81]. This protocol is entirely deterministic. Still, it requires a sufficiently high level of control on both network nodes.

A third and complementary idea to the deterministic entanglement protocol is to use correlated light sources to create a correlation between different qubits by driving them into a highly entangled state [82–98]. Contrary to the deterministic transfer protocol, here the photon source is continuously driving the qubits. In the simplest case, entangled beams of optical and/or microwave fields can be generated in a parametric down-conversion process [99], which produces a propagating two-mode squeezed state as an output. This process only requires a weak intrinsic nonlinearity as it occurs, for example, in nonlinear optical crystals [100, 101] or in driven Josephson junctions in the microwave regime [24, 25, 102–108]. In general, parametric down-conversion is currently the most common method to generate entangled pairs of optical photons [109, 110], however, usually in a probabilistic and postselected manner [20, 111]. In contrast, here we are interested in the regime where the parametric amplifier is strongly pumped, resulting in output fields with a high average photon number. The entanglement produced by the parametric amplifier can then be mapped onto an entangled qubit state. This scheme has the obvious benefit that it only relies on an externally pumped $\chi^{(2)}$-nonlinearity for generating the entanglement, which is typically much easier to realize than strong few-photon interactions or high-fidelity qubit-qubit gates. At the same time, this approach does not rely on postselection and can be used to distribute entanglement deterministically.

## 1.1 Objectives of the thesis

The first objective of this thesis is an in-depth analysis of the above-mentioned protocol for generating remote entanglement by driving distant qubits with the output of a nondegenerate parametric amplifier. This setting represents a minimal model of a quantum network. We then provide a detailed analysis of the parametric amplifier and how it couples to the qubits. This model allows us to perform both analytical and numerical calculations, and we can study the amount of entanglement one can create. Furthermore, we investigate the protocol's robustness with respect to the most common experimental imperfections, such as coupling imperfections between the parametric amplifier and the qubits or qubit dephasing. Considering all the relevant imperfections in any experimental implementation of the protocol, we then study how much entanglement can be achieved, and we also discuss possible ways to detect it.

The second main result of the thesis is the proposal and analysis of a scalable and fully autonomous scheme for preparing spatially distributed, multi-qubit entangled states in a dual-rail waveguide QED setup. In this approach, arrays of qubits located along two separated waveguides are illuminated by correlated photons from the output of a non-degenerate parametric amplifier. These photons drive the qubits into different classes of pure entangled steady states, for which the chosen pattern of local qubit-photon detunings can be used to adjust the degree of multipartite entanglement conveniently. Numerical simulations for moderate-sized networks show that the preparation time for these complex multi-qubit states increases at most linearly with the system size and that one may benefit from an additional speedup in the limit of a large amplifier bandwidth. Therefore, this scheme offers an intriguing new route for distributing ready-to-use multipartite entangled states across large quantum networks without requiring precise pulse control and relying only on a single Gaussian entanglement source.

This thesis's third and last result is a novel protocol for generating remote entanglement using a thermal photon source. While driving two qubits by a Markovian thermal reservoir would thermalize both qubits, resulting in a state which does not have quantum correlations, we show that by reducing the bandwidth of the thermal source, a finite amount of entanglement emerges. In this regime, the two qubits are driven by a non-Markovian photon source. The observed emergence of such a thermally driven, delocalized, entangled state is interesting from a conceptual and practical point of view. First of all, this effect shows how the degree of non-Markovianty of a reservoir can change not only the quantitative but also the qualitative properties of a system coupled to it [112–114]. This is different, for example, for locally coupled quantum systems, where Markovian thermal noise can already pump the system into at least a weakly entangled state [115]. Secondly, while the current protocol does not avoid the requirement to cool most of the networks, it provides a completely passive entanglement distribution scheme, which does not require coherent control fields. As illustrative examples, we describe two scenarios with qubits driven by filtered noise from a room temperature source: the entanglement of two distant superconducting qubits connected by a cryogenic quantum link and a network of SiV centers in a phononic network.

## 1.2 Outline of the thesis

The structure of this thesis is outlined as follows:

**Chapter 2** introduces the fundamental concepts and theoretical techniques necessary for a comprehensible understanding of the thesis's primary results. The chapter provides a description of quantum states as well as light-matter interaction, which is necessary for the modeling of quantum networks.

**Chapter 3** presents the first new results of the thesis, where we analyse the creation of remote qubit-qubit entanglement using correlated photons. Specifically, in this analysis, we go beyond the usual assumption of a broadband parametric amplifier and consider finite-bandwith effects, time-delays and other experimental imperfections.

**Chapter 4** investigates an extension of this protocol, namely, how the entanglement is distributed if we increase the number of qubits in each waveguide. Using techniques similar to those used before, we study its robustness and scalability under realistic conditions.

**Chapter 5** covers an alternative protocol to generate remote entanglement. Instead of using correlated photons, here we propose to use a filtered thermal cavity for the task. The chapter presents a detailed theoretical description of the protocol as well as two possible experimental implementations.

**Chapter 6** summarizes the most relevant results of this thesis and presents an outlook towards future research directions.

# Chapter 2

# Theoretical foundations of quantum networks

At the core of a quantum network is the ability to entangle qubits across spatially separated locations, creating a shared quantum state that can be manipulated and measured collectively, even at a distance. This chapter introduces fundamental concepts and theoretical techniques necessary to properly understand the thesis's main results: the creation of a qubit quantum network. We describe our qubit quantum networks in Sec. 2.1, focusing on the fundamentals of quantum states and entanglement. In Sec. 2.2, we introduce some of the relevant properties of Gaussian states. Next, in Sec. 2.3, we focus on a waveguide-based quantum network and derive an effective description of the system. We give examples of continuous-variable systems coupled to waveguides in Sec. 2.4. In Sec. 2.5, we offer a complementary description in terms of the phase space representation of the bosonic fields, which allows for an alternative way to solve hybrid systems formed by bosonic modes and qubits. To end this chapter, we present an overview of well-known remote entanglement protocols in Sec. 2.6.

## 2.1 Qubit quantum networks

A quantum network is a network infrastructure that uses the principles of quantum mechanics to its advantage to transmit, process, manipulate, and store quantum information [5]. At the core of such a quantum network, the quantum nodes are responsible for generating, processing and storing quantum information locally. We consider the quantum nodes to be described by two-level systems, also called quantum bits or qubits for short. We model each qubit by a ground state $|0\rangle$ and an excited state $|1\rangle$. The principle of superposition allows us to define the state of a single qubit as [3]

$$|\psi\rangle = \alpha|0\rangle + \beta|1\rangle, \tag{2.1}$$

where $\alpha$ and $\beta$ are called probability amplitude and are normalized complex coefficients $\alpha, \beta \in \mathbb{C}$ satisfying $|\alpha|^2 + |\beta|^2 = 1$. The single qubit state $|\psi\rangle$ belongs to a complex vector space defined by a two-dimensional Hilbert space $\mathcal{H}$. Given the state in Eq. (2.1), quantum mechanics tell us that the state is in the ground state $|0\rangle$ with probability $|\alpha|^2$ and in the excited state $|1\rangle$ with probability $|\beta|^2$. The concept of superposition is best seen when we have a balanced superposition $\alpha = \beta = 1/\sqrt{2}$. In this case, one would measure either the ground or the excited state with the same probability $|\alpha|^2 = |\beta|^2 = 1/2$. This superposition of states becomes more interesting when we consider a state formed by many qubits.

Consider now a system formed of $N_\mathrm{q}$ qubits. The state of these $N_\mathrm{q}$ qubits is a vector in the combined Hilbert space $\mathcal{H} = \mathcal{H}_1 \otimes \mathcal{H}_2 \otimes \ldots \otimes \mathcal{H}_{N_\mathrm{q}}$. A general pure state of the multi-qubit network can thus be described by

$$|\psi_0\rangle = \sum_{\boldsymbol{s}=1}^{2^{N_\mathrm{q}}} c_{\boldsymbol{s}} |\boldsymbol{s}\rangle, \tag{2.2}$$

where $c_{\boldsymbol{s}} \in \mathbb{C}$ are normalized probability amplitudes and $\boldsymbol{s} = (s_1, s_2, ..., s_{N_\mathrm{q}})$ with binary representation $s_i \in (0, 1)$. Here, we use a compact notation to describe the tensor product of the different subsystems $|\boldsymbol{s}\rangle \equiv |s_1, \cdots, s_{N_\mathrm{q}}\rangle \equiv |s_1\rangle \otimes \cdots \otimes |s_{N_\mathrm{q}}\rangle$. The basis in which we write this state is called the computational basis, and the state $|\psi_0\rangle$ is determined by $2^{N_\mathrm{q}}$ probability amplitudes. The dimension of the state grows exponentially with the number of qubits in the network. If this network were composed of $N_\mathrm{q} = 500$ qubits, this number would be larger than the estimated number of atoms in the universe [3]. In this thesis, we will be dealing mostly with $N_\mathrm{q} = 2$ in Chapter 3 and Chapter 5. In Chapter 4, we will obtain a way to characterize states for arbitrary $N_\mathrm{q}$ without having to write them down explicitly.

Due to the state's interaction with its environment or because of some uncertainty about it, most quantum systems are represented by a statistical mixture of pure states. These mixed states are formally expressed in terms of the density matrix $\rho$ defined as the weighted statistical sum of different pure states

$$\rho = \sum_{i=0} p_i |\psi_i\rangle\langle\psi_i|, \tag{2.3}$$

where $0 \leq p_i \leq 1$ is the probability of observing the state $|\psi_i\rangle$ and $\sum_i p_i = 1$. A quantum system whose state $|\psi_0\rangle$ is exactly known is called a *pure state*, and it is represented by the density matrix $\rho = |\psi_0\rangle\langle\psi_0|$. Otherwise, the state $\rho$ is called a *mixed state*, which is said to be a mixture of different pure states in an ensemble. Mathematically, this can be described by a quantity called the purity of the state $\mu$, which is obtained by taking the trace of $\rho^2$, $\mu = \mathrm{Tr}\{\rho^2\}$. We obtain $\mu = 1$ for a pure state, while a mixed state is characterized by $\mu < 1$. Generally, the purity is bounded by $\frac{1}{d} \leq \mu \leq 1$, where $d$ is the dimension of the Hilbert space where the state is defined. The concept of purity $\mu$ and pure states $|\psi_0\rangle$ will appear repetitively throughout the thesis.

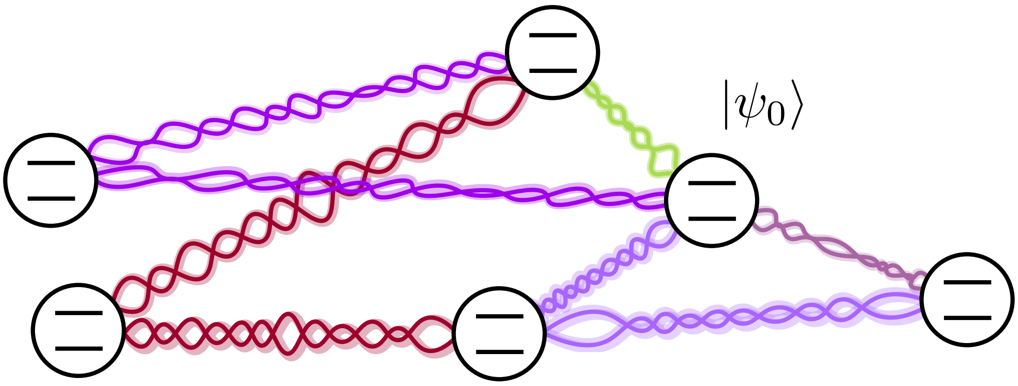


**Figure 2.1:** Schematic representation of a qubit quantum network. The qubit state is given by $|\psi_0\rangle$.

Alternatively, one can express the density matrix in terms of the Pauli operators. Those are given by

$$\hat{\sigma}^x = \begin{pmatrix} 0 & 1 \\ 1 & 0 \end{pmatrix}, \qquad \hat{\sigma}^y = \begin{pmatrix} 0 & -i \\ i & 0 \end{pmatrix}, \qquad \hat{\sigma}^z = \begin{pmatrix} 1 & 0 \\ 0 & -1 \end{pmatrix}, \tag{2.4}$$

as well as the raising and lowering operator, $\hat{\sigma}^+ = |1\rangle\langle 0|$ and $\hat{\sigma}^- = |0\rangle\langle 1|$, respectively. Those can be expressed in terms of the Pauli matrices using $\hat{\sigma}^\pm = (\hat{\sigma}^x \pm i\hat{\sigma}^y)/2$. For completeness, we define $\hat{\sigma}^0 = \mathbb{1}_2$ as the $2 \times 2$ identity matrix. This allows us to express the general density matrix in Eq. (2.3) as

$$\rho = \frac{1}{2^{N_\mathrm{q}}} \sum_{k_1,\cdots,k_{N_\mathrm{q}}} \langle \hat{\sigma}_1^{k_1} \otimes \cdots \otimes \hat{\sigma}_{N_\mathrm{q}}^{k_{N_\mathrm{q}}} \rangle \hat{\sigma}_1^{k_1} \otimes \cdots \otimes \hat{\sigma}_{N_\mathrm{q}}^{k_{N_\mathrm{q}}}. \tag{2.5}$$

Here, $k_1, \cdots, k_{N_\mathrm{q}}$ represents all possible combinations of $\{0, x, y, z\}$ for the Pauli matrices for each qubit. This is a convenient way to express the state, which is commonly used for experimental reconstruction. This process is called state tomography and requires the measurements of $4^{N_\mathrm{q}}$-1 observables.

We defined a pure multi-qubit state in Eq. (2.2). However, this is not the whole story for a quantum network, where we want the pure state to be entangled.

### 2.1.1 Entanglement

Consider a general multi-qubit state described by $\rho$ in Eq. (2.3). The state is called *separable* if it can be written as [116]

$$\rho = \sum_i p_i \rho_1^{(i)} \otimes \rho_2^{(i)} \otimes \cdots \otimes \rho_{N_\mathrm{q}}^{(i)}, \tag{2.6}$$

with $\sum_i p_i = 1$ and $p_i \geq 0$. Here, $\rho_j^{(i)}$ characterizes the state of the $j$-th subsystem. If the state cannot be written as Eq. (2.6), the state is called *entangled*. The above expression has a clear physical meaning: The state $\rho$ can be prepared by each subsystem by means of local operators (unitary operators, measurements, etc.) and classical communication (LOCC). In general, given a state $\rho$, it is a nontrivial task to decompose it according to Eq. (2.6).

The minimal working quantum network is obtained when two nodes are connected. This elementary quantum link needs two qubits $N_\mathrm{q} = 2$, and using Eq. (2.2) a pure state could be written as

$$|\psi_0\rangle = c_1|00\rangle + c_2|01\rangle + c_3|10\rangle + c_4|11\rangle, \tag{2.7}$$

for $c_i$ complex normalized coefficients. In this scenario, there is a family of states which turns out to be maximally entangled. Those states are called the *Bell states* and are given by

$$|\Psi^+\rangle = \frac{|01\rangle + |01\rangle}{\sqrt{2}}, \tag{2.8a}$$

$$|\Psi^-\rangle = \frac{|01\rangle - |01\rangle}{\sqrt{2}}, \tag{2.8b}$$

$$|\Phi^+\rangle = \frac{|00\rangle + |11\rangle}{\sqrt{2}}, \tag{2.8c}$$

$$|\Phi^-\rangle = \frac{|00\rangle - |11\rangle}{\sqrt{2}}. \tag{2.8d}$$

Those states cannot be expressed as Eq. (2.6). That is, given $\rho = |\Psi^+\rangle\langle\Psi^+|$, it is not possible to find a decomposition as Eq. (2.6). We can define the reduced density matrix as $\rho_1 = \mathrm{Tr}_2\{\rho\}$. This reduced density matrix $\rho_1$ is the state describing the subsystem, comprised of a single qubit, after tracing out all the information about the second qubit. In this case, we obtain $\rho_1 = \mathbb{1}/2$, with purity $\mu = 1/2$. This is a completely mixed state. While the state describing the two qubits was pure, that is, it was known for certainly, the state of the first qubits turns out to be completely mixed. This property is one of the ways to benchmark if a *pure* quantum state is in an entangled state, and it lets us define a way to quantify entanglement using the Von Neumann entanglement entropy [117]

$$\mathcal{S}(\rho) = -\mathrm{Tr}\{\rho \log \rho\}. \tag{2.9}$$

The entanglement entropy for our reduced qubit state $\mathcal{S}(\rho_1) = \mathcal{S}(\rho_2) = \log 2$. The entanglement entropy measures the uncertainty associated with a quantum state. A pure state's entanglement entropy is zero $\mathcal{S}(|\psi_0\rangle\langle\psi_0|) = 0$. This is because, in this case, we know for sure which state we were in. The entanglement entropy is not limited to two qubits; rather, it can be used for any bipartition in the network. For example, for a $N_\mathrm{q}$ qubit network, one can take the $n$-th bipartition by considering two subsystems, one consisting of $n$ qubits and the other of $N_\mathrm{q} - n$ qubits.

Back to our two-qubit state, many different ways exist to quantify entanglement. A common measure for entanglement is the concurrence [118–120]

$$\mathcal{C}(\rho) = \max\left(0, \lambda_1 - \lambda_2 - \lambda_3 - \lambda_4\right), \tag{2.10}$$

where $\lambda_i \geq 0$ are the eigenvalues in descending order of $R = \sqrt{\sqrt{\rho}\tilde{\rho}\sqrt{\rho}}$ and $\tilde{\rho} = (\sigma_y \otimes \sigma_y)\rho^*(\sigma_y \otimes \sigma_y)$ is the spin-flipped state with $*$ indicating the conjugate. The concurrence is zero for any separable state $C(\rho_{\text{sep}}) = 0$ and is maximal for any of the Bell states $C(\rho_{\text{Bell}}) = 1$. Some closed expressions for the concurrence can be found depending on the two-qubit density matrix $\rho$ structure. For example, assume that our density matrix is

$$\rho = \begin{pmatrix} \rho_{11} & 0 & 0 & \rho_{00,11} \\ 0 & \rho_{10} & \rho_{01,10} & 0 \\ 0 & \rho_{01,10}^* & \rho_{01} & 0 \\ \rho_{00,11}^* & 0 & 0 & \rho_{00} \end{pmatrix}. \tag{2.11}$$

In this case, the concurrence takes the form

$$\mathcal{C}(\rho) = 2\max\left(0, |\rho_{00,11}| - \sqrt{\rho_{01}\rho_{10}}, |\rho_{01,10}| - \sqrt{\rho_{00}\rho_{11}}\right). \tag{2.12}$$

This expression highlights the two main mechanisms behind the entanglement between two qubits: the appearance of antidiagonal terms in the density matrix $\rho_{00,11}$ and $\rho_{01,10}$. Those terms are called *coherences* and, as the name indicates, create a coherence between the other elements in the density matrix. In particular, they establish coherence between the diagonal terms $\rho_{ii}$, known as *populations*. For example, the term $\rho_{00,11}$ is a coherence between the population at the ground state $\rho_{00}$ and the population of the state $\rho_{11}$, which indicates the two qubits being in an excited state. Notice how the presence of those terms is not enough to create entanglement. As we see in Eq. (2.12), some populations are detrimental to entanglement. In Chapter 3 and Chapter 4, we will present a physical situation in which the entanglement is governed by $\rho_{00,11}$. Later in Chapter 5, we will consider the other scenario, where $\rho_{01,10}$ is the main contributor to the entanglement.

Alternatively, we can also define the entanglement of formation $E_{\text{F}}(\rho)$ [118], a more general measure of the amount of entanglement in a quantum state. For a two-qubit system, the entanglement of formation is closely related to the concurrence

$$E_{\text{F}}(\rho) = h\left(\frac{1 + \sqrt{1 - C(\rho)^2}}{2}\right), \tag{2.13}$$

where $h(x) = -x\log_2(x) - (1-x)\log_2(1-x)$ is the Shannon entropy function. The entanglement of formation quantifies how much entanglement (in units of ebits) is necessary, on average, to prepare such a state. It coincides with the entanglement entropy of the reduced density matrix $S(\rho_1)$ if the original state was pure $\rho = |\psi_0\rangle\langle\psi_0|$.

Throughout most of the thesis, we will deal with two-qubit systems, allowing us to use the concurrence to quantify their entanglement. Alternatively, one can quantify it using the fidelity with respect to any of the Bell states defined in Eq. (2.8),

$$\mathcal{F}(\rho) = \langle \text{Bell}|\rho|\text{Bell}\rangle. \tag{2.14}$$

This measures how close we are to a maximally entangled state rather than quantifying the amount of entanglement present in the qubit system itself. The threshold $\mathcal{F}(\rho) > 1/2$ is used to confirm that the state is indeed a Bell state. If the state is pure, $\rho = |\psi_0\rangle\langle\psi_0|$, the state fidelity reduces to $\mathcal{F}(|\psi_0\rangle\langle\psi_0|) = |\langle\psi_0|\text{Bell}\rangle|^2$.

For systems with $N_\text{q} \geq 3$, quantifying entanglement becomes more difficult [121]. In such a case, one can rely on the entanglement entropy for bipartite entangled states or use entanglement witnesses for multipartite entangled states [122]. Not only that, but Bell states are not ideal resources when considering larger systems. This is because when two qubits are maximally entangled, a third qubit cannot be entangled with any of them. This phenomenon is known as the monogamy of entanglement [123] and restricts the amount of entanglement that can be shared between more than two nodes of a network. One strategy to achieve more connectivity in the network is not to use maximally entangled states. In this case of finite but not maximal entanglement, one can share the entanglement to a larger number of qubits.

## 2.2 Continuous-variable Gaussian states

In the previous section, we considered a quantum network described by a qubit multipartite state $|\psi_0\rangle$, formed of physically separated qubits. However, by describing only the quantum nodes, our quantum network remains incomplete. This is because the isolated qubits cannot create a pure multipartite state. To create entangled states between the qubits, they must first exchange information.

We consider a system of $n$ non-interacting bosons. Such a scenario describes a continuous-variable system characterized by an infinite-dimensional Hilbert space $\mathcal{H} = \mathcal{H}_1 \otimes \mathcal{H}_2 \otimes \ldots \otimes \mathcal{H}_n$. Here, $\mathcal{H}_k$ refers to the infinite-dimensional Hilbert space of the $k$-th mode [124, 125]. Each $k$-th mode can be described as a quantum harmonic oscillator [124] with bosonic annihilation $\hat{a}_k$ and creation $\hat{a}_k^\dagger$ operator, which fulfill the bosonic commutator relations $[\hat{a}_k, \hat{a}_{k'}^\dagger] = \delta_{kk'}$ and $[\hat{a}_k, \hat{a}_{k'}] = [\hat{a}_k^\dagger, \hat{a}_{k'}^\dagger] = 0$. They allow us to define the Fock, or number, basis, which is composed of the eigenstates of the number operator $\hat{n}_k = \hat{a}_k^\dagger \hat{a}_k$, i.e. $\hat{n}_k|n_k\rangle = n_k|n_k\rangle$. The Fock basis allows us to gain further insight into the annihilation $\hat{a}_k$ and creation $\hat{a}_k^\dagger$ operators. The action of the annihilation operator on the Fock state is given by $\hat{a}_k|n_k\rangle = \sqrt{n_k}|n_k - 1\rangle$. Thus, its action of the Fock basis is to *annihilate* an excitation or photon. On the other hand, the action of the creation operator on the Fock state is $\hat{a}_k^\dagger|n_k\rangle = \sqrt{n_k + 1}|n_k + 1\rangle$, effectively *creating* a new excitation at the $k$-th mode. The annihilation operator allows us to define a state for which we cannot annihilate more excitations. This is the *vacuum state*, defined as $\hat{a}_k|0\rangle = 0$.

Similar to Eq. (2.2), a general pure state $|\Psi\rangle$ describing the $n$ modes can be written in the Fock basis as

$$|\Psi\rangle = \sum_{\boldsymbol{n}} c_{\boldsymbol{n}} |\boldsymbol{n}\rangle. \tag{2.15}$$

Here, similar to Eq. (2.2), we have defined $\boldsymbol{n} = (n_1, \cdots, n_n)$ and written the basis on a compact form. Contrary to Eq. (2.2), here $n_k$ labels the number of particles one can find in the $k$-mode.

Throughout this thesis, we can associate this bosonic excitation with excitations of the electromagnetic field, i.e. photons. It is not, however, the only bosonic field that can be quantized. For example, one can quantize the vibrations of atoms or molecules in a solid material. Such collective vibrations in the atomic lattice are called phonons and behave in the same way as photons [126]. In Chapter 5, we propose implementing a remote entanglement protocol using phonons.

Alternatively to the creation and annihilation operator, the $k$-bosonic mode can be described by the quadrature field operators, defined as

$$\hat{x}_k = \frac{\hat{a}_k + \hat{a}_k^\dagger}{\sqrt{2}}, \tag{2.16a}$$

$$\hat{p}_k = -i\frac{\hat{a}_k - \hat{a}_k^\dagger}{\sqrt{2}}. \tag{2.16b}$$

These operators, in contrast to the discrete spectra of the creation and annihilation operator, are described by a continuous eigenspectrum, $\hat{x}_k|x_k\rangle = x_k|x_k\rangle$ and $\hat{p}_k|p_k\rangle = p_k|p_k\rangle$. These quadrature field operators satisfy the canonical commutation relation $[\hat{x}_k, \hat{p}_{k'}] = i\hbar\delta_{k,k'}$. The noncommuting nature of the quadrature fields imposes a bound on their uncertainty. This can be seen from the Heisenberg uncertainty principle, which states that given two arbitrary noncommuting observables $\hat{A}$ and $\hat{B}$ for an arbitrary state, the product of their variance is given by $\langle(\Delta\hat{A})^2\rangle\langle(\Delta\hat{B})^2\rangle \geq |\langle[\hat{A}, \hat{B}]\rangle|^2/4$, where the variance for a generic operator is given by

$$\langle(\Delta\hat{A})^2\rangle = \langle\hat{A}^2\rangle - \langle\hat{A}\rangle^2. \tag{2.17}$$

For the quadrature fields, we obtain $\langle(\Delta\hat{x}_k)^2\rangle\langle(\Delta\hat{p}_k)^2\rangle \geq |\langle[\hat{x}_k, \hat{p}_k]\rangle|^2/4 = 1/4$. As we will see later, this imposes a bound on the product of variances, but some states allow the reduction of one variance at the expense of the other.

All physical information about the $n$-mode bosonic system is contained in the state described by Eq. (2.15), or the density matrix $\rho$. Equivalently, one can completely characterize any state by all possible moments of its quadrature operators $\langle\hat{x}_k^n\,\hat{p}_l^m\rangle$ for any $n, m \in \mathbb{N}$. In general, such a complete description of a multi-mode bosonic system requires an infinite amount of moments to compute due to the infinite dimensions of the Hilbert space.

However, there is a family of bosonic states, called Gaussian states, that are fully characterized by their first $\boldsymbol{\mu}$ and second order $\boldsymbol{\mathcal{V}}$ moments. It is convenient to group all the quadratures into a single vector [127]

$$\hat{\boldsymbol{s}} = (\hat{x}_1, \hat{p}_1, \ldots, \hat{x}_n, \hat{p}_n)^{\mathrm{T}}. \tag{2.18}$$

This convention allows us to rewrite the canonical commutator relations in a more compact form

$$[\hat{s}_k, \hat{s}_l] = i\Omega_{kl}, \tag{2.19}$$

where $\Omega_{kl}$ are the matrix elements of the symplectic matrix $\boldsymbol{\Omega}$ defined as

$$\boldsymbol{\Omega} = \bigoplus_{k=1}^{n}\boldsymbol{\omega}, \qquad \boldsymbol{\omega} = \begin{pmatrix} 0 & 1 \\ -1 & 0 \end{pmatrix}. \tag{2.20}$$

The first moments are then obtained by taking the expectation value of the vector $\hat{\boldsymbol{s}}$

$$\boldsymbol{\mu} = \langle\hat{\boldsymbol{s}}\rangle, \tag{2.21}$$

and the second moments are

$$\boldsymbol{\mathcal{V}} = \frac{1}{2}\langle\{\hat{\boldsymbol{s}}, \hat{\boldsymbol{s}}^{\mathrm{T}}\}\rangle - \langle\hat{\boldsymbol{s}}\rangle\langle\hat{\boldsymbol{s}}\rangle^{\mathrm{T}}, \tag{2.22}$$

where we have defined the anticommutator $\{A, B\} = AB + BA$. This defines a $2n \times 2n$ symmetric covariance matrix. The uncertainty relations among the canonical operators impose a constraint on the covariance matrix,

$$\boldsymbol{\mathcal{V}} + i\boldsymbol{\Omega} \geq 0. \tag{2.23}$$

Using this definition of the covariance matrix, the purity of a $n$-mode Gaussian state, defined as $\mu = \mathrm{Tr}\{\rho^2\}$, is easily computed as [128]

$$\mu = \frac{1}{2^n \sqrt{\det \boldsymbol{\mathcal{V}}}}. \tag{2.24}$$

Here, the purity ranges between $0 < \mu \leq 1$, as expected for a system with an infinite-dimensional Hilbert space.

### 2.2.1 Thermal state

Consider a bosonic system in thermal equilibrium at temperature $T > 0$. For simplicity, we focus on a single-mode $\hat{a}$ with frequency $\omega_{\mathrm{c}}$. This state is represented by an incoherent mixture of Fock states [126]

$$\rho_{\mathrm{th}} = \sum_n \frac{n_{\mathrm{th}}^n}{(n_{\mathrm{th}} + 1)^{n+1}} |n\rangle\langle n|, \tag{2.25}$$

where $n_{\mathrm{th}}$ follows the Planck distribution $n_{\mathrm{th}} = (e^{\hbar\omega_{\mathrm{c}}/k_{\mathrm{B}}T} - 1)^{-1}$, with $k_{\mathrm{B}} = 1.38 \times 10^{-23}\,\mathrm{J\,K^{-1}}$ the Boltzmann constant. Given the density matrix, we can compute the photon mean number and its variance. We obtain $\langle \hat{n} \rangle = n_{\mathrm{th}}$ and $(\Delta\hat{n})^2 = n_{\mathrm{th}}(n_{\mathrm{th}} + 1)$. In general, any normally-ordered moment is given by $\langle (\hat{a}^\dagger)^p \hat{a}^q \rangle = q! n_{\mathrm{th}}^q \delta_{p,q}$.

Alternatively, we can use the moments of the quadrature operators. For this thermal state, we obtain

$$\hat{\boldsymbol{\mu}} = 0, \qquad \hat{\boldsymbol{\mathcal{V}}} = \frac{1}{2} \begin{pmatrix} 1 + 2n_{\mathrm{th}} & 0 \\ 0 & 1 + 2n_{\mathrm{th}} \end{pmatrix}. \tag{2.26}$$

From this covariance matrix, one can compute the purity of the thermal state

$$\mu = \frac{1}{1 + 2n_{\mathrm{th}}}. \tag{2.27}$$

From this expression, we conclude that at $T > 0$, a thermal state is always mixed. Notice how the pure state is only possible when $T \to 0$. In this limit, the mean thermal occupation also vanishes $n_{\mathrm{th}} \to 0$ and the density matrix reduces to $\rho_{\mathrm{th}} = |0\rangle\langle 0|$. This is the previously defined vacuum state defined by $\hat{a}|0\rangle = 0$.

We can also obtain the variances of the quadrature from the covariance matrix. In this case, we obtain $(\Delta x)^2 = (\Delta p)^2 = (1 + 2n_{\mathrm{th}})/2$ as well as $(\Delta x)^2 (\Delta p)^2 = (1 + 2n_{\mathrm{th}})^2/4$.

### 2.2.2 Two-mode squeezed state

Let us now consider a two-mode continuous variable system, described by the bosonic operators $\hat{a}_A$ and $\hat{a}_B$. We define the two-mode squeezed (TMS) state $|\Psi_{\mathrm{TMS}}\rangle$ as the state produced by the action of the two-mode squeezing operator onto the two-mode vacuum state $|\Psi_{\mathrm{TMS}}\rangle \equiv S(\xi)|0,0\rangle$. Here, we define the two-mode squeezing operator as

$$\hat{S}(\xi) = e^{\chi \hat{a}_A^\dagger \hat{a}_B^\dagger - \chi^* \hat{a}_A \hat{a}_B}, \tag{2.28}$$

where we have defined $\xi = re^{i\phi}$, with $r$ as the squeezing strength and $\phi$ as the squeezing angle. Note that in the literature, the squeezing operator is sometimes defined with an opposite sign in the exponents [124, 127]. We recover the same results by changing $\chi \to -\chi$.

Applying the two-mode squeezing operator produces a state that is a superposition of pairs of Fock states.

$$|\Psi_{\mathrm{TMS}}\rangle = \frac{1}{\cosh(r)} \sum_{n=0}^{\infty} \left(e^{i\phi} \tanh(r)\right)^n |n,n\rangle. \tag{2.29}$$

For small squeezing strength, $r \ll 1$, this state can be approximated

$$|\Psi_{\mathrm{TMS}}\rangle = |0,0\rangle + re^{i\phi}|1,1\rangle + \mathcal{O}(r^2), \tag{2.30}$$

which contains mostly the vacuum state and a pair of photons in each mode. This photon-pair source has long been the basis of fiber- and satellite-based quantum communication [111, 129].

One can assume the phase $\phi$ of the TMS state to be fixed at a reference value of $\phi = 0$, such that the state is fully characterized by its squeezing strength $r$. Then, we find that its first and second moments are given by

$$\boldsymbol{\mu} = 0, \qquad \boldsymbol{\mathcal{V}} = \begin{pmatrix} \boldsymbol{\alpha} & \boldsymbol{\gamma} \\ \boldsymbol{\gamma}^{\mathrm{T}} & \boldsymbol{\beta} \end{pmatrix}. \tag{2.31}$$

where it is convenient to express the covariance matrix as

$$\boldsymbol{\alpha} = \boldsymbol{\beta} = \frac{1}{2}\begin{pmatrix} \cosh(2r) & 0 \\ 0 & \cosh(2r) \end{pmatrix}, \qquad \boldsymbol{\gamma} = \frac{1}{2}\begin{pmatrix} -\sinh(2r) & 0 \\ 0 & \sinh(2r) \end{pmatrix}. \tag{2.32}$$

The purity of the state can be computed from this covariance matrix. As expected, we obtain $\mu = 1$, since the TMS state is pure by definition. This covariance matrix also gives us relevant information about the variance of the quadrature operators. In this case, we obtain

$$(\Delta \hat{x}_A)^2 = (\Delta \hat{p}_A)^2 = (\Delta \hat{x}_B)^2 = (\Delta \hat{p}_B)^2 = (1 + 2n_{\mathrm{th}})/2, \tag{2.33}$$

where we have defined an effective thermal population $n_{\rm th} = \sinh^2(r)$ and used that $\cosh(2r) = 1 + 2\sinh^2(r)$. The definition of this effective thermal occupation number is motivated by the fact that the reduced state of each of the modes is actually a thermal state with that occupation number. To see this, one can look at the TMS state after tracing out one of the modes. Specifically, if we trace out mode $\hat{a}_B$ and focus on mode $\hat{a}_A$, $\rho_A = \mathrm{Tr}_B\left\{|\Psi_{\rm TMS}\rangle\langle\Psi_{\rm TMS}|\right\}$ ,we obtain

$$\rho_A = \sum_n \frac{\tanh^{2n}(r)}{\cosh^2(r)}|n\rangle\langle n| = \sum_n \frac{\sinh^{2n}(r)}{(\sinh^2(r)+1)^{n+1}}|n\rangle\langle n|, \tag{2.34}$$

which is the exact thermal distribution as in Eq. (2.25) with an effective thermal population $n_{\rm th} = \sinh^2(r)$.

The properties of the two-mode squeezed state are best revealed through non-local observables rather than local ones. We define the non-local quadrature operators as $\hat{x}_\pm = (\hat{x}_A \pm \hat{x}_B)/\sqrt{2}$ and $\hat{p}_\pm = (\hat{p}_A \pm \hat{p}_B)/\sqrt{2}$. The variances of those non-local quadratures are [124]

$$(\Delta\hat{x}_+)^2 = (\Delta\hat{p}_-)^2 = e^{2r}/2, \tag{2.35}$$

$$(\Delta\hat{x}_-)^2 = (\Delta\hat{p}_+)^2 = e^{-2r}/2. \tag{2.36}$$

As we increase the squeezing amplitude, two of the quadratures are amplified, while the other two are reduced below the uncertainty of the vacuum state. In the strong squeezing regime, $r \to \infty$, the TMS state is the continuous-variable equivalent to the EPR state.

It is a convention to define the squeezing level $\mathcal{S}$ to quantify the reduction in uncertainty relative to the vacuum state

$$\mathcal{S} = -10\log_{10}\left[\frac{(\Delta\hat{x}_-)^2}{(\Delta\hat{x}_-)^2_{\rm vac}}\right] = -10\log_{10}\left[e^{-2r}\right] = \frac{20\,r}{\log(10)} \approx 8.67r, \tag{2.37}$$

Thus, $\mathcal{S}$ quantifies the suppression of the minimum quadrature variance in decibels (dB).

### 2.2.3 Continuous-variable entanglement

We have described the TMS state $|\Psi_{\rm TMS}\rangle$ as a state which exhibits a suppression of the joint or nonlocal quadrature operators. This feature is linked to another feature of the state, namely the entanglement between the two modes $\hat{a}_A$ and $\hat{a}_B$.

The entanglement between a bipartite system can be quantified by checking the positivity of the partially transposed state [121, 130], sometimes called the PPT criterion. It is a necessary and sufficient condition for the separability of two-mode Gaussian states [131]. In the case of a two-mode Gaussian state, entanglement can be quantified by the negativity [132]

$$\mathcal{N}(\rho) = \frac{||\tilde{\rho}||_1 - 1}{2}, \tag{2.38}$$

where $\tilde{\rho} = \rho^{\Gamma_A}$ stands for the partially transposed density matrix with respect to subsystem A and $||\rho||_1 = \mathrm{Tr}\{\sqrt{\rho\rho^\dagger}\}$ is the trace norm of the state.

Our system, which describes a bipartite Gaussian state, can be written in terms of its covariance matrix $\boldsymbol{\mathcal{V}}$ given by Eq. (2.31). In this case, the negativity simplifies to [133, 134]

$$\mathcal{N}(\boldsymbol{\mathcal{V}}) = \max\left[0, \frac{1-2\nu}{4\nu}\right], \tag{2.39}$$

where $\nu = \sqrt{\frac{\Delta - \sqrt{\Delta^2 - 4\det\boldsymbol{\mathcal{V}}}}{2}}$ and $\Delta = \det\boldsymbol{\alpha} + \det\boldsymbol{\beta} - 2\det\boldsymbol{\gamma}$. For a pure two-mode squeezed state, it further reduces to $\nu = e^{-2r}/2$, which leads to the simplified expression for the negativity

$$\mathcal{N}(\boldsymbol{\mathcal{V}}) = e^r \sinh(r). \tag{2.40}$$

This quantity is unbounded and diverges when $r \to \infty$. In practice, the squeezing strength is always finite, which limits the achievable amount of entanglement.

### 2.2.4 Hybrid entanglement

There are scenarios where one needs to characterize bipartite (but not limited to two qubits) mixed states $\rho$. Unfortunately, most of the methods mentioned until now have something in common: They either apply only to pure states or they can be evaluated only for qubit systems or Gaussian states. A more general approach to verifying entanglement by directly measurable quantities is based on so-called entanglement witnesses. An observable $\hat{\mathcal{W}}$ is called an entanglement witness if

$$\mathcal{W}(\rho) = \mathrm{Tr}\{\hat{\mathcal{W}}\rho\} < 0 \longleftrightarrow \rho_{\text{ent.}}, \tag{2.41}$$

$$\mathcal{W}(\rho) = \mathrm{Tr}\{\hat{\mathcal{W}}\rho\} \geq 0 \longleftrightarrow \rho_{\text{sep.}}. \tag{2.42}$$

It boils down to finding the appropriate witness $\hat{\mathcal{W}}$ that detects the entanglement, as for each entangled state $\rho$ there exists always an entanglement witness to detect it [121].

There are many ways to build such a witness [120]. Motivated by experimental constraints [see Sec. 3.8.2], we construct the witness using local uncertainty relations [135]. Assume we have a set of $n$ noncommuting observables $\{\hat{A}_i\}_{i=1}^n$ and $\{\hat{B}_i\}_{i=1}^n$ for subsystem A and B, respectively. Then, the sum of the variance of those observables is always bounded from below for any state $\rho$:

$$\sum_{i=1}^n (\Delta\hat{A}_i)^2 \geq U_A; \qquad \sum_{i=1}^n (\Delta\hat{B}_i)^2 \geq U_B, \tag{2.43}$$

where $U_{A,B} > 0$. We now define a joint measurement between subsystems $A$ and $B$, that is $\hat{M}_i = \hat{A}_i \otimes \mathcal{I} + \mathcal{I} \otimes \hat{B}_i$. The inequality

$$\sum_{i=1}^{n} (\Delta \hat{M}_i)^2 \geq U_A + U_B, \tag{2.44}$$

holds for any *separable* state. A violation of this inequality implies entanglement. Therefore, we can construct a set of entanglement witnesses

$$\mathcal{W}(\rho) = \sum_{i=1}^{n} (\Delta \hat{M}_i)^2 - U_A - U_B. \tag{2.45}$$

## 2.3 Waveguide QED

In the previous section, we introduced the Gaussian states of light that carry information between our quantum nodes. Here, we further discuss how this light propagates and couples between different nodes. For that, we assume that the electromagnetic field is confined in a 1D structure. The field of quantum emitters coupled to a confined electromagnetic field is then called *waveguide QED*, and it has gained recent popularity due to the experimental progress in different platforms as well as novel theoretical predictions. [136–139]. Contrary to photons in free space, the confinement of light in such a structure allows to achieve higher qubit-photon coupling strengths as well as travelling modes which allow for the distribution of excitations along the waveguide.

The waveguide can be described by a collection of quantum harmonic oscillators, given by the following bare Hamiltonian [124]

$$\hat{H}_{\text{ph}} = \sum_{k=1}^{n} \hbar\omega_k \left(\hat{a}_k^\dagger \hat{a}_k + 1/2\right). \tag{2.46}$$

Here, $\omega_k$ indicates the angular frequency associated with the $k$-th mode. We assume a waveguide of length $L_z$ along the $z$ direction and transversal area $A$ along the $xy$ plane. Then, the electric field inside the waveguide is given by

$$\hat{\boldsymbol{E}}(z,t) = -i\sum_k \sqrt{\frac{\hbar\omega_k}{2\epsilon_0}} \left(\boldsymbol{u}_k^*(z)\,\hat{a}_k^\dagger(t) - \boldsymbol{u}_k(z)\,\hat{a}_k(t)\right). \tag{2.47}$$

Here, $\boldsymbol{u}_k(z)$ are the mode eigenfunctions, which form a normalized and orthogonal set of basis functions [137]. The mode function can be expressed in terms of traveling waves

$$\boldsymbol{u}_k(z) = \boldsymbol{e}\frac{1}{\sqrt{V}}e^{ikz}, \tag{2.48}$$

where $\boldsymbol{e}$ the polarization vector with $|\boldsymbol{e}| = 1$ and we defined the mode volume $V = L_z A$. Due to the periodic boundary condition we impose on the waveguide, each mode is given by $k \equiv k_n = \frac{2\pi}{L_z}n$, with $n = \pm1, \pm2, \ldots$.

We are interested in a regime where the light is strongly confined in the 1D plane. In this regime, we obtain a linear relation between the angular frequency $\omega_k$ and the wavenumber $k$, $\omega_k \simeq v|k|$, where $v$ is the phase velocity of the electromagnetic wave. Other regimes of light propagation can be studied with a waveguide, such as slow-light [140] and photonic gaps [141].

To model the waveguide, we assume it extends infinitely along the $z$ direction, $L_z \to \infty$. In this limit, the distance between modes decreases as $\Delta k_n = k_n - k_{n+1} = \frac{2\pi}{L_z} \to 0$. We can take the continuum limit of our discrete model by replacing sums by integrals according to

$$\sum_n f(k_n) \to \frac{1}{\Delta k}\int \mathrm{d}k f(k) = \frac{L_z}{2\pi}\int \mathrm{d}k f(k). \tag{2.49}$$

Here, it is important to emphasize that real waveguides confine light only in a certain frequency range $|k| \in [k_0 - \Delta_k, k_0 + \Delta_k]$. Therefore, the integrals are always performed over a finite bandwidth $\Delta_k$. Moreover, for a consistent description of our system, it is also important that we transform our modes of the electromagnetic field

$$\hat{a}_k \to \sqrt{\Delta k}\hat{a}(k) = \sqrt{L_z/(2\pi)}\hat{a}(k). \tag{2.50}$$

### 2.3.1 Light-matter interactions

We have now introduced all the relevant ingredients for a quantum network: the nodes that store the quantum state and photons, which can carry quantum states along waveguides. However, we must still discuss the interaction between the stationary nodes and the propagating photons.

Consider a quantum network of $N_\mathrm{q}$ qubits, as described in Sec. 2.1. Each qubit in the network is a two-level system with transition frequency $\omega_{\mathrm{q,j}}$. The bare energy of the qubit system is then given by

$$\hat{H}_\mathrm{q} = \hbar\sum_{j=1}^{N_\mathrm{q}} \frac{\omega_{\mathrm{q,j}}}{2}\hat{\sigma}_j^z. \tag{2.51}$$

We can assume that the waveguides's central wavelength $\lambda_0 = 2\pi/k_0$ is much larger than the size of the qubits. In this regime, one can perform the so-called *long wave-length approximation* [142] in which the electromagnetic field is evaluated at the exact position of the emitter $\hat{\boldsymbol{E}}(z) \approx \hat{\boldsymbol{E}}(z_i)$, where $z_i$ is the position of the $i$-qubit. In this approximation, the coupling between the qubits and the electromagnetic field is given by

$$\hat{H}_\mathrm{int} = -\sum_{j}^{N_q} \hat{\boldsymbol{d}}_j \hat{\boldsymbol{E}}(z_j), \tag{2.52}$$

where the dipole operator $\hat{\boldsymbol{d}}_j$ of the $j$-qubit is given by $\hat{\boldsymbol{d}}_j = \boldsymbol{d}(\hat{\sigma}_j + \hat{\sigma}_j^+)$. Evaluating this expression using the electric field from the waveguide in Eq. (2.47) we obtain

$$\hat{H}_\mathrm{int} = i\sum_{n,j}\sqrt{\frac{\hbar\omega_n}{2\epsilon_0}}\boldsymbol{d}_j \cdot \left(\boldsymbol{u}_n^*(z_j)\hat{a}_n^\dagger \hat{c}_j - \mathrm{h.c.}\right) = i\hbar\sum_{k,j} g_{k,i}\left(\hat{a}_k^\dagger e^{-i\omega_k z_j/v}\hat{c}_j - \hat{a}_k\hat{c}_j^\dagger e^{i\omega_k z_j/v}\right). \tag{2.53}$$

To obtain this expression, we have performed the rotating wave approximation (RWA), justified when the system's natural frequencies $\omega_j$ are much larger than other time scales.

We have also defined the qubit-photon couplings

$$g_{k,i} = \sqrt{\frac{\omega_k}{2\hbar\epsilon_0}}|\boldsymbol{d}_i \cdot \boldsymbol{\epsilon}|. \tag{2.54}$$

In general, we can assume that the coupling strength is approximately around the central wavenumber of the waveguide and in the following, we set $g_i \approx g_{i,k_0}$.

A 1D waveguide presents the versatility we need to distribute photons between different notes of our quantum network. Still, a simple waveguide presents different scenarios in which photons can propagate. When a qubit emits an excitation into the waveguide, it can travel to the left or the right. Recent experiments have shown how to engineer a waveguide in which the excitations in one direction are more favourable than in the other. These waveguides are called *chiral waveguides* [143, 144], and they are characterized by an asymmetric coupling between the left- and right-propagating modes given by $g_{j,L}$ and $g_j, R$, respectively for the $j$-th qubit. Taking this into consideration, we get the final Hamiltonian

$$\hat{H} = \hat{H}_{\text{sys}} + \hbar \sum_{d=L,R} \int_{\mathcal{B}} \mathrm{d}\omega\, \omega \hat{a}_d^\dagger(\omega)\hat{a}_d(\omega) + i\hbar \sum_{d=L,R} \sum_j \int_{\mathcal{B}} \mathrm{d}\omega\, g_{j,d} \left(\hat{a}_d^\dagger(\omega)\hat{c}_j e^{-i\omega z_j/v_d} - \text{h.c}\right), \tag{2.55}$$

where we have defined a bandwidth interval $\mathcal{B} \in [\omega_0 - \Delta_\mathrm{B}, \omega_0 + \Delta_\mathrm{B}]$ and assumed a generic Hamiltonian for the nodes of the network $\hat{H}_{\text{sys}}$ and two independent sets of modes $\hat{a}_R(\omega)$ and $\hat{a}_L(\omega)$ for the right and left propagating fields, respectively. To model the directionality of the modes, we take the convention that the phase velocity is $v_R = -v_L \equiv v > 0$.

### 2.3.2 Chiral master equation

The Hamiltonian given by Eq. (2.55) is a complex object. It involves infinite modes from the waveguide and $N_\mathrm{q}$ quantum emitters coupled to it. Solving this Hamiltonian exactly would require solving the Schrödinger equation. This can be done in specific instances, for example, if we limit ourselves to a single excitation. In general, this is intractable both numerically and analytically. However, if one is interested in only the system's dynamics, one can obtain an effective description of this system of interest, the network, in terms of a master equation for the reduced state of the qubits only.

Our goal is to obtain an effective description of the dynamics of the quantum emitters by tracing out the waveguide. To keep the derivation general, we assume that the waveguide is coupled to general quantum emitters rather than qubits. As represented in Fig. 2.2, those quantum emitters are labelled $j = 0, 1, \cdots, N_\mathrm{q}$ for later convenience, and their coupling into the waveguide is described by the operators $\hat{c}_j$ and $\hat{c}_j^\dagger$.

We start with the Heisenberg equations of motion for an arbitrary operator $\hat{O}$ of the whole system, which is given by $\dot{\hat{O}} = i[\hat{H}, \hat{O}]$ ($\hbar = 1$). The equation of motion of a mode

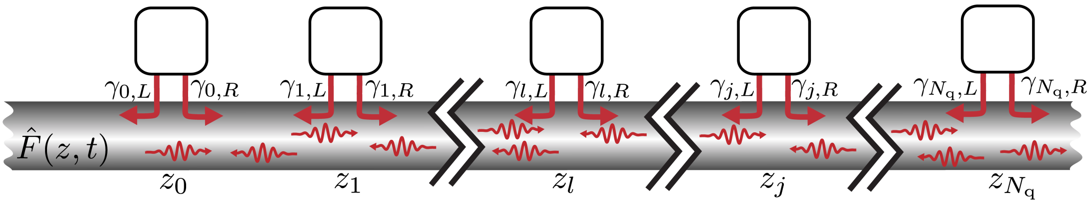


**Figure 2.2:** Schematic of a chiral waveguide coupled to $N_\mathrm{q}$ quantum emitters. The $j$-th emitter is placed at position $z_j$ and has a left and right mode with decay rates $\gamma_{j,L}$ and $\gamma_{j,R}$, respectively. The field operator $\hat{F}(z,t)$ describes the state of the waveguide. The quantum emitters are taken as general quantum objects that could represent qubits or resonators. We adopt the convention that $z_0 < z_1 < \cdots < z_l < z_j < \cdots < z_{N_\mathrm{q}}$

at fixed frequency is

$$\dot{\hat{a}}_d(\omega,t) = i[\hat{H}, \hat{a}_d(\omega,t)] = -i\omega\hat{a}_d(\omega,t) + \sum_j g_{j,d}\,\hat{c}_j(t)e^{-i\omega z_j/v_d}. \tag{2.56}$$

This differential equation can be formally integrated to

$$\hat{a}_d(\omega,t) = \hat{a}_d(\omega,0)e^{-i\omega t} + \sum_j g_{j,d}\int_0^t \mathrm{d}\tau\,\hat{c}_j(\tau)e^{-i\omega(t-\tau)}e^{-i\omega z_j/v_d}. \tag{2.57}$$

The field operator $\hat{F}_d(z,t)$ for the $d$-th propagating mode is given by

$$\begin{aligned}\hat{F}_d(z,t) &= \frac{1}{\sqrt{2\pi}}\int_{\mathcal{B}} \mathrm{d}\omega\,\hat{a}_d(\omega,t)e^{i\omega z/v_d}\\ &= \hat{f}_{\mathrm{in},d}(t-z/v_d) + \sum_j \frac{g_{j,d}}{\sqrt{2\pi}}\int_{\mathcal{B}}\mathrm{d}\omega\int_0^t \mathrm{d}\tau\,e^{i\omega z/v_d}e^{-i\omega(t-\tau)}e^{-i\omega z_j/v_d}\hat{c}_j(\tau).\end{aligned} \tag{2.58}$$

Here, we have defined an input field as

$$\hat{f}_{\mathrm{in},d}(t) = \frac{1}{\sqrt{2\pi}}\int_{\mathcal{B}}\mathrm{d}\omega\,\hat{a}_d(\omega,0)e^{-i\omega t}. \tag{2.59}$$

The same equations of motion can be derived for any operator belonging to the system under consideration $\hat{O}_s$

$$\dot{\hat{O}}_s(t) = i[\hat{H}_{\mathrm{sys}}, \hat{O}_s(t)] - \sum_{d=L,R}\sum_j \int_{\mathcal{B}}\mathrm{d}\omega\,g_{j,d}\left(\hat{a}_d^\dagger(\omega,t)[\hat{c}_j,\hat{O}_s]e^{-i\omega z_j/v_d} - \mathrm{h.c.}\right). \tag{2.60}$$

This operator differential equation can now be expressed in terms of the field operator previously defined

$$\dot{\hat{O}}_s = -i[\hat{O}_s, \hat{H}_{\text{sys}}] + \sum_{d=L,R} \sum_j \sqrt{2\pi} g_{j,d} \left( \hat{F}_d^\dagger(z_j, t)[\hat{O}_s, \hat{c}_j] - \text{h.c.} \right). \tag{2.61}$$

This equation tells us that the dynamics of the $j$-th quantum emitter is governed by its bare dynamics $\hat{H}_{\text{sys}}$ and is coupled to the others $l \neq j$ objects in the waveguide mediated by the field operator $\hat{F}(z_l, t)$. This equation of motion is exact, but it is not very useful right now. To proceed, we must assume the waveguide has a broad bandwidth $\Delta_B \gg 1$. This approximation is called the *Markov* approximation, and it allows us to express the field operators in terms of delta-correlated functions.

$$\int_{\omega_0-\Delta_B}^{\omega_0+\Delta_B} \mathrm{d}\omega \, e^{-i\omega(t-\tau)} = 2\Delta_B \text{sinc}(\Delta_B(t-\tau))e^{-i\omega_0(t-\tau)} \simeq 2\pi\delta(t-\tau)e^{-i\omega_0(t-\tau)}. \tag{2.62}$$

Under this approximation, the field operators are given by [145]

$$\hat{F}_d(z, t) = \hat{f}_{\text{in},d}(t - z/v_d) + \sum_j \sqrt{\gamma_{j,d}}\, \Theta(z/v_d - z_j/v_d)\hat{c}_j(t - z/v_d + z_j/v_d), \tag{2.63}$$

where we have introduced the Heaviside step function $\Theta(t)$ to take into account the integral limits, and we have defined $g_{j,d} = \sqrt{\gamma_{j,d}/(2\pi)}$. We can now reintroduce this expression for the field operator back into our equation of motion for the system operator

$$\begin{aligned} \dot{\hat{O}}_s =& -i[\hat{O}_s, \hat{H}_{\text{sys}}] + \sum_{d=L,R} \sum_j \sqrt{\gamma_{j,d}} \left( \hat{f}_{\text{in},d}^\dagger(t - z_j/v_d)[\hat{O}_s, \hat{c}_j] - \text{h.c.} \right) \\ &+ \sum_{d=L,R} \sum_{j,l} \sqrt{\gamma_{j,d}\gamma_{l,d}} \left( \Theta(z_j/v_d - z_l/v_d)\hat{c}_l^\dagger[\hat{O}_s, \hat{c}_j]e^{i\omega_0(z_l/v_d - z_j/v_d)} - \text{h.c.} \right). \end{aligned} \tag{2.64}$$

where to be consistent with the Markov approximation, we have assumed that the fast dynamics of the relevant system operators is given by $\hat{c}_j(t) \simeq e^{-i\omega_0(t-\tau)}\hat{c}_j(\tau)$. We can now take the expectation value of such an operator differential equation using $\langle \hat{O}_s(t) \rangle = \text{Tr}\{\hat{O}_s(t)\rho\}$. Here, we assume the waveguide to be sufficiently cold so that we can neglect thermal excitations, or in other words, we assume the waveguide to be in a vacuum state $\rho_{\text{wg}} = |0\rangle\langle 0|$. Defining the total state of the system as $\rho_{\text{full}} = \rho_{\text{sys}} \otimes \rho_{\text{wg}}$, we find $\hat{f}_{\text{in},d}(t)\rho_{\text{full}} = \rho_{\text{full}}\hat{f}_{\text{in},d}^\dagger(t) = 0$. The differential equation for the expectation value of any system operator is then

$$\begin{aligned} \langle \dot{\hat{O}}_s \rangle =& -i[\langle \hat{O}_s \rangle, \hat{H}_{\text{sys}}] \\ &+ \sum_{d=L,R} \sum_{j,l} \sqrt{\gamma_{j,d}\gamma_{l,d}} \left( \Theta(z_j/v_d - z_l/v_d)\langle \hat{c}_l^\dagger[\hat{O}_s, \hat{c}_j] \rangle e^{i\omega_0(z_l/v_d - z_j/v_d)} - \text{h.c.} \right). \end{aligned} \tag{2.65}$$

This equation for the expectation value of *any* system operator should be the same in the Heisenberg picture and in the Schrödinger picture, that is $\langle \hat{O}_s(t) \rangle = \text{Tr}\{\hat{O}_s(t)\rho\} =$

$\mathrm{Tr}\{\hat{O}_s\rho(t)\}$. We then obtain an equation of motion for the density matrix $\rho(t)$

$$\begin{aligned}\dot{\rho}(t) =& -i[\hat{H}_{\text{sys}}, \rho(t)] \\ &+ \sum_{d=L,R}\sum_{j,l}\sqrt{\gamma_{j,d}\gamma_{l,d}}\left(\Theta(z_j/v_d - z_l/v_d)[\hat{c}_j, \rho(t)\hat{c}_l^\dagger]e^{i\omega_0(z_l/v_d - z_j/v_d)} - \text{h.c.}\right).\end{aligned} \tag{2.66}$$

This is the most general master equation for left and right propagating modes under the Born-Markovian approximation. We can further simplify this by explicitly evaluating the left and right modes. In doing so, one must use $\Theta(0) = 1/2$ and we assume $z_j > z_l$ for $j > l$. Then $\Theta(z_j/v_d - z_l/v_d) = 1$ for the right-propagating modes and $\Theta(-z_j/v + z_l/v) = 1$ for the left-propagating (because $v_L < 0$). Taking this into consideration, we obtain a more compact form for our chiral master equation

$$\dot{\rho}(t) = -i[\hat{H}_{\text{sys}} + \hat{H}_{\text{L}} + \hat{H}_{\text{R}}, \rho(t)] + \mathcal{D}[\hat{L}_L]\rho(t) + \mathcal{D}[\hat{L}_R]\rho(t). \tag{2.67}$$

Here, where we have defined $\mathcal{D}[\hat{c}]\rho = \hat{c}\rho\hat{c}^\dagger - (\hat{c}^\dagger\hat{c}\rho + \rho\hat{c}^\dagger\hat{c})/2$. Due to the waveguide-mediated interactions, this chiral master equation is governed by two collective jump operators $\hat{L}_R = \sum_j \sqrt{\gamma_{j,R}}e^{-ikz_j}\hat{c}_j$ and $\hat{L}_L = \sum_j \sqrt{\gamma_{j,L}}e^{ikz_j}\hat{c}_j$ and a coherent dipole-dipole interaction

$$\hat{H}_L = \frac{i}{2}\sum_{j<l}\sqrt{\gamma_{j,L}\gamma_{l,L}}\left(e^{-ik|z_j - z_l|}\hat{c}_l^\dagger\hat{c}_j - \text{h.c}\right), \tag{2.68}$$

$$\hat{H}_R = \frac{i}{2}\sum_{j>l}\sqrt{\gamma_{j,R}\gamma_{l,R}}\left(e^{-ik|z_j - z_l|}\hat{c}_l^\dagger\hat{c}_j - \text{h.c}\right). \tag{2.69}$$

This master equation and its variations will be the main starting point throughout the thesis. While we have chosen a more *physically* motivated approach to derive it using the Heisenberg equations of motion, such master equations can also be derived from a general state in the Schrödinger picture. We refer the reader to [146] for these derivations.

In Eq. (2.67), we have not yet made any assumption about the coupling strength of each emitter to the left and right propagating modes. This allows us to study two distinct regimes.

**Bidirectional waveguide** Assume the quantum emitters couple at the same rate to the left- and right-propagating modes, $\gamma_{j,L} = \gamma_{j,R} \equiv \gamma_j$ for the $j$-emitter along the waveguide. In this case, the coherent dipole-dipole interaction exchange cancels out $\hat{H}_{\text{L}} + \hat{H}_{\text{R}} = 0$ and we are left only with the dissipative dynamics. We then obtain a bidirectional master equation

$$\dot{\rho} = -i\left[\hat{H}_{\text{sys}} + \sum_{j,l}J_{j,l}\hat{c}_j^\dagger\hat{c}_l, \rho\right] + \sum_{j,l}\Gamma_{j,l}\mathcal{D}[\hat{c}_j, \hat{c}_l]\rho, \tag{2.70}$$

where introduce the notation $\mathcal{D}[\hat{c}_j, \hat{c}_l]\rho = \hat{c}_l\rho\hat{c}_j^\dagger - (\hat{c}_j^\dagger\hat{c}_l\rho + \rho\hat{c}_j^\dagger\hat{c}_l)/2$ and defined a decay rate $\Gamma_{j,l} = 2\sqrt{\gamma_j\gamma_l}\cos(k|z_j - z_l|)$ and a coupling strength $J_{j,l} = \sqrt{\gamma_l\gamma_j}\sin(k|z_j - z_l|)$. This bidirectional master equation is also called the Dicke master equation [147] and has been used to study the phenomena of sub- and superradiant collective decay [148].

**Cascaded waveguide** Consider the highly asymmetric case when the coupling to the left-propagating mode is completely negligible $\gamma_{L,j} = 0 \; \forall j$ such that all the light emitted into the waveguide only couples to the right-propagating mode $\gamma_{R,j} = \gamma_j$. In this scenario, the previous master equation reduces to

$$\dot{\rho}(t) = -i[\hat{H}_{\text{sys}} + \hat{H}_R, \rho(t)] + \mathcal{D}[\hat{L}_R]\rho(t). \tag{2.71}$$

To be consistent with the usual conventions, we relabel the collective jump operators as $\hat{L}_R \equiv \hat{L}$ and the coherent interaction as $\hat{H}_R \equiv \hat{H}_{\text{casc}}$. As we will see in the other chapters, in the cascaded setting, the propagating phase is unimportant and only amounts to a local rotation.

More insight can be gained into this cascaded master equation if we rewrite this equation as

$$\dot{\rho}(t) = -i[\hat{H}_{\text{sys}}, \rho(t)] + \sum_j \gamma_j \underbrace{\mathcal{D}[\hat{c}_j]\rho(t)}_{\text{local decay}} + \sum_{j>l} \sqrt{\gamma_j \gamma_l} \left( \underbrace{[\hat{c}_j, \rho(t)\hat{c}_l^\dagger] - [\hat{c}_j^\dagger, \hat{c}_l \rho(t)]}_{\text{cascaded interaction}} \right). \tag{2.72}$$

As an explicit example for the cascaded interaction, consider two harmonic oscillators $\hat{a}_A$ and $\hat{a}_B$ described by Eq. (2.72), such that $\hat{a}_A$ is on the left of $\hat{a}_B$. The two oscillators are described by its individual frequency $\omega_A$ and $\omega_B$, such that the system Hamiltonian is $\hat{H}_{\text{sys}} = \omega_A \hat{a}_A^\dagger \hat{a}_A + \omega_B \hat{a}_B^\dagger \hat{a}_B$, and decay into the waveguide at rate $\kappa_A$ and $\kappa_B$. From our cascaded master equation, we can find the equation of motion for the first moments $\langle \hat{a}_n(t) \rangle = \text{Tr}\{\hat{a}_n \rho(t)\}$ for $n = A, B$. In this case, we obtain

$$\frac{\mathrm{d}}{\mathrm{d}t} \begin{pmatrix} \langle \hat{a}_A \rangle \\ \langle \hat{a}_B \rangle \end{pmatrix} = \begin{pmatrix} -i\omega_A - \kappa_A/2 & 0 \\ -\sqrt{\kappa_A \kappa_B} & -i\omega_B - \kappa_B/2 \end{pmatrix} \begin{pmatrix} \langle \hat{a}_A \rangle \\ \langle \hat{a}_B \rangle \end{pmatrix}. \tag{2.73}$$

Observe how the dynamics of the first harmonic oscillator is unaffected by the presence of the second one. On the other hand, the second oscillator couples to the first, and any excitation will be transferred.

Throughout this thesis, most of the analysis considers a unidirectional waveguide, which allows us to use the cascaded master equation in Eq. (2.72). This assumption os two-fold: On the one hand, it simplifies the theoretical analysis, as previously done in [149–151], and on the other hand, such conditions can be realized by using circulators [152–157], chiral waveguides [143], or other schemes for directional coupling [79, 144, 158–161].

**Remark on many waveguides** The theoretical description of many independent linear waveguides can be done by considering now $n$ independent waveguides. Its interaction Hamiltonian Eq. (2.55) is then extended to accommodate $n$ independent modes $\hat{b}_{d,n}(\omega)$ with $[\hat{b}_{d,n}(\omega), \hat{b}^\dagger_{d',n'}(\omega')] = \delta_{d,d'}\delta_{n,n'}\delta(\omega - \omega'))$. Equivalently, we define $n$ independent field operators $\hat{F}_n(z,t)$ to which any system operator can couple via

$$\dot{\hat{O}}_s = -i[\hat{O}_s, \hat{H}_{\text{sys}}] + \sum_n \sum_{d=L,R} \sum_j \sqrt{2\pi} g_{n,j,d} \left( \hat{F}^\dagger_{n,d}(z_j,t)[\hat{O}_s, \hat{c}_j] - \text{h.c.} \right). \tag{2.74}$$

One then finds similar results as Eq. (2.67) for a chiral master equation, considering other equivalent dissipation processes for the $n$ independent decay channels.

### 2.3.3 Semi-infinite waveguide

A 1D waveguide is characterized by its travelling modes along the $z$ direction. However, this is only the case when open boundary conditions are present. If the boundary conditions are changed, the 1D waveguide also changes its mode structure. One case would be if we put a mirror on the edge of the waveguide. In this case, travelling modes would not be possible anymore, and the mode functions would be similar to a 1D cavity with standing waves. Another case, which we motivate physically in Chapter 5, is the case of a phononic waveguide. In this case, the phononic excitations are maximal on the edge of the waveguide, also allowing for standing waves as mode functions. Specifically, in a 1D phononic waveguide, the mode functions are

$$u_k(z) = \epsilon \sqrt{\frac{2}{V}} \cos(kz), \tag{2.75}$$

where $V = AL$ and $k_n = \frac{\pi n}{L}$, with $n = 0, 1, 2, 3...$ for a closed boundary conditions. Assume the waveguide has a linear dispersion relation $\omega_k = v|k|$. The electric field then reads as

$$\hat{E}(z) = -i\epsilon \sum_n \sqrt{\frac{\hbar\omega_n}{\epsilon_0 V}} \cos(k_n z)(\hat{a}^\dagger_n - \text{h.c.}). \tag{2.76}$$

Going to a continuum model of the waveguide, its interaction with a set of quantum emitters is then given by [162]

$$\hat{H}_{\text{int}} = i\hbar \sum_j \int_{\mathcal{B}} [a^\dagger(\omega)\hat{c}_j(g_{j,R}e^{-i\omega z_j/v} + g_{j,L}e^{i\omega z_j/v}) - \text{h.c.}], \tag{2.77}$$

where we have assumed asymmetric couplings into the waveguide, $\gamma_L \neq \gamma_R$. The main difference between an infinite bidirectional waveguide and a semi-infinite waveguide is that now we only have a single stationary mode $a(\omega)$, rather than two modes $a_L(\omega)$ and $a_R(\omega)$.

As before, we find the Heisenberg equations of motion for the field $\hat{a}(\omega, t)$ and for any system operator $\hat{O}_s$. We obtain a similar equation as in Eq. (2.61) but this time with a different field operator

$$\hat{F}(z,t) = \hat{f}_{\text{in}}(t - z/v) + \sum_{j,d=L,R} \Big[ \sqrt{\gamma_{j,d}}\Theta(z/v - z_j/v_d)\hat{c}_j(t - z/v + z_j/v_d) \Big]. \tag{2.78}$$

Notice the extra term, which was not present in the bidirectional waveguide. As we can see, this term accounts for the boundary conditions and the reflection of the left mode.

$$\dot{\hat{O}}_s = -i[\hat{O}_s, \hat{H}_{\text{sys}}] + \sum_j \Big[ \Big( \sqrt{\gamma_{j,R}}\hat{F}^\dagger(z_j,t) + \sqrt{\gamma_{j,L}}\hat{F}^\dagger(-z_j,t) \Big) [\hat{O}_s, \hat{c}_j] - \text{h.c.} \Big]. \tag{2.79}$$

To proceed and simplify our results, we assume the semi-infinite waveguide behaves as a bidirectional waveguide $\gamma_{j,R} = \gamma_{j,L} \equiv \gamma_j$. Then, following a similar derivation as in the case of the chiral master equation, we obtain

$$\dot{\rho} = -i\Big[\hat{H}_{\text{sys}} + \sum_{j,l} J_{j,l}\hat{c}_j^\dagger\hat{c}_l, \rho\Big] + \sum_{j,l} \Gamma_{j,l}\mathcal{D}[\hat{c}_j, \hat{c}_l]\rho. \tag{2.80}$$

Notice the similar structure as to the bidirectional master equation Eq. (2.70), but now with slightly different decay rates $\Gamma_{j,l} = 2\sqrt{\gamma_j\gamma_l}[\cos(k(z_j + z_l)) + \cos(k|z_j - z_l|)]$ and coupling stregth $J_{j,l} = \sqrt{\gamma_j\gamma_l}[\sin(k(z_j + z_l)) + \sin(k|z_j - z_l|)]$. Notice that the main difference between a bidirectional waveguide and this semi-infinite waveguide comes from our position-dependent decay rates. Similar position-dependent setups with mirrors have been studied recently [163].

In the specific case when we place the emitters at distances commensurate with the waveguide wavelength such that $k|z_j \pm z_l| = 2\pi n$ (for $n \in \mathbb{Z}$), the master equation describing a semi-infinite waveguide reduces to

$$\dot{\rho} = -i[\hat{H}_{\text{sys}}, \rho] + 4\mathcal{D}[\hat{L}]\rho. \tag{2.81}$$

where $\hat{L} = \sum_i \sqrt{\gamma_i}\hat{c}_i^\dagger$. An interesting remark is that even in this symmetric limit, we do not recover the same master equation as for the symmetric bidirectional waveguide; instead, we obtain twice the coupling into the waveguide.

## 2.4 Photon sources

The effective description of our quantum network in terms of a master equation is given by Eq. (2.67) for a chiral master equation. This allows us to model a set of quantum emitters that interact via waveguide-mediated interactions. For convenience, we express it in terms of general system operators $\hat{c}$ and $\hat{c}^\dagger$. The reason for this is that Eq. (2.67) can be used to model not only qubits but also resonators or cavities, as demonstrated in the specific example of two harmonic oscillators coupled using Eq. (2.72). However, we have assumed the waveguide to be in a vacuum state, so currently, there are no photons in the system that can carry information between the qubits. While we could introduce the photons by locally driving each qubit [149, 150], here we take a different approach. We consider some of the emitters in our network to be not qubits but rather resonators. We then obtain a system that has both the continuous-variable and discrete-variable degrees of freedom. We then use the photon emitted by these resonators to drive the qubits along the waveguide. It is the interaction with these photons that creates our qubit quantum network. Specifically for the main parts in Chapter 3, Chapter 4, and Chapter 5, we are interested in two types of photonic fields: a thermal state and a two-mode squeezing state.

### 2.4.1 Thermal cavity

The first source of photons is a thermal cavity. This would be a physical realization of Eq. (2.25) for a single-mode resonator in a hot environment represented by Fig. 2.3. This scenario can be modeled using the theory described in Sec. 2.3, with the modification that the waveguide is no longer cold; rather, we have thermal excitations $n_{\mathrm{th}}$. The master equation of this resonator in a hot environment reads

$$\dot{\rho} = -i[\omega_{\mathrm{c}}\hat{a}^\dagger\hat{a}, \rho] + (n_{\mathrm{th}} + 1)\kappa\mathcal{D}[\hat{a}]\rho + n_{\mathrm{th}}\kappa\mathcal{D}[\hat{a}^\dagger]\rho, \tag{2.82}$$

where we have assumed a coupling rate $\kappa$ between the resonator and the waveguide. The steady state of Eq. (2.82) is the thermal distribution given in Eq. (2.25).

We can use Eq. (2.82) to derive the equation of motion for the expectation values of the field $\langle\hat{a}\rangle$ and the photon number $\langle\hat{n}\rangle = \langle\hat{a}^\dagger\hat{a}\rangle$ [126]

$$\frac{\mathrm{d}}{\mathrm{d}t}\langle\hat{a}\rangle = -i\omega_{\mathrm{c}}\langle\hat{a}\rangle - \frac{\kappa}{2}\langle\hat{a}\rangle, \tag{2.83a}$$

$$\frac{\mathrm{d}}{\mathrm{d}t}\langle\hat{n}\rangle = \kappa\langle\hat{n}\rangle + \kappa n_{\mathrm{th}}. \tag{2.83b}$$

The stationary solution is given by $\langle\hat{a}\rangle_{\mathrm{ss}} = 0$ and $\langle\hat{n}\rangle_{\mathrm{ss}} = n_{\mathrm{th}}$, confirming the results from Sec. 2.2.1. We can use the equations of motion previously derived to find the equation of motion for the two-time correlations. For that, we use the quantum regression theorem [126]. Assume a set of operator expectation values $\langle\hat{G}_i\rangle$ which evolve according

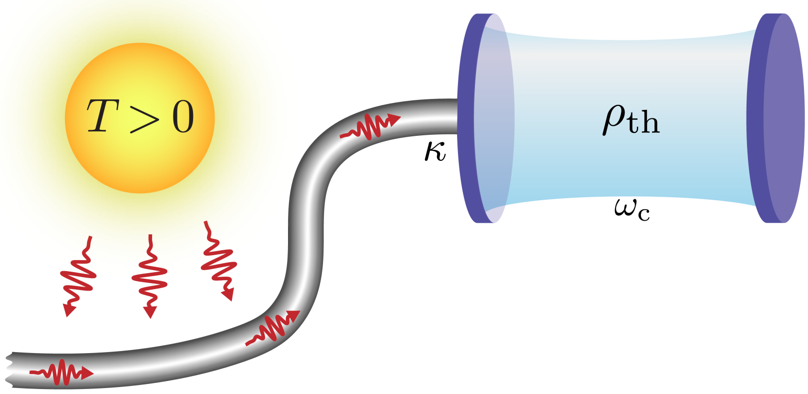


**Figure 2.3:** Schematic of a cavity of frequency $\omega$ coupled to a hot waveguide at temperature $T > 0$ at rate $\kappa$. The state of the cavity $\rho_{\rm th}$ is given by Eq. (2.25).

to the general expression

$$\frac{\mathrm{d}}{\mathrm{d}t}\langle \hat{G}_i \rangle = \sum_j M_{i,j} \langle \hat{G}_j \rangle. \tag{2.84}$$

Then, the stationary two-time correlation function obeys the same equation

$$\frac{\mathrm{d}}{\mathrm{d}t}\langle \hat{G}_i(t)\hat{G}_k(0) \rangle = \sum_j M_{i,j} \langle \hat{G}_j(t)\hat{G}_k(0) \rangle. \tag{2.85}$$

with initial conditions given by the expectation values $\langle \hat{G}_j(0)\hat{G}_k(0) \rangle$. For a thermal cavity, the stationary two-time correlation function is given by

$$\langle \hat{a}^\dagger(\tau)\hat{a}(0) \rangle = n_{\rm th} e^{(i\omega_{\rm c} - \kappa/2)|\tau|}. \tag{2.86}$$

Observe how when $\tau = 0$, we recover $\langle \hat{n} \rangle = n_{\rm th}$. Moreover, the imaginary component vanishes in a rotating frame with respect to the mode $\hat{a}$ at $\omega_c$. Given the two-time correlation, we can define the *output* spectrum of the field as

$$I_{\hat{a}^\dagger \hat{a}}(\omega) = \kappa \int_0^\infty \mathrm{d}\tau \langle \hat{a}^\dagger(\tau)\hat{a}(0) \rangle e^{-i\omega\tau}. \tag{2.87}$$

We obtain

$$I_{\hat{a}^\dagger \hat{a}}(\omega) = \frac{2\kappa n_{\rm th}}{\kappa + 2i(\omega - \omega_c)} = \frac{2\kappa^2 n_{\rm th}}{\kappa^2 + 4(\omega - \omega_{\rm c})^2} - i\frac{4\kappa n_{\rm th}(\omega - \omega_{\rm c})}{\kappa^2 + 4(\omega - \omega_{\rm c})^2}, \tag{2.88}$$

where we have decomposed the expression into real and imaginary parts. The spectrum is governed by a Lorentzian function centered around $\omega_{\rm c}$ and width $\kappa$. Similar to the two-time correlation function, at $\omega = \omega_c$, the spectrum is governed by the real part only.

In Chapter 5, we take an extension of such a master equation for a two-sided cavity, with one side coupled to this hot waveguide and the other connected to a cold waveguide in its vacuum state. We will see how to tune the coupling rates to the waveguides to generate non-trivial states.

### 2.4.2 Nondegenerate parametric amplifier

In Eq. (2.28), we have discussed the generation of a two-mode squeezed state via unitary dynamics. In practice, the two-mode squeezed Hamiltonian appears naturally when putting energy into a nonlinear medium. Such a process relies on a $\chi^{(2)}$-type process between three bosonic modes [99],

$$\hat{H}_\chi = i\chi(\hat{a}_A^\dagger \hat{a}_B^\dagger \hat{a}_0 - \hat{a}_A \hat{a}_B \hat{a}_0^\dagger), \tag{2.89}$$

where the nonlinearity $\chi$ is small, but one of the modes, $\hat{a}_0$, is strongly pumped. This process is called three-wave mixing, and while there are other processes, such as four-wave mixing, they produce similar dynamics. Under the strong pump assumption, the pumped mode can be treated as a classical field, $\langle \hat{a}_0 \rangle \to \alpha_0 \in \mathbb{C}$, and $\hat{H}_\chi$ reduces to a two-mode squeezing interaction. This process becomes most effective when the resonance condition $\omega_A + \omega_B \approx \omega_0$ between the three modes is fulfilled (see Fig. 2.4) and is frequently employed in nonlinear optical crystals to produce entangled photon pairs. Similar interactions also occur in superconducting circuits, where driven Josephson junctions, specifically nondegenerate parametric amplifiers, generate two-mode squeezed microwave beams and many other devices. An alternative way to generate a two-mode squeezed state is to consider two single-mode squeezed states with opposite phases and combine them on a balanced beam splitter [164].

One can compare a parametric amplifier and a laser [99]. Both systems exhibit threshold behavior, adjusted by the input energy, the pump, of the system, as well as to compensate for decay processes. Below the threshold, both systems exhibit a fluctuating field with zero mean amplitude, while above the threshold, both systems have a nonzero mean amplitude. There is, however, a crucial difference which makes the parametric amplifier interesting for us: its fluctuations are correlated, both below and above the threshold, exhibiting nonclassical behavior, as we have described in Eq. (2.35). We are primarily interested in the regime below threshold, as described by Eq. (2.28). We can model this physical process by assuming two 1D waveguides accommodating the emitted photons. In this case, the parametrically generated pairs of photons in modes $\hat{a}_A$ and $\hat{a}_B$ decay into the waveguides with rates $\kappa_A$ and $\kappa_B$, respectively. Using the formalism derived in Sec. 2.3, its dynamics are described by the master equation

$$\dot{\rho} = -i\left[\hat{H}_{\mathrm{TMS}}, \rho\right] + \sum_{n=A,B} \kappa_n \mathcal{D}[\hat{a}_n]\rho, \tag{2.90}$$

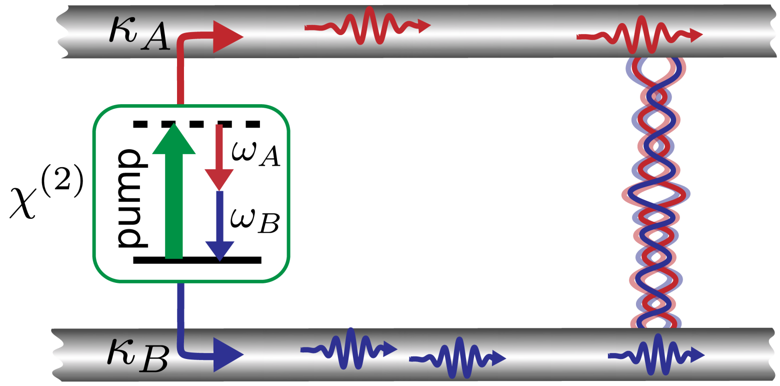


**Figure 2.4:** Schematic of a nondegenerate parametric amplifier coupled to two waveguides. The nonlinear medium emits photons of mode $\hat{a}_A$ and $\hat{a}_B$ at rate $\kappa_A$ and $\kappa_B$, respectively.

where

$$\hat{H}_{\text{TMS}} = i\frac{\sqrt{\kappa_A\kappa_B}\epsilon}{2}\left(\hat{a}_A^\dagger\hat{a}_B^\dagger - \hat{a}_A\hat{a}_B\right), \tag{2.91}$$

and $\epsilon \sim \chi|\alpha_0|$ is the dimensionless pump parameter, which we can assume to be real. The value of $\epsilon = 1$ marks the onset of the parametric instability, beyond which our linearized description of the amplifier is no longer valid. Therefore, we restrict the pumping parameter to $\epsilon \in [0, 1)$.

Here, to understand the nondegenerate parametric amplifier, we need to solve the dynamics of the two modes using its quantum Langevin equations [145, 165]. These equations read

$$\dot{\hat{a}}_A = -\left(\frac{\kappa_A}{2}\right)\hat{a}_A + \frac{\sqrt{\kappa_A\kappa_B}\epsilon}{2}\hat{a}_B^\dagger - \sqrt{\kappa_A}\hat{f}_{\text{in},A}, \tag{2.92}$$

$$\dot{\hat{a}}_B = -\left(\frac{\kappa_B}{2}\right)\hat{a}_B + \frac{\sqrt{\kappa_A\kappa_B}\epsilon}{2}\hat{a}_A^\dagger - \sqrt{\kappa_B}\hat{f}_{\text{in},B}, \tag{2.93}$$

where $\hat{f}_{\text{in,n}}$ are independent white noise operators satisfying $[\hat{f}_{\text{in,n}}(t), \hat{f}_{\text{in,n}'}^\dagger(t')] = \delta_{\text{nn}'}\delta(t-t')$. By defining the vector with operators $\hat{\boldsymbol{v}} = (\hat{a}_A, \hat{a}_B^\dagger, \hat{a}_B, \hat{a}_A^\dagger)^\top$ and the white noise operator vector $\hat{\boldsymbol{f}} = (\sqrt{\kappa_A}\hat{f}_{\text{in,A}}, \sqrt{\kappa_B}\hat{f}_{\text{in,B}}^\dagger, \sqrt{\kappa_B}\hat{f}_{\text{in,B}}, \sqrt{\kappa_A}\hat{f}_{\text{in,A}}^\dagger)^\top$, these equations can be written in a compact form as

$$\frac{\mathrm{d}}{\mathrm{d}t}\hat{\boldsymbol{v}} = \mathcal{M}\hat{\boldsymbol{v}} - \hat{\boldsymbol{f}}, \tag{2.94}$$

where the matrix $\mathcal{M}$ is given by

$$\mathcal{M} = \begin{pmatrix} -\frac{\kappa_A}{2} & \frac{\epsilon\sqrt{\kappa_A\kappa_B}}{2} & 0 & 0 \\ \frac{\epsilon\sqrt{\kappa_A\kappa_B}}{2} & -\frac{\kappa_B}{2} & 0 & 0 \\ 0 & 0 & -\frac{\kappa_B}{2} & \frac{\epsilon\sqrt{\kappa_A\kappa_B}}{2} \\ 0 & 0 & \frac{\epsilon\sqrt{\kappa_A\kappa_B}}{2} & -\frac{\kappa_A}{2} \end{pmatrix}. \tag{2.95}$$

For long times, $t \to \infty$, the formal solution of Eq. (2.94) is

$$\hat{\boldsymbol{v}}(t) = -\int_{-\infty}^{t} \mathrm{d}\tau\, e^{\mathcal{M}(t-\tau)} \hat{\boldsymbol{f}}(\tau). \tag{2.96}$$

From this result, we obtain the full covariance matrix in steady state, $\mathcal{V}_0 = \langle \hat{\boldsymbol{v}} \hat{\boldsymbol{v}}^\dagger \rangle (t \to \infty)$, as

$$\mathcal{V}_0 = \int_0^\infty ds\, e^{\mathcal{M}s} \mathcal{R} e^{\mathcal{M}^\dagger s}, \tag{2.97}$$

where $\mathcal{R} = \mathrm{diag}(\kappa_A, 0, \kappa_B, 0)$ is a diagonal matrix. Since $\mathcal{M}$ is block-diagonal, the individual entries of the covariance matrix can be solved analytically. We obtain

$$n_{\mathrm{ph,n}} = \langle \hat{a}_n^\dagger \hat{a}_n \rangle = \frac{(\bar{\kappa} - \kappa_n)\epsilon^2}{(1-\epsilon^2)\bar{\kappa}}, \tag{2.98}$$

$$m_{\mathrm{ph}} = \langle \hat{a}_A \hat{a}_B \rangle = \frac{\sqrt{\kappa_A \kappa_B}\epsilon}{(1-\epsilon^2)\bar{\kappa}}, \tag{2.99}$$

where $\bar{\kappa} = \kappa_A + \kappa_B$. All other expectation values vanish, i.e., $\langle \hat{a}_A^\dagger \hat{a}_B \rangle = \langle \hat{a}_n^2 \rangle = 0$. Similar to the thermal cavity, we can now use the expectation value together with the quantum regression theorem to evaluate the two-time correlation functions. Assuming symmetric decay rates into the waveguides $\kappa_A = \kappa_B \equiv \kappa$, they are given by

$$\langle \hat{a}_n^\dagger(\tau) \hat{a}_n(0) \rangle = \frac{\epsilon e^{-\kappa/2\tau} \left(\epsilon \cosh\left(\epsilon\kappa\tau/2\right) + \sinh\left(\epsilon\kappa\tau/2\right)\right)}{2(1-\epsilon^2)}, \tag{2.100a}$$

$$\langle \hat{a}_A(\tau) \hat{a}_B(0) \rangle = \frac{\epsilon e^{-\kappa/2\tau} \left(\cosh\left(\epsilon\kappa\tau/2\right) + \epsilon \sinh\left(\epsilon\kappa\tau/2\right)\right)}{2(1-\epsilon^2)}. \tag{2.100b}$$

As before, we can use those expressions to evaluate the output spectrum for the photon occupation number $I_{\hat{a}_n^\dagger \hat{a}_n}(\omega)$ and for the photon correlations $I_{\hat{a}_A \hat{a}_B}(\omega)$. They are given by

$$I_{\hat{a}_n^\dagger \hat{a}_n}(\omega) = \kappa \frac{2\epsilon^2(\kappa + i\omega)}{(\epsilon^2 - 1)(\kappa^2(\epsilon^2 - 1) - 4i\kappa\omega + 4\omega^2)}, \tag{2.101a}$$

$$I_{\hat{a}_A \hat{a}_B}(\omega) = \kappa \frac{\epsilon(\kappa + \epsilon^2\kappa + 2i\omega)}{(\epsilon^2 - 1)(\kappa^2(\epsilon^2 - 1) - 4i\kappa\omega + 4\omega^2)}. \tag{2.101b}$$

In general, we observe that the real part of those spectrum is given by

$$2\mathrm{Re}\{I_{\hat{a}_n^\dagger \hat{a}_n}(\omega)\} = \epsilon \left[\Gamma_-(\omega) - \Gamma_+(\omega)\right], \tag{2.102}$$

and

$$I_{\hat{a}_A \hat{a}_B}(\omega) + I_{\hat{a}_B \hat{a}_A}(-\omega) = \epsilon \left[\Gamma_-(\omega) + \Gamma_+(\omega)\right], \tag{2.103}$$

where

$$\Gamma_{\pm}(\omega) = \frac{\kappa^2}{\kappa^2(1 \pm \epsilon)^2 + 4\omega^2} \tag{2.104}$$

are Lorentzian functions. While the expressions for the output spectrum are complex to analyze, we observe that when $\omega = 0$, we can relate those with the intracavity field occupation number $n_{\mathrm{ph,n}}$ and photon correlation $m_{\mathrm{ph}}$. Specifically, we find that

$$I_{\hat{a}_n^\dagger \hat{a}_n}(0) = 4n_{\mathrm{ph}}(1 + 2n_{\mathrm{ph}}), \tag{2.105a}$$

$$I_{\hat{a}_A \hat{a}_B}(0) = 2m_{\mathrm{ph}} \sqrt{1 + (4m_{\mathrm{ph}})^2}, \tag{2.105b}$$

where for the symmetric case $n_{\mathrm{ph}} \equiv n_{\mathrm{ph,n}} = \frac{\epsilon^2}{2(1-\epsilon^2)}$ and $m_{\mathrm{ph}} = \frac{\epsilon}{2(1-\epsilon^2)}$.

In Sec. 2.2.2, we defined the squeezing level $\mathcal{S}$, which quantifies the uncertainty reduction with respect to the vacuum state. First, we can express the squeezing strength $r$ defined in Eq. (2.28) in terms of the intracavity fields as [166]

$$r = 1 + 2(n_{\mathrm{ph}} - m_{\mathrm{ph}}) = \frac{1}{1 + \epsilon}. \tag{2.106}$$

In the asymptotic limit when $\epsilon \to 1$, the intracavity squeezing strength is limited to $r \to 1/2$. This gives us the well-known bound for the intracavity squeezing of $\mathcal{S} \approx 3\,\mathrm{dB}$ [124]. As we will see in Sec. 3.3, the output fields of the parametric amplifier, contrary to the intracavity fields, are not bounded, and we can achieve perfect squeezing [165].

## 2.5 Phase space representations

Through the first sections of this chapter, we have developed a formalism to obtain an adequate description for quantum emitters coupled to a waveguide in terms of a Lindblad master equation, for example, Eq. (2.70) or Eq. (2.71). We consider only systems described by a continuous variable, as we did in Sec. 2.4, such as harmonic or anharmonic oscillators, degenerate and nondegenerate parametric amplifiers, among others, such that they are described by a set of bosonic operators $\hat{a}_n$ that fulfil the usual commutation relation $[\hat{a}_n, \hat{a}_m^\dagger] = \delta_{n,m}$. Such a system can be described by a Lindblad master equation

$$\dot{\rho}(t) = \mathcal{L}_{\mathrm{ph}}\rho(t). \tag{2.107}$$

While it is not generally possible to solve for $\rho(t)$, we have seen in Sec. 2.2 that if the continuous variables belong to the set of Gaussian states, they are fully characterized by their first $\boldsymbol{\mu}$ and second moments $\boldsymbol{\mathcal{V}}$. For more general states, one can derive the equations of motion for the populations and coherences by expressing the density matrix in a Fock basis. For simplicity, we consider a single mode $\hat{a}$ and write the density matrix as

$$\rho(t) = \sum_{n,m=0}^{\infty} \rho_{n,m}(t)|n\rangle\langle m|, \tag{2.108}$$

with $\rho_{n,m}(t) \equiv \langle n|\rho(t)|m\rangle$. Even for this single-mode example, solving the equations of motion might not be easy. It is, therefore, necessary to introduce an alternative way of solving this master equation and obtaining operator averages and correlation functions [126, 167].

### 2.5.1 P representation

We note that the Fock basis is not the only way to represent our density matrix. Alternatively, we introduce the Glauber-Sudarshan P representation [168, 169], which is diagonal expansion in terms of coherent states

$$\rho(t) = \int \mathrm{d}^2\alpha P(\alpha, \alpha^*, t)|\alpha\rangle\langle\alpha|. \tag{2.109}$$

By expressing the density matrix in this new basis, we can express any state with a quasi-probability distribution $P(\alpha, \alpha^*, t)$. This way, we obtain a classical description of the density matrix, which we can use to obtain some operator expectation values from our system. Assume a normally ordered operator of the form $(a^\dagger)^n a^m$. From a density matrix $\rho(t)$, the operator expectation value is $\langle (a^\dagger)^n a^m\rangle(t) = \mathrm{Tr}\{(a^\dagger)^n a^m \rho(t)\}$. Equivalently, our P representation allows us to find $\langle (a^\dagger)^n a^m\rangle(t) = \int \mathrm{d}^2\alpha\, (\alpha^*)^n \alpha^m P(\alpha, \alpha^*, t)$. Then, the P representation allows us to obtain the expectation values of normally ordered operators in terms of integrals over the complex amplitude $\alpha$.

Back to our master equation Eq. (2.107), in this new basis, we can find that the action of an operator acting on this density matrix is mapped to [126, 170]

$$\hat{a}\rho \quad \longrightarrow \quad \alpha\, P(\alpha,\alpha^*,t), \tag{2.110a}$$

$$\hat{a}^\dagger\rho \quad \longrightarrow \quad \left[\alpha^* - \frac{\partial}{\partial\alpha}\right] P(\alpha,\alpha^*,t), \tag{2.110b}$$

$$\rho\hat{a} \quad \longrightarrow \quad \left[\alpha - \frac{\partial}{\partial\alpha^*}\right] P(\alpha,\alpha^*,t), \tag{2.110c}$$

$$\rho\hat{a}^\dagger \quad \longrightarrow \quad \alpha^*\, P(\alpha,\alpha^*,t). \tag{2.110d}$$

Under this correspondence, any operator master equation transforms into a partially differential equation for a quasi-probability distribution $P(\alpha,\alpha^*,t)$ which represents $\rho(t)$

$$\dot{\rho}(t) = \mathcal{L}_{\mathrm{ph}}\rho(t) \qquad \longrightarrow \qquad \dot{P}(\alpha,\alpha^*,t) = L(\alpha,\alpha^*)P(\alpha,\alpha^*,t). \tag{2.111}$$

This mapping is exact and completely reproduces the dynamics of the density matrix. It can, however, lead to very complicated nonlinear partial differential equations when the original Lindblad has nonlinear operators. This is because, in this case, the operator mapping would produce higher-order partial differential equations such as $\partial^3/(\partial\alpha^3)$ among others. Neglecting those higher-order contributions is the basis of the discrete truncated Wigner approximation [171], which has shown to be an accurate approximation when the system's size is large [172]. When this partial differential equation doesn't produce higher-order terms, or because we can neglect them as an approximation, the partial differential equation takes the form of a Fokker-Planck equation [173]

$$\frac{\partial P(\boldsymbol{x},t)}{\partial t} = \left(\underbrace{-\sum_{i=1}^{2}\frac{\partial}{\partial x_i}A_i(\boldsymbol{x}) + \frac{1}{2}\sum_{i,j=1}^{2}\frac{\partial^2}{\partial x_i\partial x_j}D_{ij}(\boldsymbol{x})}_{L(\alpha,\alpha^*)}\right)P(\boldsymbol{x},t), \tag{2.112}$$

with initial conditions $P(\boldsymbol{x}_0,0)$ and where we have defined $\boldsymbol{x} = (\alpha,\alpha^*)$. The first term of the equation is called the *drift* term, and it governs the evolution for the expectation value of an observable

$$\frac{\mathrm{d}}{\mathrm{d}t}\langle x_i\rangle = \langle A_i(x)\rangle. \tag{2.113}$$

The second term is called the *diffusion* term, and it governs the equation of motion for the second-order moments

$$\frac{\mathrm{d}}{\mathrm{d}t}\langle x_i x_j\rangle = \langle x_i A_j(x)\rangle + \langle x_j A_i(x)\rangle + \frac{1}{2}\langle D_{ij} + D_{ji}\rangle. \tag{2.114}$$

Extending this formalism to $\hat{a}_n$ modes is trivial and only implies the extension of the dimension of the phase-space representation. For this, the summation limits in Eq. (2.112) extend to $2n$, and we define a vector containing all possible modes $\boldsymbol{x} = (\alpha_1, \alpha_1^*, \cdots, \alpha_n, \alpha_n^*)$.

**Stochastic differential equations** The Fokker-Planck equation describes the dynamics of a quasi-probability distribution in phase space. In the case where $\boldsymbol{D}(\boldsymbol{x})$ is positive, this probability distribution can be numerically sampled by a set of Itô stochastic differential equations [170, 174].

$$\mathrm{d}\boldsymbol{x} = \boldsymbol{A}(\boldsymbol{x})\mathrm{d}t + \boldsymbol{B}(\boldsymbol{x})\mathrm{d}\boldsymbol{W}(t), \tag{2.115}$$

where again we use the vector $\boldsymbol{x} = (\alpha_1, \alpha_1^*, \cdots, \alpha_n, \alpha_n^*)$ and we have defined the matrix $\boldsymbol{B}(\boldsymbol{x}_t)$ as the square root of the diffusion matrix $\boldsymbol{D}(\boldsymbol{x}) = \boldsymbol{B}(\boldsymbol{x})\boldsymbol{B}(\boldsymbol{x})^{\mathrm{T}}$. We have defined $\boldsymbol{A}(\boldsymbol{x})$ is a column vector of the drifts $\boldsymbol{A}(\boldsymbol{x}) = (A_1(\boldsymbol{x}), \cdots, A_{2n}(\boldsymbol{x}))^{\mathrm{T}}$. Lastly, we have defined a vector of independent infinitesimal Wiener increments $\mathrm{d}\boldsymbol{W}(t) = (\mathrm{d}W_1(t), \cdots, \mathrm{d}W_{2n}(t))^{\mathrm{T}}$. Each Wiener increment is given by

$$\mathrm{d}W(t) \equiv W(t + \mathrm{d}t) - W(t) = \mathrm{d}t\xi(t), \tag{2.116}$$

where $\xi(t)$ is a rapidly varying random process, sometimes referred to as *white noise*. This random process is a Gaussian process characterized by the two moments

$$\langle \xi(t) \rangle = 0, \tag{2.117a}$$

$$\langle \xi(t)\xi(t') \rangle = \delta(t - t'). \tag{2.117b}$$

Consequently, this translates to the the Wiener increment, which is also a stochastic process with zero $\langle \mathrm{d}W_j(t) \rangle = 0$ and variance $\langle \mathrm{d}W_i(t)\mathrm{d}W_j(t) \rangle = \mathrm{d}t\delta_{i,j}$.

**Harmonic oscillator in a thermal environment** Here, we solve a specific example, motivated in Chapter 5, of a single a single-mode harmonic oscillator with natural frequency $\omega_c$ in contact with an environment at temperature $T > 0$ and decay rate $\kappa$. The Lindblad master equation describing such a process is governed by Eq. (2.82). The corresponding Fokker-Planck equation is then described by

$$L(\alpha, \alpha^*) = \left[ \frac{\partial}{\partial \alpha} \left( i\omega_{\mathrm{c}} + \frac{\kappa}{2} \right) \alpha + \frac{\partial}{\partial \alpha^*} \left( -i\omega_{\mathrm{c}} + \frac{\kappa}{2} \right) \alpha^* + \kappa n_{\mathrm{th}} \frac{\partial^2}{\partial \alpha \partial \alpha^*} \right]. \tag{2.118}$$

The steady-state solution of such a Fokker-Planck equation can be obtained by solving for $\dot{P}(\alpha, \alpha^*) = 0$, which in this case gives

$$P_{\mathrm{ss}}(\alpha, \alpha^*) = \frac{1}{\pi n_{\mathrm{th}}} e^{-|\alpha|^2/n_{\mathrm{th}}}. \tag{2.119}$$

This steady-state distribution of the P representation can be used to calculate the steady-state expectation value of any normally ordered function $f(\hat{a}, \hat{a}^\dagger)$

$$\langle f(\hat{a}, \hat{a}^\dagger)\rangle = \frac{1}{\pi n_{\rm th}} \int \mathrm{d}^2\alpha f(\alpha, \alpha^*) e^{-|\alpha|^2/n_{\rm th}}. \tag{2.120}$$

Alternatively, this oscillator in contact with a thermal field can be described by a complex-valued Itô stochastic differential equation [126]

$$\mathrm{d}\alpha = -\frac{\kappa}{2}\alpha \mathrm{d}t + \sqrt{\kappa n_{\rm th}}\mathrm{d}W(t), \tag{2.121}$$

with complex Wiener increment $\mathrm{d}W(t) = \frac{\mathrm{d}W_1(t)+i\mathrm{d}W_2(t)}{\sqrt{2}}$, where $\mathrm{d}W_i(t)$ for $j = 1, 2$ are two independent, real-valued Wiener increments. This stochastic differential equation is also known as the complex-valued Ornstein-Uhlenbeck process. To obtain expectation values from Eq. (2.121), we formally integrate it to obtain

$$\alpha(t) = \alpha_0 e^{-\kappa/2t} + \sqrt{\kappa n_{\rm th}} \int_0^t \mathrm{d}\tau e^{-\kappa(t-\tau)/2} \xi(\tau). \tag{2.122}$$

Here, we have defined a constant initial condition $\alpha_0 = \alpha(t = 0)$ and used $\frac{\mathrm{d}W(t)}{\mathrm{d}t} = \xi(t)$, as defined in Eq. (2.116). This expression allows us to, for example, obtain the expectation value of its first moment

$$\langle \alpha(t)\rangle = \alpha_0 e^{-\kappa/2t}. \tag{2.123}$$

Observe how first-order moments are entirely governed by the initial conditions and that, as time goes on, they eventually decay to zero $\langle \alpha(t \to \infty)\rangle \to 0$. We can also use Eq. (2.122) to calculate the two-time correlation function. In our case, it reads as

$$\begin{aligned}\langle \alpha^*(t_1)\alpha(t_2)\rangle =& |\alpha_0|^2 e^{-\kappa(t_1+t_2)/2} \\ &+ \kappa n_{\rm th} \int_0^{t_1} \mathrm{d}t_1' \int_0^{t_2} \mathrm{d}t_2' e^{-\kappa/2(t_1-t_1')} e^{-\kappa/2(t_2-t_2')} \langle \xi(t_1')\xi(t_2')\rangle.\end{aligned} \tag{2.124}$$

We can then look at this expression evaluated at the steady state $t_{1,2} \to \infty$. Defining $\tau = t_1 - t_2$, it reduces to

$$\langle \alpha^*(\tau)\alpha(0)\rangle = n_{\rm th} e^{-\kappa|\tau|/2}. \tag{2.125}$$

Observe how this correlation function matches the expression given by Eq. (2.86). This emphasizes that the P representation of the field allows us to find any normally ordered expectation value that we would normally compute using the quantum regression theorem.

Our expansion in Eq. (2.109) in terms of coherent states is not unique. There are other representations, such as the Huisimi Q-distribution [175], which is defined in terms of the anti-normal ordering of the operators, and the Wigner representation [176], which is defined in terms of the symmetric, or Weyl, order of the operators. Here, our focus on the P representation of the field is two-fold: On one hand, we will see later that the application of the P representation on our systems will produce an exact Fokker-Planck equation (by that, we mean without any higher-order partial derivative terms), thus allowing us to obtain an exact mapping. On the other hand, in quantum optics, the P representation has been used to *classify* the states: the P representation makes it natural to highlight the differences between classical and nonclassical fields. This is because more classical fields, like a coherent or a thermal state, admit a stochastic description governed by the quasi-probability $P(\alpha, \alpha^*)$, while nonclassical fields such as Fock or squeezed states do not admit such a description, as in this case the quasi-probability $P(\alpha, \alpha^*)$ becomes negative. In these cases, the Fokker-Planck equation does not possess a positive semifinite diffusion matrix $\boldsymbol{D}(\boldsymbol{x})$.

### 2.5.2 Positive-P representation

To deal with such a problem, Drummond and Gardiner [177] introduced the positive-P representation

$$\rho = \int \mathrm{d}\alpha^2 \int \mathrm{d}\beta^2 \frac{|\alpha\rangle\langle\beta^*|}{\langle\beta^*|\alpha\rangle} P(\alpha, \beta), \tag{2.126}$$

with $\alpha$ and $\beta$ denote two independent complex variables. This representation of the field can always be shown to be positive, defining a probability distribution rather than a quasi-probability distribution, such as in the case of the P representation. This comes at the expense of doubling the degrees of freedom; now, for each single-mode $\hat{a}_n$, we have associated two independent phase-space variables (four real dimensions). The complex-conjugate relation is only fulfilled at the level of averages $\langle\beta\rangle = \langle\alpha\rangle^*$.

The phase-space dynamics in this representation are still represented by the Fokker-Planck equation Eq. (2.112), considering the extended dimensions. As with the P representation, when the positive-P representation doesn't involve higher-order terms, the master equation Eq. (2.107) can be mapped into a Fokker-Planck equation similar to Eq. (2.112), with the corresponding extended phase-space. If we consider a system of $\hat{a}_n$ modes, in our positive-P representation, the Fokker-Planck equation describes a dynamical equation for $\boldsymbol{x} = (\alpha_1, \beta_1, \cdots, \alpha_n, \beta_n)$.

As the positivity of the positive-P representation is guaranteed, this allows us to find a Fokker-Planck equation as Eq. (2.112), and its corresponding stochastic differential equation, Eq. (2.115), to even entangled states. One could, in general, even use the positive-P to represent states for which the P representation would be enough, such as the thermal states. However, the positive-P representation also comes with drawbacks. By introducing a new independent variable $\beta$ and expanding our phase space, the trajectories can now explore new unphysical areas. In many cases, this is then translated into *spikes* [178] or divergences for the trajectories. This has been seen in highly nonlinear systems and two-photon damping processes [99].

**Two-mode squeezed state** For a specific example of the positive-P representation, we focus on generating two-mode squeezed states, described in Sec. 2.2.2 and motivated by Chapter 4, where we will use these results. Starting from Eq. (2.90), we map the two modes $\hat{a}_A$ and $\hat{a}_B$ into positive-P distribution $\mathcal{P}(\alpha_A, \beta_A, \alpha_B, \beta_B)$, governed by Eq. (2.112), with a drift matrix given by

$$\boldsymbol{A} = \frac{1}{2}\begin{pmatrix} -\kappa_A & 0 & 0 & \sqrt{\kappa_A\kappa_B}\epsilon \\ 0 & -\kappa_B & \sqrt{\kappa_A\kappa_B}\epsilon & 0 \\ 0 & \sqrt{\kappa_A\kappa_B}\epsilon & -\kappa_A & 0 \\ \sqrt{\kappa_A\kappa_B}\epsilon & 0 & 0 & -\kappa_B \end{pmatrix}, \tag{2.127}$$

and the diffusion matrix is given by

$$\boldsymbol{D} = \frac{\sqrt{\kappa_A\kappa_B}\epsilon}{2}\begin{pmatrix} 0 & 1 & 0 & 0 \\ 1 & 0 & 0 & 0 \\ 0 & 0 & 0 & 1 \\ 0 & 0 & 1 & 0 \end{pmatrix}. \tag{2.128}$$

We can then map this Fokker-Planck equation into a set of stochastic differential equations following Eq. (2.115) by decomposing the diffusion matrix as $\boldsymbol{D} = \boldsymbol{B}\boldsymbol{B}^{\mathrm{T}}$. In our case, we find this matrix is given by

$$\boldsymbol{B} = \frac{\sqrt{\sqrt{\kappa_A\kappa_B}\epsilon/2}}{2}\begin{pmatrix} 1+i & 1-i & 0 & 0 \\ 1-i & 1+i & 0 & 0 \\ 0 & 0 & 1+i & 1-i \\ 0 & 0 & 1-i & 1+i \end{pmatrix}. \tag{2.129}$$

We then obtain a set of coupled stochastic differential equations. For the symmetric case $\kappa_A = \kappa_B = \kappa$, they are given by

$$\mathrm{d}\alpha_A = [-\alpha_A + \epsilon\beta_B]\kappa/2\mathrm{d}t + \sqrt{\epsilon\kappa/2}\frac{(1+i)\mathrm{d}W_{\alpha_A}(t) + (1-i)\mathrm{d}W_{\beta_A}(t)}{2}, \tag{2.130a}$$

$$\mathrm{d}\beta_A = [-\beta_A + \epsilon\alpha_B]\kappa/2\mathrm{d}t + \sqrt{\epsilon\kappa/2}\frac{(1-i)\mathrm{d}W_{\alpha_A}(t) + (1+i)\mathrm{d}W_{\beta_A}(t)}{2}, \tag{2.130b}$$

$$\mathrm{d}\alpha_B = [-\alpha_B + \epsilon\beta_A]\kappa/2\mathrm{d}t + \sqrt{\epsilon\kappa/2}\frac{(1+i)\mathrm{d}W_{\alpha_B}(t) + (1-i)\mathrm{d}W_{\beta_B}(t)}{2}, \tag{2.130c}$$

$$\mathrm{d}\beta_B = [-\beta_B + \epsilon\alpha_A]\kappa/2\mathrm{d}t + \sqrt{\epsilon\kappa/2}\frac{(1-i)\mathrm{d}W_{\alpha_B}(t) + (1+i)\mathrm{d}W_{\beta_B}(t)}{2}, \tag{2.130d}$$

where the Wigner increments fulfil $\langle \mathrm{d}W_i(t)\mathrm{d}W_j(t)\rangle = \mathrm{d}t\delta_{ij}$, for $i, j \in (\alpha_A, \beta_A, \alpha_B, \alpha_B)$.

### 2.5.3 Stochastic master equation

At the beginning of this section, we focus only on the continuous-variable systems, allowing us to derive an equivalent of the Fokker-Planck formalism for the master equation. In a more general setting, our system is described by a hybrid master equation, where we combine both continuous-variable and discrete-variable systems. This scenario constantly arises throughout the rest of the thesis, such as in Eq. (3.1), Eq. (4.1), and Eq. (5.1). They all have the following structure

$$\dot{\rho} = (\mathcal{L}_0 + \mathcal{L}_{\text{int}})\,\rho = (\mathcal{L}_{\text{ph}} + \mathcal{L}_{\text{q}} + \mathcal{L}_{\text{int}})\,\rho, \tag{2.131}$$

with a cascaded interaction between the continuous and the discrete systems

$$\mathcal{L}_{\text{int}}\rho = \sum_n \sqrt{\kappa_n\gamma_n}\left([\hat{a}_n\rho, \hat{\sigma}_n^+] + [\hat{\sigma}_n^-, \rho\hat{a}_n^\dagger]\right), \tag{2.132}$$

with initial conditions $\rho(0) = \rho_{\text{ph}}(0) \otimes \rho_{\text{q}}(0)$. We can now map this master master equation into an equivalent Fokker-Planck equation. We start by noting that the initial state can be written as [179]

$$\rho(0) = \int \mathrm{d}^2\alpha\, P(\alpha, \alpha^*, 0)|\alpha\rangle\langle\alpha| \otimes \rho_{\text{q}}(0), \tag{2.133}$$

where we have assumed a single-mode scenario with a mode $\hat{a}$ for simplicity. From Eq. (2.132), we can see that, due to the cascaded coupling between continuous-variable and discrete-variable, we always have $\hat{a}$ acting on the left of $\rho$ while $\hat{a}^\dagger$ acting on the right of $\rho$. This means that the discrete-variable system along the waveguide does not affect their dynamics. Therefore, their dynamics remain Gaussian and can be simulated with the Fokker-Planck equation given by Eq. (2.112) or its equivalent stochastic differential equations Eq. (2.115). That is, with the initial representation Eq. (2.133), the operators $\{\hat{a}, \hat{a}^\dagger\}$ can be replaced with complex number $\{\alpha, \alpha^*\}$. This result is a crucial aspect of the derivation and something only possible with cascaded systems. The full system density operator then can be expressed as

$$\rho(t) = \int \mathrm{d}^2\alpha\, P(\alpha, \alpha^*, t)|\alpha\rangle\langle\alpha| \otimes \rho_{\text{q}}(\alpha, \alpha^*, t). \tag{2.134}$$

One can then obtain the reduced density operator $\rho_{\text{q}}(t)$ by tracing out the bosonic degrees of freedom,

$$\rho_{\text{q}}(t) = \int \mathrm{d}^2\alpha\, P(\alpha, \alpha^*, t)\rho_{\text{q}}(\alpha, \alpha^*, t). \tag{2.135}$$

When we sample the P distribution in terms of stochastic trajectories $\alpha$, the integral in Eq. (2.135) is instead replaced over an average over a large but finite number of trajectories.

For a given trajectory, the density matrix $\rho_\mathrm{q}$ is updated according to

$$\dot{\rho}_\mathrm{q}(\boldsymbol{\alpha}, \boldsymbol{\alpha}^*, t) = \left(\mathcal{L}_\mathrm{q} + \sum_n \mathcal{L}_n[\alpha_n, \alpha_n^*]\right) \rho_\mathrm{q}(\boldsymbol{\alpha}, \boldsymbol{\alpha}^*, t), \tag{2.136}$$

where we have already generalized to $\hat{a}_n$ modes and defined $\boldsymbol{\alpha} = (\alpha_1, \cdots, \alpha_n)$. Here, we have also defined $\mathcal{L}_n[\alpha_n, \alpha_n^*]$, which is given by the cascaded coupling Eq. (2.132) after replacing $\hat{a}_n$ and $\hat{a}_n^\dagger$ by $\alpha_n$ and $\alpha_n^*$, respectively. The reduced qubit state is then obtained by solving Eq. (2.136), which is coupled to Eq. (2.115), and taking the statistical average.

**Remark for the positive-P representation** Notice that, in writing Eq. (2.133), we have taken the P-representation of the bosonic field for granted. Assuming a single mode, this can be extended to the positive-P representation by extending the complex-variable representation to $\alpha$ and $\beta$

$$\rho(t) = \int \mathrm{d}^2\alpha \int \mathrm{d}^2\beta\, P(\alpha, \beta, t) \frac{|\alpha\rangle\langle\beta^*|}{\langle\beta^*|\alpha\rangle} \otimes \rho_\mathrm{q}(\alpha, \beta, t). \tag{2.137}$$

Correspondingly, the operators $\{\hat{a}, \hat{a}^\dagger\}$ map to the complex numbers $\{\alpha, \beta\}$. For a given trajectory, similar to the P representation, the density matrix $\rho_\mathrm{q}$, generalized to $n$ modes, evolves as

$$\dot{\rho}_\mathrm{q}(\boldsymbol{\alpha}, \boldsymbol{\beta}, t) = \left(\mathcal{L}_\mathrm{q} + \sum_n \mathcal{L}_n[\alpha_n, \beta_n]\right) \rho_\mathrm{q}(\boldsymbol{\alpha}, \boldsymbol{\beta}, t). \tag{2.138}$$

This stochastic description of the bosonic field offers another advantage. In general, Eq. (2.138) describes a large stochastic master equation for $nN_\mathrm{q}$ qubits in total. However, the solution of Eq. (2.138) for a single mode $n$ is $\rho_{\mathrm{q},n}(\alpha_n, \beta_n, t)$, which is a density matrix involving $N_\mathrm{q}$ qubits. We recover the global density matrix using

$$\rho_\mathrm{q}(\boldsymbol{\alpha}, \boldsymbol{\beta}, t) = \bigotimes_n \rho_{\mathrm{q},n}(\alpha_n, \beta_n, t). \tag{2.139}$$

This form allows us to decouple the master equation, solving for each stochastic process. This way, Eq. (2.138) offers a simple way to parallelize the computation. Instead of solving the equation for $nN_\mathrm{q}$ qubits, we can solve this equation for $n$ independent modes, effectively solving $n$ decoupled equations for $N_\mathrm{q}$ qubits. The reduced qubit density matrix is then obtained by tracing out the bosonic degrees of freedom

$$\rho_\mathrm{q}(t) = \int \mathrm{d}^2\boldsymbol{\alpha} \int \mathrm{d}^2\boldsymbol{\beta}\; P(\boldsymbol{\alpha}, \boldsymbol{\beta}, t) \bigotimes_n \rho_{\mathrm{q},n}(\alpha_n, \beta_n, t). \tag{2.140}$$

## 2.6 Remote entanglement protocols

There are several approaches to generating a pure entangled state $|\psi_0\rangle$ within a quantum network. The protocol should be efficient and scalable for large-scale networks and, ideally, require minimal external control [46, 63]. Since quantum systems naturally experience decoherence over time, the protocol must operate faster than the system's decoherence rate. In the context of large quantum networks, it is also essential that the protocol is easily implementable on a large scale, preferably in a parallelizable manner. By "minimal control", we refer to protocols that can run autonomously, as relying on external manipulation of the qubits would impose an unnecessary burden on the quantum system.

Depending on the strategy used to generate remote entanglement, we distinguish between *probabilistic* and *deterministic* protocols. For simplicity, we focus mostly on two-qubit systems $N_\mathrm{q} = 2$, which forms the minimal network possible, a quantum link. A completed overview of the experimental literature can be found in Ref. [75].

**Probabilistic protocols** To generate remote entanglement between two nodes, we consider a single-photon protocol [55, 180]. The initial state is a tensor product of two decoupled qubits $|\psi_0\rangle = |\psi_1\rangle|\psi_2\rangle$, each qubit being in a superposition similar to Eq. (2.1), given by $|\psi_i\rangle = \alpha|0_i\rangle + \beta|1_i\rangle$. We distinguish between two regimes: weakly driven $|\beta|^2 \ll 1$ and strongly driven $|\beta|^2 \simeq 1$.

For weakly driven qubits, the qubits remain mostly in the ground state and, when excited, rapidly decay back to the ground state. This decay is accompanied by the emission of a photon, entangling the qubit with the emitted photon [46]. This photon travels a distance $x_i$ to a beam splitter. For the $i$-th qubit, the state is then as follows

$$|\psi_i\rangle \sim \alpha|0_i, n_i = 0\rangle + \beta e^{ikx_i}|1_i, n_i = 1\rangle, \tag{2.141}$$

where the notation $|x_i, n_i = x\rangle$ indicates the number of photons $n_i$ emitted from the $i$-th qubit. Following this protocol, the emitted photons from the qubit pair interfere at the beam splitter. The detection of a photon heralds the following qubit-qubit state [181]

$$|\psi_0\rangle \sim \frac{|01\rangle \pm e^{ik(x_i - x_j)}|10\rangle}{\sqrt{2}}. \tag{2.142}$$

This state corresponds to one of the maximally entangled states defined in Eq. (2.8), where the relative sign $\pm$ depends on which of the two photodetectors clicked. The success probability associated with creating this state is $p_\mathrm{det} \propto |\beta|^2\nu$, proportional to the excited state probability $|\beta|^2$ and the detection efficiency $\nu$, which includes any propagation losses. As the state is weakly excited, the probability detection will be small, usually around $p_\mathrm{det} \simeq 10^{-4}$ [181].

One must take into account that, given the detection of one photon, the conditional probability that the other qubit is also in $|1\rangle$ but the photon was lost is given by $p = |\beta|^2$ (in the limit that the photon detection efficiency is small $\nu \ll 1$). This degrades the heralded state from a maximally entangled Bell state to

$$\rho = |\alpha|^2 |\psi_0\rangle\langle\psi_0| + |\beta|^2 |11\rangle\langle 11|. \tag{2.143}$$

This protocol yields a fidelity of $\mathcal{F} = |\alpha|^2$ with probability $p_{\text{det}} \propto |\beta|^2 \nu$. As the state is normalized $|\alpha|^2 + |\beta|^2 = 1$, one obtains a trade-off between the state fidelity and the detection probability.

In the other scenario, the strongly driven regime, each qubit is excited with near unity probability, $|\beta|^2 \sim 1$, and the single photon carries its qubit through two distinguishable internal photonic states (usually via polarization $H$ or $V$ of the emitted photon). For example, the state of the system containing both communication and photonic qubits is written in

$$|\psi_i\rangle = \frac{|0_i, H_i\rangle + e^{ikx_i}|1_i, V_i\rangle}{\sqrt{2}}. \tag{2.144}$$

Here, similar to Eq. (2.141), we use the notation $|x_i, X_i = V, H\rangle$ to indicate the polarization of the emitter photon by the $i$-th qubit. As before, the two photons interfere at a balanced beam splitter, and coincident detection of orthogonally polarized photons heralds a state similar to Eq. (2.143) [65]. Here, however, the probability of success is given by $p_{\text{det}} \propto (|\beta|^2 \nu)^2$. Even if the state is strongly excited $|\beta|^2 \sim 1$, due to the small photon detection efficiency $\nu \ll 1$, the probability of success of this protocol is usually lower than operating in a weakly driven regime. Experimentally, however, this protocol is less sensible to path fluctuations. This is because the stability depends on the wavelength $\lambda$ of the emitted photons, typically at the centimetres scale for this photon, which is emitted from hyperfine levels of the qubits [46].

**Deterministic protocols** The protocols to generate remote entanglement between two nodes that don't require heralding are called *deterministic* remote entanglement protocols. Originally proposed in [41], it consists of applying a coherent drive to one of the qubits to create a qubit-photon entangled state

$$|\psi_0\rangle = \frac{|0_1, n = 1\rangle + |1_1, n = 0\rangle}{\sqrt{2}} \otimes |0_2\rangle. \tag{2.145}$$

Here, we use the notation $|x_1, n, x_2\rangle$ to indicate the state of the first qubit, the state of the photon, and the state of the second qubit, respectively. The photon then decays into a unidirectional waveguide, propagating until the second qubit absorbs it. For a perfect photon absorption by the second qubit, the photon shape must be time-symmetric [41]. This can be achieved by a modulation of the couplings into the waveguide of the emitter and receiver qubits [75, 182, 183]. One then obtains a travelling photon that has a time-symmetric envelope, for example, given by $\phi(t) = \frac{1}{2}\sqrt{\kappa_{\text{eff}}}\,\text{sech}\,(\kappa_{\text{eff}}t/2)$ [75], being $\kappa_{\text{eff}}$ the bandwidth of the photon. Upon perfect ideal absorption of the photon by the second qubit, the two qubits remain in a maximally entangled state $|\Psi^+\rangle$.

To model the photon loss along the transmission in the waveguide, we assume a beam splitter interaction with a fictitious environmental mode [184, 185]

$$|n=1\rangle \longrightarrow \sqrt{\nu}|n=1\rangle \otimes |n=0\rangle_E + \sqrt{1-\nu}|0\rangle \otimes |1\rangle_E. \tag{2.146}$$

This model allows us to obtain the reduced qubit state in case of imperfection transmission. After tracing out the environmental modes, the reduced two-qubit density matrix is

$$\rho = \frac{1}{2}\begin{pmatrix} 0 & 0 & 0 & 0 \\ 0 & 1 & \sqrt{\nu} & 0 \\ 0 & \sqrt{\nu} & \nu & 0 \\ 0 & 0 & 0 & 1-\nu \end{pmatrix}. \tag{2.147}$$

This density matrix allows us to estimate how close we are to the Bell state $|\Psi^+\rangle$ using the fidelity defined in Eq. (2.14). We obtain

$$\mathcal{F}(\rho) = \langle\Psi^+|\rho|\Psi^+\rangle = \frac{1}{4}(1+\sqrt{\nu})^2. \tag{2.148}$$

For the same state, one can use the concurrence defined in Eq. (2.12) to obtain

$$\mathcal{C}(\rho) = \sqrt{\nu}. \tag{2.149}$$

Surprisingly, the entanglement persists despite losses and only vanishes at the limit $\nu \to 0$. However, the state fidelity is bounded for $\mathcal{F}(\rho) = 1/2$ at $\nu = (\sqrt{2}-1)^2 \simeq 0.17$. In Chapter 3, we compare this expression to the effect of losses on our implementation.

# Chapter 3

# Qubit-qubit entanglement distribution using squeezed light

In this chapter, we analyse the creation of the smallest possible quantum network, a quantum link, by driving two qubits with the ouput of a nondegenerate parametric amplifier. As we described in Sec. 2.6, theoretical protocols to generate remote entanglement between physically separated qubits have been extensively studied in deterministic and probabilistic cases. Here, we extend the work of [82], in which the authors propose an alternative way to create highly entangled qubit-qubit states based on continuous-variable entanglement transfer to the qubits. We start with Sec. 3.1, where we introduce the theoretical model of our system. Then, in Sec. 3.2 we obtain an effective description for the qubits alone, under the assumption that the parametric amplifier is broadband. This effective description enables us, in Sec. 3.3, to map our qubit state into an effective squeezing reservoir, which provides new insight into the dynamics of the qubits. With these tools in hand, in Sec. 3.4, we focus on the steady state of the two qubits and show how the entanglement emerges. In Sec. 3.5, we solve the qubit state again for a more general scenario and introduce the filtered mode approximation, which allows us to consider the finite bandwidth of the source of photons. This allows us to obtain optimal parameters to maximize the entanglement in the presence of imperfections. In Sec. 3.6, we study the time evolution of the entanglement. In realistic networks, the photons that propagate from one node to another are always delayed. We investigate these delay effects in Sec. 3.7. We conclude this chapter with Sec. 3.8, where we provide theoretical predictions for two ongoing experimental collaborations.

## 3.1 Setup and master equation

Our protocol to generate deterministic qubit-qubit entanglement consists of two unidirectional waveguides, which we label by $n = A, B$, two physically separated qubits, and a nondegenerate parametric amplifier which emits photons into the waveguides. The setup is sketched in Fig. 3.1. Specifically, we consider the two qubits with resonant frequencies $\omega_{A,1}$ and $\omega_{B,1}$, respectively. The parametric amplifier consists of two distinct bosonic modes

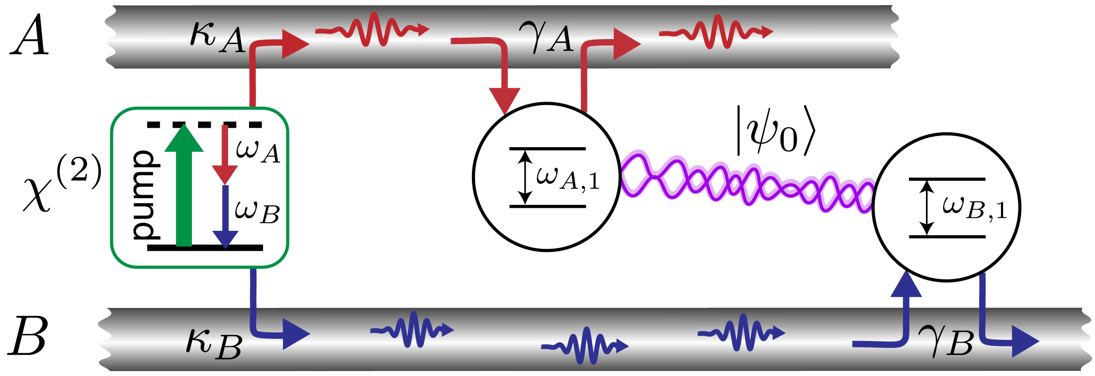


**Figure 3.1:** Schematic of the protocol for generating a qubit-qubit entangled state, where a pair of physically separated qubits are coupled to two unidirectional waveguides and driven by the correlated output of a nondegenerate parametric amplifier.

with frequencies $\omega_A$ and $\omega_B$ and annihilation operators $\hat{a}_A$ and $\hat{a}_B$, respectively. These modes are driven into a correlated two-mode squeezed state via an externally pumped $\chi^{(2)}$-process and decay into the respective waveguides with rate $\kappa_A$ and $\kappa_B$, respectively. The unidirectional waveguide then connects the emitted photons to each qubit at a rate $\gamma_A$ and $\gamma_B$ for each qubit, respectively.

The following analysis is kept deliberately general and applies to implementations in the optical and microwave domain, as well as mixed scenarios, where, for example, correlated pairs of optical and microwave photons are generated via the electro-optical effect [108, 186]. However, throughout our analysis, we will assume that all network parts are sufficiently cold such that thermal excitations can be neglected [187].

In Sec. 2.3, we derived a master equation for the reduced system by tracing out the waveguide dynamics. There, we derived a cascaded master equation for a set of $N_\mathrm{q}$ quantum emitters coupled to a single waveguide. Here, where two waveguides are present, we identify the quantum emitters for the $n$-th waveguide as $\hat{c}_{0,n} \equiv \hat{a}_n$ with decay rate $\gamma_{0,n} \equiv \kappa_n$, and $\hat{c}_{1,n} \equiv \hat{\sigma}_n^-$ with decay rate $\gamma_{1,n} \equiv \gamma_n$.

By moving into a rotating frame with respect to the photon frequencies $\omega_A$ and $\omega_B$ and with the identification we just mentioned, Eq. (2.72) describes the dynamics of the system under consideration, which reads

$$\dot{\rho} = \left(\mathcal{L}_\mathrm{ph} + \mathcal{L}_\mathrm{q} + \mathcal{L}_\mathrm{int}\right)\rho. \tag{3.1}$$

This master equation consists of three distinct terms. A term describing the dynamics of the parametric amplifier $\mathcal{L}_\mathrm{ph}$, which produces the continuous-variable Gaussian states. As introduced in Sec. 2.4.2, a nondegenerate parametric amplifier coupled into an environment (the two waveguides in this case) is modelled as

$$\mathcal{L}_{\mathrm{ph}}\rho = -i\left[\hat{H}_{\mathrm{TMS}}, \rho\right] + \sum_{n=A,B} \kappa_n \mathcal{D}[\hat{a}_n]\rho, \tag{3.2}$$

with nonlinear interaction

$$\hat{H}_{\mathrm{TMS}} = i\frac{\sqrt{\kappa_A\kappa_B}\epsilon}{2}\left(\hat{a}_A^\dagger \hat{a}_B^\dagger - \hat{a}_A\hat{a}_B\right), \tag{3.3}$$

with adimensional pump parameter $\epsilon \in [0, 1)$. In our protocol, although the modes $\hat{a}_A$ and $\hat{a}_B$ decay into independent waveguides, they are not independent; they are strongly correlated. Therefore, we are sending strongly correlated light into two independent waveguides.

The second term of the master equation $\mathcal{L}_{\mathrm{q}}$ describes the qubit system. As already described in Sec. 2.2, in the rotated frame with respect to the frequencies of the bosonic modes, the bare dynamics of the qubit system are given by

$$\mathcal{L}_{\mathrm{q}}\rho = \sum_n \left(-i\frac{\delta_{n,1}}{2}[\hat{\sigma}_n^z, \rho] + \gamma_n \mathcal{D}[\hat{\sigma}_n^-]\rho + \frac{\gamma_{\phi_n}}{2}\mathcal{D}[\hat{\sigma}_n^z]\rho\right), \tag{3.4}$$

where we have defined the detunings $\delta_{n,1} = \omega_{n,1} - \omega_n$. We have assumed that each qubit decays into the waveguide with rates $\gamma_n$ and undergoes dephasing with rate $\gamma_{\phi_n}$.

The last term of the master equation $\mathcal{L}_{\mathrm{int}}$ describes the waveguide-mediated interaction between two otherwise disconnected systems. Here, we assume both waveguides are completely cascaded such that $\gamma_L = 0$. In such a setting, all the photons emitted by the parametric amplifier drive the qubits located further along the waveguides, while the light scattering of those qubits does not return to the parametric amplifier. The cascaded interaction takes the form of

$$\mathcal{L}_{\mathrm{int}}\rho = \sum_n \sqrt{\kappa_n\gamma_n\nu^n}\left([\hat{a}_n\rho, \hat{\sigma}_n^+] + [\hat{\sigma}_n^-, \rho\hat{a}_n^\dagger]\right). \tag{3.5}$$

Additionally, in our master equation, we have included the additional parameter $\nu^n \in [0, 1]$ to model linear losses in the system. This models the probability that a photon propagating at the $n$-th waveguide is transmitted. Or, in other words, $|1-\nu^n|$ gives you the probability that a photon is lost. In this way, the $|\nu^n|$ can be adjusted to model not only linear absorption losses but also parasitic loss channels for the qubits. We have also absorbed all propagation phases $e^{\pm ik_n|z_{n,0}-z_{n,1}|}$ into a redefinition of the qubit operators, ensuring that, up to local phase rotations, all results presented in this work remain independent of the precise location of the qubits. This differs from entanglement schemes in bidirectional channels, which typically require specific arrangements [96–98]. It is also important to note that the validity of Eq. (3.1) relies on the assumption that propagation times between the nodes are negligible compared to the relevant timescales of the system dynamics.

This is usually a valid assumption for small on-chip networks, but propagation delays can become very relevant when discussing entanglement distribution in larger networks, in particular when the distance between the two qubits is distinct. This issue will be addressed in Sec. 3.7.

## 3.2 Qubit master equation

To derive the effective master equation described in Eq. (3.1), we performed an adiabatic elimination of the waveguide, allowing us to describe the waveguide-mediated photon interactions using collective jump operators. The resulting master equation describes both the nondegenerate parametric amplifier and the qubits, resulting in a hybrid master equation that governs both continuous and discrete variables. Our main goal in this section is to study the time dynamics and stationary states of the reduced qubit state, $\rho_{\mathrm{q}}(t) = \mathrm{Tr}_{\mathrm{ph}}\{\rho(t)\}$. While this generally relies on solving Eq. (3.1) numerically, in the limit $\kappa_n \to \infty$, the dynamics of the parametric amplifier modes can again be adiabatically eliminated to derive an effective master equation for the reduced qubit state. As detailed in Appendix A, the reduced master equation for the qubit system is

$$\begin{aligned}\dot{\rho}_{\mathrm{q}} =& \mathcal{L}_{\mathrm{q}}\rho_{\mathrm{q}} + \sum_{n=A,B} \gamma_n N_n \left(\mathcal{D}[\hat{\sigma}_n^-]\rho_{\mathrm{q}} + \mathcal{D}[\hat{\sigma}_n^+]\rho_{\mathrm{q}}\right) \\ &+ \sqrt{\gamma_A\gamma_B}\left(M^*[\hat{\sigma}_A, [\hat{\sigma}_B, \rho_{\mathrm{q}}]] + M[\hat{\sigma}_A^+, [\hat{\sigma}_B^+, \rho_{\mathrm{q}}]]\right).\end{aligned} \tag{3.6}$$

Two parameters govern the master equation for the reduced qubit dynamics: the photon occupation number $N_n = 2\mathrm{Re}\{I_{\hat{a}_n^\dagger \hat{a}_n}(0)\}$ and the photon correlation $M = [I_{\hat{a}_A\hat{a}_B}(0) + I_{\hat{a}_B\hat{a}_A}(0)]$. They are determined by the steady-state correlation spectra of the parametric amplifier modes, which we derived in Sec. 2.4.2. In the symmetric case $\kappa_n = \kappa$ and $\nu^n = \nu$, these parameters are given by the following simple expressions

$$N = \nu\epsilon\left[\frac{1}{(1-\epsilon)^2} - \frac{1}{(1+\epsilon)^2}\right], \tag{3.7a}$$

$$M = \nu\epsilon\left[\frac{1}{(1-\epsilon)^2} + \frac{1}{(1+\epsilon)^2}\right]. \tag{3.7b}$$

## 3.3 Effective squeezing and purity

To gain further intuition, and motivated by the effective master equation for the qubits, we now consider an alternative description of the qubit system. We map the qubits driven by the output of the parametric amplifier into a system in which the qubits are in a general two-mode squeezed reservoir.

We focus on the symmetric configuration $\kappa_n = \kappa$ and we reinterpret the output correlation parameters $N_n$ and $M$ as the photon number and photon correlation $N =$

$\langle \hat{a}_n^\dagger \hat{a}_n \rangle_{\rho_{\text{eff}}}$ and $M = \langle \hat{a}_A \hat{a}_B \rangle_{\rho_{\text{eff}}}$, of an effective two-mode squeezed thermal state

$$\rho_{\text{eff}} = \hat{S}(r_{\text{eff}})\rho_{\text{th}}(n_{\text{eff}})\hat{S}^\dagger(r_{\text{eff}}). \tag{3.8}$$

Here, $\rho_{\text{th}}(n_{\text{eff}}) = \rho_{\text{th}}^A(n_{\text{eff}})\rho_{\text{th}}^B(n_{\text{eff}})$ is a two-mode thermal state, with each thermal state $\rho_{\text{th}}^n(n_{\text{eff}})$ defined in Eq. (2.25). Since we assume a symmetric configuration, we take an identical occupation number $n_{\text{eff}}$ for both modes. For the squeezing operator $\hat{S}(r_{\text{eff}})$, previously defined in Eq. (2.28), we assume a parametrization in terms of a real parameter $r_{\text{eff}}$.

We use the state given by Eq. (3.8) to model a general two-mode reservoir for the qubits. The photon occupation number $N$ and the photon correlation $M$ of this environment are given by [146]

$$N = (\cosh^2(r_{\text{eff}}) + \sinh^2(r_{\text{eff}}))n_{\text{eff}} + \sinh^2(r_{\text{eff}}), \tag{3.9a}$$

$$M = \cosh(r_{\text{eff}})\sinh(r_{\text{eff}})(2n_{\text{eff}} + 1). \tag{3.9b}$$

We can now derive a covariance matrix for this Gaussian state, analogous to Eq. (2.31), but expressed in terms of $N$ and $M$. It reads as

$$\boldsymbol{\mathcal{V}} = \begin{pmatrix} N+1/2 & 0 & -M & 0 \\ 0 & N+1/2 & 0 & M \\ -M & 0 & N+1/2 & 0 \\ 0 & M & 0 & N+1/2 \end{pmatrix}. \tag{3.10}$$

When $n_{\text{eff}} = 0$, Eq. (2.31) is recovered. The purity of this general state is obtained from $\boldsymbol{\mathcal{V}}$ using Eq. (2.24). We obtain

$$\mu_{\text{eff}} = \frac{1}{(1+2N)^2 - 4|M|^2}, \tag{3.11}$$

from which we recover $\mu_{\text{eff}} = 1$ when $n_{\text{eff}} = 0$. We can use Eq. (3.9a) and Eq. (3.9b) to solve for the effective squeezing strength $r_{\text{eff}}$. We obtain

$$r_{\text{eff}} = \frac{1}{2}\tanh^{-1}\left[\frac{2|M|}{2N+1}\right]. \tag{3.12}$$

Going back to our effective master equation in Eq. (3.6), we can now use the parameters $N$, given by Eq. (3.7a), and $M$, in Eq. (3.7b) to evaluate our effective bath parameters. First, we realize that $|M|^2 = N(N+\nu)$ and therefore $\mu_{\text{eff}} = 1$ for a lossless channel $\nu = 1$. This implies that in the infinite-bandwidth limit, Eq. (3.6) describes two qubits that are coupled to a two-mode squeezed zero-temperature reservoir with a squeezing parameter

$$r_{\text{eff}} = 2\tanh^{-1}(\epsilon), \tag{3.13}$$

which becomes arbitrarily large when $\epsilon \to 1$. As discussed in Sec. 2.2.2, the squeezing level $\mathcal{S}$ is bounded to 3 dB for the intracavity fields. Here, the two qubits are driven by the *output* fields, from which we observe that the squeezing level becomes unbounded. However, this is a consequence of the Markov approximation, which assumes that the environment is probed only at a single frequency. We will show that this result no longer holds when a finite ratio $\kappa/\gamma$ is considered. In this case, considering a nonzero frequency window $\Delta\omega \neq 0$ [see Fig. 3.3] leads to an impure effective state with reduced squeezing. The same is true in the Markovian limit in the presence of transmission losses, $\nu < 1$.

## 3.4 Steady-state entanglement in ideal squeezed reservoirs

Our master equation in Eq. (3.6) describes two qubits in an effective two-mode thermal squeezed reservoir. However, in the ideal case of no losses and broad bandwidth, the parameters fulfil $|M|^2 = N(N+1)$. Under this condition, the system is only parametrized by the squeezing strength $r_{\text{eff}}$, and we can rewrite Eq. (3.6) as

$$\dot{\rho}_{\text{q}} = -i[\hat{H}_{\text{q}}, \rho_{\text{q}}] + \sum_{n=A,B} \gamma \mathcal{D}[\hat{J}_n]\rho_{\text{q}}, \tag{3.14}$$

for the reduced qubit density operator $\rho_{\text{q}}$. Here, $\gamma$ denotes the decay rate of each individual qubit, and we have also assumed negligible dephasing noise $\gamma_\phi = 0$. In Eq. (3.14), the dynamics are now governed by a purely coherent term describing the qubits detuning

$$\hat{H}_{\text{q}} = \sum_n \frac{\delta_{n,1}}{2} \hat{\sigma}_n^z, \tag{3.15}$$

and purely dissipative processes with collective jump operators

$$\hat{J}_A = \cosh(r_{\text{eff}})\hat{\sigma}_A^- - \sinh(r_{\text{eff}})\hat{\sigma}_B^+, \tag{3.16a}$$

$$\hat{J}_B = \cosh(r_{\text{eff}})\hat{\sigma}_B^- - \sinh(r_{\text{eff}})\hat{\sigma}_A^+. \tag{3.16b}$$

While the individual qubits are well separated and noninteracting, nontrivial correlations between qubits can emerge once the TMS source is switched on. Such a correlation arises between qubits in waveguide $A$ and waveguide $B$ mediated by the nonlocal jump operators described in Eq. (3.16), which are an effect of the adiabatically-eliminated correlated photon pairs.

In Chapter 2, we introduced our qubit quantum network and its requirements. There, we not only emphasized that we are interested in a pure state $|\psi_0\rangle$ but also that it requires minimal external control. Ideally, a protocol in which we just need to switch on the parametric amplifier and the qubit state would converge to an entangled state. Here, we show that if we let our system evolve for a long enough time, $\rho_{ss} = \rho_q(t \to \infty)$, the steady state of this system is a pure state

$$\rho_{\rm ss} = |\psi_0\rangle\langle\psi_0|. \tag{3.17}$$

To identify the condition under which this pure state emerges as a solution of Eq. (3.14), it is enough to find a qubit state that satisfies [188]

$$\textbf{(I)} \qquad \hat{J}_n|\psi_0\rangle = 0, \tag{3.18a}$$

$$\textbf{(II)} \qquad \hat{H}_{\rm q}|\psi_0\rangle = \text{constant} \equiv 0. \tag{3.18b}$$

Condition **(I)** implies that $|\psi_0\rangle$ is a so-called dark state of the collective dissipation processes, i.e., it decouples from the collective TMS environment. In addition, condition **(II)** ensures that $|\psi_0\rangle$ is also unaffected by the Hamiltonian dynamics and remains in a dark state for all times. In Ref. [149], the constraints in Eq. (3.18a) and Eq. (3.18b) have been used to construct nontrivial entangled states for an ensemble of qubits in a single waveguide, driven by a classical field. We will again use this strategy in Chapter 4 to find even more complex entangled states in a dual-waveguide setting, where, in particular, entanglement between the otherwise decoupled qubits sets arises from initial correlations in the photonic driving fields.

Back to our case, the dark state condition $\hat{J}_n|\psi_0\rangle = 0$ is satisfied by the unique state $|\psi_0\rangle = |\Phi^+_{1,1}\rangle$, where

$$|\Phi^+_{1,1}\rangle = \frac{\cosh(r_{\rm eff})|0_1 0_1\rangle + \sinh(r_{\rm eff})|1_1 1_1\rangle}{\sqrt{\cosh(2r_{\rm eff})}}. \tag{3.19}$$

Here, we follow the notation that the first(second) subindex references the qubit in the waveguide $A(B)$. In cases where no confusion can arise, we simply write $|x_1, x_1\rangle = |xx\rangle$. It is then also straightforward to show that this state is an eigenstate of the Hamiltonian $\hat{H}_{\rm q}$ if the detunings satisfy

$$\delta_{A,1} + \delta_{B,1} = 0. \tag{3.20}$$

This means that the two qubits must either be in resonance with the amplifier modes or detuned by the exact opposite amount. The state given by Eq. (3.19) was first discussed in Ref. [82], and there it was shown how it approaches a maximally entangled Bell state, as defined in Eq. (2.8), for $r_{\rm eff} \gg 1$.

Before we proceed, let us provide some additional insights about the emergence of such a pure entangled steady state by considering the coupling of two qubits to two isolated modes $\hat{a}_A$ and $\hat{a}_B$ via a Jaynes-Cummings interaction of the form

$$\hat{H}_{\text{int}} \sim i\left(\hat{\sigma}_A^- \hat{a}_A^\dagger - \hat{\sigma}_A^+ \hat{a}_A + \hat{\sigma}_B^- \hat{a}_B^\dagger - \hat{\sigma}_B^+ \hat{a}_B\right). \tag{3.21}$$

An ideal two-mode squeezed state of those two modes, following Eq. (2.29), can be written as

$$|\Psi_{\text{TMS}}\rangle = \sqrt{1-x^2} \sum_{n=0}^{\infty} x^n |n\rangle_A |n\rangle_B, \tag{3.22}$$

where we can set $x = \tanh(r_{\text{eff}})$. This expression shows that the number of photons in the two modes are perfectly correlated, suggesting that the qubits are only excited and de-excited pairwise. However, this argument is too naïve, since, for example, the action of $\hat{H}_{\text{int}}$ on the state $|00\rangle|\Psi_{\text{TMS}}\rangle$ would also generate single-excited states $\sim |10\rangle, |01\rangle$. To explain the existence of the steady state given in Eq. (3.19) it is thus important to take into account the coherence between the $|n\rangle_A|n\rangle_B$ components, which leads to the following relations

$$\hat{a}_A |\Psi_{\text{TMS}}\rangle = x \hat{a}_B^\dagger |\Psi_{\text{TMS}}\rangle, \tag{3.23a}$$

$$\hat{a}_B |\Psi_{\text{TMS}}\rangle = x \hat{a}_A^\dagger |\Psi_{\text{TMS}}\rangle. \tag{3.23b}$$

Equivalently, there exists a unique dark state of the interaction,

$$\hat{H}_{\text{int}}(|00\rangle + x|11\rangle)|\Psi_{\text{TMS}}\rangle = 0. \tag{3.24}$$

Therefore, once the system reaches the state $|\psi_0\rangle$ in Eq. (3.19), the emission of a photon by one qubit interferes destructively with the absorption of a photon in the other mode. When applied to the original setting, this argument shows that the absence of any components $\sim |01\rangle$ or $\sim |10\rangle$ in $|\psi_0\rangle$ is a consequence of a nonlocal interference effect between two separated but correlated parts of the network. As we will see now, in deviations from the Markovian regime, this interference effect is no longer ideal, and the single-excited states will be populated.

## 3.5 Realistic networks

Let us now address a more realistic scenario where finite waveguide losses, decoherence of the qubits, and, in particular, the finite bandwidth of the parametric amplifier are taken into account. In this last case, it is, in general, no longer possible to eliminate the photon modes, and the full system Eq. (3.1) must be solved numerically. Given the large Hilbert space required to represent the two-mode squeezed state, these simulations become very demanding when approaching the parametric instability at $\epsilon = 1$. Thus, when numerically solving Eq. (3.1), we restrict our simulation to values of $\epsilon \leq 0.8$, where the convergence of the results can still be ensured by truncating the Hilbert space of each photon mode.

We can still use the Markovian approximation to investigate the performance of this entanglement distribution scheme also under realistic conditions, for example, when $|M|^2 < N(N+1)$ or when a reduced master equation for $\rho_q$ is not available. We can solve Eq. (3.6) for the steady state. Then, by defining $\rho_{ij,kl} = \langle i,j|\rho_{ss}|k,l\rangle$ and the short notation $\rho_{ij} = \langle i,j|\rho_{ss}|i,j\rangle$, we obtain the following nonvanishing matrix elements,

$$\Lambda\rho_{00} = (1+N)^2(2\Gamma_\phi + 1 + 2N) - |M|^2(3+2N), \tag{3.25a}$$

$$\Lambda\rho_{10} = 2\Gamma_\phi N(N+1) + (2N+1)(N(N+1) - |M|^2), \tag{3.25b}$$

$$\Lambda\rho_{11} = N^2(1 + 2\Gamma_\phi + 2N) + |M|^2(1-2N), \tag{3.25c}$$

$$\Lambda\rho_{11,00} = M, \tag{3.25d}$$

and $\rho_{01,01} = \rho_{10,10}$ and $\rho_{00,11} = (\rho_{11,00})^*$. Here, we introduced the normalization constant $\Lambda = (1+2N)[1 + 2\Gamma_\phi + 4(N(N+1+\Gamma_\phi) - |M|^2))]$ and the normalized dephasing rate $\Gamma_\phi = \gamma_\phi/\gamma$. As we have discussed before, in the Markovian limit and ideal conditions $\gamma_\phi = 0$ and $\nu = 1$, we recover the pure state from Eq. (3.19) and the single-excitation populations disappear $\rho_{10,10} = \rho_{01,01} = 0$.

From our steady state, we can now find how close we are to the maximally entangled state $|\Phi^+\rangle = (|00\rangle + |11\rangle)/\sqrt{2}$ using the previously defined fidelity $\mathcal{F}(\rho_q) = \langle\Phi^+|\rho_q|\Phi^+\rangle$. By expressing our state $\rho_q$ in terms of the effective parameters $r_{\text{eff}}$ and $\mu_{\text{eff}}$, given by Eq. (3.12) and Eq. (3.11), the fidelity is given by

$$\mathcal{F}(\rho_{ss}) = \frac{1 + \mu_{\text{eff}} + \Gamma_\phi\sqrt{\mu_{\text{eff}}}(1 + 2\mu_{\text{eff}} + \cosh(4r_{\text{eff}}))\,\text{sech}\,(2r_{\text{eff}}) + 2\mu_{\text{eff}}\tanh(2r_{\text{eff}})}{4 + 8\Gamma_\phi\sqrt{\mu_{\text{eff}}}\cosh(2r_{\text{eff}})}. \tag{3.26}$$

While this expression encompasses all the system's parameters we care about, it is still difficult to gain some intuition. Considering the simple case where the dephasing noise is negligible $\gamma_\phi = 0$ , it simplifies to

$$\mathcal{F}(\rho_{ss}) = \frac{1}{4}\left[1 + \mu_{\text{eff}}(1 + 2\tanh(2r_{\text{eff}}))\right]. \tag{3.27}$$

In addition, we can use the concurrence of the reduced state, $\mathcal{C}(\rho_{ss})$, for a more direct way to quantify the amount of qubit-qubit entanglement. As our density matrix has the same form as Eq. (2.11), we can obtain an analytical expression for the concurrence using Eq. (2.12). In terms of the effective parameters $r_{\text{eff}}$ and $\mu_{\text{eff}}$, it has the following simple form

$$\mathcal{C}(\rho_{ss}) = \max\left(0, \mu_{\text{eff}}\tanh(2r_{\text{eff}}) - (1-\mu_{\text{eff}})/2\right). \tag{3.28}$$

For the ideal Markovian limit, $\mu_{\text{eff}} = 1$, the fidelity takes the simpler form of $\mathcal{F}(\rho_{ss}) = (1 + \tanh(2r_{\text{eff}}))/2$, which shows that even for moderate squeezing strengths of $r_{\text{eff}} \simeq 1$ ($\mathcal{S}_{\text{eff}} = 8.68\,\text{dB}$) fidelities of about $\mathcal{F}(\rho_{ss}) \approx 0.99$ can be reached. More realistic squeezing experiments [22, 24, 164] with $r_{\text{eff}} = 0.35$ ($\mathcal{S}_{\text{eff}} = 3\,\text{dB}$), would achieve a fidelity of

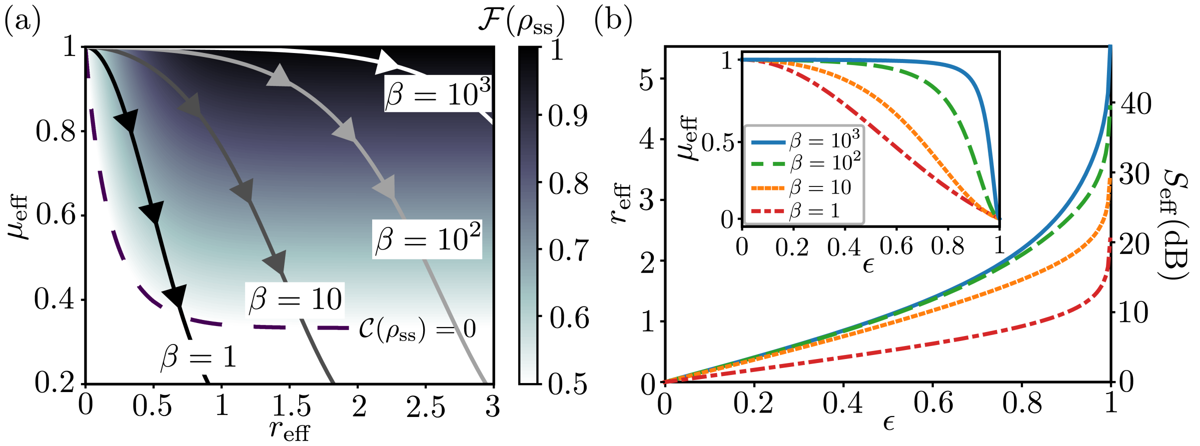


**Figure 3.2:** (a) Contour plot of the steady state fidelity $\mathcal{F}(\rho_{\rm ss})$ as a function of the effective squeezing parameter $r_{\rm eff}$ and the effective purity $\mu_{\rm eff}$. The solid lines indicate the path in this parameter space that one obtains by increasing $\epsilon$ from 0 to 1 for different values of $\beta = \kappa/\gamma$ and $\Gamma_\phi = 0$ and $\nu = 1$ [see discussion in Sec. 3.5.1]. The dashed line marks the boundary of vanishing concurrence $\mathcal{C}(\rho_{\rm ss}) = 0$, above which the reduced qubit state is entangled. (b) Dependence of the effective squeezing parameter and the effective purity on the driving strength within the FMA. The different curves are evaluated for different values of $\beta$ and assuming $\nu = 1$ and symmetric conditions, $\kappa_n = \kappa$ and $\gamma_n = \gamma$. On the right axis, we plot the squeezing factor $S_{\rm eff}$ as defined in Eq. (2.37). Note that $r_{\rm eff} \to \infty$ and $\mu_{\rm eff} \to 0$ when $\epsilon \to 1$ for all values of $\beta$.

$\mathcal{F}(\rho_{\rm ss}) \simeq 0.8$. In Fig. 3.2(a) we show a plot of the steady state fidelity $\mathcal{F}(\rho_{\rm ss})$ for the steady state of master equation (3.6), under the assumption that $\Gamma_\phi = 0$, but allowing for arbitrary values of $N_n = N$ and $|M|^2 \leq N(N+1)$. For later convenience, these parameters are, in turn, expressed in terms of the effective squeezing parameter $r_{\rm eff}$ and the effective purity $\mu_{\rm eff}$, as defined in Eq. (3.12) and Eq. (3.11). We see that for $\mu_{\rm eff} \simeq 1$, the fidelity approaches unity as the squeezing parameter is increased, consistent with the bound stated in Eq. (3.27). For values of $r_{\rm eff} \gtrsim 1$, the fidelity becomes almost independent of the squeezing parameter but decreases as $\mathcal{F}(\rho_{\rm ss}) \simeq \frac{1}{4}(1 + 3\mu_{\rm eff})$ for impure reservoirs. Entanglement is present as long as $\mathcal{F}(\rho_{\rm ss}) > 0.5$, which corresponds to a minimal purity of about $\mu_{\rm eff} \simeq 1/3 \simeq 0.33$. This result shows that improving the purity of the effective photonic bath will be most relevant for this entanglement distribution scheme.

### 3.5.1 Filtered mode approximation (FMA)

When we derived an effective master equation for the qubits assuming a Markovian limit, we took the limit where the parametric amplifier bandwidth goes to infinity $\kappa_n \to \infty$. In this limit, the characteristic bath parameters $N_n$ and $M$ are independent of $\kappa_n$ and are determined by the output fields of the amplifier at a single frequency, $\omega = 0$. As sketched in Fig. 3.3(a), in the Markovian limit, the qubit bandwidth only 'sees' the spectrum of the parametric amplifier at $\omega = 0$. To go beyond this approximation and take into account

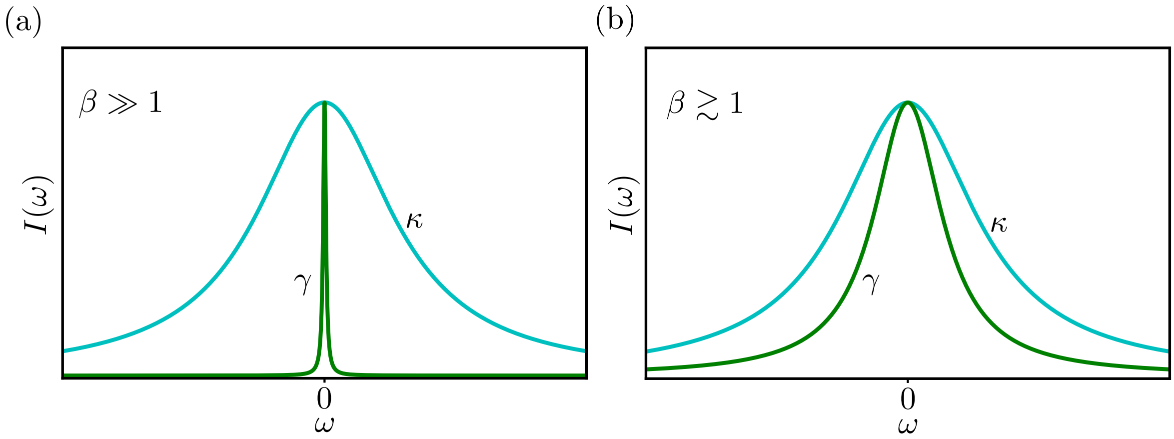


**Figure 3.3:** Sketch of the spectrum $I(\omega)$ of the parametric amplifier, given by $\kappa$ compared to the qubit, given by $\gamma$, in (a) the Markovian regime $\beta \gg 1$, (b) for finite bandwidth $\beta \gtrsim 1$.

the finite bandwidth of the parametric amplifier $\kappa$, we must take into account that the qubits will be affected by photons within a finite region of the spectrum $I_{\hat{a}_n^\dagger \hat{a}_n}(\omega)$ and $I_{\hat{a}_A \hat{a}_B}(\omega)$ that cannot be associated with a pure squeezed state [see Fig. 3.3(b)]. The relevant bandwidth of frequencies will be determined by the qubit dynamics and will be roughly given by the decay rates $\gamma_n$. Based on this intuition, we introduce the two filtered modes

$$\hat{a}_{f,n}(t) = \sqrt{\gamma_n \kappa_n \nu^n} \int_{-\infty}^{t} \mathrm{d}s\, e^{-\gamma_n (t-s)/2} \hat{a}_n(s - \tau_n), \tag{3.29}$$

where, for a later generalization, we have already included the propagation delays $\tau_n$. These modes represent the output of the two-mode amplifier but are delayed by $\tau_n$ and filtered by the response of the qubits. We can now use these filtered modes to define an adjusted set of parameters for the qubit master equation in Eq. (3.6),

$$N_n = \langle \hat{a}_{f,n}^\dagger \hat{a}_{f,n} \rangle, \qquad M = \langle \mathcal{T} \hat{a}_{f,A} \hat{a}_{f,B} \rangle, \tag{3.30}$$

where $\mathcal{T}$ denotes the time-ordering operator applied to the amplifier modes $\hat{a}_{f,A}$ and $\hat{a}_{f,B}$. These parameters include the characteristic timescales of the qubits and of the photons on an equal footing. Specifically, we obtain

$$N_n = 2\gamma_n \nu^n \int_{-\infty}^{\infty} \frac{\mathrm{d}\omega}{2\pi} \frac{I_{\hat{a}_n^\dagger \hat{a}_n}(\omega)}{\gamma_n^2/4 + \omega^2}, \tag{3.31}$$

for the occupation numbers and

$$M = \sqrt{\gamma_A \gamma_B \nu^A \nu^B} \int_{-\infty}^{\infty} \frac{\mathrm{d}\omega}{2\pi} \frac{\left[ I_{\hat{a}_A \hat{a}_B}(\omega) + I_{\hat{a}_B \hat{a}_A}(-\omega) \right] e^{i\omega(\tau_B - \tau_A)}}{(\gamma_A/2 + i\omega)(\gamma_B/2 - i\omega)}, \tag{3.32}$$

for the correlation parameter. These expressions explicitly show how the effective photonic reservoir seen by the qubits depends on the amplifier correlations within finite frequency windows set by the decay rates $\gamma_n$. The Markovian limit discussed in Sec. 3.2 is recovered in the limit $\gamma_n \to 0$ and $\tau_n \to 0$.

Before we proceed, we motivate such filtered mode approximation the following way. From the Heisenberg equations of motion Eq. (2.61), we can readily derive expectation values of qubit observables in the weak excitation limit, $\epsilon \ll 1$. In this limit we can approximate $\hat{\sigma}_n^z(t) \simeq -1$ and obtain

$$\dot{\hat{\sigma}}_n^-(t) \simeq -\frac{\gamma_n}{2}\hat{\sigma}_n^-(t) - \sqrt{\gamma_n \nu^n}\hat{f}_{\text{out},n}(t-\tau_n) - \sqrt{\gamma_n(1-\nu^n)}\hat{f}'_{\text{in},n}(t). \tag{3.33}$$

Here $\hat{f}_{\text{out},n}(t) \equiv \hat{F}_{\text{out},n}(z=0,t)$, where $\hat{F}_{\text{out},n}(z,t) = \hat{F}_{\text{in},n}(z,t) + \sqrt{\kappa_n}\hat{a}_n(t - z/v_n)$, and $\hat{f}'_{\text{in},n}(t)$ is an independent noise operator, which we have included to account for waveguide losses. Formal integration gives us

$$\hat{\sigma}_n^-(t) = -\sqrt{\gamma_n \nu^n}\int_{-\infty}^{t} \mathrm{d}s\, e^{-\gamma_n(t-s)/2}\hat{f}_{\text{out},n}(s-\tau_n), \tag{3.34}$$

where contributions from $\hat{f}'_{\text{in},n}(t)$, which always act on the vacuum state, have already been omitted. For the evaluation of the steady-state expectation value $\langle \hat{\sigma}_n^+\hat{\sigma}_n^-\rangle(t\to\infty) = N_n$ we use

$$\langle \hat{f}^\dagger_{\text{out},n}(t)\hat{f}_{\text{out},n}(t')\rangle = \kappa_n \langle \hat{a}_n^\dagger(t)\hat{a}_n(t')\rangle \tag{3.35}$$

and after some manipulations we obtain the result for $N_n$ given in Eq. (3.31). For the evaluation of the correlations, $\langle \hat{\sigma}_A^-\hat{\sigma}_B^-\rangle(t\to\infty) = M$, we must take into account that $\hat{f}_{\text{in},A}(t)$ and $\hat{a}_B(t')$ do not commute in general, as discussed in Ref. [189]

$$\langle \hat{f}_{\text{out},A}(t)\hat{f}_{\text{out},B}(t')\rangle = \sqrt{\kappa_A\kappa_B}\langle \mathcal{T}\hat{a}_A(t)\hat{a}_B(t')\rangle, \tag{3.36}$$

where $\mathcal{T}$ denotes the time-ordering operator. Again, the resulting expression for $M$ matches Eq. (3.32). Therefore, this comparison shows that the results obtained within the FMA for the steady state of the qubits becomes exact in the weak driving limit, $N_n, |M| \ll 1$.

### 3.5.2 Effective squeezing parameters for non-ideal amplifiers

While the derivation of a master equation in terms of the filtered modes is only an approximation, it becomes exact in the regime of low qubit excitations, i.e. for small values of $\epsilon$. Even for moderate and large driving strengths, it still significantly improves over the conventional Markovian master equation discussed in Sec. 3.2. In particular, the FMA allows us to account for the effects of a finite amplifier bandwidth. For example, by setting $\kappa_n = \kappa$, $\gamma_n = \gamma$ and assuming $\tau_n = 0$ for now, we obtain

$$N = \frac{2\epsilon^2\beta(1+2\beta)\nu}{[(\beta+1)^2 - \beta^2\epsilon^2](1-\epsilon^2)}, \tag{3.37}$$

$$M = \frac{2\epsilon\beta(\epsilon^2\beta+\beta+1)\nu}{[(\beta+1)^2 - \beta^2\epsilon^2](1-\epsilon^2)}, \tag{3.38}$$

where $\beta = \kappa/\gamma$ is the ratio between the amplifier bandwidth and the qubit decay.

As discussed in Sec. 3.3 and shown explicitly in Fig. 3.2(b), these parameters can be reexpressed in terms of an effective squeezing parameter $r_{\text{eff}}$ and an effective purity $\mu_{\text{eff}}$. In this way, the fidelity of the resulting steady state can be read off directly from the general plot in Fig. 3.2(a).

We also use the analytic expressions for $N$ and $M$ from above to evaluate the first-order corrections in $1/\beta$ for these quantities

$$r_{\text{eff}} \simeq 2\tanh^{-1}(\epsilon) - \frac{1}{\beta}\frac{2\epsilon}{(1-\epsilon^2)^2}, \tag{3.39}$$

$$\mu_{\text{eff}} \simeq 1 - \frac{1}{\beta}\frac{8\epsilon^2}{(1-\epsilon^2)^2}, \tag{3.40}$$

which is valid for $\beta(1-\epsilon)^2 \gg 1$ and $\nu = 1$. We see that finite-bandwidth corrections get strongly amplified as one approaches the parametric instability. In particular, the purity of the effective squeezed reservoir, which plays a crucial role in determining the entanglement of the reduced qubit state, decreases significantly. Thus, even for $\beta \gg 1$, it is impossible to assess the achievable amount of entanglement using a purely Markovian description.

### 3.5.3 Optimal fidelities

In Fig. 3.4, we summarize the performance of the entanglement distribution scheme in realistic settings. First of all, Fig. 3.4(a) shows the dependence of the fidelity $\mathcal{F}(\rho_{\text{ss}})$ on the driving strength $\epsilon$ for different ratios $\beta = \kappa/\gamma$. Here, we compare the results from a simulation of the full master equation with the predictions obtained from the FMA. In both cases, we find the expected maximum for intermediate values of $\epsilon$, which results from an increase in squeezing on the one hand and from the loss of purity on the other hand. While for moderate and large driving strengths, we observe a deviation of the approximate results from exact numerics, the qualitative trends are still accurately captured. Importantly, across all investigated parameter regimes, the FMA either agrees with or underestimates the exact fidelity, making it a reliable tool for predicting lower bounds on the achievable entanglement. In the limit of low pump values, the FMA

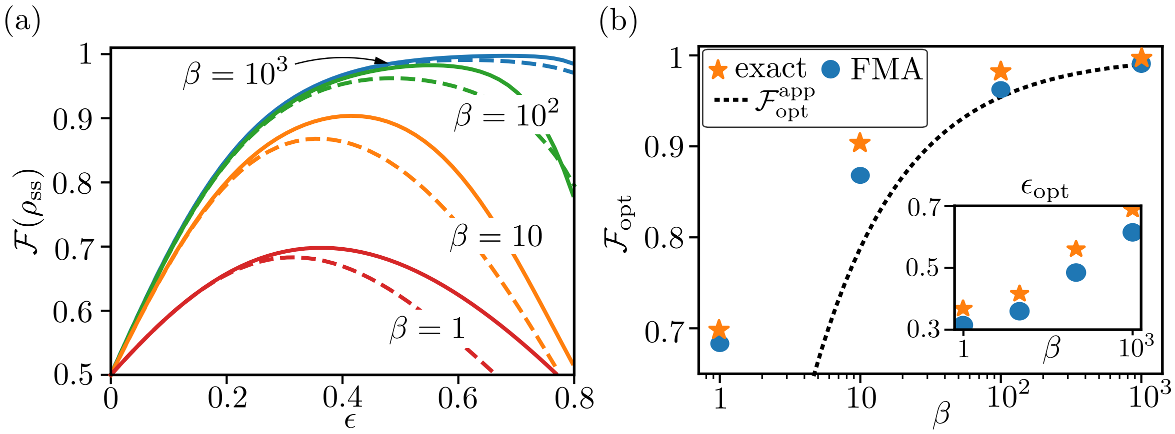


**Figure 3.4:** (a) Plot of the Bell-state fidelity $\mathcal{F}(\rho_{ss})$ as a function of the driving strength $\epsilon$ and for different amplifier bandwidths, $\beta = \kappa/\gamma$. The solid lines represent the results obtained from the numerical solution of the full cascaded master equation, Eq. (3.1), which are compared with the predictions under the FMA (dashed lines), assuming $\Gamma_\phi = 0$ and $\nu = 1$. (b) Plot of the optimal fidelity $\mathcal{F}_{\rm opt}$ and the corresponding optimal driving strength $\epsilon_{\rm opt}$ (inset) under the same conditions. The dotted line shows the analytic approximation in Eq. (3.43). For all plots in this figure we have set $\kappa_n = \kappa$ and $\gamma_n = \gamma$.

becomes exact, and we obtain a simple analytic expression for the fidelity,

$$\mathcal{F}(\epsilon \ll 1) \simeq \frac{1}{2} + \frac{2\beta\nu}{(1+\beta)(1+2\Gamma_\phi)}\epsilon. \tag{3.41}$$

Therefore, the fidelity increases linearly with the pump strength [see Fig. 3.4(a)], with a slope that depends on all sources of imperfections. To estimate the maximally achievable fidelities, we assume that this maximum is reached for a pumping strength $\epsilon \approx 1$ and expand $\mathcal{F}$ to lowest order in $(1-\epsilon)$, $1/\beta$, $\Gamma_\phi$ and $(1-\nu)$,

$$\mathcal{F}(\epsilon \approx 1) \simeq 1 - \frac{(1-\epsilon)^4}{16} - \frac{3}{(1-\epsilon)^2}\left[\frac{1}{2\beta} + \Gamma_\phi + (1-\nu)\right]. \tag{3.42}$$

By optimizing this result with respect to the driving strength we obtain an optical pump strength $\epsilon_{\rm opt} = 1 - \sqrt{2}\,3^{1/6}[\frac{1}{2\beta} + \Gamma_\phi + (1-\nu)]^{1/6}$, which translates to an optimal fidelity of

$$\mathcal{F}_{\rm opt}^{\rm app} \simeq 1 - \frac{3\sqrt[3]{9}}{4}\left[\frac{1}{2\beta} + \Gamma_\phi + (1-\nu)\right]^{\frac{2}{3}}. \tag{3.43}$$

Although the result in Eq. (3.43) is based on various crude approximations, it still gives a good estimate for the overall scaling of the maximal fidelity achievable with this scheme in the presence of imperfections. In particular, as shown in Fig. 3.4 (b), for the parameter regimes of interest, $\mathcal{F}_{\rm opt} > \mathcal{F}_{\rm opt}^{\rm app}$, where $\mathcal{F}_{\rm opt}$ is the exact optimized fidelity evaluated numerically. In Fig. 3.5, $\mathcal{F}_{\rm opt}$ is also shown for different non-ideal settings.

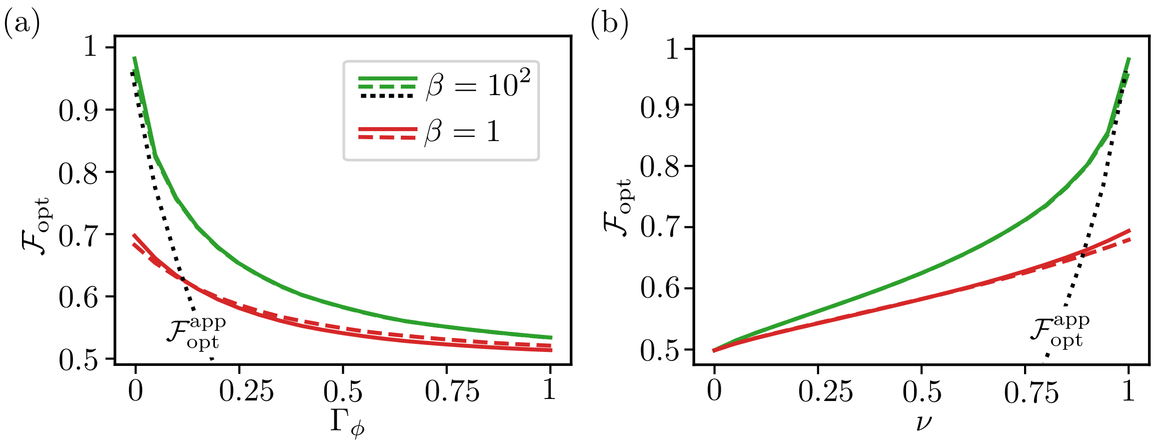


**Figure 3.5:** (a) Plot of the optimal fidelity as a function of the qubit dephasing $\Gamma_\phi$ for $\nu = 1$ and (b) as a function of the channel transmissivity $\nu$ for $\Gamma_\phi = 0$. In both plots, we assume a value of $\beta = 10^2$ for the upper curves and $\beta = 1$ for the lower curves, where the dashed lines represent the respective FMA results. For all plots in this figure we have set $\kappa_n = \kappa$ and $\gamma_n = \gamma$.

Alternatively, for a more direct measure of the entanglement present in the system, we can use the FMA with the concurrence in Eq. (3.28) in the weak-excitation limit $\epsilon \ll 1$. Assuming a finite dephasing rate $\Gamma_\phi$, it is given by

$$\mathcal{C}(\epsilon \ll 1) \simeq \frac{4\beta\epsilon\nu}{(1+\beta)(1+2\Gamma_\phi)}. \tag{3.44}$$

In Sec. 2.6, we saw that the direct entanglement protocol proposed by [41] scales as $\mathcal{C}_{\rm direct} \simeq \sqrt{\nu}$ for a lossy waveguide. As $0 \leq \nu \leq 1$, $\mathcal{C}_{\rm direct}$ gives a better performance that the one estimated here. This difference in scaling originates from the number of bosonic modes required for the protocol. While for the direct entanglement protocol, the entanglement is transferred by a single bosonic mode along the waveguide, here we need two modes to transfer the TMS, which then scales the photon losses.

## 3.6 Entanglement rates

In the previous sections, we have focused on the amount of entanglement that can be reached under stationary driving conditions. However, for practical applications, it is equally important to determine how quickly this entangled state can be achieved. In particular, given the possibility of distilling a highly entangled state from many copies of a state with a low amount of entanglement [49–54], it may be more favourable to optimize the generation rate rather than the fidelity. These considerations are specifically relevant for the current entanglement distribution scheme since, close to the parametric instability, where the correlations are maximized, the relaxation time of the parametric amplifier diverges. Therefore, even for an ideal broadband amplifier, operating close to

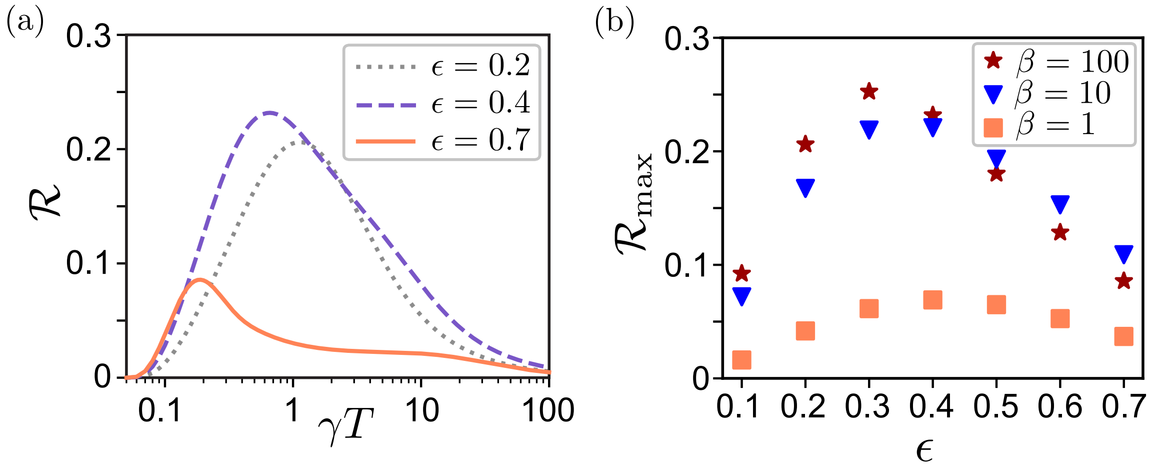


**Figure 3.6:** (a) Plot of the entanglement distribution rate $\mathcal{R}$ as a function of the pulse length $\gamma T$ for different pump strengths $\epsilon$ at fixed $\beta = 100$, $\Gamma_\phi = 0$, and $\nu = 1$. (b) Dependence of the maximally achievable entanglement rate $\mathcal{R}_{\max}$ on the driving strength $\epsilon$ for different values of $\beta$.

the threshold might not be the optimal choice [190].

The optimal trade-off between entanglement generation speed and achievable fidelity depends on various factors, particularly the local resources available for entanglement purification protocols. We consider here only the following rudimentary scenario: The two-mode squeezing source runs continuously while the qubits in each node are initialized in state $|0\rangle$. At time $t = 0$, the coupling between the qubits and the photonic channels is switched on for a duration $T$, after which the qubits are decoupled and stored in a local register. This process is then repeated with a fresh pair of qubits and so on, such that an entangled two-qubit state $\rho_q(T)$ is distributed between the two nodes every time interval $T$. We introduce the normalized entanglement distribution rate

$$\mathcal{R} = \frac{E_F(T)}{\gamma T}. \tag{3.45}$$

Here $E_F(T) \equiv E_F(\rho_q(T))$ is the entanglement of formation, as defined in Eq. (2.13). It quantifies the number of pure singlet states that are needed on average to generate the state $\rho_q(T)$ through LOCC operations only. This more intuitive interpretation, while still being easily computable, makes $E_F$ well suited for a comparative study of entanglement rates. Note, however, that $E_F$ is only an upper bound [120] on the number of singlet states that can be extracted from multiple copies of $\rho_q(T)$, which depends on the available purification protocols and many other details that go beyond the scope of this analysis. In Fig. 3.6(a), we show the entanglement rate $\mathcal{R}$ for various pump strengths $\epsilon$. We observe high rates that can be reached for moderate pump strength $\epsilon \lesssim 0.5$. For larger values, the initial peak and later decrease of the rate can be traced back to the appearance of Rabi oscillations between the states $|00\rangle$ and $|11\rangle$. In Fig. 3.6(b), we show the maximal rate $\mathcal{R}_{\max} = \max_T\{\mathcal{R}(T)\}$ as a function of $\epsilon$ for different amplifier bandwidths $\beta$. We see that the rate is maximized at $\epsilon \approx 0.3 - 0.4$. For a large bandwidth ratio of $\beta \simeq 100$, we can use our Markovian approximations to estimate the optimal squeezing strength. For that, using Eq. (3.13), the entanglement rate is maximized at $r_{\text{eff}} \approx 0.6 - 0.8$, which would correspond to a squeezing level of $\mathcal{S}_{\text{eff}} \approx 2.6 - 3.5\,\text{dB}$.

## 3.7 Quantum networks with propagation delays

In the setup we have considered, at the $n$-th waveguide, the photons with phase velocity $v_n$ take the time $\tau_n = d_n/v_n$ to propagate the distance $d_n$ between the parametric amplifier and the qubit. In a strict sense, the validity of Eq. (3.1) assumes that this time is negligible compared to the typical timescale of the system evolution. This is not a crucial assumption in situations where the qubits are located approximately equally far away from the amplifier, as the photons simply take $\tau_A \approx \tau_B$ to propagate to the qubits, and this small difference is irrelevant for steady-state correlations. However, in situations where $\tau_A \neq \tau_B$, the qubits are driven by photons that have been emitted at two different times. When the time lag $|\tau_B - \tau_A|$ is too long, correlations between these photons are lost [164]. Such situations can occur, for example, when the amplifier and one qubit are located in the same laboratory while the other photons are sent via an optical fibre to the other qubit at a remote location.

### 3.7.1 Effective environment with delay

To take into account the effect the delays have on the qubits, we can use the effective parameters derived within the filtered mode approximation. For that, in Eq. (3.31) and Eq. (3.32) we introduced the modes with a finite delay $\tau_n$. As a result, the effective two-mode squeezed reservoir is modified accordingly. To achieve this, we can use Eq. (3.12) and Eq. (3.11), together with the delayed modes, to evaluate the delayed squeezing strength $r_{\text{eff}}(\tau)$ and the delayed purity $\mu_{\text{eff}}(\tau)$, respectively. We evaluate them numerically and in Fig. 3.7, we plot them as a function of finite delay $\tau = \tau_B - \tau_A$ for different values of the bandwidth $\beta$ and pump strength $\epsilon$.

Within the filtered mode approximation, we find that in the limit of $\beta \gg 1$, the photon correlations can be approximated to

$$M(\tau) \simeq \frac{2\epsilon(1+\epsilon^2)}{(1-\epsilon^2)^2} e^{-\gamma\tau/2}. \tag{3.46}$$

This shows that in this limit, the correlations decay on the timescale set by $\gamma$, and not by the relaxation rates of the amplifier, $\kappa_\pm = \kappa(1 \pm \epsilon)$. Therefore, a finite amount of squeezing persists up to delay times of about $\tau \approx \gamma^{-1}$ for all driving strengths. In contrast, the behaviour of the effective purity $\mu_{\text{eff}}(\tau)$ depends more strongly on the driving strength.

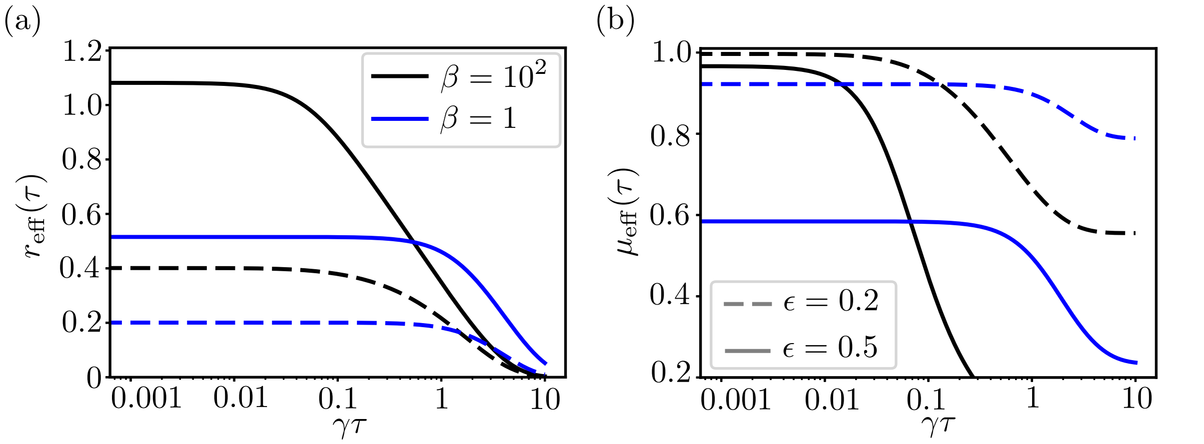


**Figure 3.7:** Time-delayed effective parameters (a) $r_{\rm eff}(\tau)$ and (b) $\mu_{\rm eff}(\tau)$ for $\epsilon = 0.4$ (solid) and $\epsilon = 0.2$ (dashed) and for different amplifier bandwidths $\beta = 1$ and $\beta = 10^3$.

This is because a larger value of $M(\tau = 0)$ implies a larger absolute change of $M(\tau)$. The timescale that determines the decay of the purity, and therefore the entanglement, can become considerably shorter than $\gamma^{-1}$ for high driving strengths. This conclusion is consistent with the entanglement decay in delayed two-mode squeezed states reported in Ref. [164]. In the opposite regime $\beta \sim 1$, the squeezing and purity parameters are initially smaller, but they are more robust and decay only after a delay $\tau > \gamma^{-1}$, roughly independently of $\epsilon$. This means that to keep the purity as high as possible, the qubits can be separated from the source by arbitrarily large distances provided that, the relative propagation times satisfy

$$\gamma|\tau_A - \tau_B| \ll 1. \tag{3.47}$$

### 3.7.2 Entanglement distribution with delays

For larger networks with non-negligible propagation delays, different choices for the definition of entanglement and correlations can be considered. For quantum key distribution schemes or similar applications, where the quantum states are only used once, one is typically interested in correlations between measurements that are delayed by the respective propagation times of the transmitting photons. However, for other applications, where quantum states are redistributed within the network multiple times, the more relevant question is how much entanglement exists between different nodes at a given time. In the following, we are interested in this second type of scenario, where signal delays become relevant.

To derive an expression for the steady-state correlations when delays are present, we use Eq. (2.74) to form a set of quantum Langevin equations for the Heisenberg operators. First, to handle finite propagation delays in a more general manner, we introduce a set of shifted Heisenberg operators

$$\hat{\sigma}_n'^k(t) = \hat{\sigma}_n^k(t+\tau_n), \qquad \hat{a}_n'(t) = \hat{a}_n(t+\tau_\varepsilon). \tag{3.48}$$

Here, $\tau_\varepsilon$ is a small time delay, which is negligible on the timescale of the system dynamics but must be kept finite when evaluating commutation relations with the waveguide fields.

The shifted Heisenberg operators obey

$$\dot{\hat{a}}_n'(t) = i[\hat{H}_{\mathrm{ph}}'(t), \hat{a}_n'(t)] - \frac{\kappa_n}{2}\hat{a}_n'(t) - \sqrt{\kappa_n}\hat{f}_{\mathrm{in},n}(t+\tau_\varepsilon), \tag{3.49}$$

$$\dot{\hat{\sigma}}_n'^-(t) = -\frac{\gamma_n}{2}\hat{\sigma}_n'^-(t) + \sqrt{\gamma_n\kappa_n}\hat{\sigma}_n'^z(t)\hat{a}_n'(t) + \sqrt{\gamma_n}\hat{\sigma}_n'^z(t)\hat{f}_{\mathrm{in},n}(t), \tag{3.50}$$

$$\begin{aligned}\dot{\hat{\sigma}}_n'^z(t) =& -2\gamma_n\hat{\sigma}_n'^+(t)\hat{\sigma}_n'^-(t) - 2\sqrt{\gamma_n\kappa_n}\left[\hat{\sigma}_n'^+(t)\hat{a}_n(t) + \hat{a}_n^\dagger(t)\hat{\sigma}_n'^-(t)\right]\\ &- 2\sqrt{\gamma_n}\left[\hat{\sigma}_n'^+(t)\hat{f}_{\mathrm{in},n}(t) + \hat{f}_{\mathrm{in},n}^\dagger(t)\hat{\sigma}_n'^-(t)\right].\end{aligned} \tag{3.51}$$

Since in these equations, all $\hat{f}_{\mathrm{in},n}(t)$ operators appear to the right and all $\hat{f}_{\mathrm{in},n}^\dagger(t)$ operators to the left, we can perform the expectation value with respect to the initial vacuum state $\rho_{\mathrm{full}}^0$ and take the limit $\tau_\epsilon \to 0$ afterwards. As a result, the expectation values for $\langle\dot{\hat{\sigma}}_n'^k(t)\rangle$ and $\langle\dot{\hat{a}}_n'(t)\rangle$ do not explicitly depend on the delay times $\tau_n$ anymore and their expressions are identical to the ones obtained for $\langle\dot{\hat{\sigma}}_n^k(t)\rangle$ and $\langle\dot{\hat{a}}_i(t)\rangle$ from the cascaded master equation given in Eq. (3.1).

As a next step, we show that the same is true for arbitrary operator products $\hat{S}_A'(t)\hat{S}_B'(t)\hat{A}'(t)$, where $\hat{S}_n'(t)$ are Pauli operators and $\hat{A}'(t)$ is an arbitrary product of operators $\hat{a}_{A,B}'(t)$ and $\hat{a}_{A,B}'^\dagger(t)$. To evaluate the time derivative of this product, we apply the product rule and use the time derivatives for the individual operators given in Eqs. (3.49)-(3.51). This results in terms of the form

$$\begin{aligned}\frac{\mathrm{d}}{\mathrm{d}t}\hat{S}_A'(t)\hat{S}_B'(t)\hat{A}'(t) =& -\sqrt{\gamma_A}[\hat{S}_A'(t), \hat{\sigma}_A'^+(t)]\hat{F}_A(d_A, t+\tau_A)\hat{S}_B'(t)\hat{A}'(t)\\ &- \sqrt{\gamma_B}\hat{S}_A'(t)\hat{F}_B^\dagger(d_B, t+\tau_B)[\hat{\sigma}_B'^-(t), \hat{S}_B'(t)]\hat{A}'(t)\\ &- \sqrt{\kappa_A}\hat{S}_A'(t)\hat{S}_B'(t)\hat{F}_A^\dagger(0, t+\tau_\epsilon)[\hat{a}_A'(t), \hat{A}'(t)]\\ &+\cdots\end{aligned} \tag{3.52}$$

Before we can take the expectation value with respect to $\rho_{\mathrm{full}}^0$, all $\hat{f}_{\mathrm{in},n}(t)$ operators must be commuted to the right and all $\hat{f}_{\mathrm{in},n}^\dagger(t)$ operators to the left. To do so, we write, for example,

$$\hat{F}_A(d_A, t+\tau_A) = \frac{\sqrt{\gamma_A}}{2}\hat{\sigma}_A'^-(t) + \hat{F}_{\mathrm{out},A}(0,t), \tag{3.53}$$

and use $\hat{F}_{\mathrm{out},A}(0,t) = \hat{F}_A(v\tau_\epsilon, t+\tau_\epsilon)$ to show that $[\hat{F}_{\mathrm{out},A}(0,t), \hat{A}'(t)] = 0$. Further, we write $\hat{S}_B'(t) = \hat{S}_B(t) + \Delta\hat{S}_B(t)$, where $\Delta\hat{S}_B(t)$ depends on the field $\hat{F}_{\mathrm{out},B}(d_B, t')$ for times $t' \in [t, t+\tau_B]$ only. Equivalently, it depends on the field $\hat{F}_B(z,t)$ located in the region

$z \in (0, d_B]$ and the operator

$$\hat{F}_{\mathrm{out},B}(0,t) = \hat{F}_B(0,t) + \frac{\sqrt{\kappa_B}}{2}\hat{a}_B(t). \tag{3.54}$$

This implies that also $[\hat{S}_B(t), \hat{F}_{\mathrm{out},A}(0,t)] = 0$ and $\hat{F}_{\mathrm{out},A}(0,t) = \hat{f}_{\mathrm{in},A}(t) + \sqrt{\kappa_A}\hat{a}_A(t)$ in the second line of Eq. (3.52) can be commuted all the way to the right. Similar arguments can also be made for all the other terms to achieve the desired operator ordering.

In summary, from this derivation we obtain a set of coupled equations of motion for the expectation values of arbitrary operator products $\langle \hat{S}'_A(t)\hat{S}'_B(t)\hat{A}'(t)\rangle$, which are independent of the delay times $\tau_n$ and have the same structure as the corresponding equations of motion derived from the time-local cascaded master equation. After taking again the limit $\tau_\epsilon \to 0$, this result implies that

$$\langle \hat{S}_A(t+\tau_A)\hat{S}_B(t+\tau_B)\hat{A}(t)\rangle = \langle \hat{S}_1\hat{S}_2\hat{A}\rangle(t)\Big|_{\mathrm{loc}}, \tag{3.55}$$

assuming appropriately matched initial conditions. This equation implies that a non-equal correlation function can be evaluated using the time-local master equation given by Eq. (3.1).

We are interested in steady-state equal-time expectation values $\lim_{t\to\infty}\langle \hat{S}_A(t)\hat{S}_B(t)\rangle$, for which Eq. (3.55) cannot be directly applied. Instead we repeat the whole derivation for the operators $\hat{S}'_A(t+t_0)$ and take the average with respect to the state $\hat{S}_B(t_0+\tau_B)\rho_{\mathrm{full}}(t_0)$. Since $\hat{S}_B(t_0+\tau_B)$ depends on $\hat{f}_{\mathrm{in},n}(t)$ for $t \le t_0$ only, it commutes with the relevant noise terms $\sim \hat{f}_{\mathrm{in},n}(t+t_0)$ and we can still make use of $\hat{f}_{\mathrm{in},n}(t+t_0)\hat{S}_B(t_0+\tau_B)\rho_{\mathrm{full}}(t_0) = 0$. Therefore, this approach provides us with the relation

$$\langle \hat{S}_A(t+\tau_A+t_0)\hat{S}_B(t_0+\tau_B)\rangle = \langle \hat{S}_A(t+t_0)\hat{S}_B(t_0)\rangle\Big|_{\mathrm{loc}}, \tag{3.56}$$

which extends the result from above to more general correlations. By assuming that $t_0$ is long enough such that the system has reached a steady state, we can redefine $t_0 \to t_0 - \tau_B$ and set $t = \tau_B - \tau_A$. This result allows us to use the master equation in Eq. (3.1) to evaluate non-equal time correlation functions, which can be related to the steady state expectation values of the actual network with time delays. More precisely, given an arbitrary product of two-qubit operators $\hat{O}_n$ and $\hat{O}_{n'}$, its steady state expectation value can be computed as

$$\langle \hat{O}_n\hat{O}_{n'}\rangle_{\mathrm{ss}} = \langle \hat{O}_n(\tau_n - \tau_{n'})\hat{O}_{n'}\rangle\Big|_{\mathrm{loc}}, \tag{3.57}$$

assuming that $\tau_n > \tau_{n'}$. Based on this relation and with the help of expressing the reduced

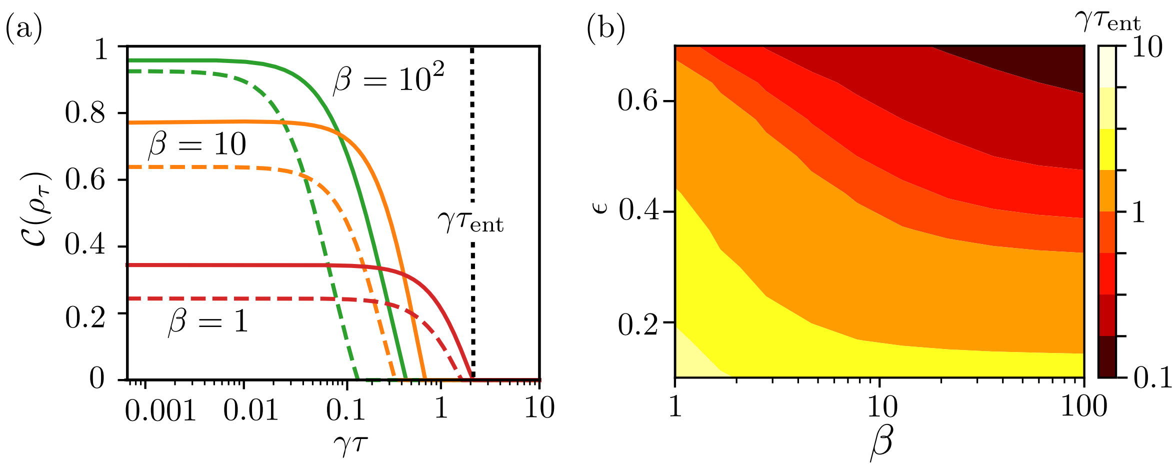


**Figure 3.8:** (a) Steady state concurrence of a network with time delays $\mathcal{C}(\rho_\tau)$ for $\epsilon = 0.5$ and different values of $\beta$. The solid lines represent the results of a full numerical simulation based on Eq. (3.58), while the dashed lines indicate the FMA predictions. (b) Plot of the entanglement time $\tau_{\rm ent}$, i.e., the smallest delay time beyond which the entanglement vanishes, $\mathcal{C}(\rho_{\tau_{\rm ent}}) = 0$. In all plots, $\nu = 1$, $\Gamma_\phi = 0$.

steady state of the two qubits as Eq. (2.5), the time-local steady state with delays then is

$$\rho_\tau = \frac{1}{4} \sum_{\mu,\nu=0,x,y,z}^{3} \langle \hat{\sigma}_A^\mu(\tau)\hat{\sigma}_B^\nu \rangle \Big|_{\rm loc} \hat{\sigma}_A^\mu \hat{\sigma}_B^\nu, \tag{3.58}$$

We can employ Eq. (3.57) to evaluate the full two-qubit density matrix of a time-delay network through numerical simulations of the time-local master equation given in Eq. (3.1). In addition, we can again use the FMA to derive a time-local master equation for $\rho_{\rm q}$ only. In this approach, all the propagation delays are already included in the parameters $N_n$ and $M$ from Eq. (3.31) and Eq. (3.32), respectively. This is the main result of the section, where we see that in the presence of delays, the correlation functions can be evaluated as non-equal time correlation functions using the time-local master equation in Eq. (3.1). Equivalently, in the broadband limit, we can use the reduced master equation from Eq. (3.6) with the new time-delayed coefficients. In Fig. 3.8(a), we evaluate the actual steady state concurrence of this system using Eq. (3.58) for a moderate driving strength of $\epsilon = 0.5$. We see that the dependence of $\mathcal{C}(\rho_\tau)$ captures the overall trend inferred from $\mu_{\rm eff}(\tau)$ from Fig. 3.7(b). However, the exact simulations not only predict consistently higher values for $\mathcal{C}(\rho_{\tau=0})$, they also show that the entanglement of the qubits is considerably more robust with respect to time delays than the entanglement of the filtered modes. In Fig. 3.8(b), we define the delay time $\tau_{\rm ent}$ as the maximal delay time for which a finite amount of steady-state entanglement can still be distributed. This timescale is roughly given by $\tau_{\rm ent} \sim \gamma^{-1}$, but can be significantly reduced for very large driving strengths.

## 3.8 Outlook: Experimental implementations

This last section is motivated by two ongoing experimental collaborations for which we provide accurate predictions. Throughout this chapter, we presented a detailed study of a remote entanglement protocol and showed how to create entanglement between two physically separated qubits using a nondegenerate parametric amplifier. While we did include some experimental imperfections to study the protocol robustness in previous sections, it is still unclear whether the qubit-qubit entanglement would survive under actual experimental conditions when all imperfections are present.

### 3.8.1 Qubit-qubit entanglement

This experimental collaboration is being done with the group of *Quantum Integrated Devices* led by Prof. Dr. Johannes Fink at ISTA. The setup consists of two qubits, two waveguides and a nondegenerate parametric amplifier, as proposed in Fig. 3.1. Based on approximated experimental data, we assume the following parameters: The coupling into the waveguide is $\gamma_A/(2\pi) = 800\,\mathrm{kHz}$ and $\gamma_B/(2\pi) = 482\,\mathrm{kHz}$ for each qubit. We have non-negligible dephasing noise, given by $\gamma_{\phi,A}/(2\pi) = 265\,\mathrm{kHz}$ and $\gamma_{\phi,B}/(2\pi) = 217\,\mathrm{kHz}$. The nondegenerate parametric amplifier has a bandwidth of $\kappa_n/(2\pi) \approx 30\,\mathrm{MHz}$ for both modes, which gives us a bandwidth ratio of $\beta_A \approx 37.5$ and $\beta_B \approx 62.25$.

Contrary to our model in Eq. (3.28) where we assumed symmetric qubits, the reality is that this is rarely the case, confirmed by the experimental parameters we have. Still, our model allows us to predict an expression for the concurrence for this asymmetric case. While it is not as simple as Eq. (3.28), it reads as $\mathcal{C}(\rho_{\mathrm{ss}}) = \max(0, \mathcal{C}_{\mathbf{asym.}})$ where $\mathcal{C}_{\mathbf{asym.}}$ is

$$\begin{aligned}\mathcal{C}_{\mathbf{asym.}} = {} & \frac{2\mu \tanh(2r)\gamma_+ \sqrt{\gamma_+^2 - \gamma_-^2}}{2\gamma_+^2 + \gamma_-^2(\cosh(4r) - 1) + 4\gamma_+\Gamma_+\sqrt{\mu}\cosh(2r)} - \frac{1}{4}\times \\ & \Big[\frac{2\gamma_-^2\cosh(4r) - 2(\gamma_-^2 + 2\gamma_+^2(\mu - 1)) + 4\gamma_+\Gamma_+\sqrt{\mu}(1 - 2\mu + \cosh(4r))\,\mathrm{sech}(2r)}{2\gamma_+^2 + \gamma_-^2(\cosh(4r) - 1) + 4\gamma_+\Gamma_+\sqrt{\mu}\cosh(2r)}\Big],\end{aligned} \tag{3.59}$$

where we have defined $\gamma_\pm = (\gamma_A \pm \gamma_B)/\sqrt{2}$ and $\Gamma_\pm = (\gamma_{\phi,A} \pm \gamma_{\phi,B})/\sqrt{2}$. To avoid overwriting this already large expression, we have not written down the effective subindex at $r_{\mathrm{eff}}$ and $\mu_{\mathrm{eff}}$. Notice how Eq. (3.59) is independent of $\Gamma_-$, indicating that *any* dephasing noise always contributes, in this case, detrimentally. In Eq. (3.59), we cannot use the filtered mode approximation derived in Sec. 3.5 for the effective parameters $r_{\mathrm{eff}}$ and $\mu_{\mathrm{eff}}$, as it was derived under symmetric conditions. We then must use the Markovian bath parameters given by Eq. (3.13) and $\mu_{\mathrm{eff}} = 1$.

In Fig. 3.9(a), we then plot Eq. (3.59) in function of the pump strength $\epsilon$ for different insertion losses $\nu$ and compare it to the concurrence obtained from the full model using Eq. (3.1) assuming the same experimental values.

It is important to emphasize that one thing is to create a remote entangled state, and

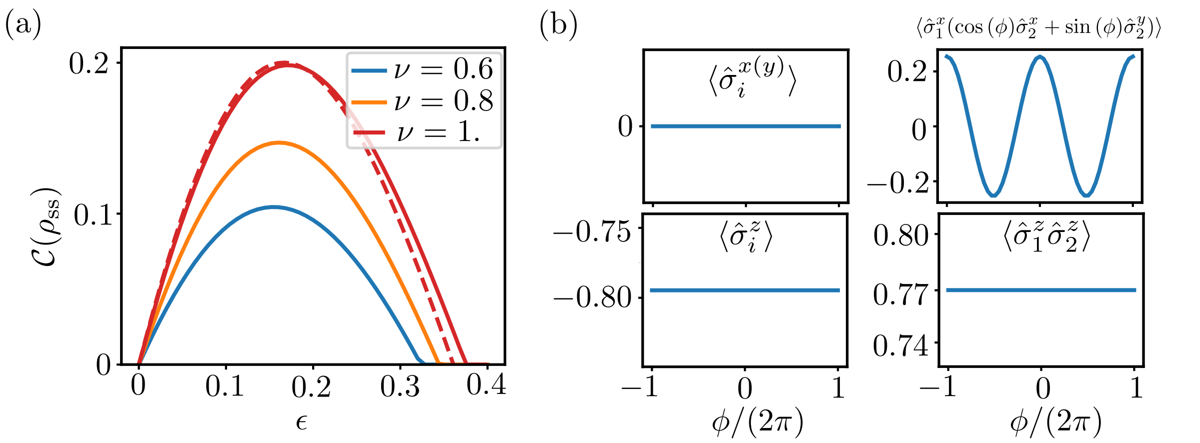


**Figure 3.9:** (a) Evaluation of the concurrence $\mathcal{C}(\rho_{ss})$ using Eq. (3.1) as a function of the pump strength $\epsilon$ for different insertion losses $\nu$. The dashed line corresponds to Eq. (3.59). (b) Expectation value for the required correlations necessary to verify our entangled state as a function of a rotation angle $\phi$ by which we rotate our second qubit $\cos(\phi)\hat{\sigma}_2^x + \sin(\phi)\hat{\sigma}_2^y$. We have assumed finite losses $\nu = 0.8$ and set the pump strength at $\epsilon = 0.2$. The values in the main text set all the other parameters.

another thing is to verify that, indeed, the state is there and that it is entangled. For that task, one must reconstruct the two-qubit density matrix $\rho$ as in Eq. (3.25). Given the structure of our density matrix, the entanglement is given by Eq. (2.10), where only three elements of the density matrix are relevant: $\rho_{00,11}$, $\rho_{10}$, and $\rho_{01}$. Experimentally, one can reconstruct these elements using the tomography of the density matrix defined in Eq. (2.5). By expressing the density matrix in terms of the Pauli operators, the matrix element can be obtained by measuring the following observables

$$\rho_{00,11} = \frac{\langle\hat{\sigma}_1^x\hat{\sigma}_2^x\rangle - i\langle\hat{\sigma}_1^x\hat{\sigma}_2^y\rangle - i\langle\hat{\sigma}_1^y\hat{\sigma}_2^x\rangle - \langle\hat{\sigma}_1^y\hat{\sigma}_2^y\rangle}{4}, \tag{3.60}$$

$$\rho_{10} = \frac{1 - \langle\hat{\sigma}_2^z\rangle + \langle\hat{\sigma}_1^z\rangle - \langle\hat{\sigma}_1^z\hat{\sigma}_2^z\rangle}{4}, \tag{3.61}$$

$$\rho_{01} = \frac{1 + \langle\hat{\sigma}_2^z\rangle - \langle\hat{\sigma}_1^z\rangle - \langle\hat{\sigma}_1^z\hat{\sigma}_2^z\rangle}{4}. \tag{3.62}$$

In the idealized case that the parametric amplifier is broadband, there are no photon losses, and the qubit's dephasing is negligible, we have seen in Sec. 3.2 that $\rho_{10} = \rho_{01} = 0$ and therefore, all the information about the entanglement would be encoded in the cross-correlations $\hat{\sigma}_1^x\hat{\sigma}_2^x$ and $\hat{\sigma}_1^y\hat{\sigma}_2^y$ correlations. In Fig. 3.9(b), we show those correlations for the experimental values described before using Eq. (3.1). As we are far from the idealized conditions, we predict non-negligible populations on $\rho_{10} \neq \rho_{01} \neq 0$. Still, for the parameters we have selected, Fig. 3.9(a) already shows that a finite amount of entanglement is present in the system. We observe this in the right-top plot of Fig. 3.9(b), where we predict the behaviour of the cross-correlations. An experimental observation of such correlations would then verify that the two qubits are entangled. Moreover, an experimental fit of the concurrence in Eq. (3.59) would also provide us information about the effective parameters of the bath $\mu_{\text{eff}}$ and $r_{\text{eff}}$. This would provide an indirect way to probe the parametric amplifier and extract its relevant parameters.

### 3.8.2 Hybrid entanglement

These results are motivated by the experimental collaboration at the Walther-Meißner-Institute with the group of *Quantum Systems* led by Prof. Dr. Rudolf Gross and Dr. Habil. Kirill Fedorov. The setup is sketched in Fig. 3.10(a). Similar to our proposal, we have a nondegenerate parametric amplifier which emits correlated photons into two separated waveguides. However, there is a small difference: only a single qubit is present in the system, coupled to mode $\hat{a}_A$, while the other mode $\hat{a}_B$ does not interact and propagates along the waveguide. This scenario can be considered a natural previous step before the qubit-qubit entanglement in which one studies the correlations between the travelling mode $\hat{a}_B$ and the qubit. This sort of entanglement, called hybrid entanglement, between continuous- and discrete-variable systems has been studied before in the optical regime [191], but to our knowledge, it has never been shown in the microwave regime.

Our model described by Eq. (3.1) needs to be modified to incorporate a few changes: First, due to experimental constraints, our qubit doesn't couple directly to the waveguide, but rather, it is mediated by a single-mode cavity described by mode $\hat{a}_c$ with resonant frequency $\omega_c$. The cavity and the qubit interact via the usual Jaynes-Cummings Hamiltonian [142]

$$\hat{H}_{\text{JC}} = ig(\hat{a}_c\hat{\sigma}_A^+ - \hat{a}_c^\dagger\hat{\sigma}_A^-). \tag{3.63}$$

Moreover, we assume the coupling between the waveguide and the cavity is given by $\gamma_A$, while the qubit doesn't have individual decay.

The second modification in Eq. (3.1) is more subtle: We need to assume that the other mode $\hat{a}_B$ is coupled, via the waveguide, to a virtual single-mode cavity described by the mode $\hat{a}_f$ with resonant frequency $\omega_f$. The reason we use this virtual cavity is because the mode $\hat{a}_B$ corresponds to the intracavity field of the parametric amplifier, not the output field. In this scenario, the virtual cavity *acts* as the output field [192]. We assume the qubit and the cavity to which is couples to be resonant at $\omega_0/(2\pi) \equiv \omega_{A,1}/(2\pi) = \omega_c/(2\pi) = 5.54\,\text{GHz}$, with coupling strength $g/(2\pi) = 50\,\text{MHz}$. Both cavities have identical bandwidth $\gamma_A/(2\pi) = \gamma_f/(2\pi) = 1\,\text{MHz}$ and also assume identical bandwidth for the nondegenerate parametric amplifier modes $\kappa_A/(2\pi) = \kappa_B/(2\pi) = 50\,\text{MHz}$. In Fig. 3.10(b), we plot the negativity $\mathcal{N}(\rho)$ of our reduced hybrid state, formed by our qubit and the virtual mode of the cavity, as a function of the frequency of the modes of parametric amplifier $\omega \equiv \omega_A = \omega_B$. As we scan the frequency, we observe two resonances rather than a single resonance at $\omega_0$. The reason is that due to the Jaynes-Cummings interaction, our qubit and cavity cannot be thought of as individual objects; rather, they

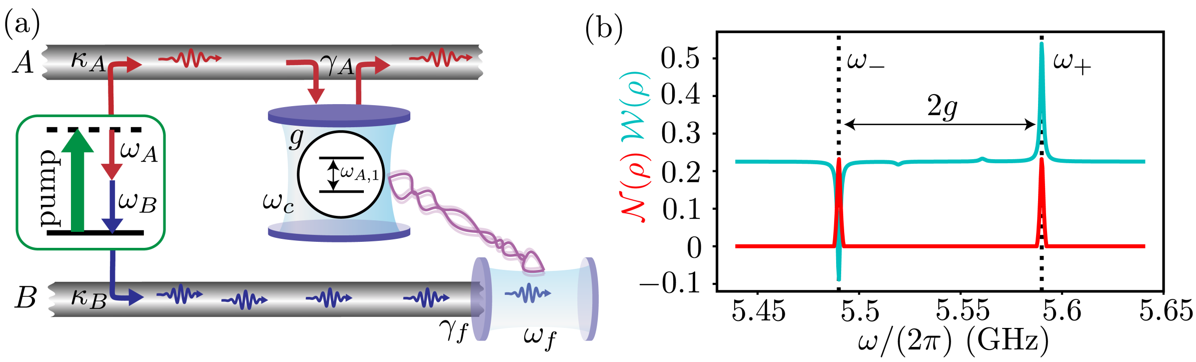


**Figure 3.10:** (a) Schematic of the setup to generate hybrid entanglement between a qubit and a continuous mode. (b) Entanglement witness $\mathcal{W}(\rho)$ (in cian) and negativity $\mathcal{N}(\rho)$ (in red) between the qubit and the virtual mode $\hat{a}_f$ as a function of the frequency of the parametric amplifier $\omega \equiv \omega_A = \omega_B$. Vertical lines correspond to the frequencies of the dressed states $\omega_\pm$ given by Eq. (3.64). We assume the frequency of the virtual cavity to be resonant with the parametric amplifier $\omega_f = \omega_A$.

form a joint system described by its dressed states and dressed energies [142]. In our case, the dress energies are given by

$$\omega_\pm = \omega_0 \pm g, \tag{3.64}$$

which match the resonances seen in Fig. 3.10(b). The negativity $\mathcal{N}(\rho)$ indicates entanglement between the qubit and the virtual mode. To verify it experimentally would require us to perform tomography on the continuous- and discrete-variable system to obtain the state $\rho$. Alternatively, we can use an alternative witness as described in Sec. 2.2.3. In our system, the observables we can measure are

$$\{\hat{A}\} = \{\hat{x}, -\hat{p}\}, \qquad \{\hat{B}\} = \{\hat{\sigma}_y, \hat{\sigma}_z\}, \qquad \to \qquad \{\hat{M}\} = \{\hat{\sigma}_y + \hat{x}, \hat{\sigma}_z - \hat{p}\}. \tag{3.65}$$

The lower bounds for our observables can be computed exactly. For the qubit system, the bound is

$$\sum_{i=1}^{n} (\Delta \hat{B}_i)^2 = (\Delta\hat{\sigma}_y)^2 + (\Delta\hat{\sigma}_z)^2 = 2 - \langle\hat{\sigma}_y\rangle^2 - \langle\hat{\sigma}_z\rangle^2 \geq 1 + \langle\hat{\sigma}_x\rangle^2 \geq 1 \to U_B = 1, \tag{3.66}$$

where we have used that the norm of the Bloch sphere is $\langle\hat{\sigma}_z\rangle^2 + \langle\hat{\sigma}_y\rangle^2 + \langle\hat{\sigma}_x\rangle^2 \leq 1$. For the continuous system

$$\sum_{i=1}^{n} (\Delta \hat{A}_i)^2 = (\Delta\hat{x})^2 + (\Delta\hat{p})^2 = (\Delta\hat{x})^2 + \frac{1}{4(\Delta\hat{x})^2} \geq 1 \to U_A = 1 \tag{3.67}$$

where we have used the Heisenberg uncertainty relation $(\Delta\hat{x})^2(\Delta\hat{p})^2 \geq |\langle[\hat{x},\hat{p}]\rangle|^2/4$ and then used that the function $f(X) = X + \frac{1}{4X}$ has a minima for $X = 1/2$. This all translates to the following entanglement witness

$$\mathcal{W}(\rho) = (\Delta(\hat{\sigma}_y + \hat{x}))^2 + (\Delta(\hat{\sigma}_z - \hat{p}))^2 - 2 \tag{3.68}$$

which must fulfil $\mathcal{W}(\rho) < 0$ to show the state $\rho$ is entangled. We plot entanglement witness in Fig. 3.10(b) superimposed with the negativity $\mathcal{N}(\rho)$. We observe that we can achieve $\mathcal{W}(\rho) < 0$, and therefore detect entanglement, for one of the dressed frequencies $\omega_-$, while at $\omega_+$, even if there is entanglement, our witness is not able to detect it. Surprisingly, the entanglement at $\omega_+$ can be detected, at the expense of not detecting it at $\omega_-$, by changing our witness to $\{\hat{M}\} = \{\hat{\sigma}_y - \hat{x}, \hat{\sigma}_z + \hat{p}\}$.

# Chapter 4

# Multi-qubit entanglement distribution

The creation of robust entanglement between two qubits, allowing for the creation of the smallest possible network, opens the question as to whether those results extend to a larger network of qubits. In this chapter, we consider such a multi-qubit extension of the entanglement distribution protocol discussed in Chapter 3. We start in Sec. 4.1 with the theoretical model of the setup, which consists of an extension of the previous system taking into account more qubits. Next, in Sec. 4.2, we derive a reduced qubit master equation and obtain its dark states. This allows us to start to gain insight into the entanglement structure of the system. We use these analytical tools to parametrize any general state in terms of only a few parameters, such as the detunings and the squeezing strength. Increasing the number of qubits in the system would also, in principle, lengthen the time required to generate the desired states. In Sec. 4.3, we show how one can parallelize this process to obtain an advantage with respect to serially using this protocol. Considering the finite bandwidth of the nondegenerate parametric amplifier, we analyze the scalability of our protocol in Sec. 4.4. In Sec. 4.5, we transform our master equation into a stochastic master equation, which allows us to simulate finite-bandwidth effects for large occupation numbers. We finish this chapter by making a theoretical prediction about the maximal number of qubit pairs that we can produce with our protocol with state-of-the-art experimental parameters.

## 4.1 Quantum network master equation

Our extended protocol to generate multi-qubit entangled states consists, as previously, of two unidirectional waveguides, labelled $n = A, B$, a nondegenerate parametric amplifier which sends correlated photons into the waveguides, and a set of qubits. We label the qubits by index $j_n = 1, \ldots, N_\mathrm{q}$ along the direction of the waveguide, from left to right. Here, we assume both waveguides have the same number of qubits. The index $j_n = 0$ corresponds to the parametric amplifier, as in the previous chapter. The setup is sketched in Fig. 4.1. To connect with the original waveguide system in Sec. 2.3.2 where we model $N_\mathrm{q}$ emitters with decay rates $\gamma_j$, we again identify $\hat{c}_0 = \hat{a}_n$ and $\gamma_0 = \kappa_n$ for waveguide $n$, and $\hat{c}_{j>0}$ with $\hat{\sigma}^-_{j>0}$. Now, we relabel the index $j$ to $j = 1, \ldots, N_\mathrm{q}$. Imposing the

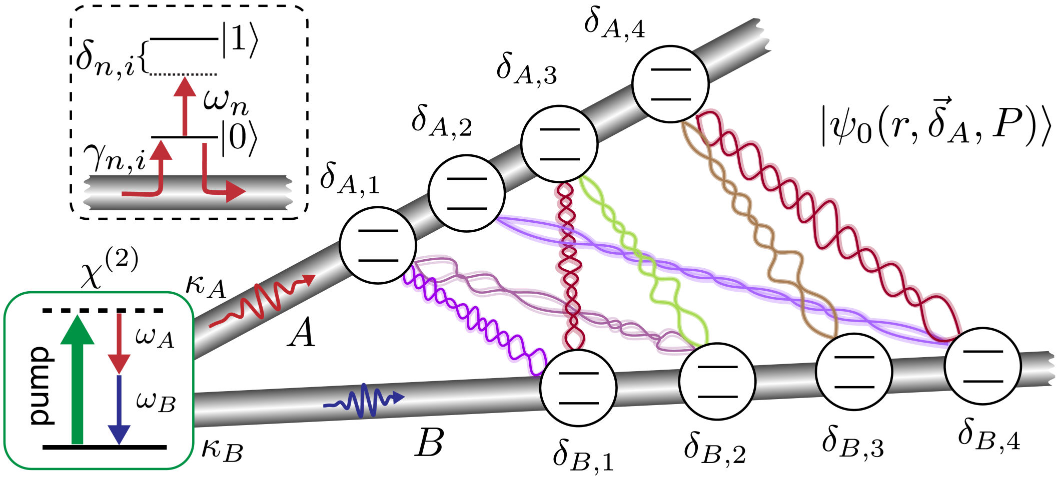


**Figure 4.1:** Schematic of a dual-rail quantum network, where qubits along two separated waveguides are driven by the correlated output of a non-degenerate parametric amplifier and relax into a pure steady state $|\psi_0(r, \vec{\delta}_A, P)\rangle$. As shown in the inset, the qubits in waveguide $A$ ($B$) are detuned from the central photon frequency $\omega_A$ ($\omega_B$) by $\delta_{A,i}$ ($\delta_{B,i}$) and the qubit-waveguide coupling is assumed to be fully directional.

same waveguide conditions as in Chapter 3, i.e. broadband and linear dispersion relation, and going to a rotating frame with respect to $\omega_A$ and $\omega_B$, we arrive at a similar master equation for the whole setup

$$\dot{\rho} = \left(\mathcal{L}_{\text{ph}} + \mathcal{L}_{\text{q}}^0 + \mathcal{L}_{\text{int}}\right) \rho. \tag{4.1}$$

Here, the Liouvillian of the parametric amplifier $\mathcal{L}_{\text{ph}}$ is the same as in Eq. (3.2), while the qubit description now takes into account all $N_{\text{q}}$ qubits per waveguide

$$\mathcal{L}_{\text{q}}^0\rho = \sum_{n,j}\left(-i\frac{\delta_{n,j}}{2}[\hat{\sigma}_{n,j}^z, \rho] + \gamma_{n,j}\mathcal{D}[\hat{\sigma}_{n,j}^-]\rho + \frac{\gamma_{\phi_j}}{2}\mathcal{D}[\hat{\sigma}_{n,j}^z]\rho\right), \tag{4.2}$$

where $\delta_{n,j} = \omega_{n,j} - \omega_n$ is the detuning of the qubit frequency $\omega_{n,j}$ from the central photon frequency $\omega_n$.

Considering the cascaded interaction in Eq. (4.1), we must account for not only the photons emitted by the parametric amplifier but also those scattered by each qubit, which influence subsequent qubits along the waveguide. Therefore, in the interaction mediated by the waveguide, we also need to consider cascaded qubit-qubit interactions

$$\begin{aligned}\mathcal{L}_{\text{int}}\rho = &\sum_{n,i} \sqrt{\kappa_n\gamma_{n,i}\nu_{0,i}^n}\left([\hat{a}_n\rho, \hat{\sigma}_{n,i}^+] + [\hat{\sigma}_{n,i}^-, \rho\hat{a}_n^\dagger]\right)\\ &+\sum_{n,j>i}\sqrt{\gamma_{n,i}\gamma_{n,j}\nu_{i,j}^n}\left([\hat{\sigma}_{n,i}^-\rho, \hat{\sigma}_{n,j}^+] + [\hat{\sigma}_{n,j}^-, \rho\hat{\sigma}_{n,i}^+]\right).\end{aligned} \tag{4.3}$$

Here, we have included the additional parameters $\nu_{i,j}^n \in [0,1]$ to model losses in the system. In general, $|\nu_{i,j}^n|$ is the loss probability for a photon propagating at waveguide $n$ between node $i$ and node $j$, where the index $i = 0$ refers to the parametric amplifier. In this way, the $\nu_{i,j}^n$ can be adjusted to model not only linear absorption losses but also parasitic loss channels for the qubits. Notice that by setting $N_\mathrm{q} = 1$, we recover the initial model from the previous chapter. As before, in Eq. (4.1) we have absorbed all propagation phases into a redefinition of the qubit operators. This means that up to local phase rotations, all results presented in this work are independent of the precise location of the qubits.

### 4.1.1 Qubit master equation

We first focus on the limit of a broadband amplifier, $\kappa_n \to \infty$, in which case the dynamics of the photons can be adiabatically eliminated to obtain an effective master equation for the reduced density operator $\rho_\mathrm{q} = \mathrm{Tr}_\mathrm{ph}\{\rho\}$ of the qubits only. To do so, first, we rewrite the full master equation as

$$\dot{\rho} = (\mathcal{L}_\mathrm{ph} + \mathcal{L}_\mathrm{q} + \mathcal{L}_\mathrm{ph-q})\,\rho, \tag{4.4}$$

where

$$\mathcal{L}_\mathrm{q}\rho = \mathcal{L}_\mathrm{q}^0\rho + \sum_{n,j>i} \sqrt{\gamma_{n,i}\gamma_{n,j}\nu_{i,j}^n}\left([\hat{\sigma}_{n,i}^-\rho, \hat{\sigma}_{n,j}^+] + [\hat{\sigma}_{n,j}^-, \rho\hat{\sigma}_{n,i}^+]\right), \tag{4.5}$$

now includes all waveguide-mediated interactions among the qubits, while

$$\mathcal{L}_\mathrm{ph-q}\rho = \sum_{n=A,B} \sqrt{\kappa}\left([\hat{a}_n\rho, \hat{L}_n^\dagger] + [\hat{L}_n, \rho\hat{a}_n^\dagger]\right). \tag{4.6}$$

Here, we have introduced the collective operators

$$\hat{L}_n = \sum_j \sqrt{\gamma_{n,j}\,\nu_{0,j}^n}\,\hat{\sigma}_{n,j}^-. \tag{4.7}$$

In this form, the master equation in Eq. (4.4) is identical to the master equation Eq. (3.1) considered in the previous chapter, but with the collective operators $\hat{L}_n$, instead of $\hat{\sigma}_n^-$, appearing in the photon qubit interaction in Eq. (4.6). Therefore, following Appendix A, we obtain

$$\dot{\rho}_\mathrm{q} = \mathcal{L}_\mathrm{q}\rho_\mathrm{q} + \sum_{n=A,B} N_n\left(\mathcal{D}[\hat{L}_n]\rho_\mathrm{q} + \mathcal{D}[\hat{L}_n^\dagger]\rho_\mathrm{q}\right) + \left(M^*[\hat{L}_A, [\hat{L}_B, \rho_\mathrm{q}]] + M[\hat{L}_A^\dagger, [\hat{L}_B^\dagger, \rho_\mathrm{q}]]\right), \tag{4.8}$$

where $N_n$ and $M$ are given, respectively, by Eq. (3.9a) and Eq. (3.9b) for $n_\mathrm{eff} = 0$, as we assume a Markovian reservoir. In the limit of negligible losses, $\nu_{i,j}^n = 1$, the Markovian parameter relation allows us to write the effective master equation as

$$\dot{\rho}_{\mathrm{q}} = -i[\hat{H}_{\mathrm{q}}, \rho_{\mathrm{q}}] + \gamma \sum_{n} \mathcal{D}[\hat{J}_n]\rho_{\mathrm{q}}. \tag{4.9}$$

In this equation, we have assumed identical decay rates for all emitters $\gamma_{n,j} = \gamma$ and negligible dephasing $\gamma_{\phi_j} = 0$. Moreover, we have already rewritten the underlying directional qubit-qubit interactions in terms of a coherent Hamiltonian evolution with

$$\hat{H}_{\mathrm{q}} = \sum_{n,i} \frac{\delta_{n,i}}{2} \hat{\sigma}^z_{n,i} + i\frac{\gamma}{2} \sum_{n,j>i} \left( \hat{\sigma}^+_{n,i} \hat{\sigma}^-_{n,j} - \mathrm{h.c.} \right), \tag{4.10}$$

and purely dissipative processes with collective jump operators

$$\hat{J}_A = \cosh(r)\hat{L}_A - \sinh(r)\hat{L}_B^\dagger, \tag{4.11}$$

$$\hat{J}_B = \cosh(r)\hat{L}_B - \sinh(r)\hat{L}_A^\dagger, \tag{4.12}$$

where $\hat{L}_n = \sum_j \hat{\sigma}^-_{n,j}$. This master equation has been derived in the broadband limit, similar to Eq. (3.6). In this case, the system is fully determined by the squeezing parameter $r$, characterizing the degree of two-mode squeezing of the photon source, and the two sets of qubit detunings, $\vec{\delta}_{n=A,B} = (\delta_{n,1}, \delta_{n,2}, \ldots, \delta_{n,N_{\mathrm{q}}})$.

## 4.2 Steady states and entanglement

Equation (4.9) describes an open quantum many-body system with competing coherent and dissipative processes, which in general drive the qubits into a highly mixed steady state. However, in the following, we show that there exist specific conditions under which the steady state of the network, $\rho_{\mathrm{ss}} = |\psi_0\rangle\langle\psi_0|$, is not only pure but also exhibits different degrees of multipartite entanglement that can be controlled by the local detunings $\delta_{n,i}$. Here, we employ the same strategy as in Sec. 3.4 to find its dark states. The main different is that now the jump operators $\hat{J}_n$ involve a collective qubit operator $\hat{L}_n$ and that the Hamiltonian $\hat{H}_{\mathrm{q}}$ involves the detuning contribution as well as a new term which includes the dipole-dipole term, due to the cascaded interaction among the qubits. To make this derivation simple, we proceed step by step, starting from smaller networks $N_{\mathrm{q}} = 1$ and $N_{\mathrm{q}} = 2$, to larger networks with a general $N_{\mathrm{q}}$.

### 4.2.1 Small quantum network

The most trivial example here is when $N_\mathrm{q} = 1$, as we recover the results from the Eq. (3.19) from Chapter 3. Specifically, there we showed that the dark state is given by

$$|\psi_0\rangle = |\Phi^+_{1,1}\rangle = \frac{\cosh(r)|0_{A,1}, 0_{B,1}\rangle + \sinh(r)|1_{A,1}, 1_{B,1}\rangle}{\sqrt{\cosh(2r)}}, \tag{4.13}$$

which approaches a Bell state when $r \to \infty$.

The first non-trivial case starts with $N_\mathrm{q} = 2$. In this case, a dark state satisfying $\hat{J}_n|\psi_0\rangle$ can be obtained by simply arranging the qubits pairwise in a state of the form given in Eq. (4.13). However, since the collective jump operators $\hat{J}_n$ are insensitive to the order of qubits, the whole subspace of dark states is spanned by states of the form

$$|\psi_0\rangle = \alpha|\Phi^+_{1,1}\rangle|\Phi^+_{2,2}\rangle + \beta|\Phi^+_{1,2}\rangle|\Phi^+_{2,1}\rangle. \tag{4.14}$$

From the second condition, $\hat{H}_\mathrm{q}|\psi_0\rangle = 0$, we then obtain the additional constraint

$$\sum_{n,i} \delta_{n,i} = 0, \tag{4.15}$$

on the sum of all detunings together with

$$\beta(\delta_{A,1} - \delta_{B,1} - \delta_{A,2} + \delta_{B,2}) = 0, \tag{4.16}$$

$$2\gamma\beta = i(\delta_{A,1} + \delta_{B,1} - \delta_{A,2} - \delta_{B,2})\alpha. \tag{4.17}$$

These conditions on the detunings can only be fulfilled when either (i) $\delta_{A,1} + \delta_{B,1} = 0$ and $\delta_{A,2} + \delta_{B,2} = 0$ or when (ii) $\delta_{A,1} + \delta_{B,2} = 0$ and $\delta_{A,2} + \delta_{B,1} = 0$. This means that for a pure steady state to exist, the detunings of the qubits in subsystem $B$ must be of opposite sign but the same in magnitude as the detunings in $A$.

In case (i) we have $\beta = 0$ and resulting dark state $|\psi_0\rangle = |\Phi^+_{1,1}\rangle|\Phi^+_{2,2}\rangle$ is simply a product of the entangled pairs given in Eq. (3.19). In case (ii), where the detunings are finite and opposite along the diagonals, we obtain instead the state

$$|\psi_0\rangle = \frac{\gamma|\Phi^+_{1,1}\rangle|\Phi^+_{2,2}\rangle + i\Delta|\Phi^+_{1,2}\rangle|\Phi^+_{2,1}\rangle}{\sqrt{\gamma^2 + \Delta^2}}, \tag{4.18}$$

where $\Delta = \delta_{A,1} - \delta_{A,2}$.

In Fig. 4.2(a) and (b), we visualize the entanglement structure of this state in terms of the steady-state concurrences $\mathcal{C}_{ij} \equiv \mathcal{C}(\rho_{A,i|B,j})$, as defined in Eq. (2.10), of the reduced bipartite qubit states, $\rho_{A,i|B,j}$. For $\Delta = 0$, we find that for parallel pairs $\mathcal{C}_{ii} \simeq 1$ already for moderate values of $r \gtrsim 1$, consistent with the state $|\Phi_{\parallel}\rangle$. We see that, as $|\Delta| \gg \gamma$, the situation is reversed, and only the diagonal qubit pairs become entangled. For

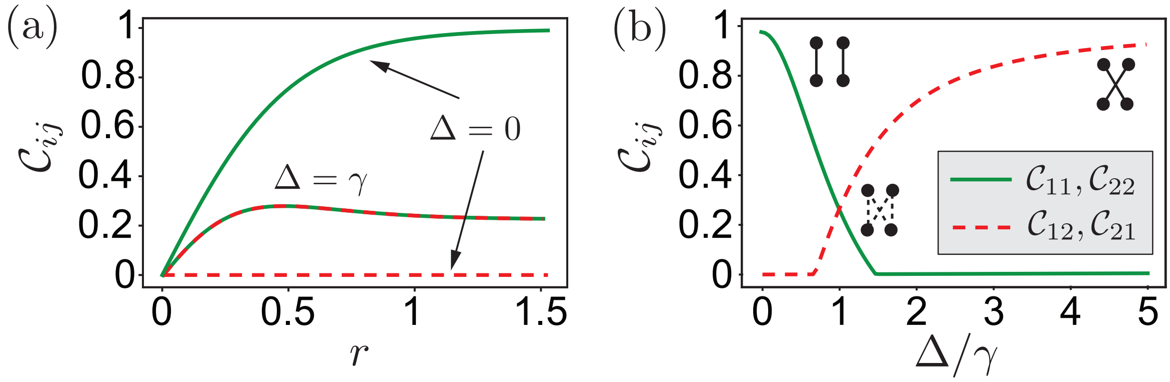


**Figure 4.2:** Bipartite entanglement expressed in terms of the concurrences $\mathcal{C}_{ij}$ for the four-qubit state in Eq. (4.18) (a) as a function of $r$ and (b) as a function of $\Delta$ for $r = 1$.

the same value of squeezing, we obtain $\mathcal{C}_{12} = \mathcal{C}_{21} \simeq 1$. For any intermediate regime, the entanglement is distributed among the four qubits. Specifically, when $\Delta = \gamma$, the four-qubit steady state takes a simplified form and can be written as

$$\begin{aligned}|\psi_0\rangle =& \frac{1}{\cosh(2r)}\Big\{\cosh^2(r)|0000\rangle + \sinh^2(r)|1111\rangle \\ &+ \cosh(r)\sinh(r)\Big(\frac{(1+i)}{2}(|1100\rangle + |0011\rangle) + \frac{(1-i)}{2}(|1001\rangle + |0110\rangle)\Big)\Big\}.\end{aligned} \tag{4.19}$$

We see that this state only contains components with an even number of excitations, which can be attributed to the emission of correlated photon pairs by the TMS source. In the limit $r \to \infty$, the concurrence saturates at $\mathcal{C}^\infty = 0.25$ for all four bipartite states. However, in Fig. 4.2(a), we observe the maximum of the two-quit concurrence is reached at a finite value of $r^\star$. This can be understood by explicitly evaluating the concurrence for this case,

$$\mathcal{C}_{1,1} = \frac{1 - \cosh(4r) + \sqrt{2(4\cosh(4r) + \cosh(8r) - 5)}}{8\cosh^2(2r)}. \tag{4.20}$$

This expression reaches a maximal value of $\mathcal{C}^\star = 0.3090$ at a squeezing parameter of $r^\star = 0.479$, which exceeds the asymptotic value of $\mathcal{C}^\infty = 0.25$. We attribute this higher concurrence to the multipartite nature of the state, as for any finite $\Delta$, the state is a genuine four-partite entangled state [122] and belongs to the set of locally maximally entanglable states [193] for $r \gg 1$.

### 4.2.2 Large quantum network

While identifying the dark states for $N_\mathrm{q} = 1$ and $N_\mathrm{q} = 2$ can be done analytically, it becomes a tedious task for a general $N_\mathrm{q}$ state. We would like to systemically identify more complex multi-qubit steady states for any $N_\mathrm{q}$.

We follow a two-step procedure: First, we set $\vec{\delta}_B = -\vec{\delta}_A$. In this scenario, from $N_{\mathrm{q}} = 2$, we showed that the two Bell states decouple, and the steady-state is given by $|\psi_0\rangle = |\Phi^+_{1,1}\rangle|\Phi^+_{2,2}\rangle$. For a general $N_{\mathrm{q}}$, qubits with the same index decouple pairwise from the photonic reservoir. The network then relaxes into the pure steady state $|\psi_0\rangle = |\Phi_{\parallel}\rangle$, where

$$|\Phi_{\parallel}\rangle = \bigotimes_{i=1}^{N_{\mathrm{q}}} |\Phi^+_{i,i}\rangle \tag{4.21}$$

is the product of $N_{\mathrm{q}}$ consecutive Bell pairs of the type given in Eq. (3.19). Interestingly, this result is independent of the total number of qubit pairs, similar to what has been found for coupled spin chains [94] or discrete cavity arrays [93]. Notice that these results show that, under the ideal conditions we assumed, in principle, we can create an infinite amount of Bell pairs along the waveguide. As we will see in Sec. 4.4, this is an artifact of the idealized infinite-bandwidth parametric amplifier, and taking a finite bandwidth into account limits the number of entangled pairs we can generate.

In the second step, we would like to include the scenario where the detuning is included. For this, we make use of the form-invariance of the cascaded master equation in Eq. (4.9) under unitary transformations of the type [149]

$$\hat{U}_{i,i+1} = e^{i\theta_{i,i+1}(\vec{s}_{B,i}+\vec{s}_{B,i+1})^2}, \tag{4.22}$$

where $\vec{s}_\mu = (\hat{\sigma}^x_\mu, \hat{\sigma}^y_\mu, \hat{\sigma}^z_\mu)/2$ and the mixing angle satisfies $\tan(\theta_{i,i+1}) = (\delta_{B,i} - \delta_{B,i+1})/\gamma$. Under these transformations, one finds that the collective jump operators $\hat{J}_n$ and Hamiltonian $\hat{H}_{\mathrm{q}}$ are given by

$$\hat{U}_{i,i+1}\hat{J}_n\hat{U}^\dagger_{i,i+1} = \hat{J}_n, \tag{4.23a}$$

$$\hat{U}_{i,i+1}\hat{H}_{\mathrm{q}}(\vec{\delta}_A, \vec{\delta}_B)\hat{U}^\dagger_{i,i+1} = \hat{H}_{\mathrm{q}}(\vec{\delta}_A, P_{i,i+1}\vec{\delta}_B). \tag{4.23b}$$

Here, we have introduced the permutation $P_{i,i+1}$, which exchanges $\delta_{B,i}$ and $\delta_{B,i+1}$. Observe how the collective jump operators are invariant under this unitary transformation, but the Hamiltonian term changes. In other words, given a pure steady state $|\psi_0\rangle$ for a certain detuning pattern $\vec{\delta}_B$, the state $|\psi_0'\rangle = \hat{U}_{i,i+1}|\psi_0\rangle$ is a pure steady state of the same network with a permuted pattern of detunings, $\vec{\delta}_B' = P_{i,i+1}\vec{\delta}_B$.

This form-invariance now allows us to construct a large family of multipartite entangled steady states, which are parametrized by (i) the squeezing parameter $r$, (ii) the set of detunings $\vec{\delta}_A$ for qubits in waveguide $A$ and (iii) a permutation $P$ that fixes the detunings in waveguide $B$ to be $\vec{\delta}_B = -P\vec{\delta}_A$. By decomposing $P = \prod_\sigma P_{i_\sigma,i_\sigma+1}$ into a product of nearest-neighbor transpositions, we can start with the state in Eq. (4.21) and then use the relation below Eq. (4.23) to derive an explicit expression for the corresponding steady state,

$$|\psi_0(r, \vec{\delta}_A, P)\rangle = \prod_\sigma \hat{U}_{i_\sigma,i_\sigma+1}|\Phi_{\parallel}\rangle. \tag{4.24}$$

A graphical illustration of Eq. (4.24) is presented in Fig. 4.3.

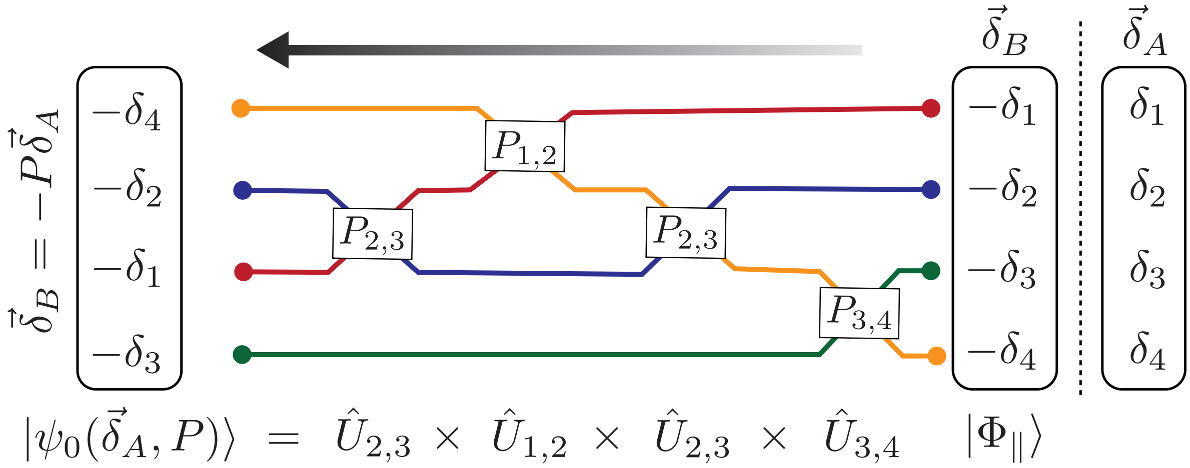


**Figure 4.3:** Graphical illustration of Eq. (4.24). Starting from $\vec{\delta}_B = -\vec{\delta}_A$, the detunings in waveguide B are reordered as $\vec{\delta}_B = -P\vec{\delta}_A$ through nearest-neighbor transpositions, following the coloured lines as a guide to the eye. Each transposition maps into one of the unitary operations $\hat{U}_{i,i+1}$ that determine the final steady state.

We can now use Eq. (4.24) to generate any quantum network. In this scenario, using concurrence might not be the most efficient way to quantify the amount of entanglement present in the network. For this task, we use the entanglement entropy defined in Eq. (2.9), $\mathcal{S}(\rho_r) = -\mathrm{Tr}\{\rho_r \ln \rho_r\}$ for a reduced state $\rho_r$ to study the entanglement between different bipartitions of the network. First of all, as sketched in Fig. 4.4(a), if we take a *local* bipartition which takes into account a local waveguide, this analysis shows that $\mathcal{S}_A \equiv \mathcal{S}(\rho_A) = -N_\mathrm{q} \ln \left[x^x(1-x)^{(1-x)}\right]$, where $x = \cosh^2(r)/\cosh(2r)$, only depends on the squeezing parameter $r$. This can be understood from the fact that the unitaries $\hat{U}_{i,i+1}$ only act within subsystem $B$. Thus, with respect to this partition, the states in Eq. (4.24) can be understood as generalized 'rainbow states' [94, 194, 195] with a volume-law entanglement $\mathcal{S}(\rho_A) \simeq N_\mathrm{q} \ln 2$ for $r \gtrsim 1$. In contrast, for partitions along the chain, the entanglement entropy $\mathcal{S}_n = \mathcal{S}(\rho_{[1,\ldots,n]})$ depends not only on the chosen permutation $P$, but also on the pattern of detunings $\vec{\delta}_A$. This is illustrated in Fig. 4.2(a) and (b), where we consider as an example the detunings $\delta_{A,i} = (i-1)\Delta$ and the reversed order, $\delta_{B,i} = -P_\mathrm{rev}\delta_{A,i} = -\delta_{A,N_\mathrm{q}+1-i}$, in waveguide $B$.

We can gain new insight into the steady-state entanglement distribution of the state in Eq. (4.24) by understanding the unitary transformation $\hat{U}_{i,i+1}$ in each case. When $\Delta \gg \gamma$, the mixing angle is given by $\theta_{i,i+1} \approx \pi/2$, for which the unitary transformation is just equivalent to a SWAP gate between neighboring sites [3]. In this regime, the entanglement entropy is then given by $\mathcal{S}_n \simeq 2n \ln 2$.

The other regime, when $\Delta \lesssim \gamma$, the mixing angle is then $\theta_{i,i+1} \approx \pi/4$. In this case, the entangling unitaries are equivalent to $\hat{U}_{i,i+1} \approx \sqrt{\mathrm{SWAP}}$, which perform a half-swap between neighboring sites. This allows for generating more multipartite entanglement

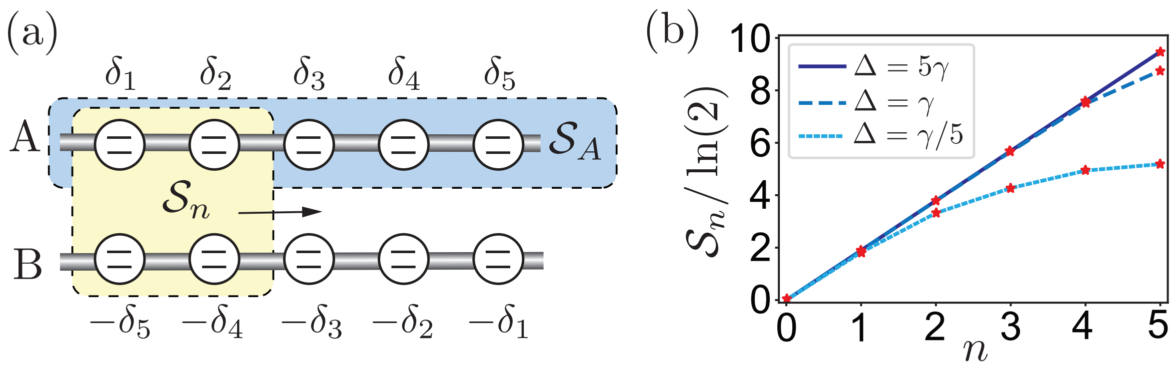


**Figure 4.4:** (a) Schematic of the detuning pattern for the family of multipartite states described in the text and different partitions for evaluating the entanglement entropy. (b) Entanglement entropy $\mathcal{S}_n$ as a function of $n$, for different detunings $\Delta$ and $r = 1$.

across the whole chain, which reduces the block-entanglement $\mathcal{S}_n$ correspondingly. In general, different choices for $\vec{\delta}_A$ and $P$ can be used to define certain blocks of qubits that are entangled among each other, independently of their physical location.

### 4.2.3 Uniqueness of the steady state

While we have had an extensive discussion of the steady state, we have not checked something important about our states: the uniqueness of the steady state. While for time-dependent protocols such as state transfer or qubit states this is not a crucial matter, we focus on ensuring that the steady state of our network is known and therefore controllable. If the steady state were not unique, the actual steady state of an ideal network would then depend on the precise initial condition, while in practice residual imperfections would create an uncontrolled mixture of multiple possible steady states. This would be detrimental to entanglement generation. In Appendix B, we prove that Eq. (4.24) is indeed the unique steady state of Eq. (4.9), and therefore the unique steady state of the quantum network.

## 4.3 Time dynamics

So far, we have shown that a single two-mode squeezing source is, in principle, enough to entangle an arbitrary number of qubits. However, for practical applications, we must still evaluate the time $T_{\text{prep}}$ that it takes to prepare this state. In Sec. 3.6, we computed the entanglement rate $\mathcal{R}$ for a single qubit pair, $N_{\text{q}} = 1$, and concluded that working with large squeezing strength $r \gg 1$ is not the optimal strategy. Here, we fix $r = 1$ and study the relaxation dynamics towards the steady state $|\psi_0\rangle$ for a larger network. For that, we consider the ideal qubit master equation Eq. (4.9), which assumes the parametric amplifier is already in the steady state. Then, similar to Sec. 3.6 at $t = 0$, all qubits are

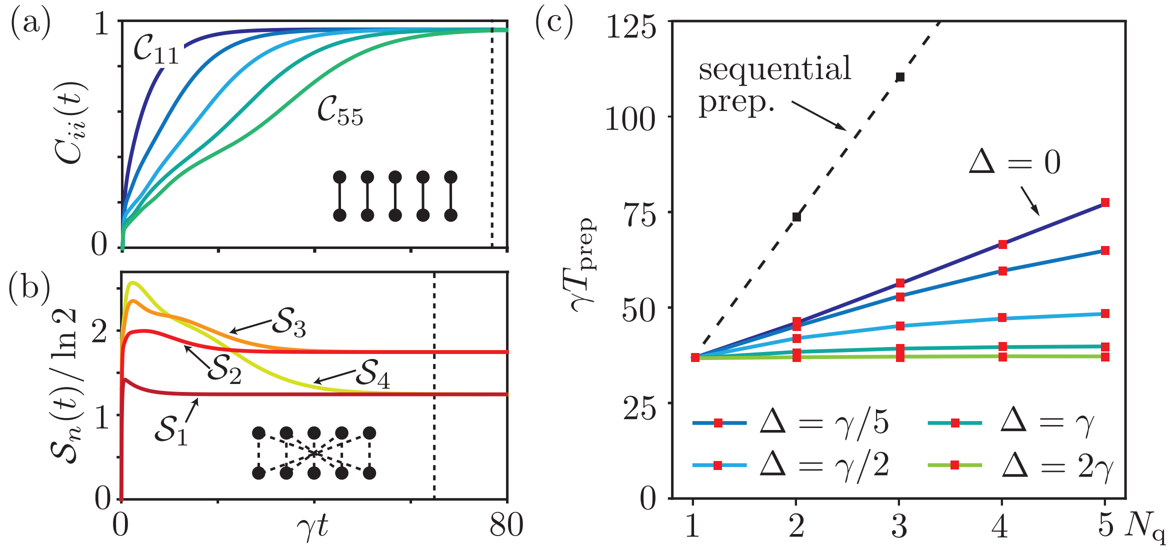


**Figure 4.5:** (a) Relaxation into a bipartite entangled state for $\vec{\delta}_A = 0$ and (b) into a multipartite entangled state for $\vec{\delta}_B = -P_{\text{rev}}\vec{\delta}_A$ and $\Delta = \gamma/5$. In both cases $N_{\text{q}} = 5$. (c) Scaling of the preparation time $T_{\text{prep}}$ for different ratios $\Delta/\gamma$, where $\delta_{A,i} = \Delta(i-1)$ and $\vec{\delta}_B = -\vec{\delta}_A$. For the examples in (a) and (b), $T_{\text{prep}}$ is indicated by the dashed vertical line. In all plots, $r = 1$.

initialized in state $|0\rangle$. We consider a larger network formed of $N_{\text{q}} = 5$ qubit pairs, and we are interested in the required time to reach the steady state, $T_{\text{prep}}$. We define $T_{\text{prep}}$ via the condition $(1 - \mu(T_{\text{prep}}))/N_{\text{q}} = 0.001$, where $\mu = \text{Tr}\{\rho_{\text{q}}^2\}$ is the purity of the total state. This condition comes from the knowledge that in the steady state, our state is pure, and it is given by Eq. (4.24).

In Fig. 4.5(a), we show the time evolution of this state when all the qubits are on resonance $\vec{\delta}_A = 0$. We know that with this detuning pattern, the steady state is given by Eq. (4.21), which is a product state of five Bell-like pairs. We observe how the entanglement builds over time as it reaches a steady state. As expected from the unidirectional waveguide, the first qubit pair is the first to reach the steady state. Observe that the second and consecutive qubit pairs do not need the first qubit pair to reach the steady state, and thus become a dark state, before they begin to create entanglement themselves.

Additionally, we consider a multipartite entangled state in Fig. 4.5(b). In this case, the detuning configuration is the same we used for the steady-state multipartite entangled state in Fig. 4.4. Here, instead of the concurrence, we use the entanglement entropy $\mathcal{S}_n$ as used in the previous section. We observe how even in this multipartite configuration, the steady state also builds up from left to right due to the cascaded interaction. As in that case, the concurrence is not a good metric to quantify the entanglement, so we show the time evolution of the entanglement entropy $S_n(t)/\ln 2$. We observe how, for this multipartite case, the state preparation $T_{\text{prep}}$ is faster than the previous case. Notice how the steady-state entanglement entropy $S_1$ and $S_4$, as well as $S_2$ and $S_3$, coincide at the steady state, as expected, but not through its time dynamics. As with the resonant case, this is because entanglement starts to build up from the left to the right.

Consider the protocol from Chapter 3, where only a single qubit pair $N_\mathrm{q} = 1$ is driven to create a Bell-like state. A sequential preparation of $N_\mathrm{q}$ independent qubit pairs would require a total time which scales linearly with the number of qubit pairs one wants to create, $T_\mathrm{prep} \sim N_\mathrm{q}$. In Fig. 4.5(c), we show the total preparation time as a function of $N_\mathrm{q}$. The dotted line represents the sequential preparation of the protocol, which scales linearly with $N_\mathrm{q}$. We then compare it with the total preparation time from Fig. 4.4(a), which is given by $\Delta = 0$. As mentioned before, the entanglement along the waveguides starts to build up even before the first qubit reaches the steady state. This gives us a faster preparation time with respect to the sequential preparation of $N_\mathrm{q}$ individual qubit pairs, i.e., $T_\mathrm{prep}(N_\mathrm{q}) < N_\mathrm{q} T_\mathrm{prep}(N_\mathrm{q} = 1)$.

Due to the dark state conditions, the same steady state is reached either on resonance $\vec{\delta}_A = 0$ or with opposite detunings $\vec{\delta}_A = -\delta_B$. We can then assume the opposite detuning pattern and take the magnitude of each detuning as $\delta_{A,i} = \Delta(i-1)$. By that, we mean that the first qubit pair is on resonance $\delta_{A,1} = 0$, the second qubit pair is detuned by $\delta_{A,2} = \Delta$, and so on. This new detuning configuration, which does not alter the steady state, does alter the time evolution of the state. We plot this also in Fig. 4.4(c), where we observe that the preparation time starts to decrease to even reach $T_\mathrm{prep}(N_\mathrm{q}) \simeq T_\mathrm{prep}(N_\mathrm{q} = 1)$ for $\Delta \gtrsim \gamma$, i.e., all pairs are prepared in parallel. The reason for that is that in this case, where the qubits are all detuned from each other, the parametric amplifier is driving them independently. It is then, in this regime, where we can achieve perfect parallelization of the protocol.

For multipartite entangled states, where the detuning differences $|\delta_{A,i} - \delta_{A,j}|$ are necessarily small, a full parallelization is not possible, but even in this case we obtain an intrinsic advantage compared to a sequential distribution of entanglement, followed by local gates.

## 4.4 Scalability in realistic networks

All the results so far have been derived within the infinite-bandwidth approximation, which underlies Eq. (4.9) and assumes that correlated photons are available at arbitrary detunings. This assumption must break down when $\delta_\mathrm{max} = \max\{|\delta_{A,i}|\} \gtrsim \kappa$, but even for $\delta_{A,i} = 0$ it has been shown in the previous chapter that any finite $\kappa$ limits the transferable entanglement. Therefore, to provide physically meaningful predictions about the scalability of the current scheme, it is necessary to go beyond the assumption of a Markovian squeezed reservoir and take finite-bandwidth effects into account, as we did in the previous chapter. To do so, we now simulate the dynamics of the state of the full network, $\rho$, as described by the quantum master equation Eq. (4.4).

Let's focus on the entanglement propagation along the waveguide. In the infinite-bandwidth limit, it seems as if one could, in principle, create an infinite amount of

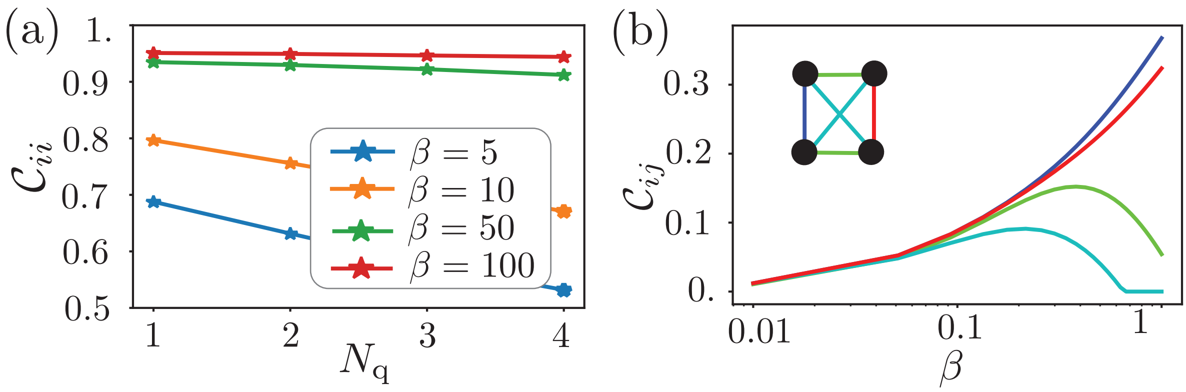


**Figure 4.6:** Steady-state entanglement (a) for different bandwidth $\beta = \kappa/\gamma$ as a function of the length of the waveguide, (b) for $N_q = 2$ in the limit when the bandwidth of the parametric amplifier becomes extremely narrow $\beta < 1$. In both plots, $r = 1$ and resonant condition $\vec{\delta}_A = 0$.

entangled pairs. Considering the finite-amplifier bandwidth, we observe a more realistic situation. In Fig. 4.6(a) we plot the steady-state concurrences $\mathcal{C}_{ii}$ for the resonant case $\vec{\delta}_A = 0$ and different bandwidth ratios $\beta = \kappa/\gamma$. We observe that the finite bandwidth of the parametric amplifier not only reduces the maximum entanglement of the first pair, as shown in Chapter 3, but also causes a gradual decay of entanglement along the chain. Thus, unlike the idealized infinite-bandwidth scenario, where, in principle, an infinite number of qubit pairs could emerge, the parametric amplifier's bandwidth imposes a realistic limitation on the number of entangled pairs. The finite-bandwidth case also allows us to explore the opposite regime, when $\beta \ll 1$. In Fig. 4.6(b), this is what we observe if we focus only on the parallel pairs $\mathcal{C}_{11}$ and $\mathcal{C}_{22}$. Surprisingly, this is not the only effect observed. At around $\beta \leq 1$, a new entanglement structure emerges, creating correlations between both diagonal and consecutive qubits. One might consider the diagonal correlations to result from the two-mode squeezer correlations, as we see similar effects when the qubits have finite but opposite detunings, as seen in Fig. 4.2. However, this is not the case, as they vanish when increasing the amplifier bandwidth. This observation cannot be fully explained here. However, in Chapter 5, we will analyze a simpler yet equivalent system where the same entanglement structure arises. There, we will be able to explain these quantum correlations as a non-Markovian effect from the parametric amplifier.

### 4.4.1 Maximal number of entangled pairs

By using a linear extrapolation, $N_{\text{ent}} = \mathcal{C}_{11}/(\mathcal{C}_{11} - \mathcal{C}_{22})$, we can use these finite-size simulations to extract the maximal number of pairs that can be entangled for more realistic scenarios, for example with finite bandwidth $\beta$ and dephasing rate $\gamma_\phi$. These results are summarized in Fig. 4.7. We see that for otherwise ideal conditions, rather large numbers of $N_{\text{ent}} \sim 10 - 100$ can be entangled for moderate $\beta$, while the presence of

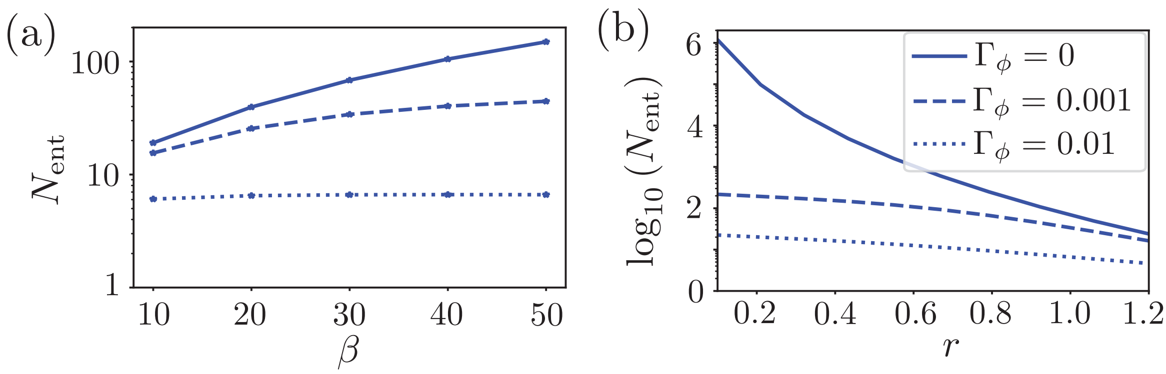


**Figure 4.7:** Maximal number of entangled pairs, $N_{\mathrm{ent}}$, as a function of (a) $\beta = \kappa/\gamma$ for different dephasing rates $\gamma_\phi$ at fixed squeezing strength $r = 1.0$ and (b) as a function of the squeezing strength $r$ for the same dephasing rates $\gamma_\phi$ at fixed $\beta = 30$. For both plots, we have assumed $\vec{\delta}_A$=0.

dephasing or other imperfections sets additional limits on $N_{\mathrm{ent}}$. Note that these results are for $\vec{\delta}_A = 0$, where the formation of the steady state is the slowest [see Fig. 4.5(c)]. Thus, these results represent approximate upper bounds for $N_{\mathrm{ent}}$ and also for all other classes of multipartite entangled states. For a more complete and detailed analysis of the protocol, we provide some additional numerical results on the dependence of $N_{\mathrm{ent}}$ on the squeezing strength and on the influence of waveguide losses and imperfect chiral couplings. In Fig. 4.7 (a), we plot $N_{\mathrm{ent}}$ as a function of $\beta = \kappa/\gamma$ for a small squeezing parameter of $r = 1.0$. In Fig. 4.7 (b) we fix the value of $\beta = 30$ and plot $N_{\mathrm{ent}}$ as a function of $r$. The decay of entanglement along the chain for smaller $r$ is much slower and also more robust with respect to qubit dephasing. Even for negligible dephasing, we observe how the number of possible entangled pairs decrease as we increase the squeezing strength $r$, indicating how fragile the states become as we increase its entanglement. On the other hand, working in a weak squeezing environment, while it would allow the creation of larger networks in close-to-ideal situations, one must take in mind that also the amount of entanglement present would be weak. In this scenario, where one is distributing a small amount of entanglement along a large network, one could think of purification protocols to increase the amount of entanglement on the smallest section. In general, this plot shows the expected trade-off between a high degree of entanglement and the number of entangled pairs.

### 4.4.2 Waveguide losses

To scale our protocol, we have begun considering finite bandwidth effects and non-negligible dephasing noise. In Fig. 4.8, we analyze a chain of $N_{\mathrm{q}} = 4$ qubit pairs and simulate the effect of waveguide losses. Although superconducting cryogenic links experience no losses due to their superconducting state, various components, such as circulators, do incur photon losses. To model this, we assume $\nu_{i,j}^n = \nu(i-j)$, meaning that a fixed loss

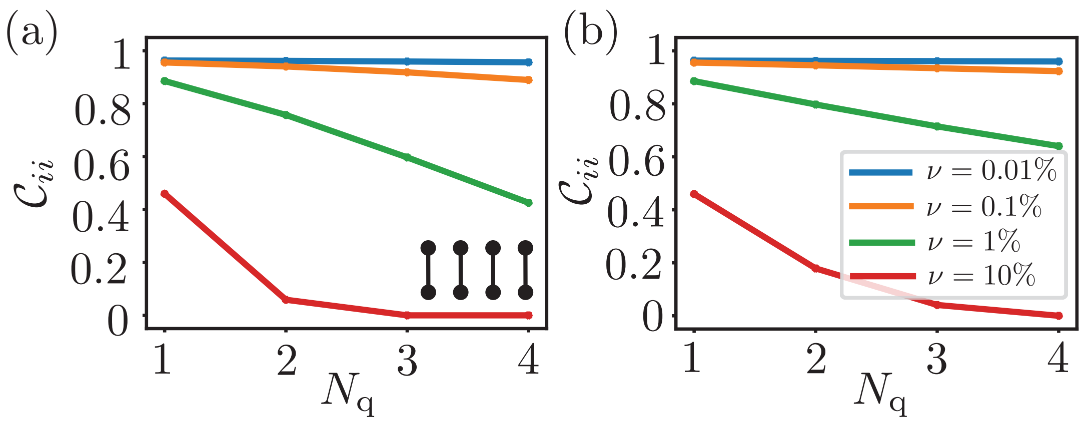


**Figure 4.8:** (a) Effect of finite propagation losses $\nu > 0$ on the steady-state entanglement for $N_\mathrm{q} = 4$ for (a) squeezing strength $r = 1$ and on resonance $\Delta = 0$, (b) for $r = 1$ and parallel configuration with detuning $\Delta = 2\gamma$. For all plots, $\nu^n_{i,j} = \nu|i - j|$ and $\beta \to \infty$ have been assumed.

probability $|\nu|$ exists between successive nodes of the network. In Fig. 4.8, we observe the detrimental effect of the losses. For small values of $\nu$, this plot predicts an approximately linear decay of the entanglement along the waveguide. For larger values, the first qubit pair has already lost half of its entanglement due to source losses, and this decay becomes faster than linear along the chain.

### 4.4.3 Nonideal chiral coupling

Throughout this chapter, we have considered the waveguide to be completely directional; that is, all the photons propagate along the same direction. While this allows us to get analytical results, realizing such directional interactions will only be possible with a certain fidelity. Here, we present additional numerical results for waveguides; the qubits along the waveguides can decay into left-propagating modes with rate $\gamma_L$ and into right-propagating modes with rate $\gamma_R$. The main results are then recovered when $\gamma_L = 0$ and $\gamma_R = \gamma$. To extend our model to a bidirectional waveguide, we include the effect of an additional left-propagating channel into our effective qubit master equation (see, e.g., Ref. [150]). We obtain

$$\dot{\rho}_\mathrm{q} = -i[\hat{H}_\mathrm{chiral}, \rho_\mathrm{q}] + \sum_{n=A,B} \gamma_R \mathcal{D}[\hat{J}_n]\rho_\mathrm{q} + \sum_{n=A,B} \gamma_L \mathcal{D}[\hat{L}_n]\rho_\mathrm{q}. \tag{4.25}$$

The new modes contribute to both the coherent and incoherent interaction. The coherent interaction now depends on the difference between left- and right-modes and vanishes at a completely bidirectional waveguide,

$$\hat{H}_\mathrm{chiral} = \frac{i(\gamma_R - \gamma_L)}{2} \sum_{n=A,B} \sum_{j>i} (\hat{\sigma}^+_{n,i}\hat{\sigma}^-_{n,j} - \mathrm{h.c}). \tag{4.26}$$

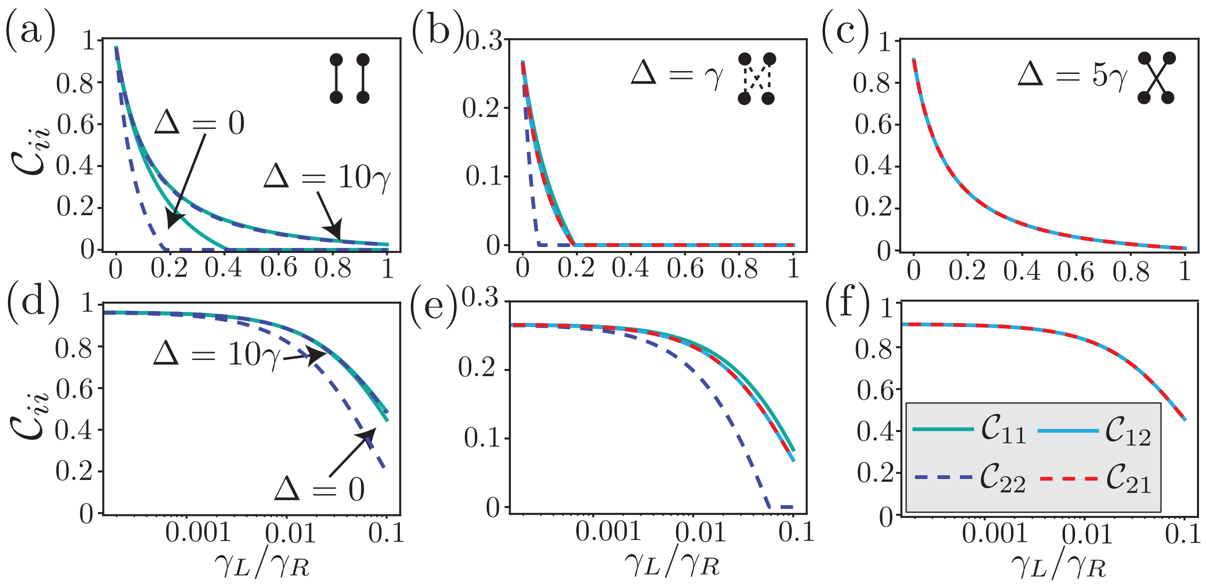


**Figure 4.9:** Plot of the bipartite concurrence of the steady state of the master equation in Eq. (4.25), which includes a decay into left-propagating waveguide modes with rate $\gamma_L$. The plots in (a) and (d) assume parallel detunings with $\vec{\delta_B} = -\vec{\delta_A}$ and $\delta_{A,i} = \Delta(i-1)$, while the plots in (b), (c), (e) and (f) assume a reversed detuning pattern $\vec{\delta_B} = -P_{\text{rev}}\vec{\delta_A}$. In all plots $r = 1$.

For the incoherent term, we have assumed that the left-propagating modes decay into vacuum modes with a collective jump operator $\hat{L}_n = \sum_{i=1}^{N_\text{q}} \hat{\sigma}_{n,i}$. Therefore, only the right-propagating modes are squeezed and correlated. Note that this form also assumes that the qubits are spaced by multiples of the central wavelength, such that all propagation phases cancel.

In Fig. 4.9, we numerically solve this master equation for different degrees of chirality, $\gamma_L/\gamma_R$. We observe that the effect of a finite $\gamma_L$ on the resulting steady state depends a lot on the type of entanglement, which in turn is determined by the detunings. While multipartite entangled states are strongly affected by a finite bidirectional coupling, bipartite entangled states are more robust, and in the far-detuned regime, a finite amount of entanglement survives up to $\gamma_L/\gamma_R = 1$.

### 4.4.4 Far-detuned qubits protocol

In Sec. 4.3, we observed a time speedup for far-detuned qubits. We now consider the effects of a finite-bandwidth amplifier. In Fig. 4.10(a), we first investigate the dependence of $\mathcal{C}_{11}$ on the detuning $\delta_{A,1} = \Delta/\kappa$. As expected, this plot shows a significant decay of the entanglement for $\Delta/\kappa > 1$, from which we also deduce that $\delta_{\max} < \kappa$ must be satisfied in the multi-qubit case. Since, for a parallel preparation with $T_{\text{prep}}(N) \sim$ const., we require $\delta_{\max} \approx \gamma N_\text{q}$, we conclude that the number of pairs that can be entangled in parallel, $N_{\|} \approx N_{\text{ent}}$, is comparable to the total number of entangled pairs for $\vec{\delta_A} = 0$. As a minimal illustration of this behaviour, we consider in Fig. 4.10(b) the example of $N_\text{q} = 4$ pairs with

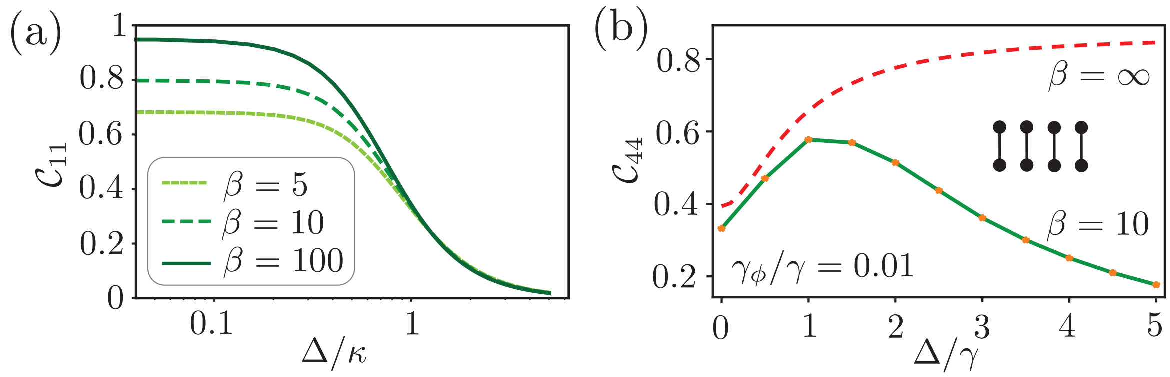


**Figure 4.10:** a) Dependence of the concurrence of a single qubit pair on the detuning $\Delta$, where $\delta_{A,1} = -\delta_{B,1} = \Delta$ and different values of $\beta$ have been assumed. (b) Plot of the concurrence $\mathcal{C}_{44}$ in a chain of $N_\mathrm{q} = 4$ qubit pairs with $\delta_{A,i} = (i-1)\Delta = -\delta_{B,i}$ and a finite dephasing rate. In all plots, $r = 1$.

$\delta_{A,i} = \Delta(i-1)$. We plot the concurrence of the last pair, $\mathcal{C}_{44}$, for a fixed dephasing rate $\gamma_\phi$ and increasing detuning $\Delta$. Up to $\Delta \sim \kappa$, entanglement increases due to a reduced preparation time, while for larger detunings finite-bandwidth effects set in and degrade the entanglement again. We observe that the initial gain from a parallel preparation when $\Delta > 0$, while the entanglement decreases again when $\delta_\mathrm{max} = (N_\mathrm{q}-1)\Delta \approx \kappa$, due to finite bandwidth effects. Note that for a parametric amplifier with asymmetric decay rates, $\kappa_A \neq \kappa_B$, the structure of the ideal qubit master equation in Eq. (4.1) remains the same, but finite-bandwidth effects are determined by the minimal rate $\kappa_\mathrm{min} = \min\{\kappa_A, \kappa_B\}$.

## 4.4.5 Entanglement purification

As we have seen throughout the previous section, entanglement distribution is fragile. As we increase the squeezing strength to stabilize a highly entangled state, it becomes more susceptible to imperfections, such as coupling inefficiencies or dephasing noise. In view of this, it might be more favorable to create a larger network of wealy entangled states and *sacrifice* some of them to boost the entanglement at the remaining qubit pairs. Here, we describe the application of an entanglement purification protocol, the DEJMPS protocol [50], to distill highly entangled states.

First, we give a general introduction to the protocol. For that, consider two identical qubit pairs $N_\mathrm{q} = 2$, given by the joint state $\rho = \rho_1 \otimes \rho_2$. To make a connection to our setup, each $\rho_{i=1,2}$ is a two-qubit state between waveguide $A$ and waveguide $B$. We then assume each qubit state has the following decomposition

$$\rho_{i=1,2} = A|\Phi^+\rangle\langle\Phi^+| + B|\Phi^-\rangle\langle\Phi^-| + C|\Psi^+\rangle\langle\Psi^+| + D|\Psi^-\rangle\langle\Psi^-|, \tag{4.27}$$

where $A+B+C+D = 1$ and $A > B \geq C \geq D$. The DEJMPS protocol works as follows:

1) Select one of the qubit pairs, $\rho_1$, for which to distill entanglement.

2) Perform $R_x(\pi/2)$ rotations both qubits at waveguide $A$, and $R_x(-\pi/2)$ on both qubits at waveguide $B$.

3) We perform two CNOT gates, one at each waveguide, between each qubit. We decided to keep $\rho_1$, so $\rho_1$ forms the control qubits, while $\rho_2$ are the target qubits.

4) The target qubits on both waveguides are measured, and their measurement results are exchanged.

5) If both measurements coincide, the protocol is successful, and the first qubit pair $\rho_1$ has been distilled. If their measurements are different, the protocol has failed, and both qubit pairs are discarded.

The successful purification probability for this protocol is given by

$$p_{\text{succ.}} = (A+D)^2 + (B+C)^2, \tag{4.28}$$

and after the successful purification, the state after the protocol has a fidelity given by

$$\mathcal{F}_{\text{succ.}} = \frac{A^2 + D^2}{p_{\text{succ.}}}, \tag{4.29}$$

which is higher than the initial fidelity $\mathcal{F}_0 = A$. Our protocol then offers the perfect scenario for the application of this purification protocol. Assume we are on resonance $\vec{\delta}_A = 0$. In this case, our steady state is given by Eq. (4.21), which is a sequence of independent Bell-like states. Specifically for $N_\text{q} = 2$, the state is

$$|\psi_0\rangle = \bigotimes_i^2 \frac{\left(\cosh{(r)}|00\rangle_{i,i} + \sinh{(r)}|11\rangle_{i,i}\right)^i}{\left(\cosh{(2r)}\right)^{i/2}}, \tag{4.30}$$

with occupation number $N = \sinh^2{(r)}$. Given our initial state, the density matrix decomposition given by Eq. (4.27) is

$$A = |\langle\Phi^+|\psi_0\rangle_i|^2 = \frac{1}{2}\left(1 + \tanh{(2r)}\right), \tag{4.31a}$$
$$B = |\langle\Phi^-|\psi_0\rangle_i|^2 = \frac{1}{2}\left(1 - \tanh{(2r)}\right), \tag{4.31b}$$
$$C = |\langle\Psi^+|\psi_0\rangle_i|^2 = 0, \tag{4.31c}$$
$$D = |\langle\Psi^-|\psi_0\rangle_i|^2 = 0. \tag{4.31d}$$

As required, they fulfill $A + B + C + D = 1$. Evaluating Eq. (4.28) with our coefficients, we obtain

$$p_{\text{succ.}} = 1 - \frac{\operatorname{sech}^2{(2r)}}{2}. \tag{4.32}$$

Then, if the protocol is successful, the remaining state's fidelity is boosted to

$$\mathcal{F}_{\text{succ.}} = \frac{1}{2}\left(1 + \tanh{(4r)}\right). \tag{4.33}$$

Observe how when $r = 0$, $A = p_{\text{succ.}} = \mathcal{F}_{\text{succ.}} = 1/2$. However, for $r > 0$, this protocol always gives a higher entangled state. Starting from relatively high squeezing strength $r = 1$, the initial fidelity is already right, $A = 0.982$, for which the purified state would reach a fidelity of $\mathcal{F}_{\text{succ.}} = 0.999$ with probability $p_{\text{succ.}} = 0.964$. Considering a more realistic squeezing of $r = 0.35$ ($\mathcal{S} = 3\,\text{dB}$), the initial fidelity is $A = 0.80$, from which we can distill $\mathcal{F}_{\text{succ.}} = 0.94$ with probability $p_{\text{succ.}} = 0.68$.

## 4.5 Stochastic master equation

Investigating multi-qubit quantum networks for the case of a finite-bandwidth parametric amplifier places a huge burden on the numerical simulations, as in solving Eq. (4.4), the Hilbert space now also needs to take into account $n = 2$ bosonic modes. To mitigate this scaling problem, we take advantage of the stochastic master equation described in Sec. 2.5.3. First, we map the bosonic modes from the parametric amplifier $\hat{a}_A$ and $\hat{a}_B$ to complex-valued stochastic variables using the positive-P representation described in Sec. 2.5.2. Thus, our parametric amplifier is characterized by 4 complex-valued variables $\{\alpha_A, \beta_A, \alpha_B, \beta_B\}$, which are governed by Eq. (2.130), and are used to drive the qubits along the waveguide, as show in Fig. 4.11(a).

Therefore, we can map our original master equation to a stochastic master equation for the qubit system that looks like

$$\dot{\rho}_{\text{q}}(\boldsymbol{\alpha}, \boldsymbol{\beta}, t) = \left(\mathcal{L}_{\text{q}} + \mathcal{L}_{\text{s}}(\boldsymbol{\alpha}, \boldsymbol{\beta})\right) \rho_{\text{q}}(\boldsymbol{\alpha}, \boldsymbol{\beta}, t), \tag{4.34}$$

with a stochastic term given by

$$\mathcal{L}_{\text{s}}(\boldsymbol{\alpha}, \boldsymbol{\beta})\rho_{\text{q}} = \sum_{n=A,B} \sqrt{\kappa\gamma} \left( [\beta_n(t)\hat{L}_n - \alpha_n(t)\hat{L}_n^\dagger, \rho_{\text{q}}] \right). \tag{4.35}$$

Here, we have defined $\boldsymbol{\alpha} = (\alpha_A, \alpha_B)$, $\boldsymbol{\beta} = (\beta_A, \beta_B)$, and we have $\hat{L}_n = \sum_i \hat{\sigma}_{n,i}^-$. The dynamics of the reduced qubit master equation are recovered by taking the statistical average of this equation $\rho_{\text{q}}(t) = \langle \rho_{\text{q}}(\boldsymbol{\alpha}, \boldsymbol{\beta}, t) \rangle$ over a finite amount of trajectories $M_{\text{traj}}$. In Fig. 4.11(b), we plot the time evolution of the concurrence $\mathcal{C}_{ij}$ for a system formed by $N_{\text{q}} = 2$ and compare it with the solution from Eq. (4.4). We observe a perfect agreement between both models due to the large averaging of the stochastic master equation.

In general, this stochastic master equation provides the advantage of mapping an infinite Hilbert space into complex-valued variables at the expense of stochastic averaging. This allows us to explore the parameter regime of strongly driven qubits. In this case, the noise fluctuations also grow, which requires further averaging. We found that, in general, the positive-P representation needs much more averaging trajectories than the P representation we employ in Chapter 5.

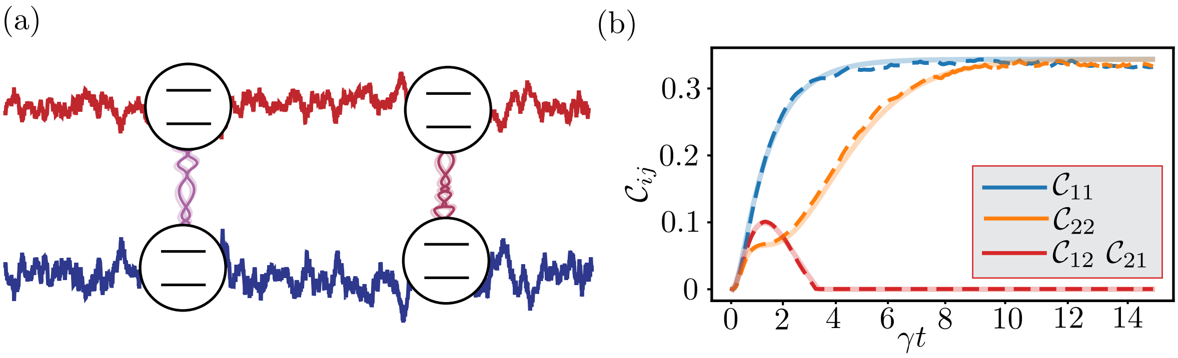


**Figure 4.11:** (a) Schematic of 4 qubits driven by a classical correlated field. (b) Comparison of the time evolution of the concurrence $\mathcal{C}_{ij}$ for $N_{\mathrm{q}} = 2$ using the stochastic master equation in Eq. (4.34) (dashed) and the original master equation in Eq. (4.4)(faded solid). We have assumed the following parameters: $\delta_A = \delta_B = 0$, $\epsilon = 0.1$, $\kappa = 10$, $\gamma = 1$, and the stochastic averaging is over $M_{\mathrm{traj}} = 50000$ with $\mathrm{d}t = 0.05$.

## 4.6 Microwave quantum networks

To illustrate the performance of this protocol in a realistic setup, where all types of imperfections are taken into account, we consider in this subsection the example of superconducting qubits connected via microwave transmission lines.

As a starting point, we use the parameters from a recent work by Joshi *et al.* [161], which describes the realization of a chiral coupling of a superconducting qubit to a microwave waveguide. From this reference, we deduce a qubit dephasing rate of $\gamma_\phi/2\pi = 50$ kHz (in accordance with other state-of-the-art experiments [160]), a directional emission rate of $\gamma_R/2\pi \simeq 1$ MHz and an unwanted decay into the opposite direction with rate $\gamma_L/\gamma_R \simeq 0.01$. In addition, in this experiment, there is a residual decay into non-guided modes with a rate $\gamma'/2\pi = 364$ kHz. In our numerical simulations, we include this process by adding a new term $\gamma' \sum_{n,i} \mathcal{D}[\hat{\sigma}^-_{n,i}]\rho$ to our master equation. For these parameters, $\Delta = 0$ and assuming an ideal two-mode squeezing source with $r = 1$, we obtain $N_{\mathrm{ent}} \simeq 1$ and the concurrence of the first pair is $\mathcal{C}_{11} \simeq 0.1$. Obviously, this poor result is mainly related to the large residual decay rate $\gamma'$. By assuming that this decay channel can be eliminated in future setups, $\gamma' \to 0$ [196], the result improves to $N_{\mathrm{ent}} \simeq 2$ and $\mathcal{C}_{11} \simeq 0.53$, now being primarily limited by decoherence with rate $\gamma_\phi/\gamma \simeq 0.05$.

Let us now consider the same parameters, but assume the finite detunings $\delta_A = (i-1)\Delta$ with $\Delta = \gamma_R$. Consistent with Fig. 4.10(b), we find that while keeping $\mathcal{C}_{11} \simeq 0.53$, this modification would already boost the total number of entangled pairs to about $N_{\mathrm{ent}} \simeq 20$ (assuming $\gamma' = 0$). Further, by improving the ratio $\gamma_\phi/\gamma_R$ by a factor of ten (which is well within the range of typical qubit coherence times) would boost this number to about $N_{\mathrm{ent}} \simeq 120$ (with $\Delta = \gamma_R$) and $N_{\mathrm{ent}} \simeq 6$ (with $\Delta = 0$) and with $C_{11} \simeq 0.85$. At this stage, the effects of a finite rate $\gamma_L$ become relevant.

Let us now address the effect of a finite amplifier bandwidth. In the microwave regime, two-mode squeezing sources are usually realized with Josephson parametric amplifiers (JPAs) or travelling wave parametric amplifiers (TWPAs). Typical bandwidths for these devices are $\kappa_{\rm JPA} \simeq 2\pi \times 10$ MHz [22] and $\kappa_{\rm TWPA} \simeq 2\pi \times 1$ GHz [197, 198]. Combining the parameters from above with the JPA, the relevant ratio between the amplifier bandwidth and the qubit decay rate is $\beta_{\rm JPA} = \kappa_{\rm JPA}/\gamma_R \simeq 10$. In this case, the finite bandwidth does not change the conclusion from above for $\Delta = 0$, and we obtain $N_{\rm ent} \simeq 2$ with $C_{11} = 0.45$ for $\gamma' = 0$. For $\Delta = \gamma_R$ our extrapolation predicts $N_{\rm ent} \approx 50$, but since we must limit the maximum detuning to $\delta_{\rm max} < \kappa$, the limit in this example is set by $N_{\rm ent} \approx \beta \simeq 10$.

To go beyond this limit, we can use a TWPA. In this case, the bandwidth ratio can reach values up to $\beta_{\rm TWPA} = \kappa_{\rm TWPA}/\gamma_R \simeq 10^3$ and all the results for $N_{\rm ent}$ and $\mathcal{C}_{11}$ reduce to the infinite-bandwidth results from above. Note, however, that this assumes an ideal amplifier without any added noise.

In summary, these estimates show that while the preparation of highly entangled multi-qubit states naturally requires sophisticated experimental setups, existing experimental techniques in the field of superconducting circuits are, in principle, already enough to demonstrate the simultaneous entanglement of $N_{\rm q} \approx 2 - 10$ qubit pairs or generate multipartite entanglement among $\sim 4 - 8$ separated qubits.

# Chapter 5

# Thermal entanglement distribution

In this chapter, we continue the investigation of a small effect that we only briefly pointed out in Sec. 4.4. There, in Fig. 4.6(b), we observed that below a certain bandwidth of the correlated photon source, entanglement was emerging between consecutive qubits along the same waveguide, in addition to the diagonal quantum correlations that appear in the diagonal-detuning configuration. To understand the emergence of these quantum correlations, in this chapter, we investigate a simpler but equivalent system in which we show that they are a direct consequence of the non-Markovianity of the photonic source. We start by introducing our system in Sec. 5.1 as well as the main theoretical techniques necessary to solve it. We apply those techniques in Sec. 5.2 and show both numerically and analytically the emergence of the quantum correlations. In Sec. 5.3, we develop an effective model to predict how much entanglement can be generated by our qubits, considering the bandwidth of the photon source. To get a better understanding of the photon source, in Sec. 5.4, we offer a detailed analysis in terms of the phase or amplitude of the photons. We end this chapter with Sec. 5.5 by offering two experimental implementations which can take advantage of the generation of entanglement with a source at room temperature.

## 5.1 A thermally driven quantum link

Consider a small quantum network as depicted in Fig. 5.1, where two spatially separated two-level systems (qubits) are coupled to a common bosonic quantum channel, for example, a photonic or phononic waveguide. At the beginning of the waveguide, we place a cavity, which we call the thermal/filter cavity. Each qubit has frequency $\omega_{\mathrm{q},i}$, and the cavity has a resonant frequency of $\omega_{\mathrm{c}} \sim \omega_{\mathrm{q},i}$. Assuming the waveguide is cascaded, we can use the results from Sec. 2.3.2 to derive an effective master equation for the system formed by the thermal cavity and the two qubits. As in the previous chapters, we assume that the waveguide is sufficiently cold, $T_0 \ll \hbar\omega_{\mathrm{q},i}/k_B$, to be in a vacuum state and has a linear dispersion relation. We then proceed with the simple identification between our system and Eq. (2.72) by assigning the first element as a cavity with bosonic mode $\hat{a}$, that is $\hat{c}_0 \equiv \hat{a}$ with decay rate $\gamma_0 = \kappa$. The two qubits's notation remains identical as in the

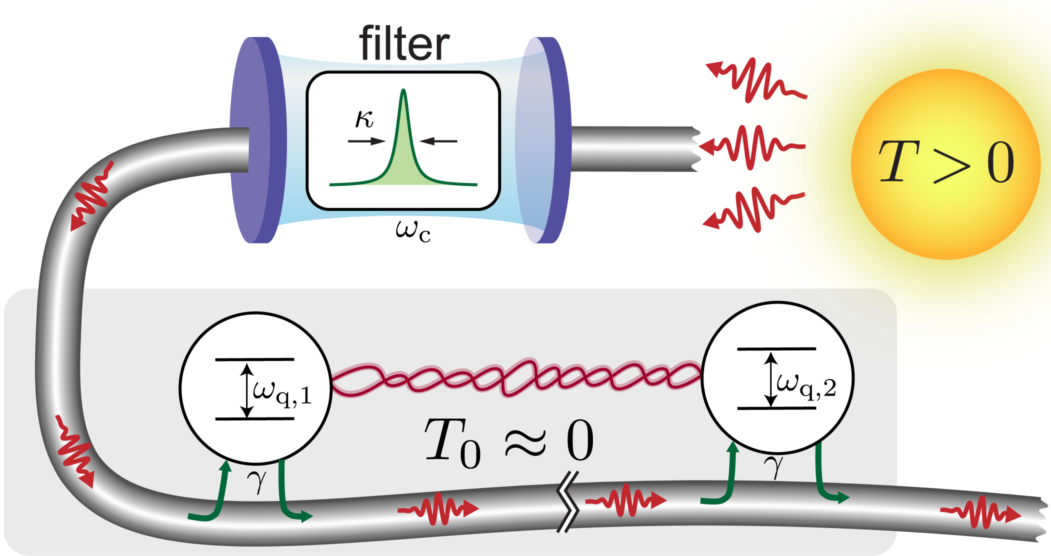


**Figure 5.1:** Schematic of the setup considered for the analysis in Chapter 5. Here, the source emits incoherent radiation at a high temperature $T$, which is successively filtered, and drives two or multiple qubits along the waveguide.

original derivation assigning the operator $\hat{c}_{1,2} = \hat{\sigma}^-_{1,2}$.

To generate excitations along the system, we connect the filter cavity to a thermal source. This can be implemented, for example, if our filter cavity is a two-sided filter cavity which separates a region of high temperature $T \gg T_0$ from the low-temperature quantum channel. To model this, we can assume that the filter cavity is coupled to another waveguide, or just any reservoir, at temperature $T > 0$ with decay rate $\kappa_{\text{hot}}$. For simplicity, we assume a symmetric two-sided cavity, with identical decay to the hot and the cold waveguides $\kappa_{\text{hot}} = \kappa$. In this case symmetric case, the qubits are driven with an average photon flux $\Phi = \kappa n_{\text{th}}/2$, where $n_{\text{th}} = (e^{\hbar\omega_c/(k_B T)} - 1)^{-1}$.

Therefore, we obtain a master equation for the density operator $\rho$, which describes the state of the qubits and the thermal source. This master equation is then of the form

$$\dot{\rho} = (\mathcal{L}_{\text{th}} + \mathcal{L}_{\text{q}} + \mathcal{L}_{\text{int}})\rho, \tag{5.1}$$

where the individual terms describe the dynamics of the thermal source, the bare evolution of the individual qubits and the waveguide-mediated interactions, respectively.

The thermal cavity, described in Sec. 2.2.1, needs to be modified to account for the two reservoirs. By changing into a frame rotating with frequency $\omega_c$, the dynamics of the thermal cavity is purely incoherent and described by the Liouville operator

$$\mathcal{L}_{\text{th}}\rho = \underbrace{\kappa(n_{\text{th}} + 1)\mathcal{D}[\hat{a}]\rho + \kappa n_{\text{th}}\mathcal{D}[\hat{a}^\dagger]\rho}_{T>0} + \underbrace{\kappa\mathcal{D}[\hat{a}]\rho}_{T=0}. \tag{5.2}$$

In the same frame, the bare dynamics of the qubits is given by

$$\mathcal{L}_{\mathrm{q}}\rho = -i[\hat{H}_{\mathrm{q}}, \rho] + \sum_i \gamma_i \mathcal{D}[\hat{\sigma}_i^-]\rho, \tag{5.3}$$

where $\hat{H}_{\mathrm{q}} = \delta_1\hat{\sigma}_1^z/2 + \delta_2\hat{\sigma}_2^z/2$, and $\delta_i = \omega_{\mathrm{q},i} - \omega_{\mathrm{c}}$ denote the detunings of the qubits from the cavity frequency. Finally, the unidirectional waveguide mediates a cascaded interaction between the cavity and the two qubits, which can be modelled as

$$\mathcal{L}_{\mathrm{int}}\rho = \sum_i \sqrt{\nu_{0,i}\gamma_i\kappa}\left([\hat{a}\rho, \hat{\sigma}_i^+] + [\hat{\sigma}_i^-, \rho\hat{a}^\dagger]\right) + \sqrt{\nu_{1,2}\gamma_1\gamma_2}\left([\hat{\sigma}_1^-\rho, \hat{\sigma}_2^+] + [\hat{\sigma}_2^-, \rho\hat{\sigma}_1^+]\right). \tag{5.4}$$

Here, as with our previous analysis in Chapter 3 and Chapter 4, we have included a coupling constant $\nu_{i,j}$ such that $|1-\nu_{i,j}|$ is the probability that a photon emitted by $i$ is lost before reaches $j$. In our initial theoretical analysis, we assume $\nu_{i,j} = 1$. In Sec. 5.5, when we investigate the protocol's performance under experimental conditions, we will again take the coupling inefficiencies into consideration.

In our analysis below, we are primarily interested in the case $\gamma_1 \simeq \gamma_2 = \gamma$, where it is more convenient to regroup the cascaded interaction in Eq. (5.4) in terms of a collective dissipation term with jump operator $\hat{L} = \hat{\sigma}_1^- + \hat{\sigma}_2^-$ and a purely coherent term with Hamiltonian

$$\hat{H}_{\mathrm{casc}} = \frac{i\gamma}{2}(\hat{\sigma}_1^+\hat{\sigma}_2^- - \hat{\sigma}_1^-\hat{\sigma}_2^+). \tag{5.5}$$

In this way, the full master equation in Eq. (5.1) can be rewritten in the form

$$\dot{\rho} = (\mathcal{L}_{\mathrm{th}} + \mathcal{L}_{\mathrm{sys}} + \mathcal{L}_{\mathrm{int}})\rho, \tag{5.6}$$

where

$$\mathcal{L}_{\mathrm{sys}}\rho = -i[\hat{H}_{\mathrm{q}} + \hat{H}_{\mathrm{casc}}, \rho] + \gamma\mathcal{D}[\hat{L}]\rho, \tag{5.7}$$

describes the dissipative dynamics of the qubit system, while

$$\mathcal{L}_{\mathrm{int}}\rho = \sqrt{\gamma\kappa}\left([\hat{a}\rho, \hat{L}^\dagger] + [\hat{L}, \rho\hat{a}^\dagger]\right), \tag{5.8}$$

accounts for the effect of the thermal driving field.

In this configuration, the two qubits can be best represented in a triplet-singlet basis, as depicted in Fig. 5.2(a). Here the triplet state $|T\rangle = (|01\rangle + |10\rangle)/\sqrt{2}$ and the fully excited state $|11\rangle$ decay via a collective emission into the waveguide, while the singlet state $|S\rangle = (|01\rangle - |10\rangle)/\sqrt{2}$ is a dark state of the collective jump operator, $\hat{L}|S\rangle = 0$. However, the singlet is coupled to the triplet state via the Hamiltonian $\hat{H}_{\mathrm{casc}}$ and eventually decays, which reflects that in a unidirectionally coupled system, there is no complete destructive interference. The thermal source, which also drives the qubits symmetrically, induces transitions between the ground state $|00\rangle$ and the states $|T\rangle$ and $|11\rangle$, while again

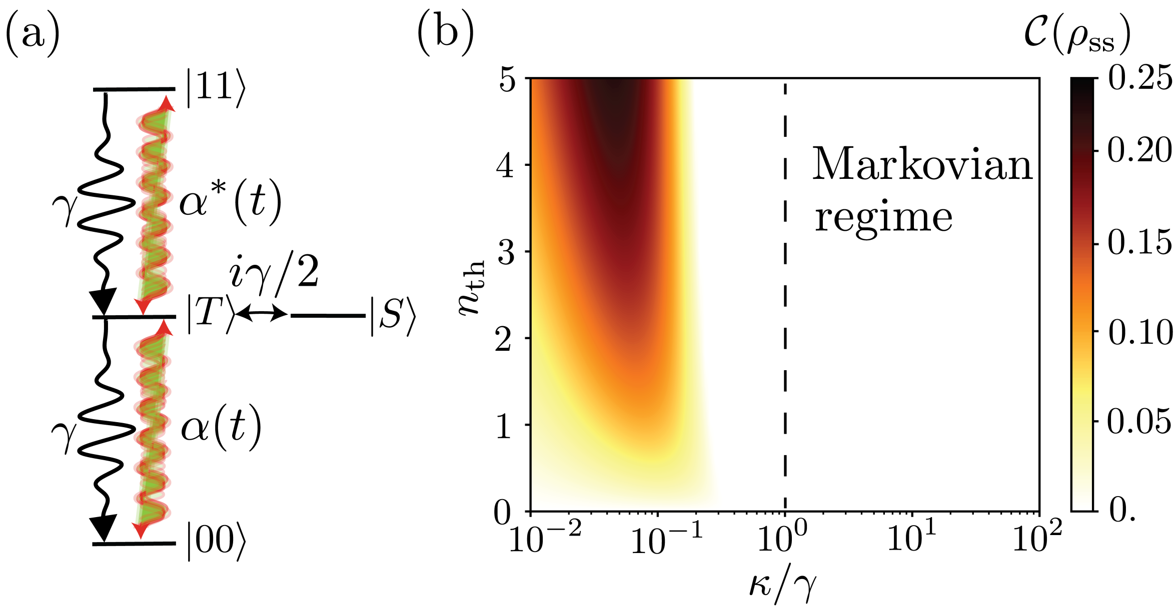


**Figure 5.2:** a) Schematic representation of the symmetric coupling basis. b) Entanglement between the two-qubis measured using the steady-state concurrence of the reduced qubit state $\mathcal{C}(\rho_{\rm ss})$ evaluating Eq. (5.6) numerically for different values of $\kappa/\gamma$ and $n_{\rm th}$.

the singlet state remains decoupled. Observe how those states are also the Bell states introduced in Eq. (2.8) with the identification $|S\rangle = |\Psi^+\rangle$ and $|T\rangle = |\Psi^-\rangle$. Therefore, stabilising our state into the singlet or the triplet is a stabilization into a highly entangled state.

### 5.1.1 Markovian master equation

In the derivation of the network master equation in Eq. (5.1), we have assumed that the waveguide connecting the source and the qubits is sufficiently broadband, and we used a Markov approximation to eliminate its dynamics. However, in this approach, we still retain the exact dynamics of the source, which evolves on a timescale set by $\kappa^{-1}$. By making the additional assumption $\kappa \gg \gamma$, we can also treat the thermal cavity as an effective Markovian reservoir and derive a master equation for the reduced two-qubit state $\rho_{\rm q}(t) = {\rm Tr}_{\rm th}\{\rho(t)\}$ [see Appendix A for more details]. This master equation reads

$$\dot{\rho}_{\rm q} = -i[\hat{H}_{\rm q} + \hat{H}_{\rm casc}, \rho_{\rm q}] + \gamma(n_{\rm th}+1)\mathcal{D}[\hat{L}]\rho_{\rm q} + \gamma n_{\rm th}\mathcal{D}[\hat{L}^\dagger]\rho_{\rm q}, \tag{5.9}$$

and describes the case of two qubits coupled to a (unidirectional) thermal quantum channel.

### 5.1.2 Stochastic master equation

While for moderate temperatures with $n_{\rm th} \sim O(10)$ the dynamics and steady states of Eq. (5.6) can still be evaluated numerically in a straightforward manner, this is no longer possible for much larger thermal occupation numbers, where a representation of the cavity state in terms of number states becomes very inefficient. To treat this high-temperature limit, it is more convenient to switch to a phase-space representation as we described in Sec. 2.5. In particular, we derived the Fokker-Planck equation in Eq. (2.118) and its associated stochastic differential equation in Eq. (2.121). Here, to take into account that our resonator is two-sided and that we are on resonance, we modify the Fokker-Planck equation to

$$L(\alpha,\alpha^*) = \kappa \left[ \frac{\partial}{\partial\alpha}\alpha + \frac{\partial}{\partial\alpha^*}\alpha^* + n_{\rm th}\frac{\partial^2}{\partial\alpha\partial\alpha^*} \right], \tag{5.10}$$

as well as its associated differential equation

$$\mathrm{d}\alpha = -\kappa\alpha\mathrm{d}t + \sqrt{\kappa n_{\rm th}}\mathrm{d}W(t), \tag{5.11}$$

where to take into account the two-sided cavity, we change the drift term $\kappa \to 2\kappa$. This also modifies the steady-state distribution to

$$P_{\rm ss}(\alpha,\alpha^*) = \frac{1}{\pi n_{\rm th}} e^{-|\alpha|^2/n_{\rm th}}. \tag{5.12}$$

After these changes, we can now transform our original master equation in Eq. (5.6) into a stochastic master equation as we did in Sec. (2.5.3). In our case, the resulting state $\rho(\alpha,\alpha^*,t)$ obeys the (stochastic) master equation

$$\dot{\rho}_{\rm q}(\alpha,\alpha^*,t) = \mathcal{L}(\alpha,\alpha^*)\rho_{\rm q}(\alpha,\alpha^*,t). \tag{5.13}$$

Here, we have introduced a new stochastic Liouvillian

$$\mathcal{L}(\alpha,\alpha^*)\rho_{\rm q} = -i[\hat{H}(\alpha,\alpha^*),\rho_{\rm q}] + \gamma\mathcal{D}[\hat{L}]\rho_{\rm q}, \tag{5.14}$$

which is governed by a stochastic Hamiltonian

$$\hat{H}(\alpha,\alpha^*) = \hat{H}_{\rm q} + \hat{H}_{\rm casc} + i\sqrt{\kappa\gamma}\left(\alpha^*\hat{L} - \alpha\hat{L}^\dagger\right). \tag{5.15}$$

Alternatively, we can express our stochastic master equation as

$$\dot{\rho}_{\rm q}(\alpha,\alpha^*,t) = \left(\mathcal{L}_0 + \alpha\mathcal{L}_+ + \alpha^*\mathcal{L}_-\right)\rho_{\rm q}(\alpha,\alpha^*,t), \tag{5.16}$$

where we split the Liouvillian into two contributions: a deterministic term $\mathcal{L}_0\rho$ and two stochastic terms given by $\mathcal{L}_+\rho = -\sqrt{\kappa\gamma}[\hat{L}^\dagger,\rho]$ and $\mathcal{L}_-\rho = \sqrt{\kappa\gamma}[\hat{L},\rho]$. The stochastic nature of this master equation comes from $\alpha$, as it appears as a fluctuating classical driving field. The actual qubit density operator can then be obtained by averaging over sufficiently many trajectories $\rho_{\mathrm{q}}(t) = \langle \rho_{\mathrm{q}}(\alpha, \alpha^*, t) \rangle$. This representation now only offers us the numerical advantage of solving the system at large thermal occupation numbers. As we will see in the next section, it also offers an intuitive understanding of the steady state in the slow-noise regime.

### 5.1.3 Continued fraction method

As mentioned, the reduced qubit state is obtained after the stochastic averaging after many trajectories. While this already offers an advantage with respect to the original master equation, the stochastic master equation also presents its disadvantages, namely that we still have to simulate a time-dependent stochastic differential equation for each parameter, which also requires an increasing number of samples as we increase the fluctuation strength $n_{\mathrm{th}}$.

Therefore, it would be more favorable to obtain an equation of motion for the deterministic reduced qubit state $\rho_{\mathrm{q}}(t) = \langle \rho_{\mathrm{q}}(\alpha, \alpha^*, t) \rangle$. In general, to find deterministic master equations from stochastic master equations is a challenging task [199]. However, since $\alpha(t)$ is described by a Fokker-Planck equation, given by Eq. (5.10), the averaged density matrix $\rho_{\mathrm{q}}(t)$ can be found by solving [200]

$$\left( \frac{\mathrm{d}}{\mathrm{d}t} + L(\alpha, \alpha^*) \right) \rho_{\mathrm{q}}(\alpha, \alpha^*, t) = \mathcal{L}(\alpha, \alpha^*) \rho_{\mathrm{q}}(\alpha, \alpha^*, t), \tag{5.17}$$

and then taking the average of the solution

$$\rho_{\mathrm{q}}(t) = \langle \rho_{\mathrm{q}}(\alpha, \alpha^*, t) \rangle = \int \mathrm{d}\alpha^2 \rho_{\mathrm{q}}(\alpha, \alpha^*, t). \tag{5.18}$$

The solution to Eq. (5.17) is obtained by expanding the solutions $\rho(\alpha, \alpha^*, t)$ in a complete biorthogonal set of eigenfunctions of $L(\alpha, \alpha^*)$ [201, 202]:

$$L(\alpha, \alpha^*) P_{m,n}(\alpha, \alpha^*) = \Lambda_{m,n} P_{m,n}(\alpha, \alpha^*), \tag{5.19}$$

$$L^\dagger(\alpha, \alpha^*) \phi_{m,n}(\alpha, \alpha^*) = \Lambda_{m,n}^* \phi_{m,n}(\alpha, \alpha^*), \tag{5.20}$$

for $n = 0, 1, 2, \ldots$ and $m = 0, \pm 1, \pm 2, \ldots$ The eigenvalues are $\Lambda_{m,n} = \kappa(2n + |m|)$ and the eigenfunction can be written as

$$P_{m,n}(\alpha, \alpha^*) = P_{\mathrm{ss}}(\alpha, \alpha^*) \phi_{m,n}(\alpha, \alpha^*), \tag{5.21}$$

where $P_{\rm ss}(\alpha,\alpha^*)$ is the steady-state distribution in Eq. (5.12) and

$$\phi_{m,n}(\alpha,\alpha^*) = \sqrt{\frac{n!}{(n+|m|)!}}\frac{|\alpha|^{|m|}}{(n_{\rm th}/2)^{|m|/2}}\left(\frac{\alpha^*}{\alpha}\right)^{m/2} L_n^{|m|}[x], \tag{5.22}$$

where $L_n^m[x]$, with $x = |\alpha|^2/(n_{\rm th}/2)$, are the generalized Laguerre polynomials. Using the orthogonality relation for this biorthogonal set [145]

$$\int {\rm d}\alpha^2 \phi^*_{m,n}(\alpha,\alpha^*)P_{m',n'}(\alpha,\alpha^*) = \delta_{n,n'}\delta_{m,m'}, \tag{5.23}$$

we can express our original state in this new basis as

$$\rho_{\rm q}(\alpha,\alpha^*,t) = \sum_{m,n} P_{m,n}(\alpha,\alpha^*)\rho^{m,n}(t), \tag{5.24}$$

where the coefficients are given by

$$\rho^{m,n}(t) = \int {\rm d}\alpha^2 \phi^*_{m,n}(\alpha,\alpha^*)\rho_{\rm q}(\alpha,\alpha^*,t) = \langle \phi^*_{m,n}(\alpha,\alpha^*)\rho_{\rm q}(\alpha,\alpha^*,t)\rangle. \tag{5.25}$$

From this coefficients, we observe that our averaged state $\rho_{\rm q}(t)$ is given by $\rho^{0,0}(t) = \langle \phi^*_{0,0}(\alpha,\alpha^*)\rho_{\rm q}(\alpha,\alpha^*,t)\rangle = \langle \rho_{\rm q}(\alpha,\alpha^*,t)\rangle$, as $\phi^*_{0,0}(\alpha,\alpha^*) = 1$.

The task is then to solve the equation of motion for $\rho^{0,0}(t)$. It turns out, however, that this leads to an infinite hierarchy of equations of motion for all the other coefficients $\rho^{m,n}(t)$. In Appendix C, we show that for our system under consideration, for the steady state, can truncate this hierarchy of equations of motion and reduce it to a matrix recursion

$$A_n\sigma^n + B_n\sigma^{n-1} + C_n\sigma^{n+1} = 0, \tag{5.26}$$

for $n = 0, 1, 2, ...$ Here, we have defined $\sigma^n = (\rho^{0,n}, \rho^{1,n}, \rho^{-1,n})^{\rm T}$ and the matrices $A_n$, $B_n$, and $C_n$ are defined in Eq. (C.12), Eq. (C.13), and Eq. (C.14) respectively. This matrix recursion can be solved in terms of a matrix continued fraction

$$\Big[A_0 + \mathcal{K}\Big]\sigma^0 = 0, \tag{5.27}$$

where the matrix continued fraction is given by

$$\mathcal{K} = C_0\cfrac{\mathcal{I}}{-A_1 - C_1\cfrac{\mathcal{I}}{-A_2 - C_2\cfrac{\mathcal{I}}{-A_3 - ...}B_3}B_2}B_1. \tag{5.28}$$

We can numerically solve this matrix continued fraction to obtain $\sigma^n$, from which we can obtain $\rho^{0,0}$, our physical state.

This method involves an infinite number of coupled equations. For numerical analysis, we truncate the expansion at $n_{\text{iter.}}$. In Fig. C.1, we show the convergence of the continued fraction method for different parameters, which we use to simulate it numerically without truncation errors.

The continued fraction method has previously been used to study the finite-bandwidth effect of a thermal source [203] and a single-mode parametric amplifier [179] in the context of a two-level system. In most cases, this method is employed for numerical solutions. Analytical results can be obtained by truncating the continued fraction expansion at first order, $n_{\text{iter.}} = 0$. As shown in Appendix C, this approximation is valid when fluctuations are either weak, $n_{\text{th}} \ll 1$, and/or fast, $\kappa \gg 1$. Our focus, however, is on the opposite parameter regime: strong and slow fluctuations. Nevertheless, we use the continued fraction method to numerically solve the qubit dynamics, and as we will see in Sec. 5.3, it also serves as the basis for an effective model.

## 5.2 Steady-State Entanglement

In the following, we are primarily interested in the stationary two-qubit state $\rho_{ss} = \text{Tr}_{\text{th}}\{\rho(t \to \infty)\}$. For this state, we quantify the amount of entanglement by the concurrence, as defined previously in Eq. (2.10). In Fig. 5.2(b) we use, first of all, exact numerical simulations of Eq. (5.6) to evaluate the steady-state entanglement, $\mathcal{C}(\rho_{ss})$, for different ratios of $\kappa/\gamma$ and moderate thermal occupation numbers $n_{\text{th}}$. We clearly see the absence of entanglement in the Markovian regime, $\kappa \gtrsim \gamma$, while finite entanglement in the steady state can be observed in the non-Markovian regime, where the bandwidth of the thermal source is much smaller than the qubit decay rate $\kappa < \gamma$. Surprisingly, the maximal amount of entanglement increases with the temperature of the source $n_{\text{th}}$.

We can now offer a partial connection to the phenomena observed in Fig. 4.6(b) from the last chapter. There, we observed the emergence of entanglement between consecutive and diagonal qubits below a certain bandwidth of the parametric amplifier, as we do here. While the system described in Chapter 4 and here might look different overall, this is no longer true if we trace out one of the waveguides. Indeed, as described in Sec. 2.2, tracing out one of the modes of the parametric amplifier gives an effective thermal state. So, effectively, if we look at one of the waveguides, what we have is a narrow bandwidth thermal state driving two qubits, which is precisely the same system considered here. Therefore, understanding the origin of the entanglement generated by a narrowband thermal source will allow us to understand the origin of the emergent entanglement from Fig. 4.6(b). There is, however, something we cannot answer fully here. That is, the emergence of entanglement between diagonal qubits. The reason is that our simple model here does not take into account two waveguides, so we can only study the serial generation of entanglement along the same waveguide.

### 5.2.1 Markovian regime

We start by obtaining an analytical confirmation that entanglement cannot emerge when the two qubits are driven by a Markovian thermal cavity. In this case, from Eq. (5.9) we can derive a closed set of equations for the steady-state matrix elements $\rho_{ij,kl} = \langle i,j|\rho_{\rm ss}|k,l\rangle$. We find that the only non-zero matrix elements are

$$\begin{aligned}\rho_{00} &= (n_{\rm th}+1)^2/(1+2n_{\rm th})^2,\\ \rho_T = \rho_S &= n_{\rm th}(n_{\rm th}+1)/(1+2n_{\rm th})^2,\\ \rho_{11} &= n_{\rm th}^2/(1+2n_{\rm th})^2,\end{aligned} \tag{5.29}$$

where we have defined the singlet and triplet populations $\rho_{S/T} = \langle S/T|\rho_{\rm q}|S/T\rangle$ and the simpler notation $\rho_{ii} \equiv \rho_{ii,ii}$ for the populations. We see that these matrix elements correspond to the separable state $\rho_{\rm ss} = \rho_{\rm th}\otimes\rho_{\rm th}$, where $\rho_{\rm th}$ corresponds to a qubit thermal state, which is equivalent to the one defined in Eq. (2.25) with the Hilbert space limited to $d = \dim(\mathcal{H}_{\rm q}) = 2$. This state describes two qubits in a thermal reservoir with no coherent interactions between them. One can calculate the amount of entanglement between the two qubits using the concurrence Eq. (2.10). Expectedly, one finds that $\mathcal{C}(\rho_{\rm ss}) = 0$ for $\forall n_{\rm th}$.

### 5.2.2 Quasi-adiabatic regime

To go beyond the Markovian regime, it is more convenient to switch to the phase-space representation introduced in Eq. (5.14). In this picture, the qubits are driven by a classical field $\alpha(t)$, which fluctuates on a timescale set by $\kappa^{-1}$. Therefore, in the limit $\kappa\to 0$ (while keeping $\kappa n_{\rm th}$ finite) we can assume that this field is approximately constant and evaluate the steady state of the qubit for a fixed amplitude $\alpha(t)\approx\alpha_0$. For this problem it is known that for $\delta_i = 0$ the steady state is a pure state, $\rho_{ss}(\alpha_0) = |\Psi(\alpha_0)\rangle\langle\Psi(\alpha_0)|$ [149, 150], where

$$|\Psi(\alpha_0)\rangle = \frac{\sqrt{\gamma}|00\rangle + 2\sqrt{2\kappa}\alpha_0|S\rangle}{\sqrt{\gamma+8\kappa|\alpha_0|^2}}. \tag{5.30}$$

This coherent superposition is a dark state of the collective jump operator, i.e. $\hat{L}|\Psi(\alpha_0)\rangle = 0$, while transitions to the triplet state $|T\rangle$ are cancelled by destructive inference between the driving term and the coupling induced by $\hat{H}_{\rm casc}$. To obtain the actual two-qubit steady state, the result from above must be averaged over a thermal distribution of amplitudes $\alpha_0$:

$$\rho_{\rm ss} = \frac{2}{\pi n_{\rm th}}\int {\rm d}^2\alpha_0 |\Psi(\alpha_0)\rangle\langle\Psi(\alpha_0)| e^{-\frac{2|\alpha_0|^2}{n_{\rm th}}}. \tag{5.31}$$

By reintroducing the flux parameter previously defined $\Phi = \kappa n_{\mathrm{th}}/2$, we obtain

$$\rho_{\mathrm{ss}} = \Upsilon(\Phi/\gamma)\rho_{00} + [1 - \Upsilon(\Phi/\gamma)]\,\rho_S, \tag{5.32}$$

where $\Upsilon(x) = e^{1/(8x)}\Gamma[0, 1/(8x)]/(8x)$ and $\Gamma[0, x]$ is the upper incomplete gamma function.

These analytic results obtained in the quasi-adiabatic limit clearly illustrate the main ingredients that lead to the emergence of entanglement out of a thermal reservoir. First of all, when the bandwidth of the source is sufficiently small, the thermal field can be considered static, and therefore coherent, over the time that it takes for the qubits to relax into a steady state. This facilitates interference effects, which, in the present setting, are responsible for the suppression of the triplet state. However, while being quasi-static it is important to keep in mind that the amplitude $\alpha_0$ has an undetermined phase and magnitude. Therefore, a second crucial feature of the state in Eq. (5.32) is that its degree of entanglement only depends on the population of the singlet state and not on the relative phase between $|00\rangle$ and $|S\rangle$.

Under the conditions considered here (symmetric coupling and no other imperfections), and due to averaging of the fluctuations, the concurrence $\mathcal{C}(\rho_{\mathrm{ss}})$ has the following simplified form

$$\mathcal{C}(\rho_{\mathrm{ss}}) = 1 - \Upsilon(\Phi/\gamma). \tag{5.33}$$

This shows that, even after averaging over the thermal distribution, the entanglement is finite and grows as $\mathcal{C}(\rho_{\mathrm{ss}}) \simeq 8\Phi/\gamma$ for small photon flux and it reaches a value of $\mathcal{C}(\rho_{\mathrm{ss}}) \simeq 1 - \gamma/(8\Phi)$ for a strong thermal source.

## 5.3 Beyond the static limit

The analytic approximations in the previous section explain the appearance of entanglement in the limit where the thermal driving field can be treated as a random but static field. There, the resulting amount of entanglement scales with $\Phi = \kappa n_{\mathrm{th}}/2$, but this result has been derived in the fully adiabatic limit $\kappa \to 0$. To understand the validity of this prediction, it is necessary to understand the non-static corrections that arise at a small, but finite value of $\kappa$.

To address this question, we extend, first of all, our numerical calculations to the high-temperature regime with thermal occupation numbers up to $n_{\mathrm{th}} = 10^6$, using the continued fraction simulation method outlined in Sec. 5.1.3. The resulting dependence of the steady-state entanglement on $n_{\mathrm{th}}$ is shown in Fig. 5.3(a) for different values of $\kappa/\gamma = 10^{-2}, 10^{-3}, 10^{-4}$ and compared to the analytic prediction of Eq. (5.32). We see indeed that for moderate values of $n_{\mathrm{th}}$, the concurrence follows the prediction of the static limit, but eventually, it deviates from this result and decreases again for very high thermal occupation numbers. The noise level at which the entanglement peaks and starts to reverse, $n_{\mathrm{th}}^{\star}$, depends on $\kappa$. The following section presents an analytical model to estimate

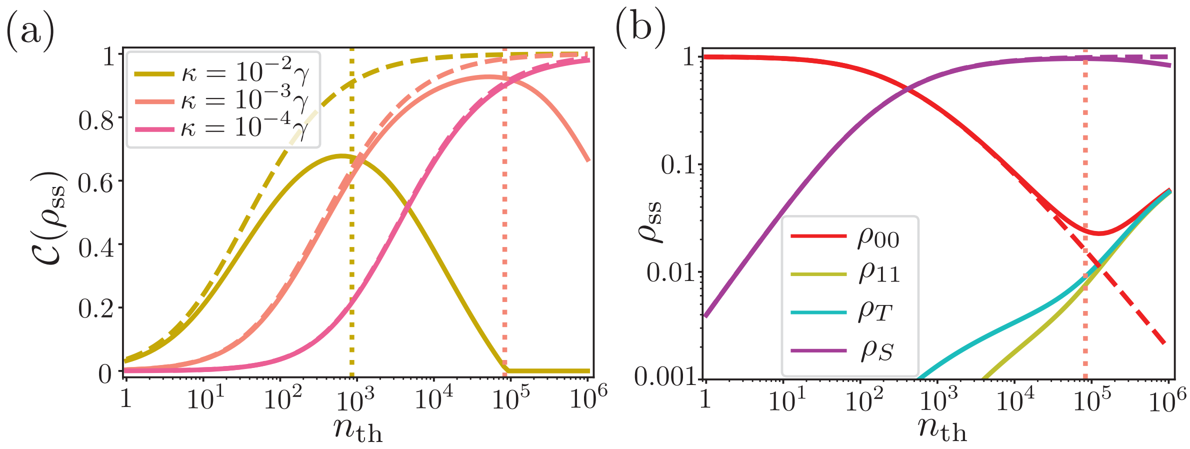


**Figure 5.3:** (a) Steady-state concurrence $\mathcal{C}(\rho_{ss})$ for different bandwidths $\kappa/\gamma$ as function of the thermal fluctuations strength $n_{th}$. (b) The population of the two-qubit state for $\kappa/\gamma = 10^{-3}$ as a function of the thermal fluctuations strength $n_{th}$. In both plots, the dashed lines always correspond to the static regime results from Eq. (5.32) and the vertical dotted line is the analytical expression for $n^{\star}_{th}$ in Eq. (5.44). In all these plots, $n_{iter.} = 50000$.

this parameter, shown as a vertical dotted line in Fig. 5.3.

In Fig. 5.3(b), we choose $\kappa/\gamma = 10^{-3}$ and plot the dependence of the two-qubit state populations as a function of $n_{th}$. For moderate $n_{th}$ only $\rho_{00}$ and $\rho_S$ are significantly different from zero and follow the prediction of Eq. (5.32). After some threshold, $n^{\star}_{th}$, the noise fluctuations are strong enough to kick us out of the quasi-static subspace. In this case, we start to populate the other states as $\rho_T$ and $\rho_{11}$. The static limit derived before does not capture this behaviour [see dashed line in Fig. 5.3(b)]. While this is reminiscent of the Markovian approximation (i.e. all populations are highly populated), we need to emphasise that we are in a completely different parameter regime, highly non-Markovian $\kappa \ll \gamma$. We will dedicate the following section to studying this behaviour and to estimating the strength $n_{th}$ where this happens.

### 5.3.1 Weak-noise approximation

We begin the analysis by considering the noise fluctuations to be weak, or equivalently, to work in a low flux regime $\Phi \ll 1$. This regime allows us to perform perturbation theory on Eq. (5.14) to derive a deterministic master equation.

Starting from our stochastic master equation from Eq. (5.16), we would like to solve for the averaged density matrix $\rho_q(t) = \langle \rho_q(\alpha, \alpha^*, t) \rangle$. To do that, we formally integrate this differential equation, iterate and take the average, obtaining [204]

$$\rho_q(t) = e^{\mathcal{L}_0 t}\rho_q(0) + \sum_{r=\pm} \int_0^t dt' e^{\mathcal{L}_0(t-t')}\mathcal{L}_r \langle \alpha^{(r)}(t') \int_0^{t'} dt'' e^{\mathcal{L}_0(t'-t'')}\mathcal{L}_r \alpha^{(r)}(t'')\rho_q(\alpha, \alpha^*, t'')\rangle, \tag{5.34}$$

where we have already used that $\langle \alpha(t) \rangle = 0$ and used the compact notation $\alpha^{(+)}(t) = \alpha(t)$ and $\alpha^{(-)}(t) = \alpha^*(t)$. We then differentiate Eq. (5.34) to obtain

$$\frac{\mathrm{d}}{\mathrm{d}t}\rho_{\mathrm{q}}(t) = \mathcal{L}_0\rho_{\mathrm{q}}(t) + \sum_{r=\pm}\int_0^t \mathrm{d}t' \mathcal{L}_r e^{\mathcal{L}_0(t-t')}\mathcal{L}_{-r}\langle \alpha(t)\alpha^*(t')\rangle \rho_{\mathrm{q}}(t'). \tag{5.35}$$

Here, we have used the *decorrelation*, or Bourret, approximation

$$\langle \alpha(t)\alpha^*(t')\rho_{\mathrm{q}}(\alpha,\alpha^*,t')\rangle \simeq \langle \alpha(t)\alpha^*(t')\rangle\langle \rho_{\mathrm{q}}(\alpha,\alpha^*,t')\rangle = \langle \alpha(t)\alpha^*(t')\rangle \rho_{\mathrm{q}}(t'). \tag{5.36}$$

The validity of this approximation requires either fast fluctuations $\kappa \gg 1$, i.e. to be in a Markovian-like reservoir, and/or small noise strength $n_{\mathrm{th}} \ll 1$. Specifically, the expansion parameter is $\frac{1}{\kappa}n_{\mathrm{th}}/2 = \phi/\kappa^2 \ll 1$, or, equivalently $\Phi \ll \kappa^2$.

Back to Eq. (5.35), notice that we have used that for the thermal noise, we have zero two-time correlations for $\langle \alpha(t)\alpha(t')\rangle = \langle \alpha^*(t)\alpha^*(t')\rangle = 0$ and that $\langle \alpha^*(t)\alpha(t')\rangle = \langle \alpha(t)\alpha^*(t')\rangle^*$. Using the two-time correlation derived in Eq. (2.86), which in this case reads, $\langle \alpha^*(t)\alpha(t')\rangle = n_{\mathrm{th}}/2e^{-\kappa|t-t'|}$, we can now solve Eq. (5.35) using the Laplace transform method, for which our differential equation is converted to

$$s\rho_{\mathrm{q}}(s) - \rho_{\mathrm{q}}(0) = \mathcal{L}_0\rho_{\mathrm{q}}(s) + \frac{n_{\mathrm{th}}}{2}\sum_{r=\pm}\mathcal{L}_{-r}[(s+\kappa)\mathcal{I} - \mathcal{L}_0]^{-1}\mathcal{L}_r\rho_{\mathrm{q}}(s). \tag{5.37}$$

This is a matrix algebraic equation which can be solved for $\rho_{\mathrm{q}}(s)$. Solving for the steady-state, in the Laplace transformed equation, is equivalent to taking the limit $\lim_{s\to 0}[s\rho_{\mathrm{q}}(s)]$. Then, the steady-state populations under the decorrelation approximation are

$$\Lambda\rho_{11} = 64\kappa\Phi^2(\gamma+\kappa), \tag{5.38a}$$
$$\Lambda\rho_T = 8\kappa\Phi(9\gamma^2 + 4\kappa(\kappa+2\Phi) + 4\gamma(3\kappa+2\Phi)), \tag{5.38b}$$
$$\Lambda\rho_S = 8\Phi(9\gamma^3 + 8\kappa\gamma(2\kappa\Phi) + 4\kappa^2(\kappa+2\Phi) + \gamma^2(21\kappa+8\Phi)), \tag{5.38c}$$
$$\begin{aligned}\Lambda\rho_{00} = {} & 9\gamma^4 + 8\gamma^3(6\kappa+\Phi) + 16\kappa^2(\kappa+2\Phi)^2 + 8\gamma^2\kappa(11\kappa+6\Phi) \\ & + 32\gamma\kappa(2\kappa^2 + 3\kappa\Phi + 2\Phi^2),\end{aligned} \tag{5.38d}$$

where the normalization is $\Lambda = (\gamma+2\kappa)(\gamma+2\kappa+8\Phi)((3\gamma+2\kappa)^2 + 8\Phi(\gamma+2\kappa))$ and we have reintroduced the photon flux $\Phi = \kappa n_{\mathrm{th}}/2$. While those results are approximate, we can still extract the relevant scaling factors. Specifically, we observe that to lowest order, both the triplet $\rho_T$ and the double excited $\rho_{11}$ state scale as $\sim \mathcal{O}(\kappa)$, vanishing at the complete static limit $\kappa \to 0$.

Due to the validity of the approximation, $\Phi \ll \kappa^2$, the Bourret approximation fails to reproduce one of the main effects seen in Fig. 5.3, i.e. that beyond the critical thermal population $n^{\star}_{\mathrm{th}}$, the concurrence decreases. To see this, we can use Eq. (5.38) to obtain the concurrence given in Eq. (2.12). Expanding around $\kappa = 0$, the concurrence is approximately given by

$$\mathcal{C}(\rho_{\mathrm{ss}}) \approx \frac{8\Phi}{\gamma + 8\Phi} - \frac{8\Phi\sqrt{\kappa}}{(\gamma + 8\Phi)\sqrt{9\gamma + 8\Phi}} - \frac{32\kappa(\Phi(3\gamma + 8\Phi)^2)}{\gamma(\gamma + 8\Phi)^2(9\gamma + 8\Phi)} + \mathcal{O}(\kappa^{3/2}). \tag{5.39}$$

When increasing the photon flux $\Phi$, equivalent to increasing $n_{\mathrm{th}}$ for fixed $\kappa$, the concurrence saturates to $\mathcal{C}(\rho_{\mathrm{ss}}) \to 1 - 4\kappa/\gamma$. While we see a correction of the order of $\kappa$, this expression does not capture the peak observed in Fig. 5.3(a). This is, of course, a consequence of the decorrelation approximation, which is only valid for weak fluctuations. The peak occurs in a regime of strong fluctuations, beyond the approximation's validity. Notice that from Eq. (5.39), we do not recover the results from the quasistatic limit, in Eq. (5.33), when $\kappa = 0$ and finite $\Phi > 0$. The reason is that Eq. (5.39) is only valid for weak driving, while in Eq. (5.33), we performed an average over the full range of noise strengths.

### 5.3.2 Continued fraction effective model

To go beyond the decoupling approximation, we can use the matrix continued fraction technique described in Sec. 5.1.3 to derive an effective model which provides us with analytical estimates of the populations as well as the critical thermal strength $n_{\mathrm{th}}^{\star}$. For that, we rely on a series of approximations which will allow us to simplify the problem considerably. We start by neglecting the population to the double excited state $\rho_{11}$. This is justified in Fig. 5.4(a), where the population $\rho_{11}$ is the smallest of the system for $\kappa \ll 1$. As shown in Appendix C, we then solve for the equations of motion and the coherences of the remaining system. There, we demonstrate how these equations can be reformulated as an equivalent, solvable recurrence relation. By solving the recurrence relation via ordinary continued fraction theory, we derive an effective population for the system near the static limit $\kappa \ll 1$. Specifically, the effective singlet population is given by

$$\rho_S = 1 - \left[\Upsilon(\Phi_{\mathrm{eff}}/\gamma)\left(1 + \frac{3\kappa}{\gamma}\right) - \frac{3\kappa}{\gamma}\right]\left(1 + \frac{16\kappa\Phi}{\gamma^2}\right), \tag{5.40}$$

while the effective triplet population is

$$\rho_T = \frac{8\kappa\Phi}{\gamma^2}[\Upsilon(\Phi_{\mathrm{eff}}/\gamma)(1 + 3\kappa/\gamma) - 3\kappa/\gamma]. \tag{5.41}$$

We have defined an effective photon flux $\Phi_{\mathrm{eff}} = \frac{\Phi\gamma^2}{\gamma^2 + 24\kappa\Phi}$. When $\Phi \to \infty$, this effective parameter saturates at $\Phi_{\mathrm{eff}} = \frac{\gamma^2}{24\kappa}$. From these effective populations, we observe that in the limit when $\kappa \to 0$, while keeping $\Phi$ finite, we recover static limit populations.

We now use these analytical expressions to estimate the two-qubit steady-state concurrence $\mathcal{C}(\rho_{\mathrm{ss}})$. Due to the 3-level approximation we have here, we cannot use Eq. (2.12),

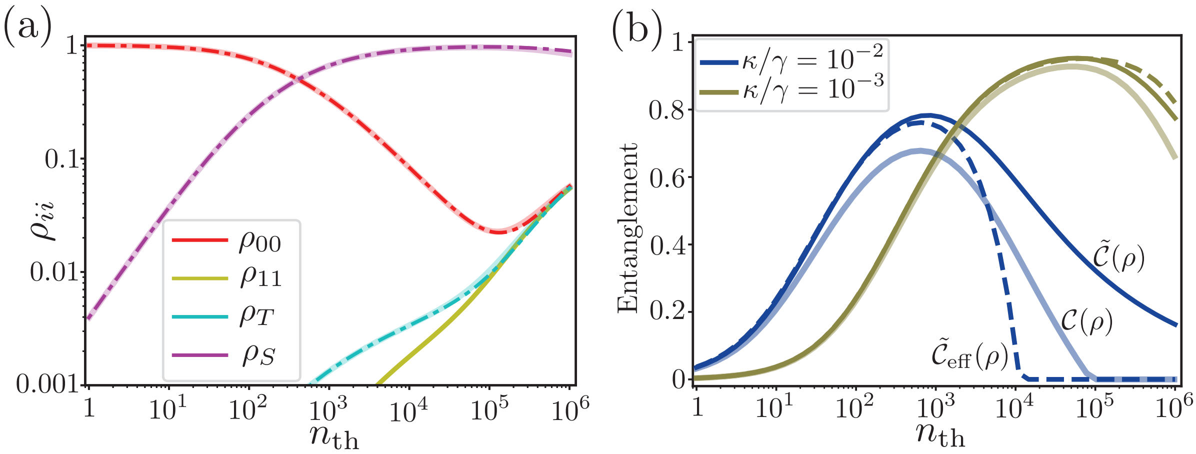


**Figure 5.4:** Comparison of the populations between a 4-level system (faded solid) and the 3-level system approximation (dashed) as a function of $n_{\rm th}$ for $\kappa/\gamma = 10^{-3}$. (b) Comparison between the exact concurrence $\mathcal{C}(\rho_{\rm ss})$ (solid line), the partial concurrence $\tilde{\mathcal{C}}(\rho_{\rm ss})$ (faded solid) with the exact populations $\rho_S$ and $\rho_T$, and the effective partial concurrence $\tilde{\mathcal{C}}_{\rm eff}(\rho_{\rm ss})$ (dashed line) with the effective populations from Eq. 5.40 and Eq. 5.41 for different values of $\kappa/\gamma$. Continued fraction is truncated at $n_{\rm iter.}$=50000.

which depends on $\rho_{11}$. Therefore, here we define a partial concurrence

$$\tilde{\mathcal{C}}(\rho_{\rm ss}) = \max\{0, \rho_S - \rho_T\}, \tag{5.42}$$

which is valid when $\rho_{11}\rho_{00} \ll 1$. Using our effective population, we get

$$\tilde{\mathcal{C}}_{\rm eff}(\rho_{\rm ss}) = 1 - \frac{\Upsilon(\Phi_{\rm eff}/\gamma)(\gamma + 3\kappa) - 3\kappa}{\gamma}\left(1 + \frac{24\kappa\Phi}{\gamma^2}\right). \tag{5.43}$$

Taking the limit $\kappa \to 0$, but keeping $\Phi$ finite, we recover the static limit results from Eq. (5.33). In Fig. 5.4(b) we compare the entanglement as a function of $n_{\rm th}$ for different $\kappa/\gamma$. Specifically, we compare the exact concurrence $\mathcal{C}(\rho_{\rm ss})$ to our partial concurrence $\tilde{\mathcal{C}}(\rho_{\rm ss})$ taking still the exact populations, with the partial concurrence taking our effective populations $\tilde{\mathcal{C}}_{\rm eff}(\rho_{\rm ss})$. Observe how $\mathcal{C}(\rho_{\rm ss})$ and $\tilde{\mathcal{C}}(\rho_{\rm ss})$ behave similarly except for a shift, which comes from the contribution from $\rho_{00}\rho_{11}$. The effective partial concurrence $\tilde{\mathcal{C}}_{\rm eff}(\rho_{\rm ss})$ describes perfectly the curve of $\tilde{\mathcal{C}}(\rho_{\rm ss})$ up to the point where it starts to deviate. Still, we observe that all the entanglement measures we define here peak approximately at the same $n_{\rm th}^\star$. We can then estimate the critical value of $n_{\rm th}^\star$ at which the concurrence reaches its maximum by solving $\frac{\partial \tilde{\mathcal{C}}_{\rm eff}(\rho_{\rm ss})}{\partial n_{\rm th}} = 0$. Solving this equation leads to a transcendental equation due to the incomplete gamma function $\Gamma[0, f(n_{\rm th})]$. Still, it can be solved approximately to

$$n_{\rm th}^\star = \frac{\gamma^2 + 3\gamma\kappa}{12\kappa^2}. \tag{5.44}$$

We can now obtain an approximate expression for the maximum effective concurrence, given by

$$\tilde{\mathcal{C}}^{\star}_{\text{eff}}(\rho_{\text{ss}}) = 1 - \frac{6\kappa\left(2e^{\frac{6\kappa}{\gamma}}(\gamma+3\kappa)\Gamma[0,\frac{6\kappa}{\gamma}]-\gamma\right)}{\gamma^2}. \tag{5.45}$$

In Fig. 5.3(d), we plot the critical thermal fluctuations and see how they match the peak of the achieved entanglement for the exact model. The critical thermal population scales as $1/\kappa^2$, diverging at the static limit $\kappa \to 0$.

## 5.4 Amplitude vs phase fluctuations

According to the phase-space representation introduced in Sec. 2.5, the thermal field is described by a fluctuating complex variable $\alpha(t)$. Alternatively, we can express this field in terms of polar coordinates as

$$\alpha(t) = r(t)e^{i\theta(t)}, \tag{5.46}$$

where the radius $r(t)$ and the phase $\theta(t)$ obey the coupled (Itô) stochastic equations [126]

$$\mathrm{d}r(t) = \left(-\kappa r(t) + \frac{\kappa n_{\text{th}}}{4r(t)}\right)\mathrm{d}t + \sqrt{\frac{\kappa n_{\text{th}}}{2}}\mathrm{d}W_r(t), \tag{5.47}$$

$$\mathrm{d}\theta(t) = \sqrt{\frac{\kappa n_{\text{th}}}{2}}\frac{\mathrm{d}W_\theta(t)}{r(t)}, \tag{5.48}$$

with two independent Wiener increments $\mathrm{d}W_r(t)$ and $\mathrm{d}W_\theta(t)$.

In contrast to the complex-valued Ornstein-Uhlenbeck process, these stochastic differential equations in polar form cannot be solved exactly but serve as a starting point for further approximations. In particular, we can ask ourselves the role of each variable and whether the breakdown of the static approximation comes from fluctuations in the phase $\theta(t)$ or in the amplitude $r(t)$.

Consider the amplitude to be fixed $r(t) = r_0$ and let the phase be governed by Eq. (5.48). In this case, our system then transforms into a phase-diffusion model. While exact deterministic (averaged) master equations have been derived using the Zwanzig-Nakajima projector operator technique for simple systems [205], this remains challenging for more general systems. Here, we solve our problem by going into a rotating basis [206], which makes our problem solvable. Our original stochastic master equation Eq. (5.16) is written as

$$\dot{\rho}_{\text{q}}(\theta,t) = (\mathcal{L}_0 + e^{i\theta}r_0\mathcal{L}_+ + e^{-i\theta}r_0\mathcal{L}_-)\rho_{\text{q}}(\theta,t). \tag{5.49}$$

By defining $\tilde{\rho}_{\text{q}}(\theta,t) = e^{-i\theta\hat{L}_z/2}\rho_{\text{q}}(\theta,t)e^{i\theta\hat{L}_z/2}$ with $\hat{L}_z = \hat{\sigma}^z_1 + \hat{\sigma}^z_2$, the equation of motion of the new rotated state is

$$\dot{\tilde{\rho}}_{\text{q}}(\theta,t) = -i\frac{\dot{\theta}}{2}[\hat{L}_z, \tilde{\rho}_{\text{q}}(\theta,t)] + e^{-i\theta\hat{L}_z/2}\dot{\rho}_{\text{q}}(\theta,t)e^{i\theta\hat{L}_z/2}. \tag{5.50}$$

The (rotated) stochastic master equation reads

$$\dot{\tilde{\rho}}_{\mathrm{q}}(\theta,t)=\mathcal{L}_0\tilde{\rho}_{\mathrm{q}}(\theta,t)+r_0\left(\mathcal{L}_+ + \mathcal{L}_-\right)\tilde{\rho}_{\mathrm{q}}(\theta,t)-i\frac{\dot{\theta}}{2}[\hat{L}_z,\tilde{\rho}_{\mathrm{q}}(\theta,t)]. \tag{5.51}$$

This is a (Stratonovich) stochastic master equation for our phase-diffused model. As the noise process $\dot{\theta}$ is a Wiener process, we can obtain an Itô stochastic differential equation by adding the Itô correction

$$\begin{aligned}\dot{\tilde{\rho}}_{\mathrm{q}}(\theta,t)=&\mathcal{L}_0\tilde{\rho}_{\mathrm{q}}(\theta,t)+r_0\left(\mathcal{L}_+ + \mathcal{L}_-\right)\tilde{\rho}_{\mathrm{q}}(\theta,t)\\ &-\frac{i}{2}\sqrt{\frac{\kappa n_{\mathrm{th}}}{2}}\frac{W_\theta(t)}{r_0}[\hat{L}_z,\tilde{\rho}_{\mathrm{q}}(\theta,t)]-\frac{1}{2}\frac{\kappa n_{\mathrm{th}}}{8r_0^2}[\hat{L}_z,[\hat{L}_z,\tilde{\rho}_{\mathrm{q}}(\theta,t)]].\end{aligned} \tag{5.52}$$

We can now take the stochastic average of this Itô differential equation since $\mathrm{d}W_\theta(t)$ is statistically independent of $\rho_{\mathrm{q}}(\theta,t)$. This leads to

$$\dot{\tilde{\rho}}_{\mathrm{q}}(t)=\mathcal{L}_0\tilde{\rho}_{\mathrm{q}}(t)+r_0\left(\mathcal{L}_+ + \mathcal{L}_-\right)\tilde{\rho}_{\mathrm{q}}(t)+\frac{\kappa n_{\mathrm{th}}}{8r_0^2}\mathcal{D}[\hat{L}_z]\tilde{\rho}_{\mathrm{q}}(t). \tag{5.53}$$

It is important to keep in mind that this is a rotated basis $\tilde{\rho}$. However, the system's populations remain invariant in this new basis. This can be seen from the action of this rotation on our basis

$$e^{-i\theta/2\hat{L}_z}|11\rangle=e^{i\theta}|11\rangle, \tag{5.54}$$
$$e^{-i\theta/2\hat{L}_z}|00\rangle=e^{-i\theta}|00\rangle, \tag{5.55}$$
$$e^{-i\theta/2\hat{L}_z}|01\rangle=|01\rangle, \tag{5.56}$$
$$e^{-i\theta/2\hat{L}_z}|10\rangle=|10\rangle. \tag{5.57}$$

From these relations, we can derive that the rotated basis does not mix the singlet and the triplet, $\tilde{\rho}_S=\rho_S$ and $\tilde{\rho}_T=\rho_T$. Observe how Eq. (5.53) is identical to the master equation one would get under coherent driving [149] with Rabi strength $\Omega=r_0\sqrt{\kappa\gamma}$ and collective dephasing noise of strength $\gamma_\phi/2=\frac{\kappa n_{\mathrm{th}}}{8r_0^2}$. This dephasing noise can then be interpreted as a system under Markovian noise.

The phase-diffusion model alone does not account for the observations in Fig. 5.3. The reason is that as we increase $n_{\mathrm{th}}$, in Fig. 5.3(a), we observe how the entanglement degrades. It is, however, not what Eq. (5.53) predicts. This is because the dephasing process, which would in other situations be the main detrimental term to the entanglement, in this case, does not scale with the thermal occupation number. To see this, observe that the dephasing process is proportional to $n_{\mathrm{th}}/r_0^2$. As $r_0\propto\sqrt{n_{\mathrm{th}}}$, the terms becomes temperature-independent. We conclude that amplitude fluctuations are the main cause of the breakdown of the quantum correlations.

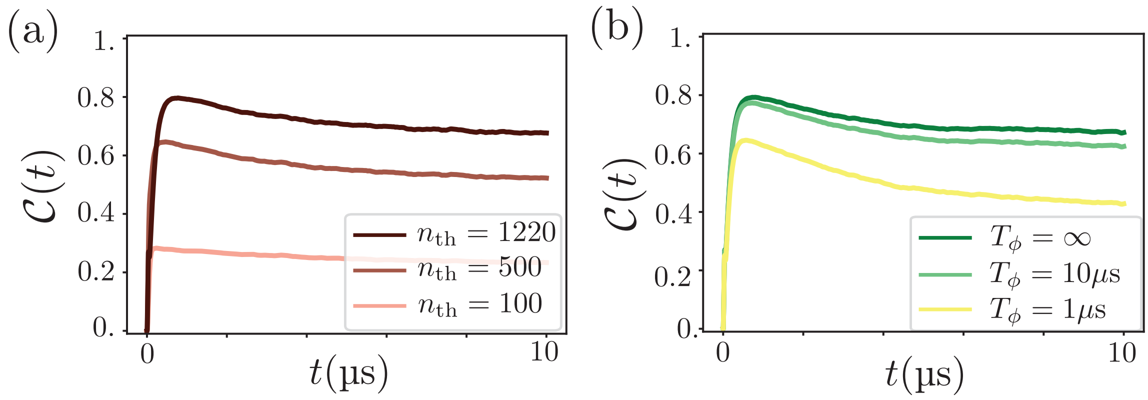


**Figure 5.5:** Time evolution of the concurrence $\mathcal{C}(t) \equiv \mathcal{C}(\rho_{\rm q}(t))$ for (a) different thermal occupation number $n_{\rm th}$ and (b) for different dephasing times $T_\phi$ at fix $n_{\rm th} = 1220$, which corresponds to room-temperature noise. We assume $\kappa/(2\pi) = 10\,$kHz, $\gamma_i/(2\pi) = 10\,$MHz, and $\delta_i = 0$.

## 5.5 Implementations

Here, we propose two possible experimental realizations of the protocol we have described and evaluate the achievable amount of entanglement under realistic experimental conditions. Until now, we have kept our discussion general, and our proposal can be implemented with optical or microwave photons. As long as the bandwidth of the filter $\kappa$ is smaller than the bandwidth of the qubits $\gamma$, as seen from Fig. (5.2)(b), entanglement between the qubits emerges as we increase $n_{\rm th}$. This raises the following question: How much entanglement can be generated and under which conditions if the photon source is at room temperature $T = 293\,$K?

### 5.5.1 Superconducting qubits thermal network

A direct implementation of our system, described by Fig. 5.1, uses a cryogenic link with superconducting qubits [207]. Here, photons are propagated along the waveguide as microwaves. To suppress thermal noise, they usually operate at low temperatures, on the order of $T_0 \sim 10\,$mK. Entanglement protocols in superconducting waveguides have been recently demonstrated [80, 208]. Here, we simulate our protocol under realistic experimental conditions. We assume an identical coupling rate from the qubits to the waveguide $\gamma/(2\pi) = 10\,$MHz, motivated by previous experimental work [80], which gives a limit of the thermal cavity bandwidth $\kappa$ to be of the order of MHz or smaller. Here, we turn on the photon source and let it reach a steady state. Then, at $t = 0$, we switch on the interaction between the cavity and the qubits. In Fig. 5.5(a), we show how the entanglement builds up for different temperatures of the source (given by $n_{\rm th}$) and show how at room temperature $T = 297\,$K, for which the amount of photons at microwave frequency $\omega_{\rm c}/(2\pi) = 5.0\,$GHz is around $n_{\rm th} \simeq 1220$, we can still extract a finite amount of entanglement. In Fig. 5.5(b), we consider the room-temperature case $n_{\rm th} = 1220$ and

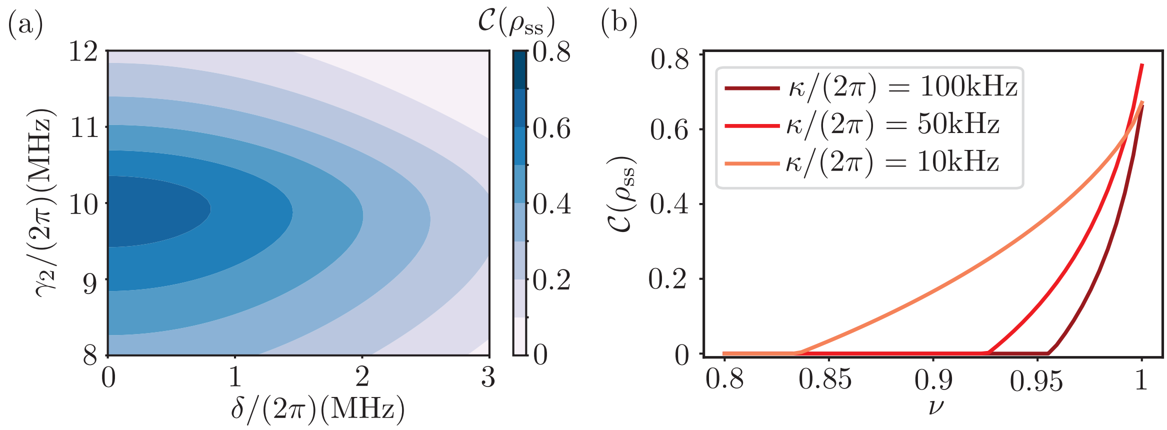


**Figure 5.6:** Steady-state concurrence $\mathcal{C}(\rho_{ss})$ at $n_{th} = 1220$ (a) as function of $\gamma_2$ and detunings $\delta_1 = \delta_2 = \delta$ for fixed $\kappa/(2\pi) = 10\,\text{kHz}$, $\gamma_1/(2\pi) = 10\,\text{MHz}$, and (b) as a function of linear loses $\nu$ for different bandwidths $\kappa$ at $n_{th} = 1220$ for fixed $\gamma_i/(2\pi) = 10\,\text{MHz}$ and $\delta_i = 0$. For both plots, $n_{\text{iter.}}$=5000.

additionally consider a dephasing processes $\gamma_\phi$, also given in terms of dephasing time $\gamma_\phi = 1/T_\phi$. To model dephasing, we simulate the stochastic master equation in Eq. (5.14) and add an additional Markovian dephasing term for each qubit, $\frac{\phi_\phi}{2}\sum_i^2 \mathcal{D}[\hat{\sigma}_i^z]\rho$.

The time needed to reach the steady state, $t_{s.s.}$, should approximately scale with the inverse of the Liouvillian gap $\lambda$ for our system, as $t_{s.s.} \propto -1/\lambda$. In the static limit, we find the gap to be $\lambda \approx -\frac{3\gamma}{2}$. This is approximately what we see in Fig. 5.5, where for a fixed $\gamma$, all the time evolutions peak approximately simultaneously. We also observe a second time scale, much slower, for which the state reaches the steady state. Our expression for the gap does not capture this because it is obtained in the static limit, where the value of $n_{th}$ does not change over time. Still, the highest possible entanglement can be achieved in timescales of the order of $1/\gamma$.

Having shown how the protocol can achieve steady-state entanglement within a realistic time for superconducting technologies, we now consider imperfections in the system. Using the continued fraction method, in Fig. 5.6(a), we show the entanglement as a function of the most common imperfection in those systems: a mismatch between the qubit coupling strength into the waveguide, $\gamma_1 \neq \gamma_2$, and a mismatch between the resonant frequency between both qubits, $\delta_1 = \delta_2 = \delta \neq 0$. It is important to point out that any mismatch between the resonant frequency and the thermal cavity can be compensated by moving the cavity resonant frequency to $\omega_c = (\omega_{q,1} + \omega_{q,2})/2$.

Lastly, our protocol, as discussed so far, relies on both a chiral interaction between the source and the qubits and the qubits themselves. This can be achieved by using circulators for long distances. To take into account insertion losses due to the circulators, we now take the insertion losses from Eq. (5.4). We see the effect on photon losses in Fig. 5.6(b), where we consider the losses to be only between qubits, i.e. $\nu \equiv \nu_{1,2}$. The reason for this is that insertion losses from the thermal cavity to each qubit $\nu_{0,i}$ results just in a renormalization of the photon numbers the qubits see, $\tilde{n}_{\text{th}} = \nu_{0,i} n_{\text{th}}$. Assuming that both qubits have the same insertion losses $\nu_{0,1} = \nu_{0,2}$, we can consider the qubits being driven by $\tilde{n}_{\text{th}}$. We observe that the qubit entanglement is more robust the smaller the bandwidth of the filter cavity, allowing up to 15% photon losses along the waveguide.

### 5.5.2 Phononic thermal network

Here, we focus on a complementary implementation of our protocol: a phonon quantum network, where emitters such as silicon-vacancy (SiV) centers are coupled to a 1D diamond waveguide [209–213]. Then, in this implementation, the carriers of information are no longer photons, but rather phonons. As depicted in Fig. 5.7, the waveguide is coupled to a mechanical resonator of bandwidth $\kappa$, which is, in turn, in contact with a phononic reservoir at temperature $T > 0$. The resonator couples to the waveguide at $z_0$, and we place $N_{\text{q}}$=2 qubits at positions $z_1$ and $z_2$ such that $z_0 < z_1 < z_2$. Contrary to the previous implementation, here the waveguide cannot be modeled as a chiral waveguide, but rather as a semi-infinite waveguide, as we described in Sec. 2.3.3. We assume a 1D phononic crystal structure for which the quantized phononic mode is given by [214]

$$\hat{u}(z) = -i \sum_n \sqrt{\frac{\hbar \omega_n}{2\rho_c}} (\zeta_n^*(z) \hat{b}_n^\dagger - \text{h.c.}), \tag{5.58}$$

being here $\rho_c$ the density of the crystal and $\zeta_n(z)$ its mode function. The phonon operators fulfil the usual commutation relations $[\hat{b}_n, \hat{b}_m^\dagger] = \delta_{n,m}$. We can then apply the derivation of Sec. 2.3.3 to obtain a master equation for the semi-infinite waveguide. As at the beginning of the chapter, with the chiral waveguide, we follow the convention that the index $i = 0$ corresponds to the thermal source, i.e. $\hat{c}_0 = \hat{a}$ and $\gamma_0 = k$, while $j \geq 1$ is the qubit index $\hat{c}_j = \hat{\sigma}_j^-$. Notice that we place the filter resonator at the edge of the semi-infinite waveguide, $z_0 = 0$, where the field is maximal. Also, to consider the coupling between the thermal reservoir and our phononic waveguide, the mechanical resonator couples to a hot reservoir at decay rate $\kappa_{\text{hot}} \equiv \kappa$. The resulting master equation is then given by

$$\begin{aligned}\dot{\rho} =& \kappa(n_{\text{th}} + 1)\mathcal{D}[\hat{a}]\rho + \kappa n_{\text{th}} \mathcal{D}[\hat{a}^\dagger]\rho \\ &- i\Big[\hat{H}_{\text{sys}} + \sum_{j,l} J_{j,l} \hat{c}_j^\dagger \hat{c}_l, \rho\Big] + \sum_{j,l} \Gamma_{j,l} \mathcal{D}[\hat{c}_j, \hat{c}_l]\rho,\end{aligned} \tag{5.59}$$

with decay rates $\Gamma_{j,l} = 2\sqrt{\gamma_j \gamma_l}[\cos(k(z_j + z_l)) + \cos(k|z_j - z_l|)]$ and coupling strength $J_{j,l} = \sqrt{\gamma_j \gamma_l}[\sin(k(z_j + z_l)) + \sin(k|z_j - z_l|)]$. Due to the semi-infinite waveguide, the coupling and decay rates are rescaled by a factor of four compared with the cascaded setting from Sec. 5.1. Here, to make an accurate comparison between the two scenarios, we rescale the couplings such that $\kappa \to \kappa/4$ and $\gamma \to \gamma/4$ in the semi-infinite waveguide. We start our analysis with some trivial examples, for example, when the emitters are at

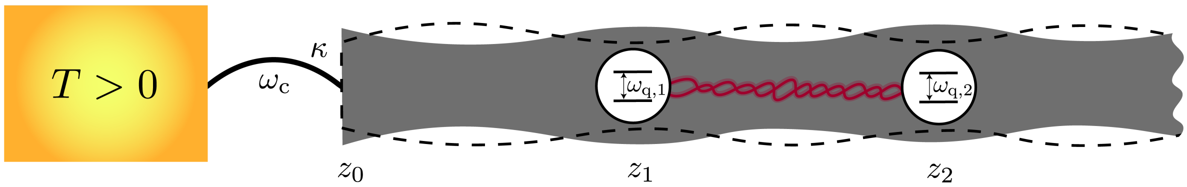


**Figure 5.7:** Schematic of the setup considered for the phononic thermal network implementation. Here, a source of incoherent phonons at temperature $T > 0$ is in contact with a 1D waveguide by a mechanical resonator of bandwidth $\kappa$ and resonant frequency $\omega_c$. A semi-infinite waveguide is in contact with the mechanical resonator at $z_0$, and we place the qubits at $z_1$ and $z_2$ such that $z_0 < z_1 < z_2$.

$kz_n = 2\pi n$, or equivalently, $z_n = \lambda_0 n$, for $n = 0, 1, 2, ...$ In this scenario, Eq. (5.59) reduces to

$$\dot{\rho} = -i[\hat{H}_{\text{sys}}, \rho] + \underbrace{\kappa(n_{\text{th}}+1)\mathcal{D}[\hat{a}]\rho + \kappa n_{\text{th}}\mathcal{D}[\hat{a}^\dagger]\rho}_{\text{thermal source}} + \underbrace{\mathcal{D}[\sqrt{\kappa}\hat{a} + \sqrt{\gamma}\hat{\sigma}_1^- + \sqrt{\gamma}\hat{\sigma}_2^-]\rho}_{\text{phonon waveguide}}. \quad (5.60)$$

This master equation represents a dissipative and bidirectional coupling between the resonator and the qubits. This dissipative coupling by itself is not enough to create entanglement. We need to break the singlet-triplet symmetry, which can be achieved by imposing finite but opposing, detunings on the qubits $\delta_1 = -\delta_2 = \delta$ such that $\hat{H}_{\text{sys}} = \delta(\hat{\sigma}_1^z - \hat{\sigma}_2^z)/2$, similar to [149, 150]. Assuming the case when $z_n = \lambda_0 n$ and with finite detuning, in Fig. 5.8(a), we plot the entanglement of the reduced qubit state in terms of the concurrence $\mathcal{C}(\rho_{\text{ss}})$ as a function of the temperature $n_{\text{th}}$ for differents $\kappa/\gamma$. For small thermal occupation $n_{\text{th}}$, we can use Eq. (5.59) [black dashed lines in Fig. 5.8(a)]. As with the unidirectional case, the entanglement is created by populating the singlet state $|S\rangle$. Notice that with this configuration, we no longer need the qubits to be resonant with the cavity field, nor do we need them to be identical. Given two distinct qubits with natural frequency $\omega_{q,1}$ and $\omega_{q,2}$, respectively, having the cavity at frequency $\omega_c = (\omega_{q,1} + \omega_{q,2})/2$ would give us the previous detuning configurations. Similarly, if we place the qubits at $kz_n = \pi n$, this will create the same amount of entanglement as with $kz_n = n\lambda_0$ case, now the mechanism is different: the qubit-qubit entanglement is created by populating the triplet state $|T\rangle$.

However, as seen in Fig. 5.8(b), in between $\pi < kz_n < 2\pi$, the qubit dynamics is non-trivial. This is because the terms mediated by $J_{i,j}$ in Eq. (5.59) allow for dipole-dipole interactions between all the emitters in the waveguide, as well as some energy shifts. This is clearly seen when we explicitly evaluate this term for our case

$$
\begin{aligned}
4\sum_{j,l} J_{j,l}\hat{c}_j^\dagger\hat{c}_l =& \kappa\sin(2kz_0)\hat{a}^\dagger\hat{a} + \gamma\sin(2kz_1)\hat{\sigma}_1^+\hat{\sigma}_1^- + \gamma\sin(2kz_2)\hat{\sigma}_2^+\hat{\sigma}_2^- \\
&+ \sqrt{\kappa\gamma}[\sin(k|z_1+z_0|) + \sin(k|z_1-z_0|)]\left(\hat{a}^\dagger\hat{\sigma}_1^- + \hat{a}\hat{\sigma}_1^+\right) \\
&+ \sqrt{\kappa\gamma}[\sin(k|z_2+z_0|) + \sin(k|z_2-z_0|)]\left(\hat{a}^\dagger\hat{\sigma}_2^- + \hat{a}\hat{\sigma}_2^+\right) \\
&+ \gamma[\sin(k|z_2+z_1|) + \sin(k|z_2-z_1|)]\left(\hat{\sigma}_1^+\hat{\sigma}_2^- + \hat{\sigma}_1^-\hat{\sigma}_2^+\right).
\end{aligned}
\tag{5.61}
$$

As we fix the resonator at $z_0 = 0$, it does not experience any frequency shift. While this term vanishes if we fix the qubit positions described before, one must consider small deviations from such fixed points. In this case, the dipole-dipole interaction starts to be relevant, and Eq. (5.59) describes a complex interacting system.

New insight can be found if we express Eq. (5.59) as a stochastic master equation, similar to what we did for Eq. (5.14). To do that, we express the coherent term of the master equation as

$$
\begin{aligned}
-i\Big[\hat{H}_{\text{sys}} + \sum_{j,l} J_{j,l}\hat{c}_j^\dagger\hat{c}_l, \rho\Big] =& -i\Big[\hat{H}_{\text{sys}} + \sum_{j=1} J_{j,j}\hat{\sigma}_j^+\hat{\sigma}_j^- + J_{1,2}\left(\hat{\sigma}_1^+\hat{\sigma}_2^- + \hat{\sigma}_1^-\hat{\sigma}_2^+\right), \rho\Big] \\
&- i\Big[\sum_{j=1} J_{0,j}\left(\hat{a}^\dagger\hat{\sigma}_j^- + \hat{a}\hat{\sigma}_j^+\right), \rho\Big],
\end{aligned}
\tag{5.62}
$$

where the first line of the right-hand side of the equation expresses the qubits energy shift and dipole interaction between them, and the second line describes the two qubits interacting with the resonator. We can now apply the P representation mapping from Eq. (2.110) to this equation, transforming Eq. (5.62) to

$$
-i\Big[\hat{H}_{\text{sys}} + \sum_{j,l} J_{j,l}\hat{c}_j^\dagger\hat{c}_l, \rho\Big] \to -i[\hat{H}_{\text{q}}(t), \rho_{\text{q}}] + i\sum_{j=1} J_{0,j}\left(\frac{\partial}{\partial\alpha}\hat{\sigma}_j^-\rho_{\text{q}} - \frac{\partial}{\partial\alpha^*}\rho_{\text{q}}\hat{\sigma}_j^+\right). \tag{5.63}
$$

Here, we have defined a new effective coherent interaction

$$
\hat{H}_{\text{q}}(t) = \hat{H}_{\text{sys}} + \sum_{j=1} J_{j,j}\hat{\sigma}_j^+\hat{\sigma}_j^- + J_{1,2}(\hat{\sigma}_1^+\hat{\sigma}_2^- + \hat{\sigma}_2^+\hat{\sigma}_1^-) + \sum_{j=1} J_{0,j}(\alpha(t)\hat{\sigma}_j^- + \alpha^*(t)\hat{\sigma}_j^+). \tag{5.64}
$$

Similarly, the dissipative term of Eq. (5.59) transforms to

$$
\begin{aligned}
&2\sum_{j,l}\Gamma_{j,l}\mathcal{D}[\hat{c}_j, \hat{c}_l]\rho = 2\sum_{j,l\neq 0}\Gamma_{j,l}\mathcal{D}[\hat{\sigma}_j^-, \hat{\sigma}_l^-]\rho_{\text{q}} \\
&+ \sum_{j=1}\Gamma_{0,j}[(\alpha^*(t)\hat{\sigma}_j^- - \alpha(t)\hat{\sigma}_j^+), \rho_{\text{q}}] + \sum_{j=1}\Gamma_{0,j}\left(\frac{\partial}{\partial\alpha}\hat{\sigma}_j^-\rho_{\text{q}} + \frac{\partial}{\partial\alpha^*}\rho_{\text{q}}\hat{\sigma}_j^+\right).
\end{aligned}
\tag{5.65}
$$

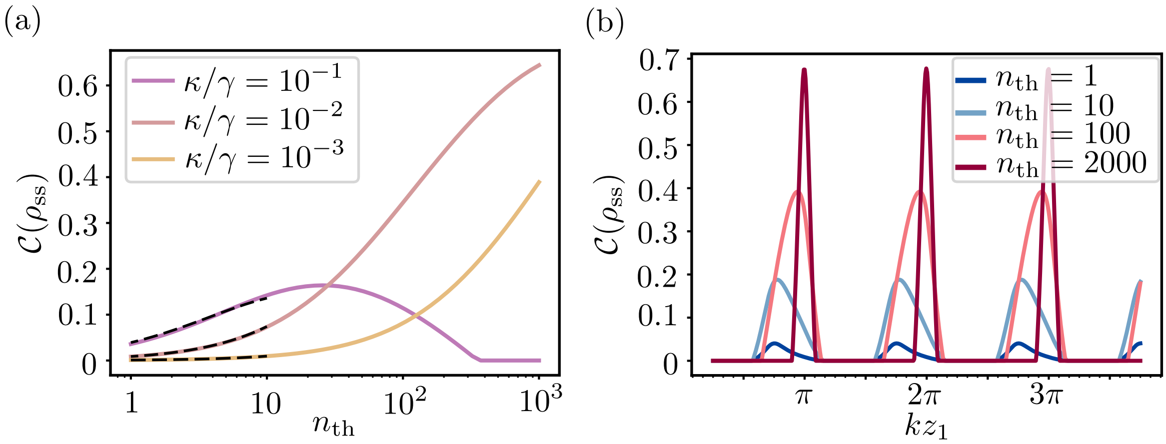


**Figure 5.8:** Steady-state entanglement between the two qubits using the concurrence $\mathcal{C}(\rho_{\rm ss})$ (a) as a function of the temperature for different bandwidths ratio $\kappa/\gamma$ and fixed qubits $kz_1 = 2\pi$ and $kz_2 = 4\pi$, (b) as a function of the position of the first qubit $kz_1$ for different photon numbers $n_{\rm th}$ at fixed $\kappa/\gamma = 0.01$. In both plots, the solid lines are obtained using the approximated P representation, which allows us to use the continued fraction method. In (a), the black dashed line represents exact simulations using Eq. (5.59). For both plots, the detuning is $\delta = \gamma/2 = 0.5$, and $n_{\rm iter.} = 5000$.

Therefore, the whole qubit master equation can be written in the following compact form

$$\begin{aligned}\dot{\rho}_{\rm q} &= -i[\hat{H}_{\rm eff}(t), \rho_{\rm q}] + \gamma\mathcal{D}[\hat{L}_{\cos}]\rho_{\rm q} \\ &+ \sum_j (\Gamma_{0,j} + iJ_{0,j})\frac{\partial}{\partial\alpha}\hat{\sigma}_j^-\rho_{\rm q} + \sum_j (\Gamma_{0,j} - iJ_{0,j})\frac{\partial}{\partial\alpha^*}\rho_{\rm q}\hat{\sigma}_j^+,\end{aligned} \tag{5.66}$$

with a collective dissipator term which involves only the qubits $\hat{L}_{\cos} = \sum_j \cos(kz_j)\hat{\sigma}_j^-$ and a time-dependent Hamiltonian

$$\begin{aligned}\hat{H}_{\rm eff}(t) &= \hat{H}_{\rm sys} + \sum_{j=1} J_{j,j}\hat{\sigma}_j^+\hat{\sigma}_j^- + J_{1,2}(\hat{\sigma}_1^+\hat{\sigma}_2^- + \hat{\sigma}_2^+\hat{\sigma}_1^-) \\ &+ \sum_{j=1}\left[(J_{0,j} - i\Gamma_{0,j})\alpha(t)\hat{\sigma}_j^+ + (J_{0,j} + i\Gamma_{0,j})\alpha^*(t)\hat{\sigma}_j^-\right].\end{aligned} \tag{5.67}$$

The initial master equation Eq. (5.59) is not unidirectional. This gives rise to terms which involve field derivatives $\partial/(\partial\alpha)$ and $\partial/(\partial\alpha^*)$. This term would vanish for a cascaded setting, meaning that the physical interpretation of this term is the action of the reflected photons back on the resonator. While it is not possible to find positions such that $\Gamma_{0,j} \pm iJ_{0,j} = 0$ and they vanish naturally (this would also make the driving term vanish), we can neglect these terms and assume we have a cascaded interaction. While this is not exact, we see from Fig. 5.8(a) that for $\kappa/\gamma$ small, this effective model captures the positions which are necessary to generate entanglement. The deviations caused by this approximation are more relevant the larger $\kappa/\gamma$. Fortunately for us, this is not the regime in which we are interested.

We can further rearrange our master equation such that it can be written in a similar structure as Eq. (5.14)

$$\dot{\rho}_{\mathrm{q}}(\alpha,\alpha^*,t) = -i[\hat{H}_{\mathrm{phon.}}(\alpha,\alpha^*),\rho_{\mathrm{q}}(\alpha,\alpha^*,t)] + \gamma\mathcal{D}[\hat{L}_{\cos}]\rho_{\mathrm{q}}(\alpha,\alpha^*,t), \tag{5.68}$$

with an effective (stochastic) phonon-mediated Hamiltonian

$$\hat{H}_{\mathrm{phon.}}(\alpha,\alpha^*) = \hat{H}'_{\mathrm{sys}} + \hat{H}'_{\mathrm{casc}} + \frac{i\sqrt{\kappa\gamma}}{2}[\alpha^*(t)\hat{L}_{\mathrm{phon.}} - \alpha(t)\hat{L}^\dagger_{\mathrm{phon.}}], \tag{5.69}$$

where we have now defined a position-dependent collective spin operator $\hat{L}_{\mathrm{phon.}} = e^{-ikz_1}\hat{\sigma}_1 + e^{-ikz_2}\hat{\sigma}_2$, a position-dependent energy shift for the qubits

$$\hat{H}'_{\mathrm{sys}} = \hat{H}_{\mathrm{sys}} + \sum_j J_{j,j}\hat{\sigma}_j^+\hat{\sigma}_j^-, \tag{5.70}$$

and a position-dependent dipole interaction between the qubits

$$\hat{H}'_{\mathrm{casc}} = \frac{\gamma}{2}\sin kz_1 \cos kz_2(\hat{\sigma}_1^+\hat{\sigma}_2^- + \hat{\sigma}_2^+\hat{\sigma}_1^-). \tag{5.71}$$

Expressing the stochastic master equation like this allows us now to use the continued fraction method we derived in Sec. 5.1.3. In Fig. 5.8, the solid lines are obtained using this method, which agrees with exact simulations for small occupation number and $\kappa/\gamma$ small.

Observe that the stochastic master equation for the semi-infinite waveguide also presents some other differences compared to Eq. (5.14). Specifically, neglecting the position-dependent offset, we have two crucial distinctions between this system and our previous case: a new dipole terms, which vanish at $kz_1 = 2\pi n$, which contributes when $kz_1 \neq 2\pi n$ and a position-dependent driving. The dipolar term resembles, with the collective decay channel, a cascaded interaction. Looking at Fig. 5.8(b), the maximum seems to be around $kz_1 \sim \pi(3/4 + n)$. At this point, the generated entanglement seems to contribute from both the driving term and the dipole interaction. We can further justify this by observing that as we increase $n_{\mathrm{th}}$, the qubit dipolar contribution becomes small compared with the driving term. In this case, the driving term should dominate and peak around $kz_1 \sim \pi n$. To complete the implementation, we also discuss the possibility of achieving entanglement by a phononic source at room temperature. If we consider the SiV centers to form a two-level system of frequency $\omega_{\mathrm{q},i}/(2\pi) \approx 3\,\mathrm{GHz}$ [214], at this frequency we would have around $n_{\mathrm{th}} \approx 2000$ phonons at room temperature. In Fig. 5.8, we observe that highly entangled states can be achieved by properly positioning the qubits and using a narrowband resonator.

# Chapter 6

# Conclusion and outlook

## 6.1 Conclusion

In this thesis, we developed an in-depth theoretical analysis of the remote entanglement distribution for small- and large-scale quantum networks by driving qubits with photons.

We derived a master equation for the nondegenerate parametric amplifier, which generates continuous variable Gaussian states, and its interaction with spatially separated qubits. Assuming a broadband amplifier, we formulated an effective master equation that describes the qubits as a two-mode squeezed reservoir, offering insight into their dynamics. Under ideal conditions, the steady state is a pure, entangled state that converges to a Bell state as the amplifier power increases. We analyzed the fidelity of this state and found that entanglement emerges only if the environment's purity satisfies $\mu_{\text{eff}} \geq 1/3$. Recent experiments have demonstrated purities above this threshold in microwaves [24] and hybrid microwave-optics [25], even reaching values up to $\mu_{\text{eff}} \approx 0.9$ [215]. We demonstrated that, considering a finite bandwidth of the parametric amplifier, the qubit no longer converts to a maximally entangled state when we increase the power. In this scenario, we show how we can still obtain a large amount of entanglement and find the optimal pump strength as well as the optimal fidelity. We also examined its robustness with respect to coupling inefficiencies and dephasing noise. In superconducting circuits, circulators typically introduce photon losses of 15% [75], ($\nu = 0.85$), and we compared our scheme to other deterministic protocols, showing that our approach is more sensitive to losses due to its dependence on two bosonic modes. Finally, we evaluated the entanglement distribution rate, which remains high, $R \sim \gamma^{-1}$, and avoids the limitations of probabilistic schemes. We concluded this part with predictions for two upcoming experiments: one validating entanglement extraction in a qubit-qubit system and another providing a theoretical framework and entanglement witnesses for a hybrid protocol.

We then explored the creation of a larger network by increasing the number of qubits in each waveguide while still using a similar parametric amplifier to generate correlated photons. Using similar theoretical techniques as before, we showed that the steady state exhibits varying degrees of bi- and multipartite entanglement, which can be controlled by adjusting the squeezing strength and local qubit detunings. We then proposed a detuning configuration that parallelizes the protocol, allowing the network to scale linearly with the number of qubit pairs. We investigated the performance of this scheme under realistic experimental conditions, taking into account finite amplifier bandwidth, waveguide losses, and propagation delays. This analysis shows that while achieving extremely high fidelities of the entangled state still requires near-ideal conditions, the scheme remains highly efficient in distributing non-ideal entangled states and is rather robust against common experimental imperfections. Our quantum network provides an ideal setting for entanglement purification protocols. We investigate such a protocol and demonstrate how one can distill states with a larger amount of entanglement with high success probability.

The finite-bandwidth parametric amplifier revealed a surprising phenomenon: the emergence of quantum correlations when the bandwidth of the source is smaller than that of the qubits. This effect motivated the final chapter of the thesis. Here, we presented an equivalent but simpler scenario in which qubits are driven by a thermal cavity. We showed that under Markovian conditions, entanglement between qubits cannot be generated. However, we numerically observed that as we gradually decreased the bandwidth of the thermal cavity, entanglement emerged among the qubits. We provided several numerical and analytical techniques to understand this phenomenon. Finally, we proposed two experimental implementations of the protocol based on either superconducting qubits in a cryogenic link or SiV centers in a diamond phononic waveguide. In both cases, we show that it is possible to drive the qubits with an incoherent thermal source at room temperature to create highly entangled states.

## 6.2 Outlook

The work done within this thesis paves the way to the realization of large-scale quantum networks. As we have described in Chapter 3 and Chapter 4, the creation of small- and large-scale networks relies on the generation of correlated photons by a nondegenerate parametric amplifier. While such sources are available in microwave and optical domains, generating such states in phononic platforms remains challenging. Therefore, it is a crucial task to look for alternatives that generate correlated phonons. To achieve this, one can rely on the well-known Mollow triplet [216], where by continuously driving a two-level system, the sidebands of the emitted spectrum are correlated, similar to the nondegenerate parametric amplifier. Additionally, recent experiments with superconducting qubits have demonstrated entangled correlated photons [217]. In this implementation, the parametric amplifier would be substituted by a driven two-level system, whose output is coupled into a single waveguide. The correlated photons would then continuously drive two two-level systems, as in our protocols. An initial exploration of this protocol has led to positive results. It requires, however, putting cavities around the qubits to filter out the unwanted modes. Still, the achievable amount of entanglement is an open question.

This thesis also opens another completely new direction of research. That is, instead of relying on a two-mode squeezing interaction to produce two-mode squeezes states, one could explore more exotic Hamiltonians with richer and more intricate structures. Both general Gaussian and non-Gaussian states of light can be considered. For the general Gaussian states, exploring the output of a generic quadratic Hamiltonian and using it to drive individual qubits can lead to the formation of complex qubit networks. We performed initial research along those lines, where we drive multiple qubits by the output of a bosonic Kitaev chain [218], and we observed how the correlations from the bosonic system mapped onto the qubit networks. However, initial work showed that this qubit state is not pure. It remains an open question how one could either purify those states or make use of the entanglement present in such a mixed state. For that, the size of the bosonic system plays a crucial role. It is still an open question to what degree we can use the phase-space representations from Sec. 2.5 to obtain stochastic master equations for the qubits, as well as the use of the continued fraction method from Sec. 5.1.3.

The final chapter revealed a completely different effect. Namely, the generation of possible entanglement as a byproduct of the non-Markovianity of the photon source. While outside the scope of remote entanglement distribution, this effect can be used to explore other areas, such as many-body effects. By considering a large and complex system in contact with such a non-Markovian reservoir, one could explore how the phase transition of such a many-body system changes.

# Appendix A

# Effective master equation for the qubit system

As stated in the thesis, after the adiabatic elimination of the waveguide, we obtain a master equation describing both the bosonic degrees of freedom and the qubits. In general, it takes the following form

$$\dot{\rho} = \left(\mathcal{L}_{\mathrm{ph}} + \mathcal{L}_{\mathrm{q}} + \mathcal{L}_{\mathrm{int}}\right)\rho. \tag{A.1}$$

Here, we have split it into three distinct terms

$$\mathcal{L}_{\mathrm{ph}}\rho = -i\left[\sum_n \omega_{\mathrm{ph},n}\hat{a}_n^\dagger\hat{a}_n + \hat{H}_{\mathrm{ph}}, \rho\right] + \sum_n \kappa_n \mathcal{D}[\hat{a}_n]\rho, \tag{A.2a}$$

$$\mathcal{L}_{\mathrm{q}}\rho = -i\left[\sum_n \frac{\omega_n}{2}\hat{\sigma}_n^z + \hat{H}_{\mathrm{q}}, \rho\right] + \sum_n \gamma_n \mathcal{D}[\hat{\sigma}_n^-]\rho, \tag{A.2b}$$

$$\mathcal{L}_{\mathrm{int}}\rho = \sum_n \sqrt{\nu^n\kappa_n\gamma_n}\left([\hat{a}_n\rho, \hat{\sigma}_n^+] + [\hat{\sigma}_n^-, \rho\hat{a}_n^\dagger]\right), \tag{A.2c}$$

where each of them describes the bosonic subsystem of $n$-modes, the qubit subsystem, and its interaction, respectively. Moreover, we have explicitly written down the bare Hamiltonian with the natural frequencies of each system. The oscillation frequencies are the largest scales in the system. Specifically, $\omega_{\mathrm{ph},n} \sim \omega_n \gg \kappa_n \gg \gamma_n$ and any parameters encoded in the remaining Hamiltonians.

To proceed, we need to go to a rotating frame with respect to the bare frequencies of the bosonic modes $\omega_{\mathrm{ph},n}$. In this frame, the bare frequencies of the qubit system $\omega_n$ are detuned by $\delta_n = \omega_n - \omega_{\mathrm{ph},n}$. They will be either zero (on resonance) or small with respect to the decay rate of the photons $\kappa_n$.

After this transformation, the master equation describes a system with two distinct timescales. On one hand, the photon source is governed by $1/\kappa$. On the other hand, the qubits are governed by $1/\gamma$. Here, we are interested in the regime where the photon timescales are much faster than the qubits. This is achieved by setting $\kappa \to \infty$.

Our goal then is to perform another adiabatic elimination, this time of the fast system, allowing us to obtain an effective description of the slow system alone. For that, we follow the adiabatic elimination given in Ref. [99]. Alternatively, the same adiabatic elimination can be performed using the projector operator approach [219].

We start by taking our initial Lindblad master equation Eq. (A.1) in the rotated basis and go to an interaction picture with respect to the free evolution, $\mathcal{L}_0$, by writing $\rho(t) = e^{\mathcal{L}_0 t}\rho_{\rm I}(t)$. In this representation, the master equation reads as $\dot{\rho}_{\rm I}(t) = \mathcal{L}_{\rm int}(t)\rho_{\rm I}(t)$ with time-dependent interaction $\mathcal{L}_{\rm int}(t) = e^{-\mathcal{L}_0 t}\mathcal{L}_{\rm int}e^{\mathcal{L}_0 t}$.

We then derive a master equation for the qubit subsystem after tracing out the bosonic degrees of freedom $\rho_{\rm q,I} = {\rm Tr}_{\rm ph}\{\rho_{\rm I}(t)\}$. First, we make use of the *Born* approximation by replacing the full density operator by the tensor product $\rho_{\rm I}(t) \simeq \rho_{\rm q,I}(t) \otimes \rho^0_{\rm ph}$, where $\rho^0_{\rm ph}$ is the steady state density matrix of the bosonic subsystem, $\mathcal{L}_{\rm ph}\rho^0_{\rm ph} = 0$. Following standard second-order perturbation theory, we find

$$\dot{\rho}_{\rm q,I}(t) = \int_{-\infty}^{t} {\rm d}t'\, {\rm Tr}_{\rm ph}\{\mathcal{L}_{\rm int}(t)\mathcal{L}_{\rm int}(t')\rho_{\rm q,I}(t') \otimes \rho^0_{\rm ph}\}. \tag{A.3}$$

By explicitly inserting the expression of $\mathcal{L}_{\rm int}(t')$, we obtain

$$\begin{aligned}\dot{\rho}_{\rm q,I}(t) = \sum_m \sqrt{\nu^m\kappa_m\gamma_m}\int_{-\infty}^{t} {\rm d}t'\, {\rm Tr}_{\rm ph}\{\mathcal{L}_{\rm int}(t)\\ \times \Big([\hat{a}_m(t')(\rho_{\rm q,I}(t')\otimes\rho^0_{\rm ph}), \hat{\sigma}^+_m(t')] + [\hat{\sigma}^-_m(t'), (\rho_{\rm q,I}(t')\otimes\rho^0_{\rm ph})\hat{a}^\dagger_m(t')]\Big)\}.\end{aligned} \tag{A.4}$$

where each time-dependent operator is given by $\hat{a}_m(t') = e^{-\mathcal{L}_{\rm ph}t'}\hat{a}_m e^{\mathcal{L}_{\rm ph}t'}$ and $\hat{\sigma}^-_m(t') = e^{-\mathcal{L}_{\rm q}t'}\hat{\sigma}^-_m e^{\mathcal{L}_{\rm q}t'}$. By acting with the other superoperator $\mathcal{L}_{\rm int}(t')$, we now obtain the following expression

$$\begin{aligned}\dot{\rho}_{\rm q,I}(t) =& \sum_{n,m}\int_{-\infty}^{t} {\rm d}t' \times \\ & {\rm Tr}_{\rm ph}\Big\{[\hat{a}_n(t)[\hat{a}_m(t')\rho(t'), \hat{\sigma}^+_m(t')], \hat{\sigma}^+_n(t)] + [\hat{a}_n(t)[\hat{\sigma}^-_m(t'), \rho(t')\hat{a}^\dagger_m(t')], \hat{\sigma}^+_n(t)] \\ & + [\hat{\sigma}^-_n(t), [\hat{a}_m(t')\rho(t'), \hat{\sigma}^+_m(t')]\hat{a}^\dagger_n(t)] + [\hat{\sigma}^-_n(t), [\hat{\sigma}^-_m(t'), \rho(t')\hat{a}^\dagger_m(t')]\hat{a}^\dagger_n(t)]\Big\}.\end{aligned} \tag{A.5}$$

Here, we have used the compact state notion $\rho(t) \equiv \rho_{\rm q,I}(t) \otimes \rho^0_{\rm ph}$ and have not written down the prefactor $\sqrt{\nu^m\nu^n\kappa_m\kappa_n\gamma_m\gamma_n}$ to avoid overwriting. We can now trace out the bosonic degrees of freedom

$$\begin{aligned}\dot{\rho}_{\rm q,I}(t) = \sum_{n,m}\int_{-\infty}^{t} {\rm d}t' \Big( & {\rm Tr}_{\rm ph}\Big\{\hat{a}_n(t)\hat{a}_m(t')\rho^0_{\rm ph}\Big\}[\hat{\sigma}^+_n(t), [\hat{\sigma}^+_m(t'), \rho_{\rm q,I}(t')]] \\ & - {\rm Tr}_{\rm ph}\Big\{\hat{a}^\dagger_m(t')\hat{a}_n(t)\rho^0_{\rm ph}\Big\}[\hat{\sigma}^+_n(t), [\hat{\sigma}^-_m(t'), \rho_{\rm q,I}(t')]] \\ & - {\rm Tr}_{\rm ph}\Big\{\hat{a}^\dagger_n(t)\hat{a}_m(t')\rho^0_{\rm ph}\Big\}[\hat{\sigma}^-_n(t), [\hat{\sigma}^+_m(t'), \rho_{\rm q,I}(t')]] \\ & + {\rm Tr}_{\rm ph}\Big\{\hat{a}^\dagger_m(t')\hat{a}^\dagger_n(t)\rho^0_{\rm ph}\Big\}[\hat{\sigma}^-_n(t), [\hat{\sigma}^-_m(t'), \rho_{\rm q,I}(t')]]\Big).\end{aligned} \tag{A.6}$$

To obtain this expression, we have used the cyclic property of the trace to order the bosonic operators and used the commutator property $[A, B] = -[B, A]$. As the bandwidth $\kappa_n$ of the photons is very large, or in other words, the correlation time $1/\kappa_n$ is very short, we can use the *Markov* approximation, $\rho_{\mathrm{q,I}}(t') \simeq \rho_{\mathrm{q,I}}(t)$. By defining $\tau = t - t'$, we can rewrite our equation the following compact form

$$\dot{\rho}_{\mathrm{q,I}}(t) = \sum_{n,m} \sqrt{\nu^m \nu^n \gamma_n \gamma_m} \sum_{s,s'=\pm} \int_0^\infty \mathrm{d}\tau \, C_{n,m}^{s,s'}(\tau) \, ss' [\sigma_n^{-s}(t), [\sigma_m^{-s'}(t-\tau), \rho_{\mathrm{q,I}}(t)]]. \quad \text{(A.7)}$$

Here, we have introduced the bosonic correlation functions

$$C_{n,m}^{s,s'}(\tau) = \sqrt{\kappa_n \kappa_m} \langle : \hat{a}_n^s(\tau) \hat{a}_m^{s'}(0) : \rangle, \quad \text{(A.8)}$$

where we identified $\hat{a}_n^+ \equiv \hat{a}_n^\dagger$ and $\hat{a}_n^- \equiv \hat{a}_n$ and assumed the normal ordering prescription $\langle : \hat{a}^s(\tau)\hat{a}(0) : \rangle = \mathrm{Tr}_{\mathrm{ph}}\{\hat{a}^s e^{\mathcal{L}_{\mathrm{ph}}\tau}(\hat{a}\rho_{\mathrm{ph}}^0)\} = \langle \hat{a}^s(\tau)\hat{a}(0) \rangle$, while $\langle : \hat{a}^s(\tau)\hat{a}^\dagger(0) : \rangle = \mathrm{Tr}_{\mathrm{ph}}\{\hat{a}^s e^{\mathcal{L}_{\mathrm{ph}}\tau}(\rho_{\mathrm{ph}}^0 \hat{a}^\dagger)\} = \langle \hat{a}^\dagger(0)\hat{a}^s(\tau) \rangle$. Finally, consistent with the Markov approximation, the slow dynamics of the qubits can be neglected. Then, after going back to the Schrödinger equation, the resulting qubit master equation takes the following form

$$\dot{\rho}_{\mathrm{q}}(t) = \mathcal{L}_{\mathrm{q}}\rho_{\mathrm{q}}(t) + \sum_{n,m} \sqrt{\nu^m \nu^n \gamma_n \gamma_m} \sum_{s,s'=\pm} ss' I_{n,m}^{s,s'}(0) [\sigma_n^{-s}, [\sigma_m^{-s'}, \rho_{\mathrm{q}}(t)]], \quad \text{(A.9)}$$

where $I_{n,m}^{s,s'}(\omega) = \int_0^\infty \mathrm{d}\tau \, C_{n,m}^{s,s'}(\tau) e^{-i\omega\tau}$ is evaluated at resonance $\omega = 0$. Therefore, the master equation for the qubits system is governed by the output spectrum of the bosonic system evaluated at resonance. Depending on the spectrum correlations $I(\omega)$ of the bosonic system, we obtain different master equations. In Sec. 2.4, we derived the spectrum correlations for the two-mode squeezed state and the thermal state, which we use now to find the corresponding master equations.

## A.1 Nondegenerate parametric amplifier

This case was studied in both Chapter 3 and Chapter 4. For the first case, our master equation in Eq. (3.1) is completely equivalent to Eq. (A.1) in the rotated frame. For the second case, we identify the coupling operators as $\hat{L}_n \to \sigma_n^-$ and $\hat{L}_n^\dagger \to \sigma_n^+$. In Sec. 2.4.2, we derived the general expressions for the spectrum, which we now evaluate at resonance. First of all, we need to match our notation from this section to Sec. 2.4.2. For that, we identify $I_{n,m}^{s,s'}(\omega) = I_{\hat{a}_n^s \hat{a}_m^{s'}}(\omega)$. Then, we find that for the parametric amplifier, some of them vanish $I_{A,A}^{s,s}(\omega) = I_{B,B}^{s,s}(\omega) = I_{A,B}^{s,-s}(\omega) = I_{B,A}^{s,-s}(\omega) = 0$. The non-vanishing spectrum can be regrouped together with into the final expression for the master equation, which is given by

$$\begin{aligned}\dot{\rho}_{\mathrm{q}} =& \mathcal{L}_{\mathrm{q}}\rho_{\mathrm{q}} + \sum_{n=A,B}\gamma_n N_n\left(\mathcal{D}[\hat{\sigma}_n^-]\rho_{\mathrm{q}} + \mathcal{D}[\hat{\sigma}_n^+]\rho_{\mathrm{q}}\right)\\ &+\sqrt{\gamma_A\gamma_B}\left(M^*[\hat{\sigma}_A,[\hat{\sigma}_B,\rho_{\mathrm{q}}]] + M[\hat{\sigma}_A^+,[\hat{\sigma}_B^+,\rho_{\mathrm{q}}]]\right),\end{aligned} \tag{A.10}$$

where we have defined the occupation number $N_n = 2\nu\mathrm{Re}\{I_{n,n}^{+,-}(0)\}$ and the correlation number $M = \nu(I_{A,B}^{-,-}(0) + I_{B,A}^{-,-}(0))$. Taking the expressions from Eq. (2.101), those parameters take the simple form of given in Eq. (3.7a) and Eq. (3.7b).

## A.2 Thermal cavity

For the specific case of a thermal cavity studied in Chapter 5, from Eq. (5.6) we have a single mode $\hat{a}$ and we identify $\hat{L} \to \hat{\sigma}^-$ and $\hat{L}^\dagger \to \hat{\sigma}^+$. We also go to a rotating frame with respect to the thermal cavity at $\omega_{\mathrm{c}}$ to obtain an equivalent master equation to our starting equation. Then, in Sec. 2.4.1, we derived the two-time correlation function and the spectrum for the thermal cavity. The two-sided cavity only adds small corrections to the expressions evaluated there. Specifically, the two-time correlation function now reads

$$\langle\hat{a}^\dagger(\tau)\hat{a}(0)\rangle = \frac{\kappa_1 n_{\mathrm{th}}}{\kappa_1+\kappa_2}e^{-(\kappa_1+\kappa_2)/2|\tau|}, \tag{A.11}$$

where $\kappa_1$ is the decay rate of the hot reservoir and $\kappa_2$ is the decay rate to the cold waveguide. Therefore, the output spectrum to the cold reservoir, contrary to Eq. (2.88), and given by

$$I_{\hat{a}^\dagger\hat{a}}(\omega) = \frac{2\kappa_1\kappa_2 n_{\mathrm{th}}}{(\kappa_1+\kappa_2)^2+4\omega^2} - i\frac{4\kappa_1\kappa_2 n_{\mathrm{th}}\omega}{(\kappa_1+\kappa_2)((\kappa_1+\kappa_2)^2+4\omega^2)}. \tag{A.12}$$

According to Eq. (A.9), we evaluate this expression on resonance, which simplifies the spectrum to

$$I_{\hat{a}^\dagger\hat{a}}(0) = n_{\mathrm{th}}/2, \tag{A.13}$$

where we have assumed a symmetric two-sided cavity $\kappa_1 = \kappa_2 = \kappa$ as in Chapter 5. This allows us to identify the occupation number parameter $N = 2\nu I_{\hat{a}^\dagger\hat{a}}(0) = \nu n_{\mathrm{th}}$, for which the master equation for the two qubits is

$$\dot{\rho}_{\mathrm{q}} = \mathcal{L}_{\mathrm{q}}\rho_{\mathrm{q}} + \nu n_{\mathrm{th}}\gamma\mathcal{D}[\hat{L}]\rho_{\mathrm{q}} + \nu n_{\mathrm{th}}\gamma\mathcal{D}[\hat{L}^\dagger]\rho_{\mathrm{q}}, \tag{A.14}$$

which is the same result as in Eq. (5.9) when $\nu = 1$.

# Appendix B

# Uniqueness of the steady state

In Chapter 3 and Chapter 4, the master equation for $N_{\mathrm{q}}$ qubit pairs in the ideal Markovian regime is given by

$$\dot{\rho}_{\mathrm{q}} = \mathcal{L}_{N_{\mathrm{q}}}\rho_{\mathrm{q}} = -i[\hat{H}_{\mathrm{q}}, \rho_{\mathrm{q}}] + \sum_{n=A,B} \gamma\mathcal{D}[\hat{J}_n]\rho_{\mathrm{q}}. \tag{B.1}$$

It is clear that given a state $|\psi_0\rangle$ that satisfies the dark-state conditions $\hat{J}_n|\psi_0\rangle = 0$ and $\hat{H}_{\mathrm{q}}|\psi_0\rangle = 0$, the density operator $\rho_0 = |\psi_0\rangle\langle\psi_0|$ is a pure steady state of this master equation, i.e. $\mathcal{L}_{N_{\mathrm{q}}}\rho_0 = 0$. However, this condition does not guarantee that $\rho_0$ is the unique steady state, as there could be other mixed or pure states $\rho_0'$ with $\mathcal{L}_{N_{\mathrm{q}}}\rho_0' = 0$.

To prove that the state $|\psi_0(r, \vec{\delta}_A, P)\rangle$ defined in Eq. (4.24) is indeed the unique steady state of the network for a given detuning pattern $\vec{\delta}_A$ and permutation $P$, we start with the case $N_{\mathrm{q}} = 1$ and $\delta_{A,1} = -\delta_{B,1}$. In this case, we can calculate the eigenvalues of the Liouvillian $\mathcal{L}_{N_{\mathrm{q}}=1}$ analytically and verify that for any finite squeezing strength $r$ there is only a single eigenvalue $\lambda_0 = 0$, which corresponds to the state $\rho_0^{(N_{\mathrm{q}}=1)} = |\Phi^+_{1,1}\rangle\langle\Phi^+_{1,1}|$. We also find that the smallest non-zero eigenvalue is $\lambda_1 = \gamma\cosh(2r)/2$ for $r < r^*$ and $\lambda_1 = \gamma(6\cosh(2r) - \sqrt{18\cosh(4r) - 14})/4$ for $r > r^*$, where $r^* \simeq 0.356$. This eigenvalue determines the gap in the Liouvillian spectrum and, therefore, for any finite $r$, there is a finite relaxation rate toward the steady state.

We prove the uniqueness of the steady state by induction. We assume that we already know that the product state $\rho_0^{(N_{\mathrm{q}})} = |\Phi_\parallel(N_{\mathrm{q}})\rangle\langle\Phi_\parallel(N_{\mathrm{q}})|$ defined in Eq. (4.21) is the unique steady state of $\mathcal{L}_{N_{\mathrm{q}}}$ for $\vec{\delta}_{A,i} = -\vec{\delta}_{B,i}$ and that it satisfies the dark-state conditions $\hat{J}_n|\Phi_\parallel(N_{\mathrm{q}})\rangle = 0$ and $\hat{H}_{\mathrm{q}}|\Phi_\parallel(N_{\mathrm{q}})\rangle = 0$. We now show that under this assumption, it is also true that $\rho_0^{(N_{\mathrm{q}}+1)}$ is the unique steady state of the network with $N_{\mathrm{q}} + 1$ qubit pairs.

Let us first verify that $|\Phi_\parallel(N_{\mathrm{q}} + 1)\rangle$ is a dark state. The conditions $\hat{J}_n|\Phi_\parallel(N_{\mathrm{q}} + 1)\rangle = 0$ are straightforward to verify since it holds for each qubit pair individually. For the second condition, $\hat{H}_{\mathrm{q}}|\Phi_\parallel(N_{\mathrm{q}} + 1)\rangle = 0$, we write the Hamiltonian as

$$\hat{H}_{\mathrm{q}}^{(N+1)} = \hat{H}_{\mathrm{q}}^{(N_{\mathrm{q}})} - i\frac{\gamma}{2}\sum_n \left(\hat{L}_n(N_{\mathrm{q}})\hat{\sigma}^+_{n,N_{\mathrm{q}}+1} - \hat{L}_n^\dagger(N_{\mathrm{q}})\hat{\sigma}_{n,N_{\mathrm{q}}+1}\right), \tag{B.2}$$

and recall that

$$|\Phi_{\parallel}(N_{\rm q}+1)\rangle \sim |\Phi_{\parallel}(N_{\rm q})\rangle \otimes (\cosh(r)|0_{A,N_{\rm q}+1}\rangle|0_{B,N_{\rm q}+1}\rangle + \sinh(r)|1_{A,N_{\rm q}+1}\rangle|1_{B,N_{\rm q}+1}\rangle). \quad (B.3)$$

It follows that

$$\begin{aligned}\hat{H}_{\rm q}^{(N_{\rm q}+1)}|\Phi_{\parallel}(N_{\rm q}+1)\rangle &\sim \Big[\cosh(r)L_A(N_{\rm q}) - \sinh(r)L_B^\dagger(N_{\rm q})\Big]\,|\Phi_{\parallel}(N_{\rm q})\rangle \otimes |1_{A,N_{\rm q}+1}\rangle|0_{B,N_{\rm q}+1}\rangle \\ &+ \Big[\cosh(r)L_B(N_{\rm q}) - \sinh(r)L_A^\dagger(N_{\rm q})\Big]\,|\Phi_{\parallel}(N_{\rm q})\rangle \otimes |0_{A,N_{\rm q}+1}\rangle|1_{B,N_{\rm q}+1}\rangle = 0.\end{aligned} \quad (B.4)$$

To prove that $\rho_0^{(N_{\rm q}+1)}$ is also the unique steady state, we use the fact that in a fully directional network the reduced steady state of the first $N_{\rm q}$ pairs of qubits, $\rho_0^{(N_{\rm q})} = {\rm Tr}_{i=N_{\rm q}+1}\{\rho_0^{(N_{\rm q}+1)}\}$ is unaffected by adding an additional pair. Further, because $\rho_0^{(N_{\rm q})}$ is pure, there is no entanglement between the subsystems and we can write $\rho_0^{(N_{\rm q}+1)} = \rho_0^{(N_{\rm q})} \otimes \rho_0^{(x)}$, with a steady state $\rho_0^{(x)}$ for the last pair, which still must be determined (to simplify notation, we use the index $x$ to refer to the extra qubit pair with index $i = N_{\rm q}+1$). To do so, we write

$$\dot{\rho}_0^{(N_{\rm q}+1)} = \mathcal{L}_{N_{\rm q}}\rho_0^{(N_{\rm q})} \otimes \rho_0^{(x)} + \rho_0^{(N_{\rm q})} \otimes \mathcal{L}_x\rho_0^{(x)} + \mathcal{L}_{N_{\rm q}-x}\rho_0^{(N_{\rm q}+1)}. \quad (B.5)$$

Here $\mathcal{L}_x \widehat{=} \mathcal{L}_{N_{\rm q}=1}$ is the single-pair Liouville operator acting on the state of the last qubit pair and

$$\begin{aligned}\mathcal{L}_{N_{\rm q}-x}\rho_0^{(N_{\rm q}+1)} = &-\frac{\gamma}{2}\sum_{n=A,B}\Big[\hat{L}_n(N_{\rm q})\hat{\sigma}_{n,x}^+ - \hat{L}_n^\dagger(N_{\rm q})\hat{\sigma}_{n,x}^-, \rho_0^{(N_{\rm q}+1)}\Big] \\ &-\frac{\gamma}{2}\Big\{\hat{J}_A^\dagger(N_{\rm q})\Big(\cosh(r)\hat{\sigma}_{A,x}^- - \sinh(r)\hat{\sigma}_{B,x}^+\Big) \\ &+ \hat{J}_B^\dagger(N_{\rm q})\Big(\cosh(r)\hat{\sigma}_{B,x}^- - \sinh(r)\hat{\sigma}_{A,x}^+\Big), \rho_0^{(N_{\rm q}+1)}\Big\}_+,\end{aligned} \quad (B.6)$$

accounts for the remaining cross terms. Note that here we have already used that $\hat{J}_n(N_{\rm q})\rho_0^{(N_{\rm q}+1)} = \rho_0^{(N_{\rm q}+1)}\hat{J}_n^\dagger = 0$ due to the dark-state condition for $|\Phi_{\parallel}(N_{\rm q})\rangle$. By looking at all the different contributions in Eq. (B.6) we can collect terms such as

$$\begin{aligned}&\Big[-\hat{L}_A(N_{\rm q}) + \sinh(r)\hat{J}_B^\dagger(N_{\rm q})\Big]\,\hat{\sigma}_{A,x}^+\rho_0^{(N_{\rm q}+1)} = \\ &= \Big[-\hat{L}_A(N_{\rm q}) + \sinh(r)\cosh(r)\hat{L}_B^\dagger(N_{\rm q}) - \sinh^2(r)\hat{L}_A(N_{\rm q})\Big]\,\hat{\sigma}_{A,x}^+\rho_0^{(N_{\rm q}+1)} \\ &= -\cosh(r)\,\underbrace{\Big[\cosh(r)\hat{L}_A(N_{\rm q}) - \sinh(r)\hat{L}_B^\dagger(N_{\rm q})\Big]}_{=\hat{J}_A(N_{\rm q})}\,\hat{\sigma}_{A,x}^+\rho_0^{(N_{\rm q}+1)} = 0,\end{aligned} \quad (B.7)$$

and find that they vanish independently of $\rho_0^{(x)}$. The same is true for other combinations such that $\mathcal{L}_{N_{\rm q}-x}\rho_0^{(N_{\rm q}+1)} = 0$. Therefore, when tracing over the first $N_{\rm q}$ qubit pairs, the steady state $\rho_0^{(x)}$ satisfies

$$\rho_0^{(x)} = \mathcal{L}_x \rho_0^{(x)} = 0, \tag{B.8}$$

which has a unique solution given by $\rho_0^{(x)} = |\Phi_x^+\rangle\langle\Phi_x^+|$.

Finally, we consider non-trivial detuning patterns $\vec{\delta}_B = -P\vec{\delta}_A$ and show that also in this case the steady state $\rho_0^{(N_\mathrm{q})} = |\psi_0(r, \vec{\delta}_A, P)\rangle\langle\psi_0(r, \vec{\delta}_A, P)|$ is unique. This can be done by simply assuming that there is another steady state $\rho_0' \neq \rho_0^{(N_\mathrm{q})}$ of the Liouvillian $\mathcal{L}_{N_\mathrm{q}}$. Then we can simply invert the arguments about the form invariance of the master equation presented in Chapter 4, below Eq. (4.23), and obtain a steady state for the network with $\vec{\delta}_B = -\vec{\delta}_A$,

$$\rho_0'(\vec{\delta}_B = -\vec{\delta}_A) = \hat{\mathcal{U}}^\dagger \rho_0' \hat{\mathcal{U}}, \qquad \hat{\mathcal{U}} = \prod_\sigma \hat{U}_{i_\sigma, i_\sigma+1}. \tag{B.9}$$

However, since we know that there is only one unique steady state for this detuning pattern, it means that $\rho_0'(\vec{\delta}_B = -\vec{\delta}_A) = |\Phi_\parallel(N_\mathrm{q})\rangle\langle\Phi_\parallel(N_\mathrm{q})|$ and $\rho_0' = |\psi_0(r, \vec{\delta}_A, P)\rangle\langle\psi_0(r, \vec{\delta}_A, P)|$.

# Appendix C

# Continued fraction method

Here, we present the derivation of the continued fraction method described in Sec. 5.1.3, where we obtain a solution of a stochastic differential matrix equation in terms of an infinite set of algebraic equations, which we can then express as a matrix continued fraction. We start with our stochastic master equation from Eq. (5.16)

$$\dot{\rho}_{\mathrm{q}}(\alpha, \alpha^*, t) = (\mathcal{L}_0 + \alpha\mathcal{L}_+ + \alpha^*\mathcal{L}_-)\, \rho_{\mathrm{q}}(\alpha, \alpha^*, t), \tag{C.1}$$

where we explicitly split our Liouvillian into a deterministic term $\mathcal{L}_0$ and two stochastic contributions $\mathcal{L}_{\pm}$. As the stochastic variable $\alpha$ can be described by the Fokker-Planck equation in Eq. (5.10), the stochastic master equation takes the form [200]

$$\left(\frac{\mathrm{d}}{\mathrm{d}t} + L(\alpha, \alpha^*)\right) \rho_{\mathrm{q}}(\alpha, \alpha^*, t) = \mathcal{L}(\alpha, \alpha^*)\rho_{\mathrm{q}}(\alpha, \alpha^*, t). \tag{C.2}$$

From this expression, observe that the averaged solution could be obtained from

$$\rho_{\mathrm{q}}(t) = \langle \rho_{\mathrm{q}}(\alpha, \alpha^*, t)\rangle = \int \mathrm{d}\alpha^2 \rho_{\mathrm{q}}(\alpha, \alpha^*, t). \tag{C.3}$$

To solve Eq. (C.2), we use the biorthogonal basis given by Eq. (5.21) and Eq. (5.22). This new basis allows us to expand our initial state as

$$\rho_{\mathrm{q}}(\alpha, \alpha^*, t) = \sum_{n,m} P_{m,n}(\alpha, \alpha^*)\rho^{m,n}(t), \tag{C.4}$$

where the coefficients are given by

$$\rho^{m,n}(t) = \int \mathrm{d}\alpha^2 \phi^*_{m,n}(\alpha, \alpha^*)\rho_{\mathrm{q}}(\alpha, \alpha^*, t) = \langle \phi^*_{m,n}(\alpha, \alpha^*)\rho_{\mathrm{q}}(\alpha, \alpha^*, t)\rangle. \tag{C.5}$$

To obtain this expression, we have used the orthogonal relation given by Eq. (5.23). As stated in Sec. 5.1.3, the averaged solution is given by $\rho_{\mathrm{q}}(t) = \rho^{0,0}(t)$. We calculate the equations of motion for $\rho^{m,n}(t)$ by expressing Eq.(C.2) in this new basis, obtaining

$$\begin{aligned}\left(\frac{\mathrm{d}}{\mathrm{d}t}+\Lambda_{m,n}\right)\rho^{m,n}(t) &= \sum_{m',n'}\int \mathrm{d}^2\alpha\phi^*_{m,n}(\alpha,\alpha^*)\mathcal{L}(\alpha,\alpha^*)P_{m',n'}(\alpha,\alpha^*)\rho^{m',n'}(t)\\ &= \mathcal{L}_0\rho^{m,n}(t)\\ &\quad+\sum_{m',n'}\int \mathrm{d}^2\alpha\phi^*_{m,n}(\alpha,\alpha^*)\alpha\mathcal{L}_+P_{m',n'}(\alpha,\alpha^*)\rho^{m',n'}(t)\\ &\quad+\sum_{m',n'}\int \mathrm{d}^2\alpha\phi^*_{m,n}(\alpha,\alpha^*)\alpha^*\mathcal{L}_-P_{m',n'}(\alpha,\alpha^*)\rho^{m',n'}(t).\end{aligned} \tag{C.6}$$

To solve this equation of motion, we need to use the recursion relations for the generalized Laguerre polynomials [220]

$$L_n^{m-1}(x) = L_n^m(x) - L_{n-1}^m(x), \tag{C.7a}$$
$$xL_n^{m+1}(x) = (N+m+1)L_n^m(x) - (n+1)L_{n+1}^m(x), \tag{C.7b}$$

which then allows us to evaluate Eq. (C.6). However, we need to evaluate 3 different cases depending on the value of $m$. For $m=0$, they reduce to

$$\begin{aligned}\left(\frac{\mathrm{d}}{\mathrm{d}t}+2\kappa n\right)\rho^{0,n}(t) &= \mathcal{L}_0\rho^{0,n}(t)\\ &\quad+\sqrt{\frac{n_{\mathrm{th}}}{2}}\mathcal{L}_+\left(\sqrt{n+1}\rho^{1,n}(t)-\sqrt{n}\rho^{1,n-1}(t)\right)\\ &\quad+\sqrt{\frac{n_{\mathrm{th}}}{2}}\mathcal{L}_-\left(\sqrt{n+1}\rho^{-1,n}(t)-\sqrt{n}\rho^{-1,n-1}(t)\right).\end{aligned} \tag{C.8}$$

For $m>0$, they are

$$\begin{aligned}\left(\frac{\mathrm{d}}{\mathrm{d}t}+\kappa(2n+m)\right)\rho^{m,n}(t) &= \mathcal{L}_0\rho^{m,n}(t)\\ &\quad+\sqrt{\frac{n_{\mathrm{th}}}{2}}\mathcal{L}_+\left(\sqrt{n+m+1}\rho^{m+1,n}(t)-\sqrt{n}\rho^{m+1,n-1}(t)\right)\\ &\quad+\sqrt{\frac{n_{\mathrm{th}}}{2}}\mathcal{L}_-\left(\sqrt{n+m}\rho^{m-1,n}(t)-\sqrt{n+1}\rho^{m-1,n+1}(t)\right),\end{aligned} \tag{C.9}$$

and lastly, for $m<0$, we obtain

$$\begin{aligned}\left(\frac{\mathrm{d}}{\mathrm{d}t}+\kappa(2n+|m|)\right)\rho^{m,n}(t) &= \mathcal{L}_0\rho^{m,n}(t)\\ &\quad+\sqrt{\frac{n_{\mathrm{th}}}{2}}\mathcal{L}_+\left(\sqrt{n+|m|}\rho^{m+1,n}(t)-\sqrt{n+1}\rho^{m+1,n+1}(t)\right)\\ &\quad+\sqrt{\frac{n_{\mathrm{th}}}{2}}\mathcal{L}_-\left(\sqrt{n+|m|+1}\rho^{m-1,n}(t)-\sqrt{n}\rho^{m-1,n-1}(t)\right).\end{aligned} \tag{C.10}$$

This is the most general formulation, which gives an infinite set of coupled differential equations for $n = 0, 1, 2...$ and $m = 0, \pm1, \pm2, ....$ Focusing on the steady state, those differential equations transform into an infinite set of algebraic equations, from which we want to solve for $\rho^{0,0}$. Depending on $\mathcal{L}_\pm$, the structure of the set of algebraic equations simplifies considerably. In our specific system, by explicit evaluation of Eq. (C.8), Eq. (C.9), and Eq. (C.10), we observe that $m = 0$ only couples to $m = \pm1$ and $m = \pm2$. Therefore, our infinite set of algebraic equations reduce to a set of 5 coupled equations $\rho^{0,n}, \rho^{\pm1,n}$, and $\rho^{\pm2,n}$ for $n = 0, 1, 2, ....$ We can reduce this number further by integrating out $\rho^{\pm2,n}$, which leads to a set of coupled equations which can be cast in vector form. By defining $\sigma^n = (\rho^{0,n}, \rho^{1,n}, \rho^{-1,n})^{\mathrm{T}}$, the remaining equations can be written as the following matrix recursion

$$A_n\sigma^n + B_n\sigma^{n-1} + C_n\sigma^{n+1} = 0, \tag{C.11}$$

with matrices

$$A_n = \begin{pmatrix} 2n\kappa - \mathcal{L}_0 & -\sqrt{\frac{n_{\mathrm{th}}(n+1)}{2}}\mathcal{L}_+ & -\sqrt{\frac{n_{\mathrm{th}}(n+1)}{2}}\mathcal{L}_- \\ -\sqrt{\frac{n_{\mathrm{th}}(n+1)}{2}}\mathcal{L}_- & a_+ & 0 \\ -\sqrt{\frac{n_{\mathrm{th}}(n+1)}{2}}\mathcal{L}_+ & 0 & a_- \end{pmatrix}, \tag{C.12}$$

$$B_n = \sqrt{n}\begin{pmatrix} 0 & \sqrt{\frac{n_{\mathrm{th}}}{2}}\mathcal{L}_+ & \sqrt{\frac{n_{\mathrm{th}}}{2}}\mathcal{L}_- \\ 0 & \sqrt{n+1}\mathcal{P}_+^0 & 0 \\ 0 & 0 & \sqrt{n+1}\mathcal{P}_-^0 \end{pmatrix}, \tag{C.13}$$

$$C_n = \sqrt{n+1}\begin{pmatrix} 0 & 0 & 0 \\ \sqrt{\frac{n_{\mathrm{th}}}{2}}\mathcal{L}_- & \sqrt{n+2}\mathcal{P}_+^2 & 0 \\ \sqrt{\frac{n_{\mathrm{th}}}{2}}\mathcal{L}_+ & 0 & \sqrt{n+2}\mathcal{P}_-^2 \end{pmatrix}. \tag{C.14}$$

Here, we have defined the following matrix elements

$$a_\pm = \kappa(2n+1) - \mathcal{L}_0 - (n+2)\mathcal{P}_\pm^2 - n\mathcal{P}_\pm^0, \tag{C.15}$$

and

$$\mathcal{P}_\pm^x = \frac{n_{\mathrm{th}}}{2}\mathcal{L}_\pm[\kappa(2n+x) - \mathcal{L}_0]^{-1}\mathcal{L}_\mp. \tag{C.16}$$

This allows us to build the matrix continued fraction in Eq. (C.11) and solve it as [173]

$$\Big[A_0 + \mathcal{K}\Big]\sigma^0 = 0, \tag{C.17}$$

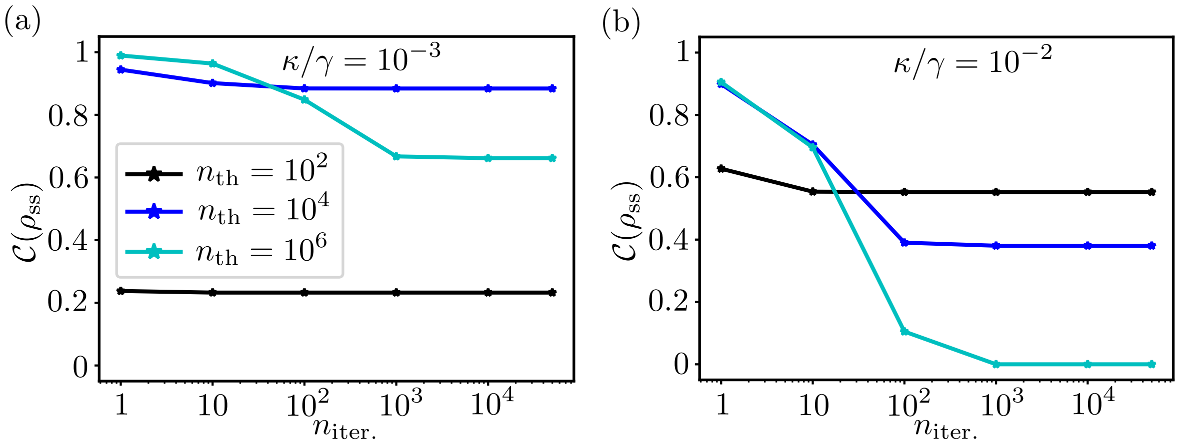


**Figure C.1:** Steady-state concurrence $\mathcal{C}(\rho_{\rm ss})$ as a function of the number of iterations $n_{\rm iter.}$ to solve Eq. (C.17) for different thermal occupation $n_{\rm th}$ at (a) $\kappa/\gamma = 10^{-3}$ and (b) $\kappa/\gamma = 10^{-2}$.

where the matrix continued fraction is given by

$$\mathcal{K} = C_0 \cfrac{\mathcal{I}}{-A_1 - C_1 \cfrac{\mathcal{I}}{-A_2 - C_2 \cfrac{\mathcal{I}}{-A_3 - \dots} B_2} B_2} B_1. \tag{C.18}$$

Solving this matrix continued fraction numerically involves numerically inverting an infinite amount of matrices. Therefore, we truncate this continued matrix fraction to some finite index $n_{\rm iter.}$. After numerically solving the matrix continued fraction, we can solve for $\sigma^0$, from which we obtain $\rho^{0,0}$, our averaged state. In Fig. C.1 we check the convergence of the continued fraction method by plotting the steady-state concurrence $\mathcal{C}(\rho_{\rm ss})$ as a function of the number of iterations $n_{\rm iter.}$ for different thermal occupation $n_{\rm th}$ and bandwidths $\kappa/\gamma$. We observe that for $n_{\rm th} \sim 10$, convergence is reached around $n_{\rm iter.} \sim 10$. In Chapter 5, the largest occupation number is $n_{\rm th} = 10^6$, which converges at $n_{\rm iter.} \sim 10^4$. We then use these references to numerically solve the matrix continued fraction, ensuring no truncation errors.

By truncating to first order, $n_{\rm iter.} = 0$, Eq. (C.17) reduces to

$$\left(\mathcal{L}_0 + \frac{n_{\rm th}}{2}\left[\mathcal{L}_+[\kappa\mathcal{I} - \mathcal{L}_0]^{-1}\mathcal{L}_- + \mathcal{L}_-[\kappa\mathcal{I} - \mathcal{L}_0]^{-1}\mathcal{L}_+\right]\right)\rho^{0,0} = 0. \tag{C.19}$$

One then recovers the Bourret approximation's results in Eq. (5.37) for the steady state as a solution to such an equation. Therefore, keeping the lowest-order contribution is equivalent to performing the decoupling approximation from Sec. 5.3.1.

## C.1 Effective model in the quasistatic limit

The method outlined before allows us to transform the stochastic master equation from Eq. (5.14) into an infinite set of algebraic equations (for the steady state), which can be solved, numerically, using a matrix continued fraction.

Here, we use this method to derive an effective analytical expression for the population of our qubits around the quasistatic limit described in Sec. 5.2. For that, we rely on a series of approximations which will allow us to simplify the problem considerably. We start by neglecting the population to the double excited state $\rho_{11}$. This is justified in Fig. 5.4(a), where the population $\rho_{11}$ is the smallest of the system for $\kappa \ll 1$. In this case, we explicitly evaluate the equations of motion for the populations and coherences produced by Eq. (C.11). Under this 3-level approximation, our equations of motion do not involve terms with $m = \pm 2$, which allows us to trace out the terms with $m = \pm 1$ to obtain the set of equations only for $m = 0$. We then use a more convenient notation $\rho^n \equiv \rho^{0,n}$ to express them. They read

$$(2\gamma + 2\kappa n)\, \rho_T^n = \frac{\gamma}{2}\chi_{S,T}^n - \sqrt{2\gamma\Phi}\left(\sqrt{n+1}\chi_{0,T}^n - \sqrt{n}\chi_{0,T}^{n-1}\right), \tag{C.20a}$$

$$2\kappa n \rho_S^n = -\frac{\gamma}{2}\chi_{S,T}^n, \tag{C.20b}$$

$$(\gamma + 2\kappa n)\chi_{S,T}^n = \gamma(\rho_S^n - \rho_T^n) - \sqrt{2\gamma\Phi}\left(\sqrt{n+1}\chi_{0,S}^n - \sqrt{n}\chi_{0,S}^{n-1}\right), \tag{C.20c}$$

$$\kappa(2n+1)\chi_{0,S}^n = -\frac{\gamma}{2}\chi_{0,T}^n + \sqrt{2\gamma\Phi(n+1)}\left(\chi_{S,T}^n - \chi_{S,T}^{n+1}\right), \tag{C.20d}$$

$$(\gamma + \kappa(2n+1))\,\chi_{0,T}^n = \frac{\gamma}{2}\chi_{0,S}^n - 2\sqrt{2\gamma\Phi(n+1)}\left(\rho_{0,0}^n - \rho_{0,0}^{n+1} - \rho_T^n + \rho_T^{n+1}\right), \tag{C.20e}$$

where we have reintroduced the photon flux parameter $\Phi = \kappa n_{\mathrm{th}}/2$ and defined $\chi_{i,j}^n = \rho_{i,j}^n + \rho_{j,i}^n$ for the coherences. The equation for the remaining population $\rho_{00}^n$, the ground state, follows from the normalization condition $\rho_{00}^n = \delta_{n,0} - \rho_S^n - \rho_T^n$, where $\delta_{n,0}$ is the Kronecker delta.

As a starting point, we recover the result from the static limit. Setting $\kappa = 0$ while $\Phi > 0$, most of the equations of motion vanish. The only non-vanishing equations can be recast as a three-term continued fraction for the steady-state population of the singlet. It reads

$$[\gamma + 8\Phi(2n+1)]\rho_S^n = 8\Phi(n+1)\rho_S^{n+1} + 8\Phi n\rho_S^{n-1} + 8\Phi(\delta_{n,0} - \delta_{n-1,0}). \tag{C.21}$$

This three-term ordinary recurrence relation has the general form of

$$a_n X^n = b_n X^{n+1} + c_n X^{n-1} + Y_0(\delta_{n,0} - \delta_{n-1,0}), \tag{C.22}$$

which can be solved in terms of a continued fraction as

$$X^0 = \frac{\mathcal{I}}{a_0 - c_0 \frac{\mathcal{I}}{a_1 - c_1 \frac{\mathcal{I}}{a_2 - \dots} b_2} b_1} \left(1 - c_0 \frac{\mathcal{I}}{a_1 - c_1 \frac{\mathcal{I}}{a_2 - \dots} b_2}\right) Y_0. \tag{C.23}$$

After some algebra, this gives the same result as in Eq. (5.32). An alternative method to solve this family of continued fractions as a solution to ordinary differential equations will be presented in Sec. C.1.1.

The static regime is the starting point of our effective model, as we want corrections around it. The main idea is that being close to the static regime, some states will be similar. For example, in the static limit, we found that $\chi^n_{S,T} = 0 \ \forall n$. The term $\chi^n_{S,T}$ corresponds to the coherence between the singlet and the triplet state. Therefore, we assume $\chi^n_{S,T} = 0 \ \forall n$ as a starting point. This assumption simplifies the previous equations of motion, reducing them to two coupled three-term recurrence relations

$$\begin{aligned}
&\left[\gamma - \frac{16\Phi\gamma^2(n+1)}{(\gamma + 2\kappa(2n+1))^2} - \frac{16\Phi\gamma^2 n}{(\gamma + 2\kappa(2n-1))^2}\right]\rho^n_T \\
&- \left[\gamma + \frac{8\Phi\gamma^2(n+1)}{(\gamma + 2\kappa(2n+1))^2} + \frac{8\Phi\gamma^2 n}{(\gamma + 2\kappa(2n-1))^2}\right]\rho^n_S = \\
&- \frac{8\gamma^2\Phi(n+1)}{(\gamma + 2\kappa(2n+1))^2}(\delta_{n,0} - \delta_{n+1,0} + \rho^{n+1}_S + 2\rho^{n+1}_T) \\
&+ \frac{8\gamma^2\Phi n}{(\gamma + 2\kappa(2n-1))^2}(\delta_{n-1,0} - \delta_{n,0} - \rho^{n-1}_S - 2\rho^{n-1}_T),
\end{aligned} \tag{C.24}$$

and

$$\begin{aligned}
2(\gamma + \kappa n)\rho^n_T = &- \frac{16\kappa(2n+1)\gamma\Phi(n+1)}{(\gamma + 2\kappa(2n+1))^2}(\delta_{n,0} - \delta_{n+1,0} - \rho^n_S + \rho^{n+1}_S - 2\rho^n_T + 2\rho^{n+1}_T) \\
&+ \frac{16\kappa(2n-1)\gamma\Phi n}{(\gamma + 2\kappa(2n-1))^2}(\delta_{n-1,0} - \delta_{n,0} - \rho^{n-1}_S + \rho^n_S - 2\rho^{n-1}_T + 2\rho^n_T).
\end{aligned} \tag{C.25}$$

To make our assumption consistent, we must assume that we are in the $\kappa \ll 1$ regime, which allows us to expand the previous expressions around $\kappa = 0$. Keeping only the lowest-order terms, we obtain

$$\begin{aligned}
&\left[\gamma - 16\Phi(2n+1)\right]\rho^n_T - \left[\gamma + 8\Phi(2n+1)\right]\rho^n_S = \\
&- 8\Phi(n+1)(\delta_{n,0} - \delta_{n+1,0} + \rho^{n+1}_S + 2\rho^{n+1}_T) \\
&+ 8\Phi n(\delta_{n-1,0} - \delta_{n,0} - \rho^{n-1}_S - 2\rho^{n-1}_T),
\end{aligned} \tag{C.26}$$

and

$$
\begin{aligned}
2\gamma\rho_T^n = &-\frac{16\kappa\Phi(2n+1)(n+1)}{\gamma}(\delta_{n,0}-\delta_{n+1,0}-\rho_S^n+\rho_S^{n+1}-2\rho_T^n+2\rho_T^{n+1}) \\
&+\frac{16\kappa\Phi(2n-1)n}{\gamma}(\delta_{n-1,0}-\delta_{n,0}-\rho_S^{n-1}+\rho_S^n-2\rho_T^{n-1}+2\rho_T^n).
\end{aligned}
\tag{C.27}
$$

Unfortunately, to our knowledge, this system of equations cannot be solved exactly. We require an additional approximation in Eq. (C.27). We consider a different and simpler recurrence relation, which still exhibits the same behaviour. We proceed as follows: First, numerical analysis shows that the weight of the coefficients follows $\rho_T^{n\pm1} < \rho_T^n$, which allows us to discard those terms. Secondly, we neglect the higher-order coefficients of the prefactor, retaining only $n = 0$. The resulting equation is given by

$$
2\gamma\rho_T^n = -16\kappa\Phi/\gamma(\delta_{n,0}-\delta_{n+1,0}-\rho_S^n-2\rho_T^n)+16\kappa\Phi/\gamma(\delta_{n-1,0}-\delta_{n,0}+\rho_S^n+2\rho_T^n), \tag{C.28}
$$

where, as we will see from its final form, it captures the expected behaviour. We can now obtain two uncoupled recurrence relations for the singlet and the triplet. Combing Eq. (C.28) and Eq. (C.26), the three-term recurrence relation for the singlet is

$$
\begin{aligned}
\Big(\gamma^2+8\Phi[(2n+1)\gamma+3\kappa]\Big)\rho_S^n =& 8n\Phi\gamma\rho_S^{n-1}+8(n+1)\Phi\gamma\rho_S^{n+1} \\
&+8\Phi(\gamma+\kappa)\delta_{n,0}-8\Phi(\gamma+3\kappa+48\Phi\kappa^2/\gamma^2)\delta_{n-1,0},
\end{aligned}
\tag{C.29}
$$

while the three-term recurrence relation for the triplet is

$$
\begin{aligned}
\Big(\gamma^2+8\Phi[(2n+1)\gamma+3\kappa]\Big)\rho_T^n =& 8\Phi n\gamma\rho_T^{n-1}+8(n+1)\Phi\gamma\rho_T^{n+1} \\
&+8\Phi\kappa\delta_{n,0}+\frac{3(4\Phi\kappa)^2}{\gamma^2}\delta_{n-1,0}.
\end{aligned}
\tag{C.30}
$$

In general, they follow the structure

$$
a_nX_n = b_nX_{n-1}+c_nX_{n+1}+Y_0\delta_{n,0}+Y_1\delta_{n-1,0}, \tag{C.31}
$$

where the only difference between Eq. (C.29) and Eq. (C.30) are the terms $Y_0$ and $Y_1$. This general three-term recurrence relation can be solved using an ordinary continued fraction

$$
X_0 = \frac{\left(Y_0+\frac{c_0}{a_1-\frac{c_1b_2}{a_2-\ldots}}Y_1\right)}{a_0-\frac{c_0b_1}{a_1-c_1\frac{c_1b_2}{a_2-\ldots}}} = \mathcal{F}_1(Y_0+\mathcal{F}_2Y_1), \tag{C.32}
$$

where we have defined

$$\mathcal{F}_1 = \cfrac{1}{a_0 - \cfrac{c_0 b_1}{a_1 - c_1 \cfrac{c_1 b_2}{a_2 - \dots}}}, \tag{C.33}$$

and

$$\mathcal{F}_2 = \cfrac{c_0}{a_1 - \cfrac{c_1 b_2}{a_2 - \dots}}. \tag{C.34}$$

As previously stated, the difference between the singlet and triplet recurrences are in $Y_0$ and $Y_1$, not in $\mathcal{F}_1$ and $\mathcal{F}_2$.

### C.1.1 Theory of continued fractions

Here, we show that ordinary continued fractions can be solved by evaluating their continuants. Assume an ordinary generalized continued fraction $\mathcal{F}$. A closed expression can be found by [173]

$$\mathcal{F} = b_0 + \frac{a_0}{b_1 + \frac{a_1}{b_2 + \dots}} = \lim_{n\to\infty} \frac{P_n}{Q_n}, \tag{C.35}$$

where $P_n$ and $Q_n$ are the so-called continuants of the fraction and fulfil

$$\begin{aligned} P_n &= b_n P_{n-1} + a_n P_{n-2}, \\ Q_n &= b_n Q_{n-1} + a_n Q_{n-2}, \end{aligned} \tag{C.36}$$

for $n \geq 1$. Defining $R_n = (P_n, Q_n)$, it allows for a more compact form

$$R_n = b_n R_{n-1} + a_n R_{n-2}, \tag{C.37}$$

for $n \geq 1$ and initial conditions $R_0 = (b_0, 1)$ and $R_{-1} = (1, 0)$. We are left with solving a three-term recurrence relation for $R_n$. To solve this three-term recurrence, assume an ordinary generating function $R(z) = \sum_{n\geq 0} R_n z^n$ [221]. Then, we multiply Eq. (C.37) by $\sum_{n\geq 2} z^n$ such that we obtain

$$\sum_{n\geq 2} R_n z^n = \sum_{n\geq 2} b_n R_{n-1} z^n + \sum_{n\geq 2} a_n R_{n-2} z^n. \tag{C.38}$$

To proceed, one would need to know the coefficients $R_n$. In general, if $R_n$ is a polynomial of order $n$, it produces an ordinary differential equation (ODE) for $R(z)$ of order $n$. More insight can be gained later when we work out specific examples.

Once the recurrence relation has been expressed as an ODE, we can solve for $R(z)$. Then, following Abel's theorem for the power series [221, 222], which states that the limit of a power series $R(z)$ is related to the sum of its coefficients $R_n$, we get

$$\lim_{n\to\infty}\frac{P_n}{Q_n}=\lim_{z\to z^\star}\frac{P(z)}{Q(z)}, \tag{C.39}$$

being $z^\star$ the radius of convergence of $R(z)$, i.e. its singular point if any.

In our case, we have 2 continued fractions: $\mathcal{F}_1$ in Eq. (C.33) and $\mathcal{F}_2$ in Eq. (C.34). For the first case $\mathcal{F}_1$, the convergents give the following recurrence relation

$$R_{n+2}=a_{n+1}R_{n+1}-c_nb_{n+1}R_n, \tag{C.40}$$

with $n\geq 0$ and initial condition $R_0=(0,1)$ and $R_1=(1,a_0)$. Specifically,

$$R_{n+2}=[\gamma_{\text{eff}}+x(2n+3)]R_{n+1}-x^2(n+1)^2R_n, \tag{C.41}$$

with $x=8\Phi\gamma$, $\gamma_{\text{eff}}=\gamma^2+24\kappa\Phi$ and $a_0=\gamma_{\text{eff}}+x$. Define $R_n=n!S_n$. This transforms our recurrence relation to

$$(n+2)S_{n+2}=[\gamma_{\text{eff}}+x(2n+3)]S_{n+1}-x^2(n+1)S_n. \tag{C.42}$$

Assume the following generating function $S(z)=\sum_{n\geq 0}S_nz^n$. This yields the following first-order ODE,

$$S'(z)(1-xz)^2z=S(z)[(\gamma_{\text{eff}}+x)z-x^2z^2]-z(\gamma_{\text{eff}}+x)S_0+zS_1, \tag{C.43}$$

with initial condition $S(0)=S_0=R_0$. Its solution is

$$S(z)=\frac{e^{\frac{z\gamma_{\text{eff}}}{1-xz}}}{x(1-xz)}\left[xS_0+e^{\frac{\gamma_{\text{eff}}}{x}}S_1\left(\Gamma[0,\gamma_{\text{eff}}/x]+\Gamma[0,\frac{\gamma_{\text{eff}}}{x(xz-1)}]\right)\right]. \tag{C.44}$$

This solution has a singularity at $z=1/x$, which means that

$$\mathcal{F}_1=\lim_{z\to 1/x}\frac{P(z)}{Q(z)}=\frac{e^{\frac{\gamma_{\text{eff}}}{x}}\Gamma[0,\frac{\gamma_{\text{eff}}}{x}]}{x}. \tag{C.45}$$

The other continued fraction $\mathcal{F}_2$ fulfils a similar recurrence

$$R_{n+2}=a_{n+2}R_{n+1}-c_{n+1}b_{n+2}R_n, \tag{C.46}$$

with initial conditions $R_0=(0,1)$, $R_1=(c_0,a_1)=(x,\gamma_{\text{eff}}+3x)$. Define $R_n=(n+1)!S_n$, then

$$(n+3)S_{n+2}=[\gamma_{\text{eff}}+x(2n+5)]S_{n+1}-x^2(n+2)S_n. \tag{C.47}$$

As before, we can find its associated ODE.

$$S'(z)(1-xz)^2 z = S(z)[z(\gamma_{\text{eff}}+3x)-2x^2z^2-1]+(1-z(\gamma_{\text{eff}}+3x))S_0+2zS_1, \quad \text{(C.48)}$$

with initial condition $S(0)=S_0$. Using the same method as before, we find

$$\mathcal{F}_2 = 1+\frac{\gamma_{\text{eff}}}{x}-\frac{e^{-\gamma_{\text{eff}}/x}}{\Gamma[0,\gamma_{\text{eff}}/x]}. \quad \text{(C.49)}$$

These closed expressions of the continued fractions allow us to find the singlet and triplet populations. Using Eq. (C.32) we obtain Eq. (5.40) and Eq. (5.41) from Chapter 5.

# Bibliography


1. Schrödinger, E. Quantum mechanics 100 years on: an unfinished revolution. *Nature* **637,** 251 (2025).
2. Heisenberg, W. Über quantentheoretische Umdeutung kinematischer und mechanischer Beziehungen. *Z. Physik* **33,** 879–893 (1985).
3. Nielsen, M. A. & Chuang, I. L. *Quantum computation and quantum information* (Cambridge University Press, Cambridge, 2010).
4. Devoret, M. H. & Schoelkopf, R. J. Superconducting circuits for quantum information: an outlook. *Science* **339,** 1169–1174 (2013).
5. Kimble, H. J. The quantum internet. *Nature* **453,** 1023–1030 (2008).
6. Lodahl, P. & Stobbe, S. Solid-state quantum optics with quantum dots in photonic nanostructures. *Nanophotonics* **2,** 39–55 (2013).
7. O'brien, J. L., Furusawa, A. & Vučković, J. Photonic quantum technologies. *Nature photon* **3,** 687–695 (2009).
8. Shor, P. W. *Algorithms for quantum computation: discrete logarithms and factoring* in *Proceedings 35th Annual Symposium on Foundations of Computer Science* (1994), 124–134.
9. Grover, L. K. *A fast quantum mechanical algorithm for database search* in *Proceedings of the twenty-eighth annual ACM symposium on Theory of computing* (1996), 212–219.
10. Deutsch, D. & Jozsa, R. Rapid solution of problems by quantum computation. *Proceedings of the Royal Society of London. Series A: Mathematical and Physical Sciences* **439,** 553–558 (1992).
11. Knill, E., Laflamme, R. & Milburn, G. J. A scheme for efficient quantum computation with linear optics. *Nature* **409,** 46–52 (2001).
12. Raussendorf, R. & Briegel, H. J. A one-way quantum computer. *Phys. Rev. Lett.* **86,** 5188 (2001).
13. Leuenberger, M. N. & Loss, D. Quantum computing in molecular magnets. *Nature* **410,** 789–793 (2001).

14. Gottesman, D. & Chuang, I. L. Demonstrating the viability of universal quantum computation using teleportation and single-qubit operations. *Nature* **402,** 390–393 (1999).

15. Kitaev, A. Y. Fault-tolerant quantum computation by anyons. *Annals of physics* **303,** 2–30 (2003).

16. Blais, A., Huang, R.-S., Wallraff, A., Girvin, S. M. & Schoelkopf, R. J. Cavity quantum electrodynamics for superconducting electrical circuits: An architecture for quantum computation. *Phys. Rev. A* **69,** 062320 (2004).

17. DiVincenzo, D. P. The physical implementation of quantum computation. *Fortschritte der Physik: Progress of Physics* **48,** 771–783 (2000).

18. Bouwmeester, D., Pan, J.-W., Mattle, K., Eibl, M., Weinfurter, H. & Zeilinger, A. Experimental quantum teleportation. *Nature* **390,** 575–579 (1997).

19. Gisin, N. & Thew, R. Quantum communication. *Nature photon* **1,** 165–171 (2007).

20. Chen, Y.-A., Zhang, Q., Chen, T.-Y., Cai, W.-Q., Liao, S.-K., Zhang, J., Chen, K., Yin, J., Ren, J.-G., Chen, Z., *et al.* An integrated space-to-ground quantum communication network over 4,600 kilometres. *Nature* **589,** 214–219 (2021).

21. Yin, J., Li, Y.-H., Liao, S.-K., Yang, M., Cao, Y., Zhang, L., Ren, J.-G., Cai, W.-Q., Liu, W.-Y., Li, S.-L., *et al.* Entanglement-based secure quantum cryptography over 1,120 kilometres. *Nature* **582,** 501–505 (2020).

22. Fedorov, K. G., Renger, M., Pogorzalek, S., Di Candia, R., Chen, Q., Nojiri, Y., Inomata, K., Nakamura, Y., Partanen, M., Marx, A., *et al.* Experimental quantum teleportation of propagating microwaves. *Science advances* **7,** eabk0891 (2021).

23. Fesquet, F., Kronowetter, F., Renger, M., Yam, W. K., Gandorfer, S., Inomata, K., Nakamura, Y., Marx, A., Gross, R. & Fedorov, K. G. Demonstration of microwave single-shot quantum key distribution. *Nat Commun* **15,** 7544 (2024).

24. Abdo, B., Shanks, W., Jinka, O., Rozen, J. & Orcutt, J. Teleportation and Entanglement Swapping of Continuous Quantum Variables of Microwave Radiation. *arXiv:2501.05537* (2025).

25. Sahu, R., Qiu, L., Hease, W., Arnold, G., Minoguchi, Y., Rabl, P. & Fink, J. M. Entangling microwaves with light. *Science* **380,** 718–721 (2023).

26. Pirandola, S., Andersen, U. L., Banchi, L., Berta, M., Bunandar, D., Colbeck, R., Englund, D., Gehring, T., Lupo, C., Ottaviani, C., *et al.* Advances in quantum cryptography. *Advances in optics and photonics* **12,** 1012–1236 (2020).

27. Gisin, N., Ribordy, G., Tittel, W. & Zbinden, H. Quantum cryptography. *Rev. Mod. Phys.* **74,** 145 (2002).

28. Bennett, C. H., Bessette, F., Brassard, G., Salvail, L. & Smolin, J. Experimental quantum cryptography. *J. Cryptology* **5,** 3–28 (1992).

29. Pirandola, S., Bardhan, B. R., Gehring, T., Weedbrook, C. & Lloyd, S. Advances in photonic quantum sensing. *Nature Photon* **12,** 724–733 (2018).

30. Degen, C. L., Reinhard, F. & Cappellaro, P. Quantum sensing. *Rev. Mod. Phys.* **89,** 035002 (2017).

31. Lawrie, B. J., Lett, P. D., Marino, A. M. & Pooser, R. C. Quantum sensing with squeezed light. *ACS Photonics* **6,** 1307–1318 (2019).

32. Kim, Y., Eddins, A., Anand, S., Wei, K. X., Van Den Berg, E., Rosenblatt, S., Nayfeh, H., Wu, Y., Zaletel, M., Temme, K., *et al.* Evidence for the utility of quantum computing before fault tolerance. *Nature* **618,** 500–505 (2023).

33. Acharya, R., Aleiner, I., Allen, R., *et al.* Suppressing quantum errors by scaling a surface code logical qubit. *Nature* **614,** 676–681 (2023).

34. Sivak, V. V., Eickbusch, A., Royer, B., Singh, S., Tsioutsios, I., Ganjam, S., Miano, A., Brock, B., Ding, A., Frunzio, L., *et al.* Real-time quantum error correction beyond break-even. *Nature* **616,** 50–55 (2023).

35. Putterman, H., Noh, K., Hann, C. T., MacCabe, G. S., Aghaeimeibodi, S., Patel, R. N., Lee, M., Jones, W. M., Moradinejad, H., Rodriguez, R., *et al.* Hardware-efficient quantum error correction using concatenated bosonic qubits. *Nature* **638,** 927–934 (2025).

36. Acharya, R., Aghababaie-Beni, L., Aleiner, I., Andersen, T. I., Ansmann, M., Arute, F., Arya, K., Asfaw, A., Astrakhantsev, N., Atalaya, J., *et al.* Quantum error correction below the surface code threshold. *arXiv:2408.13687* (2024).

37. Smith, M., Leu, A., Miyanishi, K., Gely, M. & Lucas, D. Single-qubit gates with errors at the $10^{-7}$ level. *arXiv:2412.04421* (2024).

38. Bernien, H., Schwartz, S., Keesling, A., Levine, H., Omran, A., Pichler, H., Choi, S., Zibrov, A. S., Endres, M., Greiner, M., *et al.* Probing many-body dynamics on a 51-atom quantum simulator. *Nature* **551,** 579–584 (2017).

39. Krinner, S., Lacroix, N., Remm, A., Di Paolo, A., Genois, E., Leroux, C., Hellings, C., Lazar, S., Swiadek, F., Herrmann, J., *et al.* Realizing repeated quantum error correction in a distance-three surface code. *Nature* **605,** 669–674 (2022).

40. Wehner, S., Elkouss, D. & Hanson, R. Quantum internet: A vision for the road ahead. *Science* **362,** eaam9288 (2018).

41. Cirac, J. I., Zoller, P., Kimble, H. J. & Mabuchi, H. Quantum state transfer and entanglement distribution among distant nodes in a quantum network. *Phys. Rev. Lett.* **78,** 3221 (1997).

42. Northup, T. & Blatt, R. Quantum information transfer using photons. *Nature photon* **8,** 356–363 (2014).

43. Reiserer, A. & Rempe, G. Cavity-based quantum networks with single atoms and optical photons. *Rev. Mod. Phys.* **87,** 1379–1418 (2015).

44. Awschalom, D., Berggren, K. K., Bernien, H., Bhave, S., Carr, L. D., Davids, P., Economou, S. E., Englund, D., Faraon, A., *et al.* Development of Quantum Interconnects (QuICs) for Next-Generation Information Technologies. *PRX Quantum* **2,** 017002 (2021).

45. Jiang, L., Taylor, J. M., Sørensen, A. S. & Lukin, M. D. Distributed quantum computation based on small quantum registers. *Phys. Rev. A* **76,** 062323 (2007).

46. Monroe, C., Raussendorf, R., Ruthven, A., Brown, K. R., Maunz, P., Duan, L.-M. & Kim, J. Large-scale modular quantum-computer architecture with atomic memory and photonic interconnects. *Phys. Rev. A* **89,** 022317 (2014).

47. Cacciapuoti, A. S., Caleffi, M., Tafuri, F., Cataliotti, F. S., Gherardini, S. & Bianchi, G. Quantum internet: Networking challenges in distributed quantum computing. *IEEE Network* **34,** 137–143 (2019).

48. Reiserer, A. Colloquium: Cavity-enhanced quantum network nodes. *Rev. Mod. Phys.* **94,** 041003 (2022).

49. Bennett, C. H., Brassard, G., Popescu, S., Schumacher, B., Smolin, J. A. & Wootters, W. K. Purification of noisy entanglement and faithful teleportation via noisy channels. *Phys. Rev. Lett.* **76,** 722 (1996).

50. Deutsch, D., Ekert, A., Jozsa, R., Macchiavello, C., Popescu, S. & Sanpera, A. Quantum privacy amplification and the security of quantum cryptography over noisy channels. *Phys. Rev. Lett.* **77,** 2818 (1996).

51. Dür, W., Briegel, H.-J., Cirac, J. I. & Zoller, P. Quantum repeaters based on entanglement purification. *Phys. Rev. A* **59,** 169 (1999).

52. Cirac, J. I., Ekert, A., Huelga, S. F. & Macchiavello, C. Distributed quantum computation over noisy channels. *Phys. Rev. A* **59,** 4249 (1999).

53. Kent, A., Linden, N. & Massar, S. Optimal entanglement enhancement for mixed states. *Phys. Rev. Lett.* **83,** 2656 (1999).

54. Yan, H., Zhong, Y., Chang, H.-S., Bienfait, A., Chou, M.-H., Conner, C. R., Dumur, É., Grebel, J., Povey, R. G. & Cleland, A. N. Entanglement purification and protection in a superconducting quantum network. *Phys. Rev. Lett.* **128,** 080504 (2022).

55. Cabrillo, C., Cirac, J. I., Garcia-Fernandez, P. & Zoller, P. Creation of entangled states of distant atoms by interference. *Phys. Rev. A* **59,** 1025 (1999).

56. Gao, W., Fallahi, P., Togan, E., Miguel-Sánchez, J. & Imamoglu, A. Observation of entanglement between a quantum dot spin and a single photon. *Nature* **491,** 426–430 (2012).

57. Blinov, B. B., Moehring, D. L., Duan, L.-M. & Monroe, C. Observation of entanglement between a single trapped atom and a single photon. *Nature* **428,** 153–157 (2004).

58. Togan, E., Chu, Y., Trifonov, A. S., Jiang, L., Maze, J., Childress, L., Dutt, M. G., Sørensen, A. S., Hemmer, P. R., Zibrov, A. S., *et al.* Quantum entanglement between an optical photon and a solid-state spin qubit. *Nature* **466,** 730–734 (2010).

59. De Greve, K., Yu, L., McMahon, P. L., Pelc, J. S., Natarajan, C. M., Kim, N. Y., Abe, E., Maier, S., Schneider, C., Kamp, M., *et al.* Quantum-dot spin–photon entanglement via frequency downconversion to telecom wavelength. *Nature* **491,** 421–425 (2012).

60. Duan, L.-M. & Kimble, H. J. Efficient Engineering of Multiatom Entanglement through Single-Photon Detections. *Phys. Rev. Lett.,* 253601 (2003).

61. Simon, C. & Irvine, W. T. Robust Long-Distance Entanglement and a Loophole-Free Bell Test with Ions and Photons. *Phys. Rev. Lett.* **91,** 110405 (2003).

62. Moehring, D. L., Maunz, P., Olmschenk, S., Younge, K. C., Matsukevich, D. N., Duan, L.-M. & Monroe, C. Entanglement of single-atom quantum bits at a distance. *Nature* **449,** 68–71 (2007).

63. Duan, L.-M. & Monroe, C. Colloquium: Quantum networks with trapped ions. *Rev. Mod. Phys.* **82,** 1209–1224 (2010).

64. Stolk, A. J., van der Enden, K. L., Slater, M.-C., te Raa-Derckx, I., Botma, P., van Rantwijk, J., Biemond, J. J. B., Hagen, R. A. J., Herfst, R. W., Koek, W. D., Meskers, A. J. H., Vollmer, R., van Zwet, E. J., Markham, M., Edmonds, A. M., Geus, J. F., Elsen, F., Jungbluth, B., Haefner, C., Tresp, C., Stuhler, J., Ritter, S. & Hanson, R. Metropolitan-scale heralded entanglement of solid-state qubits. *Science Advances* **10,** eadp6442 (2024).

65. Krutyanskiy, V., Galli, M., Krcmarsky, V., Baier, S., Fioretto, D., Pu, Y., Mazloom, A., Sekatski, P., Canteri, M., Teller, M., *et al.* Entanglement of Trapped-Ion Qubits Separated by 230 Meters. *Phys. Rev. Lett.* **130,** 050803 (2023).

66. Hensen, B., Bernien, H., Dréau, A. E., Reiserer, A., Kalb, N., Blok, M. S., Ruitenberg, J., Vermeulen, R. F. L., Schouten, R. N., Abellán, C., Amaya, W., Pruneri, V., Mitchell, M. W., Markham, M., Twitchen, D. J., Elkouss, D., Wehner, S., Taminiau, T. H. & Hanson, R. Loophole-free Bell inequality violation using electron spins separated by 1.3 kilometres. *Nature* **526,** 682–686 (2015).

67. Riedinger, R., Wallucks, A., Marinković, I., Löschnauer, C., Aspelmeyer, M., Hong, S. & Gröblacher, S. Remote quantum entanglement between two micromechanical oscillators. *Nature* **556,** 473–477 (2018).

68. Matsukevich, D., Chaneliere, T., Jenkins, S., Lan, S.-Y., Kennedy, T. & Kuzmich, A. Entanglement of remote atomic qubits. *Phys. Rev. Lett.* **96,** 030405 (2006).

69. Barrett, S. D. & Kok, P. Efficient high-fidelity quantum computation using matter qubits and linear optics. *Phys. Rev. A* **71,** 060310 (2005).

70. Duan, L.-M., Lukin, M. D., Cirac, J. I. & Zoller, P. Long-distance quantum communication with atomic ensembles and linear optics. *Nature* **414,** 413–418 (2001).

71. Pompili, M., Hermans, S. L., Baier, S., Beukers, H. K., Humphreys, P. C., Schouten, R. N., Vermeulen, R. F., Tiggelman, M. J., dos Santos Martins, L., Dirkse, B., *et al.* Realization of a multinode quantum network of remote solid-state qubits. *Science* **372,** 259–264 (2021).

72. Ruskuc, A., Wu, C.-J., Green, E., Hermans, S. L. N., Pajak, W., Choi, J. & Faraon, A. Multiplexed entanglement of multi-emitter quantum network nodes. *Nature* (2025).

73. Duan, L.-M., Cirac, J. I., Zoller, P. & Polzik, E. S. Quantum communication between atomic ensembles using coherent light. *Phys. Rev. Lett.* **85,** 5643 (2000).

74. Julsgaard, B., Kozhekin, A. & Polzik, E. S. Experimental long-lived entanglement of two macroscopic objects. *Nature* **413,** 400–403 (2001).

75. Kurpiers, P., Magnard, P., Walter, T., Royer, B., Pechal, M., Heinsoo, J., Salathé, Y., Akin, A., Storz, S., Besse, J.-C., Gasparinetti, S., Blais, A. & Wallraff, A. Deterministic quantum state transfer and remote entanglement using microwave photons. *Nature* **558,** 264–267 (2018).

76. Chou, K. S., Blumoff, J. Z., Wang, C. S., Reinhold, P. C., Axline, C. J., Gao, Y. Y., Frunzio, L., Devoret, M., Jiang, L. & Schoelkopf, R. Deterministic teleportation of a quantum gate between two logical qubits. *Nature* **561,** 368–373 (2018).

77. Magnard, P., Storz, S., Kurpiers, P., Schär, J., Marxer, F., Lütolf, J., Walter, T., Besse, J.-C., Gabureac, M., Reuer, K., Akin, A., Royer, B., Blais, A. & Wallraff, A. Microwave quantum link between superconducting circuits housed in spatially separated cryogenic systems. *Phys. Rev. Lett.* **125,** 260502 (2020).

78. Zhong, Y., Chang, H.-S., Bienfait, A., Dumur, É., Chou, M.-H., Conner, C. R., Grebel, J., Povey, R. G., Yan, H., Schuster, D. I. & Cleland, A. N. Deterministic multi-qubit entanglement in a quantum network. *Nature* **590,** 571–575 (2021).

79. Almanakly, A., Yankelevich, B., Hays, M., Kannan, B., Assouly, R., Greene, A., Gingras, M., Niedzielski, B. M., Stickler, H., Schwartz, M. E., *et al.* Deterministic remote entanglement using a chiral quantum interconnect. *arXiv:2408.05164* (2024).

80. Shah, P. S., Yang, F., Joshi, C. & Mirhosseini, M. Stabilizing Remote Entanglement via Waveguide Dissipation. *PRX Quantum* **5,** 030346 (2024).

81. Bienfait, A., Satzinger, K. J., Zhong, Y., Chang, H.-S., Chou, M.-H., Conner, C. R., Dumur, É., Grebel, J., Peairs, G. A., Povey, R. G., *et al.* Phonon-mediated quantum state transfer and remote qubit entanglement. *Science* **364,** 368–371 (2019).

82. Kraus, B. & Cirac, J. I. Discrete entanglement distribution with squeezed light. *Phys. Rev. Lett.* **92,** 013602 (2004).

83. Agustí, J., Minoguchi, Y., Fink, J. M. & Rabl, P. Long-distance distribution of qubit-qubit entanglement using Gaussian-correlated photonic beams. *Phys. Rev. A* **105,** 062454 (2022).

84. Agustí, J., Zhang, X. H. H., Minoguchi, Y. & Rabl, P. Autonomous Distribution of Programmable Multiqubit Entanglement in a Dual-Rail Quantum Network. *Phys. Rev. Lett.* **131,** 250801 (2023).

85. Paternostro, M., Son, W. & Kim, M. Complete conditions for entanglement transfer. *Phys. Rev. Lett.* **92,** 197901 (2004).

86. Serafini, A., Paternostro, M., Kim, M. S. & Bose, S. Enhanced dynamical entanglement transfer with multiple qubits. *Phys. Rev. A* **73,** 022312 (2006).

87. Muschik, C. A., Polzik, E. S. & Cirac, J. I. Dissipatively driven entanglement of two macroscopic atomic ensembles. *Phys. Rev. A* **83,** 052312 (2011).

88. Felicetti, S., Sanz, M., Lamata, L., Romero, G., Johansson, G., Delsing, P. & Solano, E. Dynamical Casimir Effect Entangles Artificial Atoms. *Phys. Rev. Lett.* **113,** 093602 (2014).

89. Grimsmo, A. L. & Blais, A. Squeezing and quantum state engineering with Josephson travelling wave amplifiers. *npj Quantum Inf* **3,** 20 (2017).

90. Didier, N., Guillaud, J., Shankar, S. & Mirrahimi, M. Remote entanglement stabilization and concentration by quantum reservoir engineering. *Phys. Rev. A* **98,** 012329 (2018).

91. You, J., Liao, Z., Li, S.-W. & Zubairy, M. S. Waveguide quantum electrodynamics in squeezed vacuum. *Phys. Rev. A* **97,** 023810 (2018).

92. Govia, L. C. G., Lingenfelter, A. & Clerk, A. A. Stabilizing two-qubit entanglement by mimicking a squeezed environment. *Phys. Rev. Research* **4,** 023010 (2022).

93. Zippilli, S., Paternostro, M., Adesso, G. & Illuminati, F. Entanglement replication in driven dissipative many-body systems. *Phys. Rev. Lett.* **110,** 040503 (2013).

94. Pocklington, A., Wang, Y.-X., Yanay, Y. & Clerk, A. A. Stabilizing volume-law entangled states of fermions and qubits using local dissipation. *Phys. Rev. B* **105,** L140301 (2022).

95. Lingenfelter, A., Yao, M., Pocklington, A., Wang, Y.-X., Irfan, A., Pfaff, W. & Clerk, A. A. Exact Results for a Boundary-Driven Double Spin Chain and Resource-Efficient Remote Entanglement Stabilization. *Phys. Rev. X* **14,** 021028 (2024).

96. Agarwal, G. & Puri, R. Cooperative behavior of atoms irradiated by broadband squeezed light. *Phys. Rev. A* **41,** 3782 (1990).

97. Gutiérrez-Jáuregui, R., Asenjo-Garcia, A. & Agarwal, G. Dissipative stabilization of dark quantum dimers via squeezed vacuum. *Phys. Rev. Research* **5,** 013127 (2023).

98. Karnieli, A., Tziperman, O., Roques-Carmes, C. & Fan, S. Decoherence-free many-body Hamiltonians in nonlinear waveguide quantum electrodynamics. *Phys. Rev. Research* **7,** L012014 (1 2025).

99. Carmichael, H. J. *Statistical methods in quantum optics 2: Non-classical fields* (Springer Science & Business Media, 2007).

100. Kwiat, P. G., Mattle, K., Weinfurter, H., Zeilinger, A., Sergienko, A. V. & Shih, Y. New High-Intensity Source of Polarization-Entangled Photon Pairs. *Phys. Rev. Lett.* **75,** 4337 (1995).

101. Kim, T., Fiorentino, M. & Wong, F. N. Phase-stable source of polarization-entangled photons using a polarization Sagnac interferometer. *Phys. Rev. A* **73,** 012316 (2006).

102. Eichler, C., Bozyigit, D., Lang, C., Baur, M., Steffen, L., Fink, J. M., Filipp, S. & Wallraff, A. Observation of Two-Mode Squeezing in the Microwave Frequency Domain. *Phys. Rev. Lett.* **107,** 113601 (2011).

103. Menzel, E., Di Candia, R., Deppe, F., Eder, P., Zhong, L., Ihmig, M., Haeberlein, M., Baust, A., Hoffmann, E., Ballester, D., *et al.* Path Entanglement of Continuous-Variable Quantum Microwaves. *Phys. Rev. Lett.* **109,** 250502 (2012).

104. Flurin, E., Roch, N., Mallet, F., Devoret, M. H. & Huard, B. Generating Entangled Microwave Radiation Over Two Transmission Lines. *Phys. Rev. Lett.* **109,** 183901 (2012).

105. Roy, A. & Devoret, M. Introduction to parametric amplification of quantum signals with Josephson circuits. *Comptes Rendus Physique* **17,** 740–755 (2016).

106. Winkel, P., Takmakov, I., Rieger, D., Planat, L., Hasch-Guichard, W., Grünhaupt, L., Maleeva, N., Foroughi, F., Henriques, F., Borisov, K., *et al.* Nondegenerate parametric amplifiers based on dispersion-engineered Josephson-junction arrays. *Phys. Rev. Applied* **13,** 024015 (2020).

107. Peugeot, A., Ménard, G., Dambach, S., Westig, M., Kubala, B., Mukharsky, Y., Altimiras, C., Joyez, P., Vion, D., Roche, P., *et al.* Generating two continuous entangled microwave beams using a dc-biased Josephson junction. *Phys. Rev. X* **11,** 031008 (2021).

108. Rueda, A., Hease, W., Barzanjeh, S. & Fink, J. M. Electro-optic entanglement source for microwave to telecom quantum state transfer. *npj Quantum Inf* **5,** 108 (2019).

109. Torres, J. P., Banaszek, K. & Walmsley, I. A. in *Progress in Optics* 227–331 (Elsevier, 2011).

110. Couteau, C. Spontaneous parametric down-conversion. *Contemporary Physics* **59,** 291–304 (2018).

111. Yin, J., Cao, Y., Li, Y.-H., Liao, S.-K., Zhang, L., Ren, J.-G., Cai, W.-Q., Liu, W.-Y., Li, B., Dai, H., *et al.* Satellite-based entanglement distribution over 1200 kilometers. *Science* **356,** 1140–1144 (2017).

112. Ask, A. & Johansson, G. Non-Markovian steady states of a driven two-level system. *Phys. Rev. Lett.* **128,** 083603 (2022).

113. Keefe, A., Agarwal, N. & Kamal, A. Quantifying spectral signatures of non-Markovianity beyond the Born-Redfield master equation. *arXiv:2405.01722* (2024).

114. De Vega, I. & Alonso, D. Dynamics of non-Markovian open quantum systems. *Rev. Mod. Phys.* **89,** 015001 (2017).

115. Brask, J. B., Haack, G., Brunner, N. & Huber, M. Autonomous quantum thermal machine for generating steady-state entanglement. *New J. Phys.* **17,** 113029 (2015).

116. Lewenstein, M., Bruß, D., Cirac, J. I., Kraus, B., Kuś, M., Samsonowicz, J., Sanpera, A. & Tarrach, R. Separability and distillability in composite quantum systems-a primer. *Journal of Modern Optics* **47,** 2481–2499 (2000).

117. Eisert, J., Cramer, M. & Plenio, M. B. Colloquium: Area laws for the entanglement entropy. *Rev. Mod. Phys.* **82,** 277–306 (2010).

118. Hill, S. A. & Wootters, W. K. Entanglement of a Pair of Quantum Bits. *Phys. Rev. Lett.* **78,** 5022 (1997).

119. Wootters, W. K. Entanglement of Formation of an Arbitrary State of Two Qubits. *Phys. Rev. Lett.* **80,** 2245 (1998).

120. Horodecki, R., Horodecki, P., Horodecki, M. & Horodecki, K. Quantum entanglement. *Rev. Mod. Phys.* **81,** 865–942 (2009).

121. Horodecki, M., Horodecki, P. & Horodecki, R. Separability of n-particle mixed states: necessary and sufficient conditions in terms of linear maps. *Physics Letters A* **283,** 1–7 (2001).

122. Jungnitsch, B., Moroder, T. & Gühne, O. Taming Multiparticle Entanglement. *Phys. Rev. Lett.* **106,** 190502 (2011).

123. Coffman, V., Kundu, J. & Wootters, W. K. Distributed entanglement. *Phys. Rev. A* **61,** 052306 (2000).

124. Braunstein, S. L. & Van Loock, P. Quantum information with continuous variables. *Rev. Mod. Phys.* **77,** 513–577 (2005).

125. Weedbrook, C., Pirandola, S., García-Patrón, R., Cerf, N. J., Ralph, T. C., Shapiro, J. H. & Lloyd, S. Gaussian quantum information. *Rev. Mod. Phys.* **84,** 621–669 (2012).

126. Gardiner, C. & Zoller, P. *The Quantum World of Ultra-Cold Atoms and Light. Book I: Foundations of Quantum Optics* (Imperial College Press, London, 2014).

127. Ferraro, A., Olivares, S. & Paris, M. G. Gaussian states in continuous variable quantum information. *arXiv:0503237* (2005).

128. Serafini, A., Illuminati, F. & De Siena, S. Symplectic invariants, entropic measures and correlations of Gaussian states. *J. Phys. B.: At. Mol. Opt. Phys.* **37,** L21 (2003).

129. Kwiat, P. G., Mattle, K., Weinfurter, H., Zeilinger, A., Sergienko, A. V. & Shih, Y. New High-Intensity Source of Polarization-Entangled Photon Pairs. *Phys. Rev. Lett.* **75,** 4337 (1995).

130. Peres, A. Separability Criterion for Density Matrices. *Phys. Rev. Lett.* **77,** 1413 (1996).

131. Adesso, G. & Illuminati, F. Gaussian measures of entanglement versus negativities: Ordering of two-mode Gaussian states. *Phys. Rev. A* **72,** 032334 (2005).

132. Życzkowski, K., Horodecki, P., Sanpera, A. & Lewenstein, M. Volume of the set of separable states. *Phys. Rev. A* **58,** 883 (1998).

133. Vidal, G. & Werner, R. F. Computable measure of entanglement. *Phys. Rev. A* **65,** 032314 (2002).

134. Adesso, G., Serafini, A. & Illuminati, F. Extremal entanglement and mixedness in continuous variable systems. *Phys. Rev. A* **70,** 022318 (2004).

135. Gühne, O. & Tóth, G. Entanglement detection. *Physics Reports* **474,** 1–75 (2009).

136. Chang, D. E., Douglas, J. S., González-Tudela, A., Hung, C.-L. & Kimble, H. J. Colloquium: Quantum matter built from nanoscopic lattices of atoms and photons. *Rev. Mod. Phys.* **90,** 031002 (2018).

137. Sheremet, A. S., Petrov, M. I., Iorsh, I. V., Poshakinskiy, A. V. & Poddubny, A. N. Waveguide quantum electrodynamics: Collective radiance and photon-photon correlations. *Rev. Mod. Phys.* **95,** 015002 (2023).

138. Lodahl, P., Mahmoodian, S. & Stobbe, S. Interfacing single photons and single quantum dots with photonic nanostructures. *Rev. Mod. Phys.* **87,** 347–400 (2015).

139. Gu, X., Kockum, A. F., Miranowicz, A., Liu, Y.-x. & Nori, F. Microwave photonics with superconducting quantum circuits. *Physics Reports* **718,** 1–102 (2017).

140. Calajó, G., Ciccarello, F., Chang, D. & Rabl, P. Atom-field dressed states in slow-light waveguide QED. *Phys. Rev. A* **93,** 033833 (2016).

141. Hood, J. D., Goban, A., Asenjo-Garcia, A., Lu, M., Yu, S.-P., Chang, D. E. & Kimble, H. Atom-atom interactions around the band edge of a photonic crystal waveguide. *Proc. Natl. Acad. Sci. U.S.A.* **113** (2016).

142. Scully, M. O. & Zubairy, M. S. *Quantum optics* (Cambridge University Press, 1997).

143. Lodahl, P., Mahmoodian, S., Stobbe, S., Rauschenbeutel, A., Schneeweiss, P., Volz, J., Pichler, H. & Zoller, P. Chiral quantum optics. *Nature* **541,** 473–480 (2017).

144. Suárez-Forero, D., Mehrabad, M. J., Vega, C., González-Tudela, A. & Hafezi, M. Chiral quantum optics: recent developments, and future directions. *arXiv:2411.06495* (2024).

145. Gardiner, C. & Zoller, P. *Quantum noise: a handbook of Markovian and non-Markovian quantum stochastic methods with applications to quantum optics* (Springer Science & Business Media, 2004).

146. Breuer, H.-P. & Petruccione, F. *The theory of open quantum systems* (OUP Oxford, 2002).

147. Gross, M. & Haroche, S. Superradiance: An essay on the theory of collective spontaneous emission. *Physics reports* **93,** 301–396 (1982).

148. Walls, D., Drummond, P., Hassan, S. & Carmichael, H. Non-equilibrium phase transitions in cooperative atomic systems. *Progress of Theoretical Physics Supplement* **64,** 307–320 (1978).

149. Stannigel, K., Rabl, P. & Zoller, P. Driven-dissipative preparation of entangled states in cascaded quantum-optical networks. *New J. Phys.* **14,** 063014 (2012).

150. Pichler, H., Ramos, T., Daley, A. J. & Zoller, P. Quantum optics of chiral spin networks. *Phys. Rev. A* **91,** 042116 (2015).

151. Liedl, C., Pucher, S., Tebbenjohanns, F., Schneeweiss, P. & Rauschenbeutel, A. Collective Radiation of a Cascaded Quantum System: From Timed Dicke States to Inverted Ensembles. *Phys. Rev. Lett.* **130,** 163602 (2023).

152. Sliwa, K., Hatridge, M., Narla, A., Shankar, S., Frunzio, L., Schoelkopf, R. & Devoret, M. Reconfigurable Josephson Circulator/Directional Amplifier. *Phys. Rev. X* **5,** 041020 (2015).

153. Kerckhoff, J., Lalumière, K., Chapman, B. J., Blais, A. & Lehnert, K. On-Chip Superconducting Microwave Circulator from Synthetic Rotation. *Phys. Rev. Applied* **4,** 034002 (2015).

154. Chapman, B. J., Rosenthal, E. I., Kerckhoff, J., Moores, B. A., Vale, L. R., Mates, J., Hilton, G. C., Lalumiere, K., Blais, A. & Lehnert, K. Widely Tunable On-Chip Microwave Circulator for Superconducting Quantum Circuits. *Phys. Rev. X* **7,** 041043 (2017).

155. Lecocq, F., Ranzani, L., Peterson, G., Cicak, K., Simmonds, R., Teufel, J. & Aumentado, J. Nonreciprocal Microwave Signal Processing with a Field-Programmable Josephson Amplifier. *Phys. Rev. Applied* **7,** 024028 (2017).

156. Masuda, S., Kono, S., Suzuki, K., Tokunaga, Y., Nakamura, Y. & Koshino, K. Nonreciprocal microwave transmission based on Gebhard-Ruckenstein hopping. *Phys. Rev. A* **99,** 013816 (2019).

157. Wang, Y.-Y., van Geldern, S., Connolly, T., Wang, Y.-X., Shilcusky, A., McDonald, A., Clerk, A. A. & Wang, C. Low-Loss Ferrite Circulator as a Tunable Chiral Quantum System. *Phys. Rev. Applied* **16,** 064066 (2021).

158. Guimond, P.-O., Vermersch, B., Juan, M., Sharafiev, A., Kirchmair, G. & Zoller, P. A unidirectional on-chip photonic interface for superconducting circuits. *npj Quantum Inf* **6,** 32 (2020).

159. Gheeraert, N., Kono, S. & Nakamura, Y. Programmable directional emitter and receiver of itinerant microwave photons in a waveguide. *Phys. Rev. A* **102,** 053720 (2020).

160. Kannan, B., Almanakly, A., Sung, Y., Di Paolo, A., Rower, D. A., Braumüller, J., Melville, A., Niedzielski, B. M., Karamlou, A., Serniak, K., *et al.* On-demand directional microwave photon emission using waveguide quantum electrodynamics. *Nat. Phys.* **19,** 394–400 (2023).

161. Joshi, C., Yang, F. & Mirhosseini, M. Resonance Fluorescence of a Chiral Artificial Atom. *Phys. Rev. X* **13,** 021039 (2023).

162. Pichler, H. & Zoller, P. Photonic Circuits with Time Delays and Quantum Feedback. *Phys. Rev. Lett.* **116,** 093601 (2016).

163. Fayard, N., Henriet, L., Asenjo-Garcia, A. & Chang, D. Many-body localization in waveguide quantum electrodynamics. *Phys. Rev. Research* **3,** 033233 (2021).

164. Fedorov, K. G., Pogorzalek, S., Las Heras, U., Sanz, M., Yard, P., Eder, P., Fischer, M., Goetz, J., Xie, E., Inomata, K., *et al.* Finite-time quantum entanglement in propagating squeezed microwaves. *Sci Rep* **8,** 6416 (2018).

165. Collett, M. & Gardiner, C. Squeezing of intracavity and traveling-wave light fields produced in parametric amplification. *Phys. Rev. A* **30,** 1386 (1984).

166. Qin, W., Miranowicz, A. & Nori, F. Beating the 3 dB Limit for Intracavity Squeezing and Its Application to Nondemolition Qubit Readout. *Phys. Rev. Lett.* **129,** 123602 (2022).

167. Carmichael, H. J. *Statistical methods in quantum optics 1: master equations and Fokker-Planck equations* (Springer Science & Business Media, 2013).

168. Glauber, R. J. Coherent and Incoherent States of the Radiation Field. *Phys. Rev.* **131,** 2766 (1963).

169. Sudarshan, E. C. G. Equivalence of semiclassical and quantum mechanical descriptions of statistical light beams. *Phys. Rev. Lett.* **10,** 277 (1963).

170. Wiseman, H. M. & Milburn, G. J. *Quantum Measurement and Control* (Cambridge University Press, 2009).

171. Schachenmayer, J., Pikovski, A. & Rey, A. M. Many-Body Quantum Spin Dynamics with Monte Carlo Trajectories on a Discrete Phase Space. *Phys. Rev. X* **5,** 011022 (2015).

172. Huber, J., Rey, A. M. & Rabl, P. Realistic simulations of spin squeezing and cooperative coupling effects in large ensembles of interacting two-level systems. *Phys. Rev. A* **105,** 013716 (2022).

173. Risken, H. *The Fokker-Planck Equation* (Springer, 1996).

174. Gardiner, C. *Stochastic Methods* (Springer Berlin Heidelberg, 2009).

175. Husimi, K. Some Formal Properties of the Density Matrix. *Proceedings of the Physico-Mathematical Society of Japan. 3rd Series* **22,** 264–314 (1940).

176. Wigner, E. On the Quantum Correction For Thermodynamic Equilibrium. *Phys. Rev.* **40,** 749 (1932).

177. Drummond, P. D. & Gardiner, C. W. Generalised P-representations in quantum optics. *J. Phys. A: Math. Gen.* **13,** 2353 (1980).

178. Carmichael, H., Satchell, J. & Sarkar, S. Nonlinear analysis of quantum fluctuations in absorptive optical bistability. *Phys. Rev. A* **34,** 3166 (1986).

179. Ritsch, H. & Zoller, P. Systems driven by colored squeezed noise: The atomic absorption spectrum. *Phys. Rev. A* **38,** 4657 (1988).

180. Bose, S., Knight, P., Plenio, M. & Vedral, V. Proposal for teleportation of an atomic state via cavity decay. *Phys. Rev. Lett.* **83,** 5158 (1999).

181. Humphreys, P. C., Kalb, N., Morits, J. P., Schouten, R. N., Vermeulen, R. F., Twitchen, D. J., Markham, M. & Hanson, R. Deterministic delivery of remote entanglement on a quantum network. *Nature* **558,** 268–273 (2018).

182. Campagne-Ibarcq, P., Zalys-Geller, E., Narla, A., Shankar, S., Reinhold, P., Burkhart, L., Axline, C., Pfaff, W., Frunzio, L., Schoelkopf, R. J. & Devoret, M. H. Deterministic Remote Entanglement of Superconducting Circuits through Microwave Two-Photon Transitions. *Phys. Rev. Lett.* **120,** 200501 (2018).

183. Axline, C. J., Burkhart, L. D., Pfaff, W., Zhang, M., Chou, K., Campagne-Ibarcq, P., Reinhold, P., Frunzio, L., Girvin, S., Jiang, L., *et al.* On-demand quantum state transfer and entanglement between remote microwave cavity memories. *Nature Phys* **14,** 705–710 (2018).

184. Kurpiers, P. *Quantum Networks with Superconducting Circuits* PhD thesis (ETH Zurich, 2019).

185. Magnard, P. *Meter-Scale Microwave Quantum Networks for Superconducting Circuits* PhD thesis (ETH Zurich, 2021).

186. Krastanov, S., Raniwala, H., Holzgrafe, J., Jacobs, K., Lončar, M., Reagor, M. J. & Englund, D. R. Optically Heralded Entanglement of Superconducting Systems in Quantum Networks. *Phys. Rev. Lett.* **127,** 040503 (2021).

187. Flurin, E., Roch, N., Pillet, J.-D., Mallet, F. & Huard, B. Superconducting Quantum Node for Entanglement and Storage of Microwave Radiation. *Phys. Rev. Lett.* **114,** 090503 (2015).

188. Kraus, B., Büchler, H. P., Diehl, S., Kantian, A., Micheli, A. & Zoller, P. Preparation of entangled states by quantum Markov processes. *Phys. Rev. A* **78,** 042307 (2008).

189. Gardiner, C. W. & Collett, M. J. Input and output in damped quantum systems: Quantum stochastic differential equations and the master equation. *Phys. Rev. A* **31,** 3761 (1985).

190. Pocklington, A. & Clerk, A. A. Universal Time-Entanglement Trade-Off in Open Quantum Systems. *PRX Quantum* **5,** 040305 (2024).

191. Huang, K., Le Jeannic, H., Morin, O., Darras, T., Guccione, G., Cavaillès, A. & Laurat, J. Engineering optical hybrid entanglement between discrete-and continuous-variable states. *New J. Phys.* **21,** 083033 (2019).

192. Kiilerich, A. H. & Mølmer, K. Input-Output Theory with Quantum Pulses. *Phys. Rev. Lett.* **123,** 123604 (2019).

193. Kruszynska, C. & Kraus, B. Local entanglability and multipartite entanglement. *Phys. Rev. A* **79,** 052304 (2009).

194. Vitagliano, G., Riera, A. & Latorre, J. I. Volume-law scaling for the entanglement entropy in spin-1/2 chains. *New J. Phys.* **12,** 113049 (2010).

195. Zhang, Z., Ahmadain, A. & Klich, I. Novel quantum phase transition from bounded to extensive entanglement. *Proceedings of the National Academy of Sciences* **114,** 5142–5146 (2017).

196. Mlynek, J. A., Abdumalikov, A. A., Eichler, C. & Wallraff, A. Observation of Dicke superradiance for two artificial atoms in a cavity with high decay rate. *Nat Commun* **5,** 5186 (2014).

197. Esposito, M., Ranadive, A., Planat, L. & Roch, N. Perspective on traveling wave microwave parametric amplifiers. *Appl. Phys. Lett.* **119** (2021).

198. Esposito, M., Ranadive, A., Planat, L., Leger, S., Fraudet, D., Jouanny, V., Buisson, O., Guichard, W., Naud, C., Aumentado, J., *et al.* Observation of Two-Mode Squeezing in a Traveling Wave Parametric Amplifier. *Phys. Rev. Lett.* **128,** 153603 (2022).

199. Budini, A. A. Quantum systems subject to the action of classical stochastic fields. *Phys. Rev. A* **64,** 052110 (2001).

200. Van Kampen, N. G. Stochastic differential equations. *Physics reports* **24,** 171–228 (1976).

201. Zoller, P. Resonant multiphoton ionization by finite-bandwidth chaotic fields. *Phys. Rev. A* **19,** 1151 (1979).

202. Zoller, P. ac Stark splitting in double optical resonance and resonance fluorescence by a nonmonochromatic chaotic field. *Phys. Rev. A* **20,** 1019 (1979).

203. Cirac, J. I., Ritsch, H. & Zoller, P. Two-level system interacting with a finite-bandwidth thermal cavity mode. *Phys. Rev. A* **44,** 4541 (1991).

204. Chaturvedi, S. & Gardiner, C. Resonance fluorescence of a two-level atom driven by a fluctuating laser field: an application of a multiple time scale method. *J. Phys. B: Atom. Mol. Phys.* **14,** 1119 (1981).

205. Cresser, J. & Facer, C. Master equations with memory for systems driven by classical noise. *Optics Communications* **283,** 773–780 (2010).

206. Agarwal, G. Quantum statistical theory of optical-resonance phenomena in fluctuating laser fields. *Phys. Rev. A* **18,** 1490 (1978).

207. Yam, W., Renger, M., Gandorfer, S., Fesquet, F., Handschuh, M., Honasoge, K., Kronowetter, F., Nojiri, Y., Partanen, M., Pfeiffer, M., *et al.* Cryogenic microwave link for quantum local area networks. *arXiv:2308.12398* (2023).

208. Zanner, M., Orell, T., Schneider, C. M., Albert, R., Oleschko, S., Juan, M. L., Silveri, M. & Kirchmair, G. Coherent control of a multi-qubit dark state in waveguide quantum electrodynamics. *Nat. Phys.* **18,** 538–543 (2022).

209. Doherty, M. W., Manson, N. B., Delaney, P., Jelezko, F., Wrachtrup, J. & Hollenberg, L. C. The nitrogen-vacancy colour centre in diamond. *Physics Reports* **528,** 1–45 (2013).

210. Childress, L., Walsworth, R. & Lukin, M. Atom-like crystal defects: From quantum computers to biological sensors. *Physics Today* **67,** 38–43 (2014).

211. Evans, R. E., Bhaskar, M. K., Sukachev, D. D., Nguyen, C. T., Sipahigil, A., Burek, M. J., Machielse, B., Zhang, G. H., Zibrov, A. S., Bielejec, E., Park, H., Lončar, M. & Lukin, M. D. Photon-mediated interactions between quantum emitters in a diamond nanocavity. *Science* **362,** 662 (2018).

212. Nguyen, C. T., Sukachev, D. D., Bhaskar, M. K., Machielse, B., Levonian, D. S., Knall, E. N., Stroganov, P., Riedinger, R., Park, H., Lončar, M. & Lukin, M. D. Quantum Network Nodes Based on Diamond Qubits with an Efficient Nanophotonic Interface. *Phys. Rev. Lett.* **123,** 183602 (2019).

213. Ruf, M., Wan, N. H., Choi, H., Englund, D. & Hanson, R. Quantum networks based on color centers in diamond. *J. Appl. Phys.* **130** (2021).

214. Arrazola, I., Minoguchi, Y., Lemonde, M.-A., Sipahigil, A. & Rabl, P. Toward high-fidelity quantum information processing and quantum simulation with spin qubits and phonons. *Phys. Rev. B* **110,** 045419 (2024).

215. Dassonneville, R., Assouly, R., Peronnin, T., Clerk, A., Bienfait, A. & Huard, B. Dissipative Stabilization of Squeezing Beyond 3 dB in a Microwave Mode. *PRX Quantum* **2,** 020323 (2021).

216. Mollow, B. R. Power Spectrum of Light Scattered by Two-Level Systems. *Phys. Rev.* **188** (1969).

217. Yang, J., Strandberg, I., Vivas-Viana, A., Gaikwad, A., Castillo-Moreno, C., Kockum, A. F., Ullah, M. A., Munoz, C. S., Eriksson, A. M. & Gasparinetti, S. Entanglement of photonic modes from a continuously driven two-level system. *arXiv:2407.07991* (2024).

218. McDonald, A., Pereg-Barnea, T. & Clerk, A. A. Phase-Dependent Chiral Transport and Effective Non-Hermitian Dynamics in a Bosonic Kitaev-Majorana Chain. *Phys. Rev. X* **8,** 041031 (2018).

219. Gonzalez-Ballestero, C. Tutorial: projector approach to master equations for open quantum systems. *Quantum* **8,** 1454 (2024).

220. Georges, A. T. Resonance fluorescence in Markovian stochastic fields. *Phys. Rev. A* **21,** 2034 (1980).

221. Wilf, H. S. *generatingfunctionology* (CRC press, 2005).

222. Kauers, M. & Paule, P. *The Concrete Tetrahedron: Symbolic Sums, Recurrence Equations, Generating Functions, Asymptotic Estimates* (Springer, 2011).

# List of publications

1. J. Agustí, Y. Minoguchi, J. M. Fink, P. Rabl, "Long-distance distribution of qubit-qubit entanglement using Gaussian-correlated photonic beams", Phys. Rev. A **105**, 062454 (2022).

2. J. Agustí, X. H. H. Zhang, Y. Minoguchi, P. Rabl, "Autonomous Distribution of Programmable Multiqubit Entanglement in a Dual-Rail Quantum Network", Phys. Rev. Lett. **131**, 250801 (2023).

# Acknowledgments

This thesis is the culmination of more than four years of work, which I could not have accomplished alone. For this reason, I dedicate this last page to all the people I wish to thank:

First, I would like to thank my doctoral advisor, Prof. Dr. Peter Rabl, for the opportunity to pursue a PhD under his supervision. I cannot thank him enough for all the discussions, support, and inspiration he has given me.

I cannot thank Yuri Minoguchi enough for being my supervisor when it all started. I will always admire your insight and broad knowledge. My project would not have been the same without our many discussions.

This PhD started back in Vienna, and for that, I am grateful to all who welcomed me at the Freihaus and, later, at the Atominstitut. For that, I would like to thank Daniele, Julian, Iñigo, Rocío, Louis, Przemyk, and Aliya. The group then moved to the Walther-Meißner-Institut, where the group grew, and I want to thank Xin, Jacquelin, Lucia, Lukas, Gesa, Philipp, Franz, Philippe, and Adrián for enriching me scientifically and personally.

I cannot forget all the people at the Walther-Meißner-Institut who welcomed me and made it a very enjoyable experience. I want to thank Matze, Daniil, Kedar, Kevin, Leon, Max, David, Frederik, Florian, and Johannes, among many others, for all our beers and coffee breaks.

I want to express my gratitude to the people outside my research in Munich. For that, I thank you, Rafa, Laura, Andrés, Marta, Carla, Joan (and future Marina). I will never forget our time at the Englischer Garten playing volleyball, at the Isar enjoying a swim, or a nice paella.

I thank my parents, siblings, and cousins for the encouragement, support, and confidence they gave me more than four years ago when I decided to embark on this adventure.

Finally, I especially want to thank you, Maria. Thank you for being there, and thank you for all the patience you had, even though I told you four years ago that I would finish my PhD in two years. Thank you for coming to Munich at a time when I needed you the most. This thesis could not have been completed without your support. This thesis is the beginning of a new chapter together in Madrid.